Universidade de Aveiro Departamento de Física
2013

Ana Cordeiro Pires

Modelação da circulação na Margem Ibérica Ocidental: presente e futuro

Modeling the Western Iberian Margin circulation: present and future

Ana Cordeiro Pires

Modelação da circulação na Margem Ibérica Ocidental: presente e futuro

Modeling the Western Iberian Margin circulation: present and future

Dissertação apresentada à Universidade de Aveiro para cumprimento dos requisitos necessários à obtenção do grau de Doutor em Física, realizada sob a orientação científica do Doutor Jesús Dubert, Professor Auxiliar do Departamento de Física da Universidade de Aveiro, e da Doutora Rita Nolasco, Investigadora do Departamento de Física da Universidade de Aveiro

Apoio financeiro da Fundação para a Ciência e Tecnologia (FCT) através da bolsa de doutoramento SFRH/BD/47500/2008, no âmbito do Quadro de Referência Estratégico Nacional (QREN) e do Programa Operacional de Potencial Humano (POPH), comparticipado pelo Fundo Social Europeu e por fundos nacionais do Ministério da Ciência, Tecnologia e Ensino Superior (MCTES), agora Ministério da Educação e Ciência (MEC)

o júri / the jury

presidente / president

Valeri Skliarov
Professor Catedrático da Universidade de Aveiro (por delegação do Reitor da Universidade de Aveiro)

vogais / examiners committee

Jesús Manuel Pedreira Dubert
Professor Auxiliar da Universidade de Aveiro (orientador)

Xosé Antón Álvarez Salgado
Investigador Científico do Instituto de Investigaciones Marinas (IIM), CSIC, Vigo

Pablo Otero Tranchero
Investigador Contratado do Instituto Español de Oceanografía (IEO), A Coruña

Isabel Iglesias Fernández
Investigadora Pós-Doc do CIMAR, Universidade do Porto

Alfredo Moreira Caseiro Rocha
Professor Associado com Agregação da Universidade de Aveiro

agradecimentos

Os primeiros agradecimentos vão para o Prof. Jesús Dubert, por me ter dado esta oportunidade sem duvidar das minhas capacidades de a levar a cabo e por nunca perder o seu lado humano, tornando-o na pessoa mais atenciosa com quem já trabalhei, e para a Doutora Rita Nolasco, investigadora incansável, técnica de serviço, perfeccionista extrema, polivalente a um nível elevadíssimo, figura materna e excelente amiga. Estes agradecimentos estendem-se ao Prof. Alfredo Rocha pela troca de ideias e pelo seu importante contributo neste trabalho.

Quero agradecer também aos meus colegas de laboratório, sem os quais tudo teria sido muito mais difícil. À Rosa, pela sua generosidade, perseverança inspiradora e permanente bom humor, recordando-me constantemente de que não se varre uma rua num só dia. À Magda, companheira de longa data de caminhos tortuosos e uma lutadora afincada. À Fabíola e à Nayara, amigas de além-mar que vieram animar e enriquecer os programas sócio-culturais aveirenses, tal como o Daniel e a Ana Sousa. Ao Nuno, a minha boleia até meio-caminho de casa e companheiro de reuniões infindáveis, pela sua disponibilidade e pelas piadas ribeirinhas. À Ana Picado, Sandra, João, Ana Cristina, Carlos, Susana e Tiago, pela sua boa disposição. E, ainda, à Teresa por me ter recebido em sua casa.

Estes anos em Aveiro teriam sido mais solitários e tristes se não fosse pela presença, mesmo à distância, da Raquel, irmã em espírito, da Rita, a minha *Ohana*, da Sofia, do outro lado do mundo, da Ana Bento, em terras de Sua Majestade, da Irene, pelos Alentejos, e dos intrépidos companheiros de aventuras: Ricardo, Tomás, Pedro, Daniela, Ivo, Hugo, Filipa, a pequena Magui, Jorge, Carina, e agora a Catarina e a Rita. Um agradecimento também à Ana Machado e Ana Aguiar pelos piqueniques e trocas de ideias no relvado do IO.

Esta viagem não teria sido a mesma sem a minha maravilhosa estadia em Brest e sem ter conhecido os extraordinários Francesca, Nico, Rui, Xavier, Dhouha, Luís, Emanuella, Simone, Pierre, Guillaume, Camille, e todos os que me receberam de braços abertos no LPO/UBO, em especial Bernard Le Cann e Bruno Blanke.

Aos meus pais, deixo um agradecimento do fundo do coração, por toda a ajuda que me deram nestes longos e, por vezes, dolorosos anos e por me incitarem sempre a ser o melhor que posso ser. À minha família, em particular à Ângela e à Andreia, pelo casamento mais bonito e feliz que eu poderia ter desejado, e à família nova que ganhei, principalmente à Zé e à Sofia, pela sua força, coragem e generosidade.

Por fim, ao Alexandre, o meu porto seguro, o meu companheiro de centenas de viagens, geográficas e emocionais, e agora meu marido. Que isto tenha sido só o princípio da nossa história!

acknowledgements

My first acknowledgments go to Professor Jesús Dubert, for giving me this opportunity without questioning if I could see it through and for never losing his humanity, which makes him the most thoughtful person I have worked with, and to Doctor Rita Nolasco, tireless researcher, on-duty technician, thoroughly perfectionist, multitasker to a higher level, motherly figure and wonderful friend. These acknowledgements extend to Professor Alfredo Rocha, for his input and important contributions to this work.

I would also like to thank my working colleagues, without whom it would all have been much more difficult. To Rosa, for her generosity, inspiring resilience and constant good humor, always reminding me that a street cannot be swept in one day. To Magda, with whom I have walked many a long and winding road and who is an admirable fighter. To Fabíola and Nayara, friends from beyond the seas who have come to cheer up and improve Aveiro's social and cultural programs, and also Daniel and Ana Sousa. To Nuno, my ride to halfway home and companion of endless meetings, for his availability and un-funny jokes. To Ana Picado, Sandra, João, Ana Cristina, Carlos, Susana and Tiago, for their high spirits. And finally to Teresa, for having received me in her home.

These years in Aveiro would have been lonelier and sadder if not for the presence, even at a distance, of Raquel, my soul sister, Rita, my *Ohana*, Sofia, on the other side of the world, Ana Bento, on Her Majesty's land, Irene, in Alentejo, and my intrepid adventure companions: Ricardo, Tomás, Pedro, Daniela, Ivo, Hugo, Filipa, little Magui, Jorge, Carina, and lately Catarina and Rita. A thank you also to Ana Machado and Ana Aguiar for the conversations and lunch picnics outside IO.

This journey would not have been the same without my wonderful stay in Brest and if I had not met the extraordinary Francesca, Nico, Rui, Xavier, Dhouha, Luís, Emanuella, Simone, Pierre, Guillaume, Camille, and all those who have received me arms wide open at LPO/UBO, especially Bernard Le Cann and Bruno Blanke.

To my parents, I leave a thank you from the bottom of my heart, for all the help they have given me throughout these long and sometimes painful years, and for urging me to always be the best I can be. To my family, particularly to Ângela and Andreia, for having given me the happiest and most beautiful wedding I could have wished for, and to the family I was adopted into, especially Zé and Sofia, for their strength, courage and generosity.

Last but not least, to Alexandre, my safe haven, my companion of hundreds of journeys, both geographical and emotional, and now my husband. Let this be just the beginning of our story!

Palavras-chave

Península Ibérica, afloramento costeiro, alterações climáticas, IPCC, modelação oceânica regional, ROMS, dinâmica costeira, hidrografia, ecossistema, larvas, estado médio, variabilidade inter-anual.

Resumo

O objectivo deste trabalho é realizar um estudo abrangente da circulação na Margem Ibérica Ocidental (WIM) através da modelação numérica, e postular sobre como essa circulação será no futuro. A abordagem adoptada foi o desenvolvimento de uma configuração regional de alta resolução num modelo oceânico, capaz de reproduzir a dinâmica de larga e pequena escala na zona de transição costeira.

Quatro experiências numéricas foram efectuadas para este efeito: (1) uma corrida climatológica, a fim de estudar o comportamento sazonal do sistema e caracterizar o estado médio; (2) uma corrida forçada com ventos e fluxos reais para o período de 2001-2011, a fim de estudar a variabilidade inter-anual do sistema; (3) uma corrida forçada com campos médios de modelos climáticos globais (GCMs) para o presente, a fim de validar GCMs como forçamento adequado para modelação oceânica regional; (4) semelhante à corrida (3) para o período 2071-2100, a fim de avaliar possíveis consequências de um cenário climático futuro na hidrografia e dinâmica da WIM. Para além disso, foram realizados dois estudos com partículas Lagrangianas: um a fim de traçar a origem das águas afloradas ao longo da WIM; outro a fim de retratar os padrões de dispersão, acumulação e conectividade larval.

Constatou-se que a configuração numérica é adequada para a reprodução do estado médio do sistema, caracterização sazonal e estudo da variabilidade inter-anual. Concluiu-se que há prevalência de escoamento para o pólo junto à vertente, fluxo este que co-existe com o jacto de afloramento no Verão, embora haja evidência do seu desvio para o largo, e que está associado ao escoamento da Água Mediterrânica nos níveis inferiores, sugerindo um carácter barotrópico. Da aplicação de um futuro cenário climático retiraram-se as seguintes conclusões: há um aquecimento e um decréscimo de salinidade generalizados nos níveis superiores; a tendência para o escoamento para o pólo mantém-se, e apesar da intensificação dos ventos favoráveis ao afloramento no Verão a respectiva banda costeira está mais restringida em largura e profundidade. No que diz respeito à conectividade e dispersão larval ao longo da WIM, observou-se que a migração vertical diurna aumenta o recrutamento em todo o domínio, e enquanto que as linhas de costa mais suaves são melhores fornecedores, há maior acumulação em zonas de topografia mais recortada.

Keywords Iberian Peninsula, coastal upwelling, climate change, IPCC, regional ocean modeling, ROMS, coastal dynamics, hydrography, ecosystem, larvae, mean state, interannual variability.

Abstract The purpose of this work is to carry out a comprehensive study on the Western Iberian Margin (WIM) circulation my means of numerical modeling, and to postulate what this circulation will be in the future. The adopted approach was the development of a regional ocean model configuration with high resolution, capable of reproducing the large- and small-scale dynamics of the coastal transition zone.
Four numerical experiences were carried out according to these objectives: (1) a climatological run, in order to study the system's seasonal behavior and its mean state; (2) a run forced with real winds and fluxes for period 2001-2011 in order to study the interannual variability of the system; (3) a run forced with mean fields from Global Climate Models (GCMs) for the present, in order to validate GCMs as adequate forcing for regional ocean modeling; (4) a similar run (3) for period 2071-2100, in order to assess possible consequences of a future climate scenario on the hydrography and dynamics of the WIM. Furthermore, two Lagrangian particle studies were carried out: one in order to trace the origin of the upwelled waters along the WIM; the other in order to portrait the patterns of larval dispersal, accumulation and connectivity.
The numerical configuration proved to be adequate in the reproduction of the system's mean state, seasonal characterization and an interannual variability study. There is prevalence of poleward flow at the slope, which coexists with the upwelling jet during summer, although there is evidence of its shifting offshore, and which is associated with the Mediterranean Water flow at deeper levels, suggesting a barotropic character. From the future climate scenario essay, the following conclusions were drawn: there is general warming and freshening of upper level waters; there is still poleward tendency, and despite the upwelling-favorable winds strengthening in summer the respective coastal band becomes more restricted in width and depth. In what concerns larval connectivity and dispersion along the WIM, diel vertical migration was observed to increase recruitment throughout the domain, and while smooth coastlines are better suppliers, there is higher accumulation where the topography is rougher.

Contents

List of Figures

List of Tables

Acronyms

AzC Azores Current

CGCM Coupled Global Climate Model

COADS Comprehensive Ocean Atmosphere Data Set

DVM Diel Vertical Migration

E-P Evaporation minus Precipitation

EKE Eddy Kinetic Energy

ENACW Eastern North Atlantic Central Water (sp: subpolar origin; st: subtropical origin)

EOF Empirical Orthogonal Functions

EP Estremadura Promontory

FD First Domain

GCM Global Climate Model

GHER-NEA GeoHydrodynamics and Environmental Research - NorthEast Atlantic climatology

GR Galician Rias

IBM Individual Based Model

IPC Iberian Poleward Current

IPCC Intergovernmental Panel for Climate Change

LW Long Wave flux

MAR Mid-Atlantic Ridge

MW Mediterranean Water

NC Northern Coast

NCEP/NCAR National Center for Atmospheric Research / National Centers for Environmental Prediction reanalysis data

NH Net Heat balance flux

RMSE Root Mean Square Error

ROMS Regional Ocean Modelling System

S Salinity

SC Southern Coast

SD Second Domain

SH Specific Humidity

SLP Sea Level Pressure

SSS Sea Surface Salinity

SST Sea Surface Temperature

SW Short Wave flux

Tx Wind stress zonal component

Ty Wind stress meridional component

u Wind zonal component

UI Upwelling Index

v Wind meridional component

WIBP Western Iberian Buoyant Plume

WIM Western Iberian Margin

WOA World Ocean Atlas

Chapter 1

Introduction

1.1 Overview, Motivation and Objectives

Portugal is often called "the little corner planted by the sea" by its natives because, with a shape strongly resembling a rectangle, two of its four sides are bathed by ocean. For a small country (roughly 92,000 km^2), it possesses almost 1,000 km of coast (islands not included). Therefore, the sea has always played a major role throughout its history, since before the Discovery travels in the 15th and 16th centuries. Furthermore, the ocean has always provided numerous resources, and was once the sole means of income for the majority of the port towns along the Portuguese coast. Portugal's location, besides bestowing it with the most tender of climates, is most fortunate for fisheries, since it corresponds to an ocean eastern boundary and therefore favorable for the occurrence of coastal upwelling, a phenomenon that strongly stimulates primary productivity. Fisheries are still an important trade nowadays.

Moreover, it is well known that the ocean is a key factor of the climate system; it absorbs large quantities of heat in the tropics and re-distributes it throughout the planet by means of the large-scale ocean currents that compose the thermohaline circulation (e.g. Pond and Pickard, 1983). The ocean is also a very efficient CO_2 sink, which has been of the utmost importance given the alarming increase of this greenhouse gas emission in the last decades, and the consequent increase in global temperatures (e.g. Hansen et al., 2010). How much heat and CO_2 can the ocean absorb, and how have these quantities changed in the past decades, have been questions addressed by many environmental works (e.g. Levitus et al., 2001; Levitus et al., 2012). The warming of the world's oceans has also been increasingly documented in recent years (e.g. Levitus et al., 2000, 2005; Casey and Cornillon, 2001; Domingues et al., 2008; among others).

These considerations are also true for the coastal ocean. Coastal thermohaline characteristics define the marine species that inhabit these waters and their life cycle and migration patterns, whereas the regional hydrography defines the regional dynamics and the way these properties are transported. In the case of Portugal, for a country so dependent on maritime resources for its economy, whether directly related like fisheries or indirectly

related like tourism, understanding the dynamics of the coastal ocean and studying present and future changes at different space and time scales becomes relevant.

The aim of this work was to carry out, by means of numerical modeling, a comprehensive study of the Western Iberian coastal ocean circulation at the upper levels. First, a thorough description of its seasonality and mean hydrography and dynamics was performed, including an essay on the origin of upwelled waters in summer. Second, a study focusing on the system's interannual variability followed, based on an 11-year simulation and the analysis of temperature anomalies, salinity, and meridional transport. By the application of a climate change future scenario to our ocean model, the consequences at the ocean's upper layers were evaluated in terms of mean thermohaline distribution and dynamics. Finally, a Lagrangian module was applied in order to address larval distribution and behavior in this region. The region and sub-regions are described in section 1.3. The regional modeling configurations are described in section 1.4, and all the respective runs are summarized in section 1.5.

1.2 The Eastern North Atlantic Ocean

The North Atlantic (Figure 1.1, after Tomczak and Godfrey, 2003) is dominated at mid-latitudes by the typical Subtropical Gyre, which is composed by the Gulf Stream, flowing northeastward along the eastern North America coast that in turn bifurcates at about 40^oN, 45^oW into two other large-scale currents: the North Atlantic Current, which flows northward/northeastward into the Arctic Ocean, and the Azores Current (AzC), which consists in the northern limit of the gyre. Within the gyre at the bottom of the ocean lies the Mid-Atlantic Ridge (MAR), a strong bathymetric feature that splits the North Atlantic into approximately two halves (an eastern and a western one), and reaches in average 2000 m but can rise to less than 1000 m (Tomczak and Godfrey, 2003). The AzC crosses the MAR at about 35^oN, 45^oW, after which it flows eastward in a mostly zonal pathway along $\sim 34^o$N. In the proximity of the European southwestern coast, it veers southward, partly recirculating in the Gulf of Cadiz (Peliz et al., 2007) and partly joining the Canary Current along the northwestern African coast (Barton et al., 1998). The loop of the gyre closes with the westward-flowing North Equatorial Current that links to the Gulf Stream by means of the Central America eastern coast complex current system (Tomczak and Godfrey, 2003). The eastern boundary current system is concluded with the weak large-scale current that flows mostly southward along the Iberian Peninsula, frequently named the Portugal Current, with typical velocities of a few centimeters per second (Saunders, 1982).

The Eastern North Atlantic is one of the world's main eastern boundary current systems, also called Eastern Boundary Upwelling Systems. Eastern boundaries have in common the fact that, in summer, atmospheric high-pressure systems relocate to the mid-latitudes and in the proximity of the western coasts. In particular for the Eastern North Atlantic, the wind regime is dictated by the relative location of the anticyclonic system of the Azores High and the cyclonic system of the Iceland Low. The position of the Azores

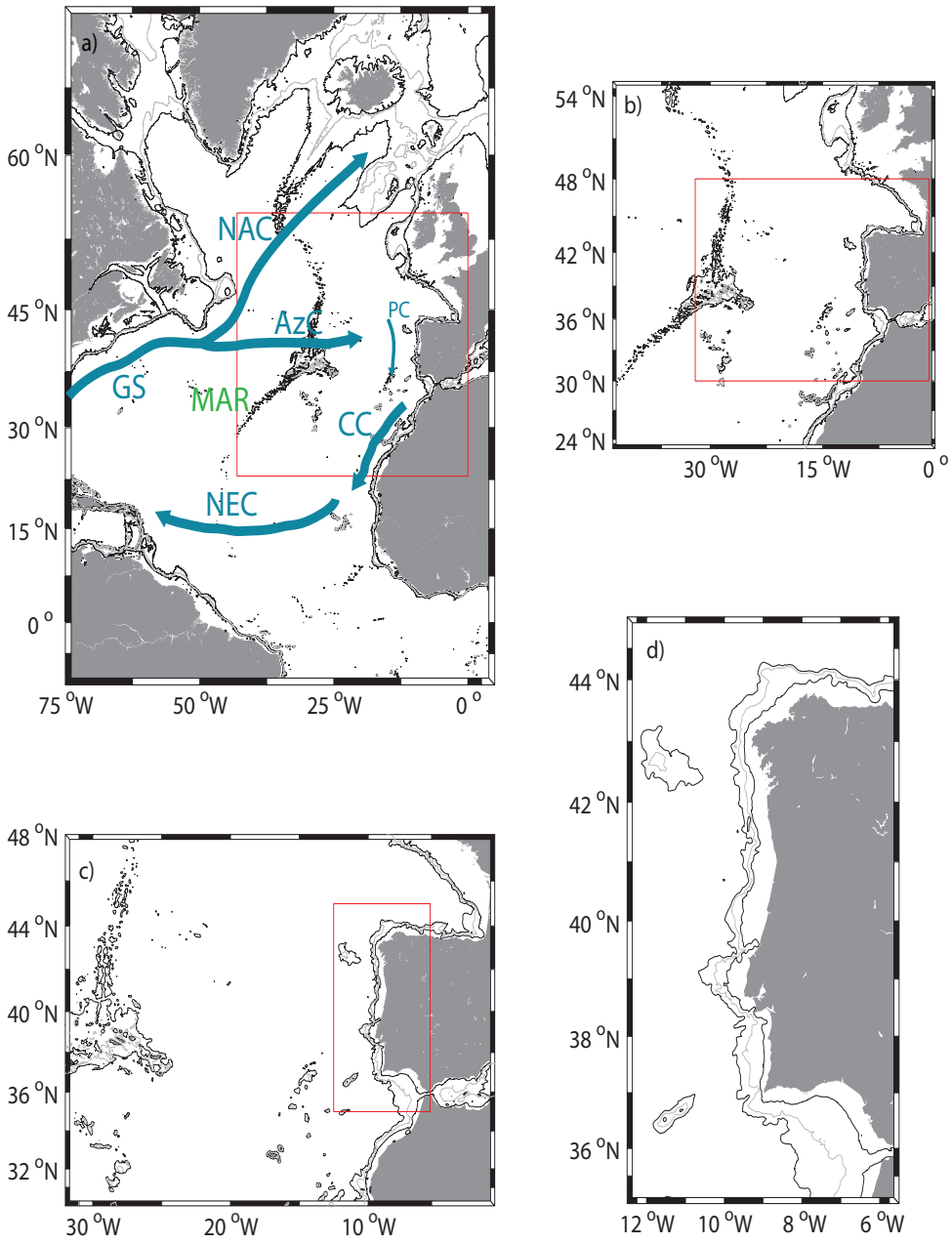

Figure 1.1: The four areas focused on this study. (a) North Atlantic; (b) Eastern North Atlantic Basin (ENAB); (c) Iberian Basin; (d) Western Iberian Margin (WIM). The main currents are shown for the North Atlantic (after Tomczak and Godfrey, 2003): the Gulf Stream (GS); the North Atlantic Current (NAC); the Azores Current (AzC); the Canary Current (CC); the Portugal Current (PC); the North Equatorial Current (NEC). The 200-m, 1000-m and 2000-m isobaths are shown and the Mid-Atlantic Ridge (MAR) is indicated.

High oscillates between northern locations off the Iberian Peninsula during summer and a southern position during winter in front of Morocco, while the Iceland low intensifies leaving room to the eastward passage of low pressure systems, that introduce a strong variability in the circulation at the Iberian Peninsula during wintertime. These atmospheric regimes are the reason why in late spring and summer there is coastal upwelling. Its dynamics will be further discussed in section 1.3.1.

The eastern North Atlantic upwelling system differs from the others in that it is interrupted in the Strait of Gibraltar, being divided in a northern upwelling region — the western coast of the Iberian Peninsula — and a southern one in the region of the Canary Current. That is why this system is also called the Canary Upwelling System (Barton et al., 1998). The Strait of Gibraltar divides the Atlantic Ocean from the Mediterranean Sea, enclosed between Europe and Africa. This gap between the two continents gives rise to the other most important dynamical feature of this region: the Mediterranean Water outflow into the Atlantic, further detailed in section 1.3.2.

This is thus the environment of the small region under scope that is the coastal transition zone off the western coast of the Iberian Peninsula, henceforth called the Western Iberian Margin (WIM), described below. The main rivers and topographic features are shown in Figure 1.2 b.

1.3 The Western Iberian Margin (WIM)

1.3.1 Shelf/Slope Circulation

a. Coastal Upwelling

The summer mid-latitude high pressure systems described in the previous section produce equatorward winds (northerly in the northern hemisphere, southerly in the southern hemisphere) along the coast, which results in an offshore displacement of surface warm waters and rising of deep, cool, nutrient-rich waters to replace them (e.g. Wooster et al., 1976). When the wind blows, a current is created at the ocean surface with a direction 45^o to the right of the wind direction (northern hemisphere) due to the Coriolis effect. The action of wind stress is felt in the water column down to the basis of the so-called Ekman layer, which has typical several tens of meters ($<$100 m). In this layer, successive water levels undergo the same effect as the surface, that is, deflection of velocity to the right, while the velocity's module weakens in depth. The result is a spiral with a net water transport perpendicular to wind stress — the Ekman transport, which can be computed as follows:

$$\vec{Q}_{EK} = \frac{\vec{\tau} \times \vec{k}}{f} \tag{1.1}$$

where $\vec{\tau}$ is the wind stress, $\vec{k}$ is the unitary vector perpendicular to $\vec{\tau}$ and $f = 2\Omega \sin\theta$ is the Coriolis parameter (Ω is the rotational velocity of the Earth and θ the latitude).

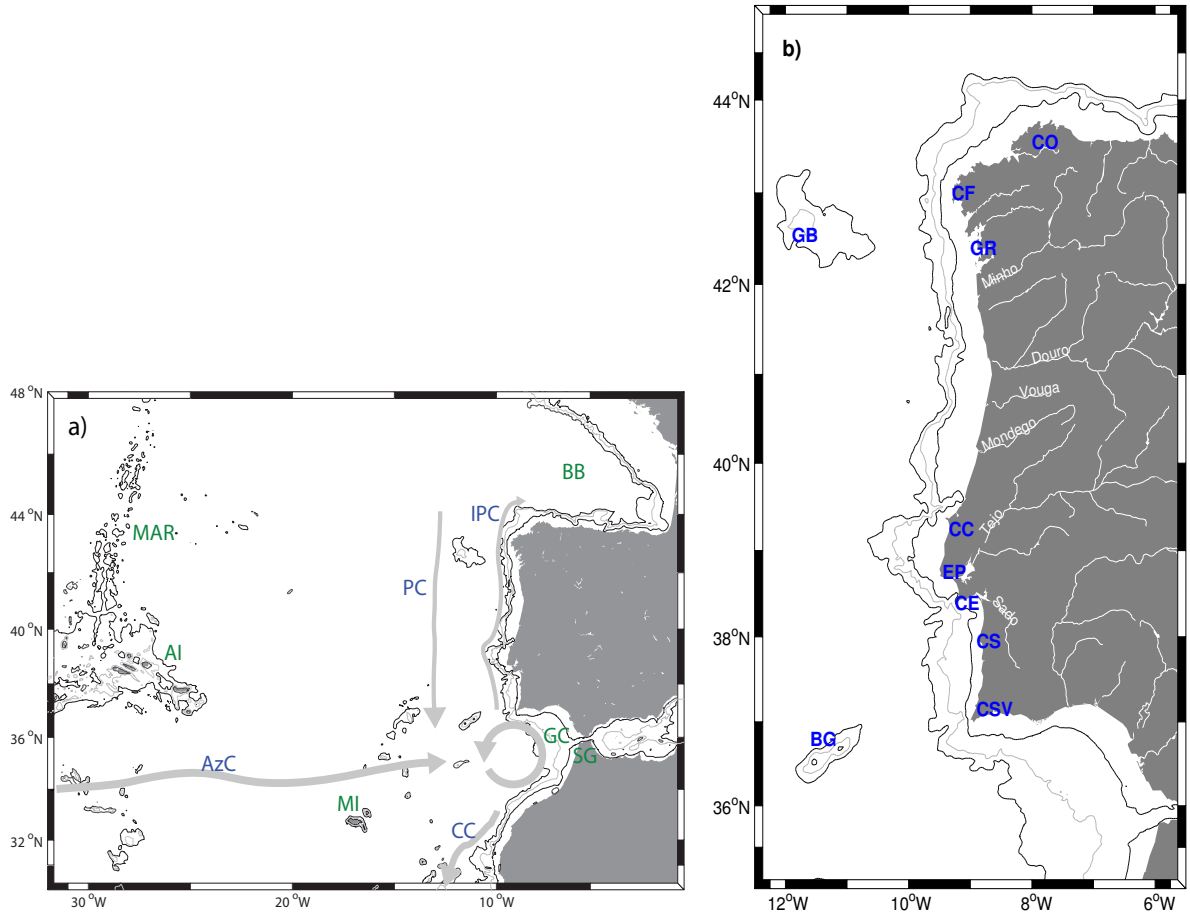

Figure 1.2: Map of the two main regions of study, corresponding to the two numerical configurations. (a) the large domain (FD) and a schematics of the mean currents. Coastline features labeled in black (BB: Bay of Biscay; GC: Gulf of Cadiz; SG: Strait of Gibraltar; AI: Azores Islands; MI: Madeira Islands). Dynamical features labeled in blue (IPC: Iberian Poleward Current; PC: Portugal Current; AzC: Azores Current; CC: Canary Current). (b) the high-resolution domain (SD) marked with the main bathymetric and topographic features: Cape St Vincent (CSV), Gorringe Bank (BG), Cape Sines (CS), Cape Espichel (CE), Estremadura Promontory (EP), Cape Carvoeiro (CC), Galicia Bank (GB), Galicia Rias (GR), Cape Finisterre (CF) and Cape Ortegal (CO). Isobaths 200 m and 2000 m are shown in black, and 1000 m in gray. The main rivers are also indicated in white.

The Ekman transport causes divergence at the upper layers (lowering of the sea surface at the coastal boundary). This in turn causes convergence in the lower layers, inducing onshore motion. These waters then rise when approaching the coast and replace the ones advected offshore.

These upwelled waters are then advected equatorward because a coastal jet is created due to the rising of the isotherms and the geostrophic balance that is created between the consequent pressure gradient and the Coriolis force. This alongshore jet has its maximum speed at mid-shelf, weakening seaward and also toward the coast due to friction.

Another mechanism that generates vertical upward velocities is the Ekman pumping, which occurs due to wind stress curl near the coast. This curl exists because, when approaching land, wind stress decreases due to friction. Vertical velocities due to Ekman pumping are computed as follows:

$$w_{EK} = \frac{1}{\rho f}\left(\frac{\partial \tau_y}{\partial x} - \frac{\partial \tau_x}{\partial y}\right) \tag{1.2}$$

Lower level waters are rich in nutrients and thus promote phytoplankton blooms when reaching the surface, which in turn are the crucial factor for primary productivity (Relvas et al., 2007). This is why upwelling systems are some of the most productive regions of the world's ocean.

b. Poleward Flow

Besides the upwelling circulation during late spring and summer, the large-scale temperature and salinity meridional gradients (Peliz et al., 2003b), which dictate the thermohaline structure of the water masses, together with wind forcing, promote a system of poleward currents along the Atlantic Iberian Peninsula observed mainly during autumn and winter, as described in the classic references of Frouin et al. (1990) and Haynes and Barton (1990) for the western Iberian Peninsula, and continuing along the Bay of Biscay as described by Pingree and Le Cann (1990). This northward circulation is typical of mid-latitude eastern continental margins (Neshyba, 1986). A consensual denomination for this poleward flow is the Iberian Poleward Current (IPC). The classic view of the IPC presents it as an upper-slope baroclinic current, associated with the downwelling of the isopycnal field in a width of about 40 km, and positive temperature and salinity anomalies from the surface down to typically 400 m. It was suggested that poleward flows are not a winter phenomenon only, but are present throughout the year (Peliz et al, 2005; Relvas et al., 2007).

There is another factor at play in the WIM shelf circulation that originates from freshwater input from the many rivers along the coast (see Figure 1.2 b), which consists in recurrent lenses of low salinity water in the upper 10-20 m close to the coast, that can be advected offshore. Peliz et al. (2002) have named it Western Iberian Bouyant Plume (WIBP) and determined its maximum salinity in 35.7. The WIBP is more evident and frequently wider in winter due to the stronger river discharge in that season. The IPC sometimes works as a barrier for the offshore displacement of the WIBP (Santos et al.,

2004). In summer and in the presence of coastal upwelling, the WIBP is advected both equatorward and offshore through the Ekman layer (Peliz et al., 2002).

1.3.2 Mediterranean Water Outflow

Upon exiting the 300-m deep Strait of Gibraltar, the dense Mediterranean Water (MW) flows downslope within the Gulf of Cadiz until it reaches neutral buoyancy. The intermediate-level resulting current is denoted Mediterranean Undercurrent in the Gulf of Cadiz (Ambar and Howe, 1979a) and Mediterranean Water Vein along the Western Iberian Peninsula (Daniault et al., 1994). Here, it flows at mid-depths often in two cores, typically at 800 m (the upper core), where a temperature maximum is reached, and at 1200 m (the lower core), the depth at which the salinity maximum is found. The signature of the hydrographic properties of both cores attenuates (specially the upper core) poleward along the Western Iberian Peninsula. Associated with this flow, there are mesoscale structures that are formed and which are responsible for a relevant part of this water mass properties transport: the Mediterranean eddies (Meddies), anticyclonic vortices with radii of several tens of kilometers, occurring typically between 700 m and 1300 m deep (Bower et al., 1995). Meddies propagate typically southwestward into the North Atlantic (Richardson et al., 2000). MW is further discussed in the following sub-section.

1.3.3 Water Masses

Figure 1.3 shows a typical θ-S diagram for WIM, adapted from Fiúza et al. (1998). The least dense waters correspond to near-surface waters ($\sigma_\theta < 26.6$), reflecting their strong seasonal variability. These waters have temperatures varying between 14^oC and more than 20^oC. Salinities lower than 35.7 in the surface water density range are the signature of the WIBP.

The upper limit of the central waters is identified by a salinity maximum found in the interval $26.5 < \sigma_\theta < 27$, with values varying between 36.0 and 36.2. According to Ríos et al. (1992), two types of central waters can be identified off Western Iberian Peninsula: Eastern North Atlantic Central Water of subpolar origin (ENACW_{sp}) and Eastern North Atlantic Central Water of subtropical origin (ENACW_{st}). ENACW_{sp} is related with Subpolar Mode Water, which forms due to deep convection that occurs during winter north of 46^oN (McCartney and Talley, 1982). The ENACW_{st}, formed to the north of the Azores Current at approximately 35^oN, is advected northwestward.

The basis of the ENACW_{sp} is characterized by a salinity minimum (~ 35.6 at the WIM) and marks the transition toward the Mediterranean Water (MW). The MW flows through the Gulf of Cadiz and the entire basin with a typical tongue structure, reaching the Bay of Biscay as described in the literature and as observed in many available climatologies (Reynaud et al., 1998; Iorga and Lozier, 1999; Troupin et al., 2010). Two cores can be distinguished: a less dense ($\sigma_\theta \sim$ 27.5-27.6) upper core (MW_U), with typical values found along the WIM of θ = 11-12^oC and S = 36.1-36.2; and a denser ($\sigma_\theta \sim 27.8$) lower core

(MW_L), with a lower temperature (θ<11^oC) and a higher salinity (S = 36.3-36.4) (Ambar and Howe, 1979b).

The deeper waters (below MW) are not within the scope of this work, but they influence the intermediate levels and hence a brief description follows. The two most important are the Labrador Sea Water (LSW) and the North Atlantic Deep Water (NADW). The LSW is characterized by very low salinities ($\sim$ 34.9) and $\theta = 3.50^oC$. These values were measured near the Mid-Atlantic Ridge at about 50^{o}N (Talley and McCartney, 1982). The NADW has higher salinities and lower temperatures than the LSW, and was defined by Saunders (1982) as $\theta = 2.50^oC$ and S = 34.94.

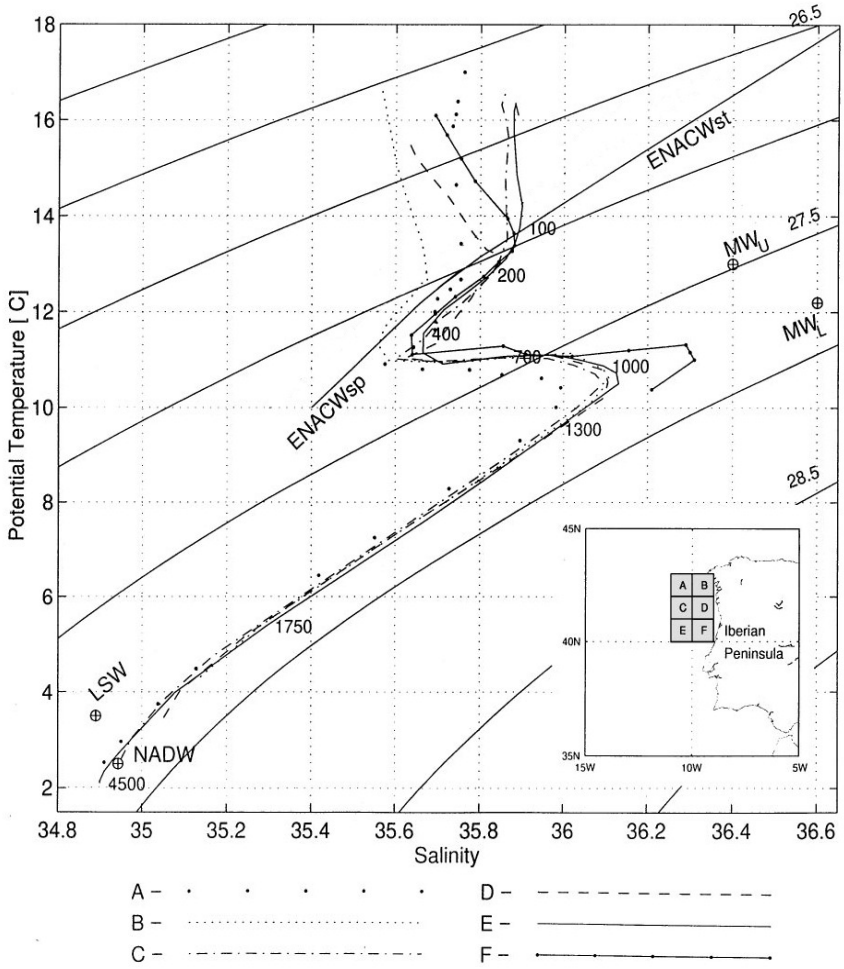

Figure 1.3: Typical θ-S diagram for the Western Iberian Margin (adapted from Fiúza et al., 1998). θ and S values correspond to a climatological dataset described in Fiúza et al. (1998) for the 6 regions showed in the map in the lower right corner of the Figure.

1.4 Regional Modeling

1.4.1 Overview

The numerical study of the circulation of the WIM is a challenge for modelers, for several reasons: i) the presence of a narrow shelf and a steep slope, as well as the presence of numerous canyons and promontories, requiring high resolution to properly resolve the shelf/slope circulation; ii) the presence of a unique oceanographic feature, which is the Mediterranean outflow, generated at the Strait of Gibraltar and spreading into the north-eastern Atlantic giving rise to the large scale MW anomaly; iii) the strong influence of the open ocean circulation (the Azores Current system and meridional pressure gradients) on the coastal transition zone, that forces the circulation in this region.

Eastern boundary currents, due to their complexity and to the importance in studying the upwelling phenomenon, have been the subject of several regional modeling studies over the past years. The following works are important efforts toward a better knowledge of the dynamics of these systems: Marchesiello et al. (2003), concerning the California Current System; Penven et al. (2005), who focused on the Peru Current System; Veitch et al. (2010), with respect to the Benguela Current System; and Mason et al. (2011) for the Canary Current System.

In what concerns numerical modeling regional studies at the full scale of the region, some previous works contributed to the study of this particular circulation. Some of them were carried out at a resolution of about 9 km (Stevens et al., 2000; Coelho et al., 2002) and focused on spring and winter circulation; others were idealized studies at a high resolution (Røed and Shi, 1999; Peliz et al., 2003a). Batteen et al. (2000, 2007) carried out sensitivity studies in order to assess the different mechanisms controlling the circulation in the region. The study by Serra et al. (2010) resolves the circulation in this region with realistic forcing and very high resolution, focusing on the study of the influence of the MW vein on the surface circulation, with emphasis on the mesoscale phenomena. On the other hand, from the point of view of operational oceanography of the Western Iberian Margin, Mateus et al (2012) focused on the application of an operational configuration ($\sim 1/16^o$ resolution) to discuss its potential for products and services for scientific and coastal management activities. In the neighborhood of the region, and also at a high resolution, Friocourt et al. (2007) and Peliz et al. (2007) studied the Bay of Biscay and the Gulf of Cadiz circulation, respectively.

In this light, the purpose of this work is to carry out a comprehensive study of the entire region, where all the factors that dictate its dynamics are taken into account, including river discharge and the Mediterranean Water flow, all combined to address different aspects of the current system.

1.4.2 The Model (Regional Ocean Modelling System — ROMS)

ROMS is a free-surface, terrain following coordinate model, designed to resolve regional problems (Shchepetkin and McWilliams, 2003, 2005). ROMS solves the incompressible

primitive equations based on the Boussinesq and hydrostatic approximations, and is coupled with advection/diffusion schemes for potential temperature and salinity as well as a nonlinear equation of state.

A brief account of the main equations, approximations and parameterizations follows.

The equation of state (ρ is the sea water density) depends on temperature (T), salinity (S) and pressure (p):

$$\rho = \rho\ (T,\ S,\ p) \tag{1.3}$$

The primitive equations of the ocean state obey the laws of conservation of properties, such as mass (equation of continuity):

$$\frac{d\rho}{dt} + \rho \nabla . \vec{u} = 0 \tag{1.4}$$

where $\vec{u} = u\ \vec{e_x} + v\ \vec{e_y} + w\ \vec{e_z}$ and, through the principle of fluid incompressibility ($d\rho/dt = 0$), gives:

$$\nabla . \vec{u} = 0 \tag{1.5}$$

The conservation of momentum (the equation of motion), based on Netwon's 2nd law of motion ($\vec{F} = m\ \vec{a}$) is:

$$\frac{d\vec{u}}{dt} = -\frac{\nabla p}{\rho} - 2\vec{\Omega} \times \vec{u} + \vec{g} + \vec{\mathcal{F}} + \vec{\mathcal{D}} \tag{1.6}$$

where on the right hand of the equation are (from left to right) the pressure gradient force, the Coriolis force, gravity, friction and dissipation. Likewise, the equations of conservation of heat and salt are, respectively:

$$\frac{dT}{dt} = \vec{\mathcal{F}}_T + \vec{\mathcal{D}}_S \quad \text{and} \quad \frac{dS}{dt} = \vec{\mathcal{F}}_S + \vec{\mathcal{D}}_S \tag{1.7}$$

The vertical component is obtained through the hydrostatic approximation, which considers that w and $\partial w/\partial t$ are very small in comparison with the horizontal velocities and their variation in time. Thus, gravity balances the vertical pressure gradient.

The equations of motion also assume the Boussinesq approximation for geostrophic currents (that is, when the Coriolis force balances the horizontal pressure gradient), which states that horizontal variations of density are negligible except in the buoyancy term. Hence, the previous conservation equations can be expressed as:

$$\frac{\partial u}{\partial t} = -u\frac{\partial u}{\partial x} - v\frac{\partial u}{\partial y} - w\frac{\partial u}{\partial z} + fv - \frac{1}{\rho}\frac{\partial p}{\partial x} + \mathcal{F}_u + \mathcal{D}_u \tag{1.8a}$$

$$\frac{\partial v}{\partial t} = -u\frac{\partial u}{\partial y} - v\frac{\partial v}{\partial y} - w\frac{\partial v}{\partial z} - fu - \frac{1}{\rho}\frac{\partial p}{\partial y} + \mathcal{F}_v + \mathcal{D}_v \tag{1.8b}$$

$$\frac{\partial p}{\partial z} = -\rho g \tag{1.8c}$$

$$\frac{\partial T}{\partial t} = -u\frac{\partial T}{\partial x} - v\frac{\partial T}{\partial y} - w\frac{\partial T}{\partial z} + \mathcal{F}_T + \mathcal{D}_T \tag{1.8d}$$

$$\frac{\partial S}{\partial t} = -u\frac{\partial S}{\partial y} - v\frac{\partial S}{\partial y} - w\frac{\partial S}{\partial z} + \mathcal{F}_S + \mathcal{D}_S \tag{1.8e}$$

$$0 = \frac{\partial u}{\partial x} + \frac{\partial v}{\partial y} + \frac{\partial w}{\partial z} \tag{1.8f}$$

where x, y, z are the Cartesian coordinates; u, v, w are the velocity $\vec{u}$ Cartesian components; f is the Coriolis parameter ($f = 2\Omega\sin(\theta)$, where Ω is the angular velocity of the Earth and θ the latitude; $\rho = \rho_0 + \rho$' is the sea water density (ρ_0 the average density and ρ' the perturbation); g the acceleration of gravity.

The vertical boundary conditions imposed to the model configurations are as follows:

at the top: z = ζ

$$\kappa_M\frac{\partial u}{\partial z} = \tau_s^x \tag{1.9a}$$

$$\kappa_M\frac{\partial v}{\partial z} = \tau_s^y \tag{1.9b}$$

$$\kappa_T\frac{\partial T}{\partial z} = \frac{Q_T}{\rho_0 C_p} \tag{1.9c}$$

$$\kappa_S\frac{\partial S}{\partial z} = \frac{(E-P)S}{\rho_0} \tag{1.9d}$$

$$w = \frac{\partial \zeta}{\partial t} + u\frac{\partial \zeta}{\partial x} + v\frac{\partial \zeta}{\partial y} \tag{1.9e}$$

at the bottom: z = -h

$$\kappa_M\frac{\partial u}{\partial z} = \tau_b^x \tag{1.10a}$$

$$\kappa_M\frac{\partial v}{\partial z} = \tau_b^y \tag{1.10b}$$

$$\kappa_T\frac{\partial T}{\partial z} = 0 \tag{1.10c}$$

$$\kappa_S\frac{\partial S}{\partial z} = 0 \tag{1.10d}$$

$$w = -u\frac{\partial H}{\partial x} - v\frac{\partial H}{\partial y} \tag{1.10e}$$

where ζ is the free surface elevation; $\kappa_M, \kappa_T, \kappa_S$ are the vertical turbulent mixing coefficients; τ_s^x, τ_s^y are the surface wind stress components; τ_b^x, τ_b^y are the bottom stress components (parameterized); Q_T is the surface heat flux; C_p is the heat capacity of the ocean; $E-P$ is the evaporation minus precipitation; H is the resting thickness of the water column.

ROMS coordinates are topography-following (or σ coordinates), which means that there are the same number of levels near the coast than at locations with higher depths. Taking this into account, a stretching factor is applied to the surface (θ_s) and to the bottom (θ_b), in order to define where to attribute the best resolution (surface or bottom). If θ_s is large, then σ levels are more concentrated in the surface, providing it a finer resolution; if $\theta_b = 1$ ($0 < \theta_b < 1$), then it is the bottom that is enhanced.

During the equations discretization process, which is carried out on an Arakawa C grid (meaning that u and v are defined on the grid lines and all other variables inside each grid cell), it is necessary to add a bathymetry correction for the slope, as to smooth the transition toward shallower depths. This criterion of stability is defined as:

$$r = \frac{\delta h}{2h} \tag{1.11}$$

where δh is the depth difference between neighbor cells, h is the local depth.

The advection scheme is based on the work done by Marchesiello et al. (2009), in order to reduce spurious diapycnal mixing in σ-coordinate models characteristic of higher-order diffusive advection schemes. This scheme involves the split of advection and diffusion, as a biharmonic operator. Lateral viscosity is set to zero, except in the sponge layers, where it increases linearly toward the boundaries of the model. Vertical mixing consists in the KPP (K-profile parameterization) scheme (Large et al., 1994).

To this set of equations must be added, to a given configuration, a set of initial and boundary conditions, as well as surface forcing, which will be detailed in part in the configuration description, and in part throughout the work, because each chapter requires a different forcing, depending on the particular study and its objectives.

The configurations discussed in this work, not only resolve the large-scale circulation patterns and their influence on the coastal transition zone of WIM, but also resolve explicitly a unique small-scale feature consisting in the Mediterranean outflow through the Strait of Gibraltar. Given the different scales that influence the circulation of the WIM, ranging from the few kilometers of the Strait of Gibraltar dynamics, to the hundreds to thousands kilometers scale of the Azores Current system, a simulation based on nesting techniques was performed, as detailed below.

As a final note, most of the computations, from ROMS data handling to grid interpolation, were possible through the use of the ROMS_tools provided by Penven et al. (2008).

1.4.3 Large Domain

The strategy to manage a large range of scales consists in the implementation of a two-domain approach. A large-scale first domain (FD — Figure 1.2 a) is run independently in order to provide initial and boundary conditions to our second domain (SD — Figure 1.2 b)

through an offline nesting. The first domain horizontal resolution is $1/10^o$ ($\sim 9\ km$ in longitude), and the main aim for this domain is to resolve the large-scale circulation features such as the Azores Current, and its interaction with the Atlantic margin of the Iberian Peninsula.

For this domain, 30 sigma vertical levels are used, with a stretching factor of $\theta_s = 7$ and $\theta_b = 0$ to conserve a good near-surface resolution over the entire domain. The bathymetry is based on ETOPO1 (Amante and Eakins, 2009), with corrections near the slope and a smoothing filter to fulfill the $r = \delta h/2h$ criteria (Haidvogel and Beckmann, 1999), $r < 0.2$.

The World Ocean Atlas 2009 (WOA-2009) climatology is used as the initial value for the temperature (Locarnini et al., 2010) and salinity (Antonov et al., 2010) fields, and also to recycle these fields along the nudging bands, providing open boundary conditions. These open boundary conditions were established by Marchesiello et al. (2001), with inflow (outflow) nudging timescales of 1 (360) day(s) for tracers and 10 (360) days for momentum, respectively. Sponge layers are applied along the edges with a band of 120 km, with a lateral viscosity coefficient ranging from 600 $m^2 s^{-1}$ at the boundary to zero at the interior. Explicit viscosity and diffusivity is null, and a linear drag formulation with coefficient $r = 3 \times 10^{-4}\ m\ s^{-1}$ is applied at the bottom.

Surface forcing varies, depending on what is intended from a given ROMS run. Since this work focused on different aspects of the WIM dynamics, in different space and time scales, several simulations are carried out, each forced with a different dataset, described in due course. However, the surface forcing computation is similar: initial velocities are zero, and monthly geostrophic velocities (with level of reference 1200 m) and Ekman velocities are calculated from the dataset and applied along the open boundaries. The Mediterranean undercurrent is introduced as a nudging zone, in the interior, as described by Peliz et al. (2007), in order to restore the hydrographic properties of the Mediterranean levels.

1.4.4 High-Resolution Domain

The target domain, SD (stands for second domain, see Figure 1.2) has a horizontal resolution of $1/27^o$ ($\sim 3\ km$ in longitude), and includes the Gulf of Cadiz, the WIM, and part of the western Bay of Biscay, extending for $\sim 1300\ km$ in the meridional direction, from 34^oN to 46^oN. In the zonal direction, the domain extends from the Strait of Gibraltar, located at 5.5^oW to 12.5^oW, representing a width of about 600 km.

Sixty sigma vertical levels with $\theta_s = 4$ and $\theta_b = 0$ are used to properly resolve the Mediterranean undercurrent with enough near-bottom resolution. In this way, the grid has $60 \times 188 \times 389$ cells.

The topography by Sibuet et al. (2004) was used, which has a resolution of $\sim 1\ km$ and was smoothed in order to fulfill the same r-factor criteria ($r < 0.2$) of the large-scale domain.

The initialization and the boundary conditions are obtained using one year from FD, with average data stored every 3 days. The choice of the year that provides these conditions to SD was based on the kinetic energy (KE), averaged over the entire FD. Year 5 was the year that showed the least fluctuations in KE, and therefore was used as initial and

boundary conditions for SD. An experiment using year 7 of FD showed similar results for the SD run.

Also, similarly to the large-scale simulation, a nudging sponge layer is introduced. Open boundary conditions are the same as for the FD configuration; however the sponge layers are applied to a band of 40 km, with a lateral viscosity coefficient ranging from 200 $m^2 s^{-1}$ at the boundary to zero at the interior. A quadratic drag coefficient of 5×10^{-3} is used. At the Strait of Gibraltar, at the southeastern boundary, the water exchange with the Mediterranean basin is explicitly represented in the domain, with the methodology of Peliz et al. (2007), consisting in the imposition of vertical profiles of temperature, salinity, and zonal velocity at the 5 grid points at the Strait. This condition is designed to setup a transport of 0.8 Sv leaving the domain through the surface layer, and 0.7 Sv entering the domain through the bottom layer. The process of entrainment of Atlantic Central Waters with the Mediterranean outflow is also parameterized by increasing the viscosity and diffusivity coefficients in a region in which the MW is strongly mixed with the overlying Atlantic waters, until the MW vein forms along the northern slope of the Gulf of Cadiz.

The inflow of freshwater in the ocean, originated from the main rivers of the region (white lines in Figure 1.2 b), is included. For the Portuguese rivers, climatological values were provided by INAG (Water Institute of Portugal); the information on the Spanish rivers was provided by Barja and Lestegás (1992).

The spin-up time for this domain, in which the KE stabilizes, is 5 years, as the adjustment time of the Mediterranean outflow along the western and northern Iberian Margin is quite a slow process.

Surface forcings are in agreement with the corresponding large domain configuration for a given run. More information on the configurations is given each chapter / section.

1.5 Outline

Table 1.1 summarizes all the ROMS simulations carried out. Our target domain is SD; hence it is the one we focus on most. The numerical approach is always offline nesting, which means that in all cases there are always two runs carried out: one FD, one SD. Furthermore, each run has always the same dataset as initial and boundary conditions: the former WOA09, the latter one year of FD.

Run	Surface Forcing	Run years	Initial & boundary conditions
Climatological	COADS (1945-1989)	14	FD: World Ocean Atlas 2009 SD: one year of FD
Yearly	"Real" Winds and Fluxes (NCEP/QuikSCAT-ASCAT) (2001-2011)	11	
CGCM present ensemble	IPCC (1945-1989)	10	
CGCM future ensemble	IPCC (2071-2100)	10	

Table 1.1: Summary of all performed ROMS simulations.

The outline of this work is as follows: chapter 2 presents a climatological study of the mean and seasonal dynamics off WIM; chapter 3 addresses the interannual variability of the upper ocean circulation for period 2001-2011; for the same period, a larval connectivity and dispersal study is carried out in chapter 4; chapter 5 consists in a sensitivity study on the ability of global climate models to force regional ocean configurations; finally, in chapter 6, this is put to use in a future ocean simulation where possible changes in hydrography and dynamics are explored.

Chapter 2

Mean and Seasonal Characterization of the Upper Ocean off Western Iberian Margin

The contents of this chapter have been published by Nolasco et al. (2013a) and Cordeiro Pires et al. (2013a).

2.1 Overview

This chapter focuses on the equilibrium circulation of the WIM current system. The main purpose is to characterize the mean seasonal hydrography and the resulting circulation in the upper layers of the ocean, including the surface layer, the underlying central waters, and the intermediate Mediterranean Water levels. In order to do so, numerical simulations were setup forced by climatological heat and momentum fluxes, that is, the circulation is dictated by the intrinsic variability of the model, and in the absence of any external interannual atmospheric or oceanic forcing.

The study will particularly aim at an integrated discussion of the three main dynamical phenomena of WIM: coastal upwelling, poleward flow (IPC) and Mediterranean Water outflow, which, although independent, are intimately linked. Although the region dynamics is strongly seasonal, the question of the prevalence of poleward flow throughout the year is addressed, based also on observational studies, as well as the generation of vorticity structures of the mean flow along the WIM.

Furthermore, in this chapter, a Lagrangian study is carried out, with the purpose of evaluating the origin of the waters that are upwelled along the WIM, from a climatological point of view. Studying the origin of upwelled waters in an upwelling system may be useful for several purposes: providing scales of dispersion in the marine environment, regarding biological issues (e.g. larval dispersal lengths or fisheries) or pollution studies; studying connectivity between marine populations (further carried out in chapter 4); indicating climate variability; amongst others. The development of regional ocean modeling

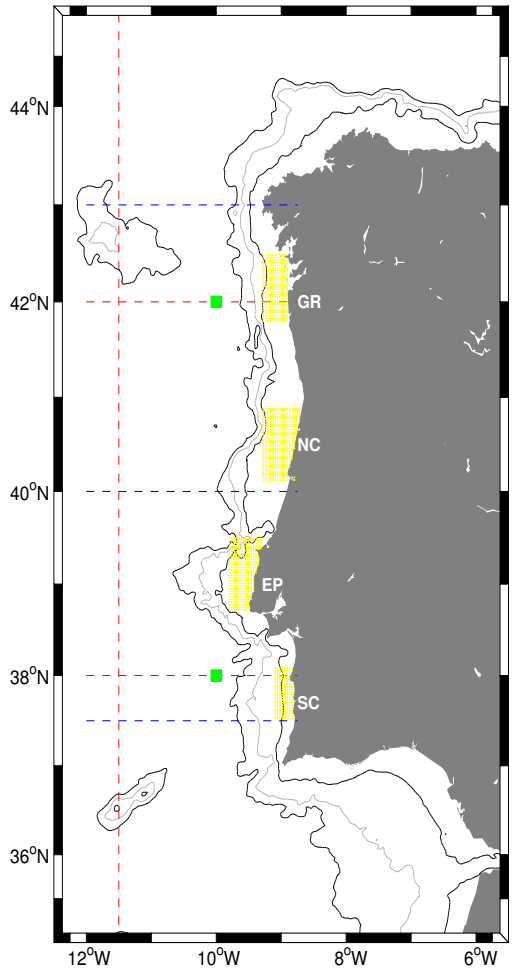

Figure 2.1: Map of the region under study (SD). Green squares mark the points of the θ-S diagrams of Figure 2.5; Dashed red lines are the T and S sections of Figures 2.6, 2.8 and 2.7; Dashed blue lines are the meridional v and transport sections of Figure 2.10 and Figure 2.11, respectively; Yellow regions mark the Lagrangian particle regions of arrival (section 2.6): Galician Rias (GR); Portuguese Northern Coast (NC); Estremadura Promontory (EP); Portuguese Southern Coast (SC).

---

and their increasing resolution and features have made it possible to apply particle modules to the ocean model 3D grid and trace the particles throughout the model run. In this way, one is able to follow the 3D trajectories, and even hydrographic and dynamical properties, allowing studies of a diverse nature to be carried out (e.g. Domingues et al., 2012). Chhak and Di Lorenzo (2007) found that during the warm/cold phase of the Pacific Decadal Oscillation upwelled waters at the California upwelling system originated at shallower/deeper levels. Blanke et al. (2009) were able to study the variability of water transfers between the adjacent regions of the Benguela upwelling system, which strongly influence the spawning of anchovies. Albert et al. (2010) showed, through the same means,

that the distance and depth of origin of the particles surfacing at the Humboldt upwelling system were dependent on the coastal wind stress curl. At the North American western coast, the origin of upwelled waters off Oregon was addressed by Rivas and Samelson (2011) through numerical modeling, who found that the waters that upwell there could come from alongshore northern locations or from offshore sites to the west, mostly from depths greater than 100 m, although the sources depended strongly on the region and the tendency to generate mesoscale features.

The chapter is organized as such: after a description of the data and the methodology (section 2.2), a brief validation of FD is carried out (section 2.3), followed by an hydrographic validation of the high-resolution domain, SD (section 2.4). Then, the mean flow vertical and horizontal structure is analyzed in detail (section 2.5), and the final section addresses the Lagrangian study carried out over the same climatological ROMS run (section 2.6).

2.2 Data and Methodology

2.2.1 Model Configurations

Surface fluxes are provided by the Comprehensive Ocean and Atmosphere Data Set (COADS). COADS has been, by excellence, the used climatology for such regional ocean modeling studies (e.g. Marchesiello et al. 2001). This COADS version is an enhanced climatology originated from a joint effort of the University of Wisconsin-Milwaukee (UWM) and the National Oceanographic Data Center (NODC — http://www.nodc.noaa.gov/) (da Silva et al. 1994) which resulted in an optimized COADS for the period 1945-1989 climatology for both atmosphere and ocean, with an improved resolution of $0.5^o \times 0.5^o$ (except sea surface salinity, which has a resolution of $1^o \times 1^o$). This is a monthly mean climatology without interannual variability comprised by heat fluxes (shortwave, longwave and latent), water fluxes (evaporation minus precipitation), wind stress, sea surface temperature (SST), and sea surface salinity (SSS).

The absence of an ocean-atmosphere feedback term can lead to model SST drift. This problem is addressed in ROMS by an air-sea feedback parameterization that is added to the surface flux (Veitch et al. 2010). This is done using the COADS SST distribution, and a similar correction scheme is used for SSS.

2.2.2 Climatology

The first part of the model output analysis is a comparison with climatological data. Two datasets were chosen to carry out this comparison: the recent climatological GHER atlas for the Northeast Atlantic (Troupin et al., 2010) (hereafter GHER-NEA climatology) and satellite products. The GHER-NEA climatology was chosen for its high resolution (0.1^o), which properly resolves the slope and shelf regions unlike most available climatologies, and both temperature and salinity are compared to model results.

2.2.3 Satellite Products

For the sea surface temperature (SST), the comparison is carried out with data from the Advanced Very High Resolution Radiometer (AVHRR) of the National Oceanic and Atmospheric Administration (NOAA). The data was extracted from the EUMETSAT Ocean & Sea Ice Satellite Application Facility (OSI-SAF) (www.osi-saf.org) and was made available by CERSAT (IFREMER, France). The product has an approximate resolution of 2 km. The final data consists in 7-year averages, corresponding to years 2002 to 2008, for January and July, of the night satellite sweep (hereafter satellite climatology).

2.2.4 Altimetry Products

The altimetry data were retrieved from the AVISO (Archiving, Validation and Interpretation of Satellite Oceanographic data) website (http://www.aviso.oceanobs.com/). The altimeter products were made available by Ssalto/Duacs (Segment Sol multimissions d'ALTimétrie, d'Orbitographie et de localisation précise / Data unification and altimetry combination system), with support from Cnes (French national center for space studies). Ssalto/Duacs system processes data from all altimeter missions (Jason-1&2, T/P, Envisat, GFO, ERS-1 & 2 and Geosat) to provide a consistent and homogeneous catalog of products for varied applications, both for near real time applications and offline studies. Altimetry weekly data was obtained from AVISO for the period October 1992 to July 2011.

2.3 Large Domain Validation

The FD domain was designed to solve the large-scale circulation in order to provide boundary conditions to the target domain SD. It is not intended to discuss the circulation resulting from this domain, but to show an example of how the large-scale circulation is solved for this domain. For that purpose, an Eddy Kinetic Energy (EKE) comparison between altimetry and FD output is done in Figure 2.2. The signature of the Azores Current is clear between 33^oN and 36^oN, and the signal extends east to $\sim 12^o$W in both. There is also evidence of the North Atlantic Current at the northwestern corner of the FD domain. In terms of magnitude, EKE is more intense in ROMS for the Azores Current, and more intense in AVISO for the North Atlantic Current. Nevertheless, the comparison is acceptable and hence FD is reproducing well the regional dynamics energetically.

2.4 High-Resolution Domain Validation

The WIM hydrography resulting from the model solutions is analyzed by comparing the modeled horizontal and vertical temperature and salinity distributions with the GHERNEA climatological data described above, with the exception of SST, which is compared to satellite data. Therefore, both SD and climatology temperature and salinity fields are represented through mean seasonal surface fields, θ-S diagrams and zonal vertical sections.

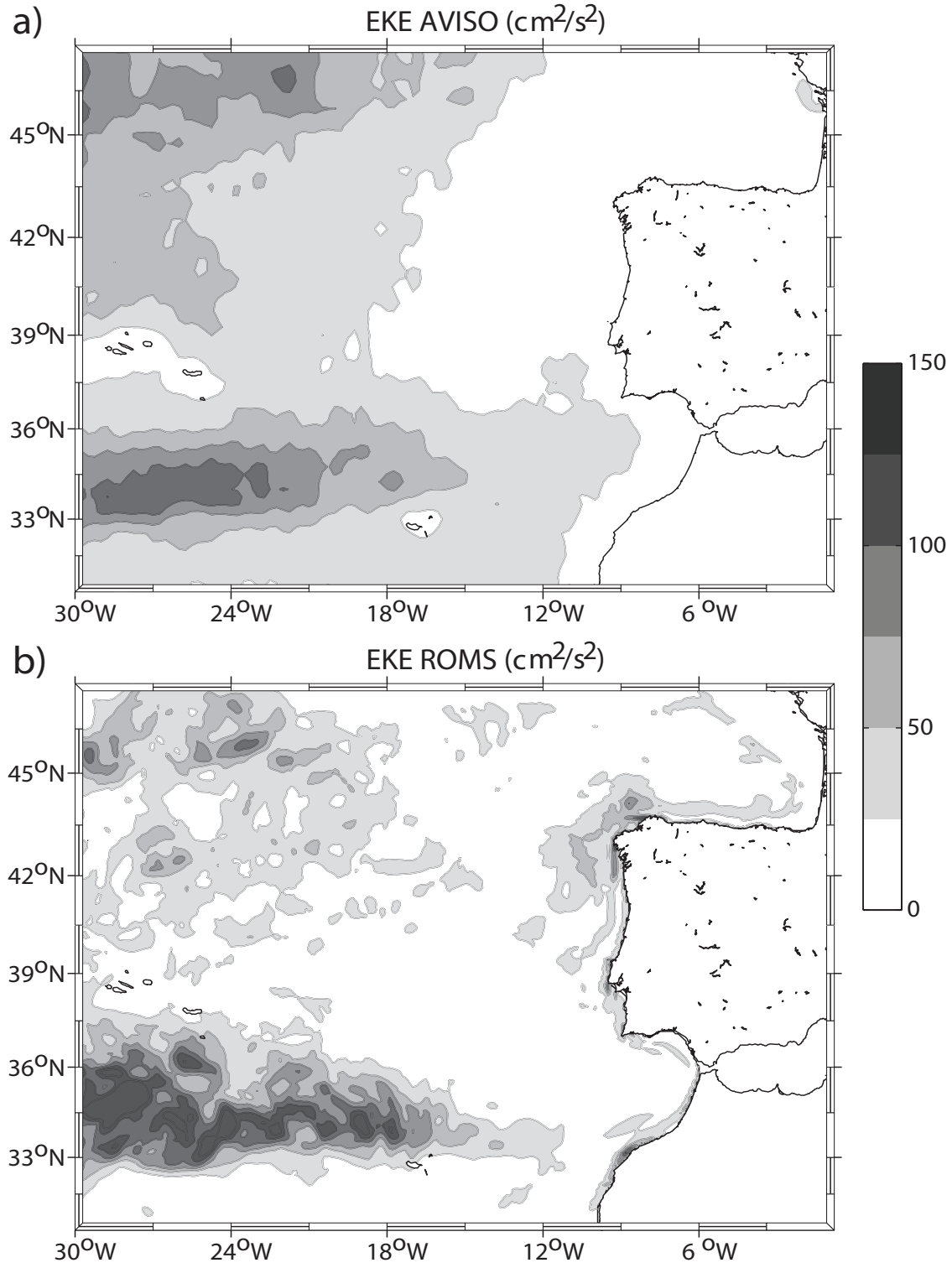

Figure 2.2: Eddy Kinetic Energy (EKE, $cm^2\ s^{-2}$) annual average for (a) altimetry data, and (b) FD model results.

2.4.1 Surface Fields

Figure 2.3 presents the January mean sea surface temperature (SST) (upper row) and salinity (SSS) (lower row) of both SD and the corresponding climatology, as well as the difference between the modeled and the climatological fields. Figure 2.4 is the corresponding image for the month of July.

a. Winter

During winter (Figure 2.3), both SD and the climatologies show the existence of a meridional gradient of sea surface temperature and salinity. A tongue of saltier and warmer water centered at approximately 9.5^oW-10^oW is also observed, which is associated with the poleward advection of waters with subtropical origin, frequently referred to in the literature as the Iberian Poleward Current (IPC) (Álvarez-Salgado et al., 2003). Although this tongue is visible in both SST and SSS, it is less evident in the SST satellite field. Moreover, the poleward penetration of the climatological tongue reaches farther north than the SD one, causing a difference of about -0.1 in salinity between 39^oN and 42^oN.

Along the continental shelf, north of the Estremadura Promontory, a band of buoyant fresher and colder waters is observed in the SST and SSS climatologies, as well as in the SD averages. This band is associated with the presence of winter river inflow along the western coast, mainly contributed to by Tagus, Mondego, Douro, Minho and the Galician Rias rivers (see Figure 1.2 b). This fresh water signature lingers over the continental shelf, generating the Western Iberian Buoyant Plume (WIBP) (Peliz et al., 2002; Otero et al., 2008), that can reach as far as 40 km offshore.

b. Summer

During summer (Figure 2.4), the most important phenomenon observed is coastal upwelling induced by the predominant equatorward winds along the WIM, which results in the presence of a coastal band of cold and fresh waters. From north to south, both the SD (Figure 2.4 a,d) and the climatological (Figure 2.4 b,e) offshore temperature (salinity) fields increase from 18^oC (35.7) in the northern region to 22^oC (36.4) in the Gulf of Cadiz. Moreover, the offshore isotherms and isohalines bend southward encompassing the presence of the coastal band of upwelled water from the southern coast of Portugal up to Cape Ortegal, the northern tip of the Iberian Peninsula.

Thus, the main patterns of the July average temperature and salinity for the offshore region are well reproduced in SD, resulting in low temperature and salinity differences (Figure 2.4 c,f). However, SD tends to overestimate the intensity of upwelling, presenting a coastal water band that is colder than the satellite climatology. As discussed by Veitch et al. (2010), and references herein, the climatological winds do not account for the drop-off of the wind stress in the neighborhood of the coast.

There are also regions in which SD, on the contrary, overestimates the surface temperature. Along the Galician coast, north of Cape Finisterre, unlike SD results, filaments are

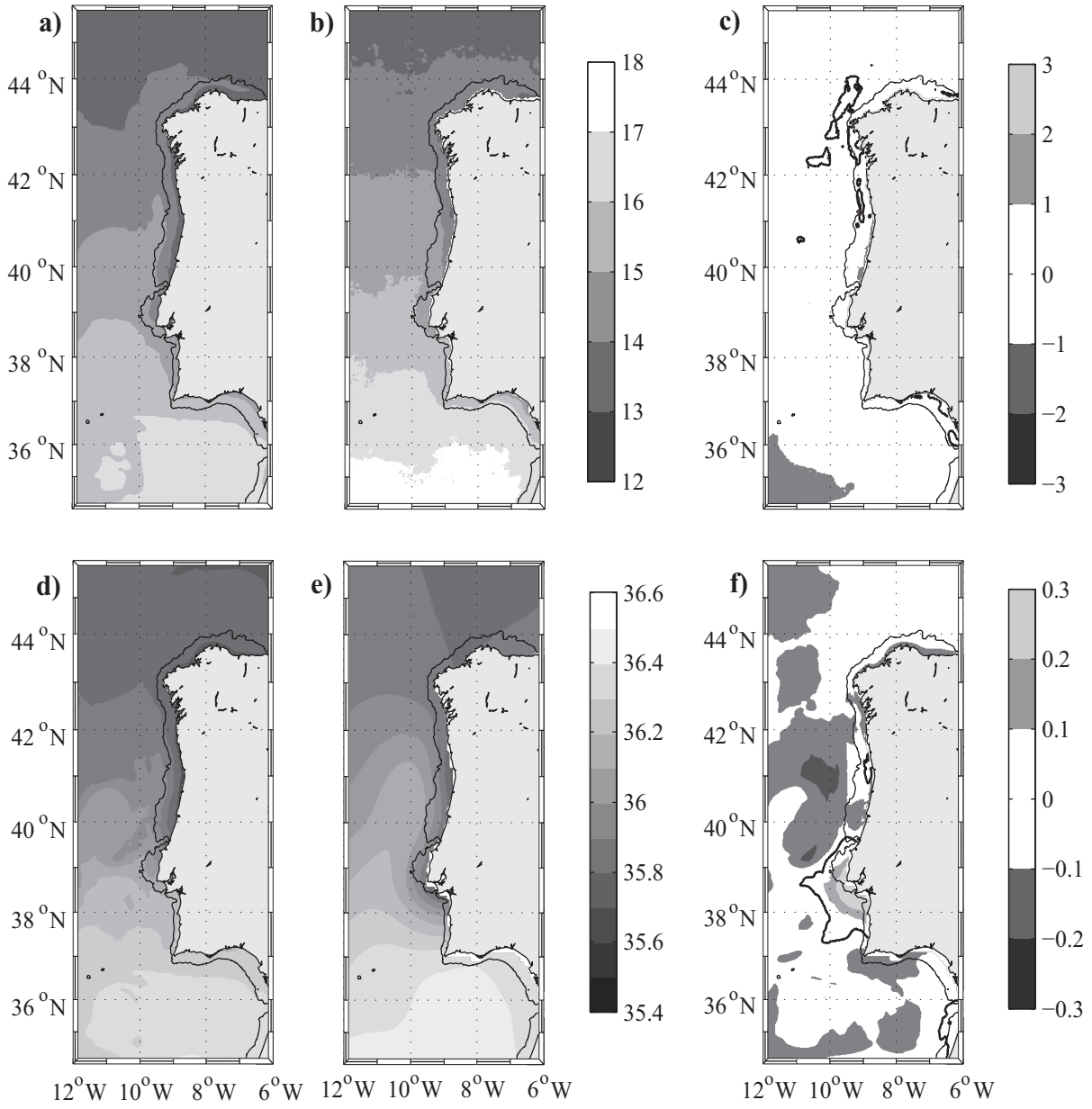

Figure 2.3: SST in ^oC (upper row) and SSS (lower row) for January. (a,d) 5-year mean of ROMS output; (b,e) 7-year mean of AVHRR at 02 h and GHER-NEA climatology, respectively; (c,f) Difference between (a) and (b) and between (d) and (e), respectively. Thick contours outline null difference. The 200-m isobath is shown (thin black line).

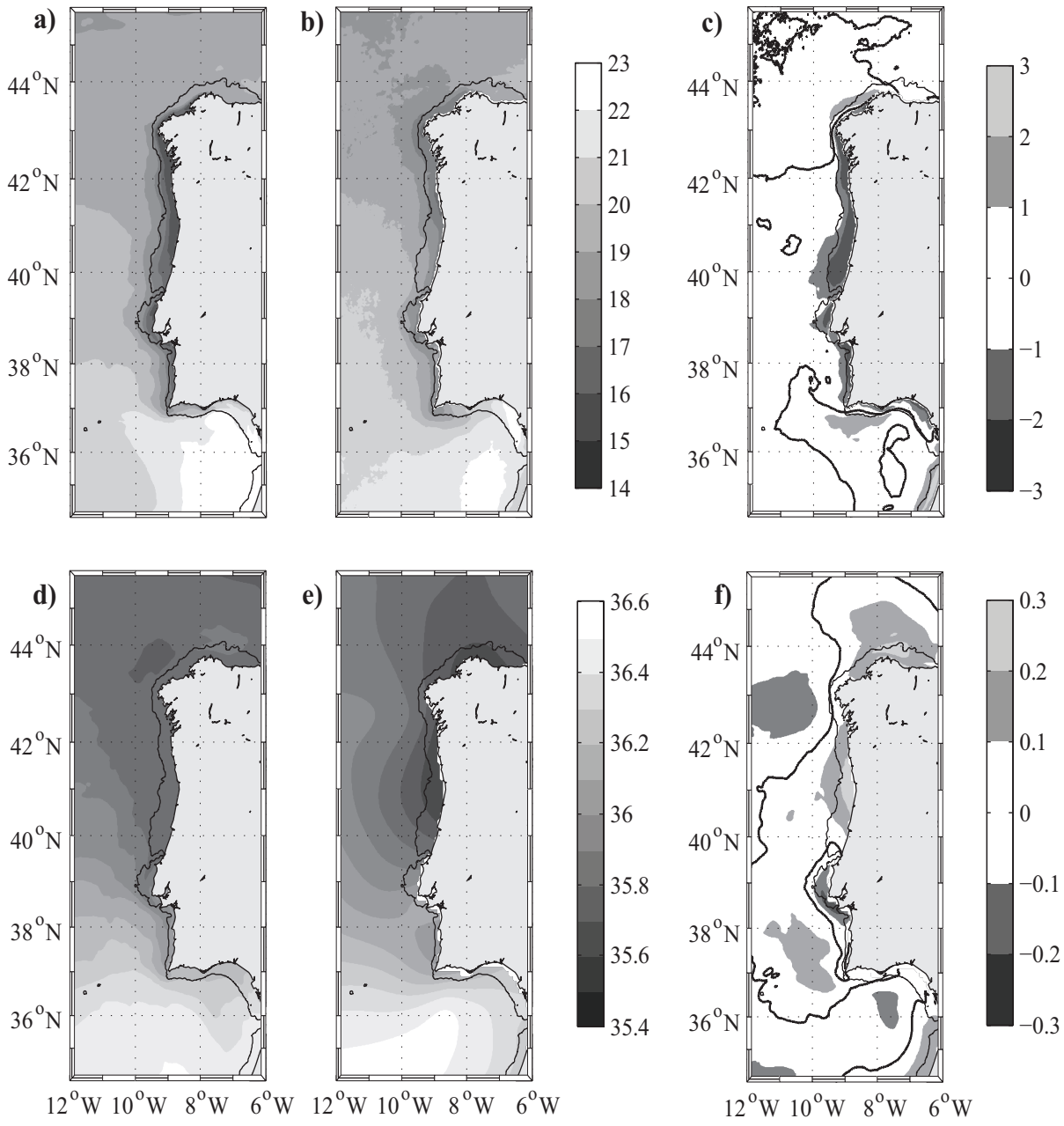

Figure 2.4: Same as Figure 2.3 but for July .

frequently observed by satellite in this area (Torres et al., 2003).

Other regions where SD temperatures are warmer than observed are northern Gulf of Cadiz (Portuguese southern coast) and the northern coast of Morocco. These regions are influenced by the gap winds, which consist in strong easterly winds associated with pressure differences between both sides of the Strait of Gibraltar (Peliz et al, 2009), not represented in the climatological winds.

The summer SSS field (Figure 2.4 d) is characterized by the upwelling of Eastern North Atlantic Central Waters with northern origin (ENACW$_{sp}$), which are advected southward. This upwelled water has a typical salinity signature of about 35.8. Underlying the upwelled Central Water, there is a low salinity surface water (lower than 35.7) observed in the GHER-NEA climatology (Figure 2.4 e), which is associated with the remnant of the WIBP advected offshore by Ekman transport, giving rise to a low salinity plume at the surface. This band of fresher water is not well resolved by SD, and accounts for the major differences between model and the GHER-NEA climatology (Figure 2.4 f). The reason for this is that COADS winds are almost constant during summer, which promotes, through Ekman transport, the offshore dispersal of the WIBP and its dilution, while in nature, in the presence of variable winds, the plume remains trapped to the coastal region. On the other hand, in the remaining places, the salinity differences are mostly within ± 0.1 between SD and the climatology.

2.4.2 Water Masses

To compare the SD water mass properties with the climatological values, θ-S diagrams were elaborated for two regions (boxes with 1^o of length and width) centered at 10^oW and latitudes 38^oN and 42^oN (see Figure 2.1 for location). These diagrams are displayed in Figure 2.5. For each box, monthly (January, April, July and October) mean profiles of potential temperature and salinity were calculated from years 10 to 14 of the simulation (one dashed line per year, in order to show the interannual variability), and are superimposed to the GHER-NEA climatology (solid line).

The seasonal evolution of the thermohaline properties of the central and surface waters is reasonably well reproduced by SD when compared with the climatological values. Concerning the Central Water properties of both SD and climatology, by comparison with the standard straight lines in the θ-S space for ENACW$_{st}$ and ENACW$_{sp}$, it is clear that the northern (southern) region is more influenced by the presence of the subpolar (subtropical) branch of the ENACW.

For the southern region, in January (Figure 2.5 a), the Central Waters have their thermohaline properties superimposed with the ENACW$_{st}$ line, typical of the waters that give origin to the IPC. Below the surface, salinity decreases linearly to a minimum of 35.7, near the 27.1 isopycnal, and increases downward due to the influence of the underlying MW mass, up to a maximum of 36.2 on the 27.6 isopycnal, which is about 0.15 lower than the climatological value. In April (Figure 2.5 b), a decrease of the surface salinity maximum is observed, associated with the start of the upwelling season. During summer (Figure 2.5 c), the seasonal heating modifies the θ-S structure at the surface, by increasing the temperature

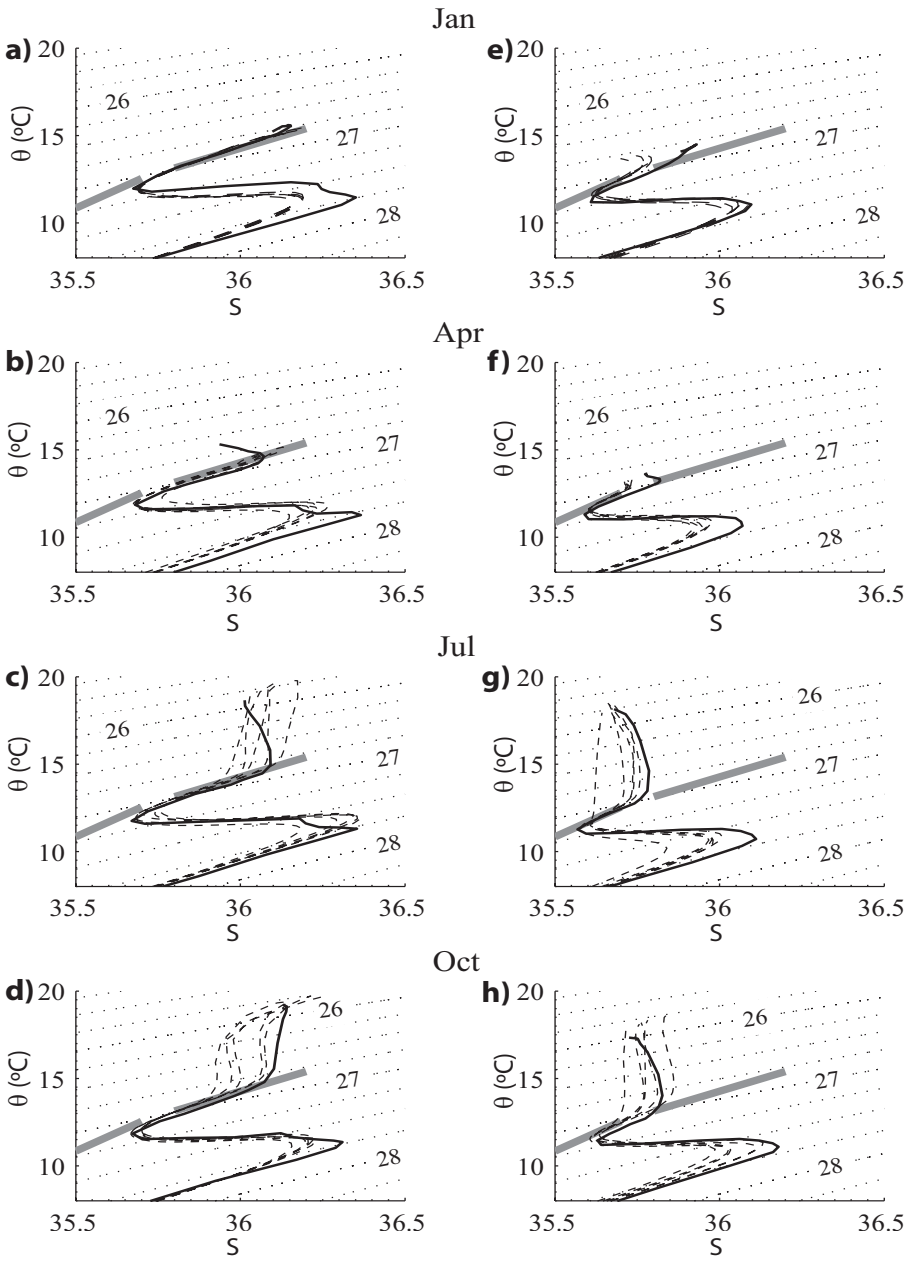

Figure 2.5: θ-S diagrams of 5-year monthly means of ROMS output (dashed lines) and GHER-NEA climatology (solid line) for January (a,e), April (b,f), July (c,g) and October (d,h) for two regions: one centered at 38^{o}N, 10^{o}W (a-d), the other centered at 42^{o}N, 10^{o}W (e-h). Potential density anomaly (σ_θ) is superimposed in dotted lines every 0.2 $kg\ m^{-3}$; the shaded line corresponds to the standard definitions of ENACW$_{st}$ and ENACW$_{sp}$, defined as $\theta = 10 + 8.462(S - 35.4)$ for the subpolar branch (34.8 < S < 35.7) and $\theta = 13.13 + 5.653(S - 35.8)$ for the subtropical branch (35.8 < S <36.2), as defined by Fiúza et al. (1998).

of the surface layer. There is also interannual variability of the temperature at the surface layers. The SD MW mass is fairly well reproduced, ranging from 36.2 to 36.35, which includes the climatological value. In October (Figure 2.5 d), after the upwelling season, the signature of saltier surface waters associated with the IPC is visible both in the SD and the climatology, although SD underestimates the surface salinity by about -0.1 units, and presents this same difference in respect to the MW mass.

Regarding the northern region (centered at 42^oN, 10^oW, Figure 2.5 e-h), the seasonal evolution of the θ-S field follows a similar pattern to that described for the southern region, since the main differences are observed in the salinity field at the surface levels, with lower maximum values of salinity in both winter and summer. At the MW levels, the salinity signature decreases poleward as expected.

Overall, the SD configuration not only follows the seasonal cycle of temperature and salinity for the surface and central waters, but also reproduces the MW hydrographic properties, although some negative biases are observed (as well as in the MW core depths, as discussed later).

2.4.3 Vertical Structure

As a complementary analysis of the water masses in the two regions discussed above, we intend to study the vertical distribution of the hydrographic properties, and to compare the modeled values with the GHER-NEA climatology. The aim is to show and discuss the modeled temperature and salinity fields and to compare them to climatological values across two latitudes, 42^oN and 38^oN, representative of the northern and southern WIM, respectively. Additionally, a meridional section of temperature and salinity off WIM concludes the winter hydrography characterization. The averages for SD were computed for January and July of simulation years 10 to 14, down to 1500 m in depth.

a. Winter Hydrography

At 42^oN (Figure 2.6 a,c), the winter distribution of temperature and salinity shows a general downward sloping of the isohalines in the upper slope region (down to about 400 m), between 9.5^oW and 11^oW. This downward tendency is associated with the presence of the IPC during wintertime, with salinities higher than 35.9 and temperatures around 14.5^o. The SD IPC (Figure 2.6 a) shows evidence of this poleward advection at the surface; however, there is a bias of about -1^oC in temperature and -0.1 in salinity. On the other hand, the salinity minimum of ENACW$_{sp}$ of 35.65 (see Figure 2.5 e) is reached at depths around 400 m, shallower than the climatological minimum (450 m). Below that depth lies the MW and thus the salinity field increases accordingly to 36 near the slope at an approximate depth of 900 m, which is -0.1 fresher and 100 m shallower than the climatological value.

For the southern latitude, 38^oN (Figure 2.6 b,d), the surface layers are characterized by the presence of saltier and warmer waters when compared to the northern section. In January, for the surface and central water range, the hydrographic properties reflect the straight line observed in the θ-S diagrams (Figure 2.5 a). Concerning the MW, below the

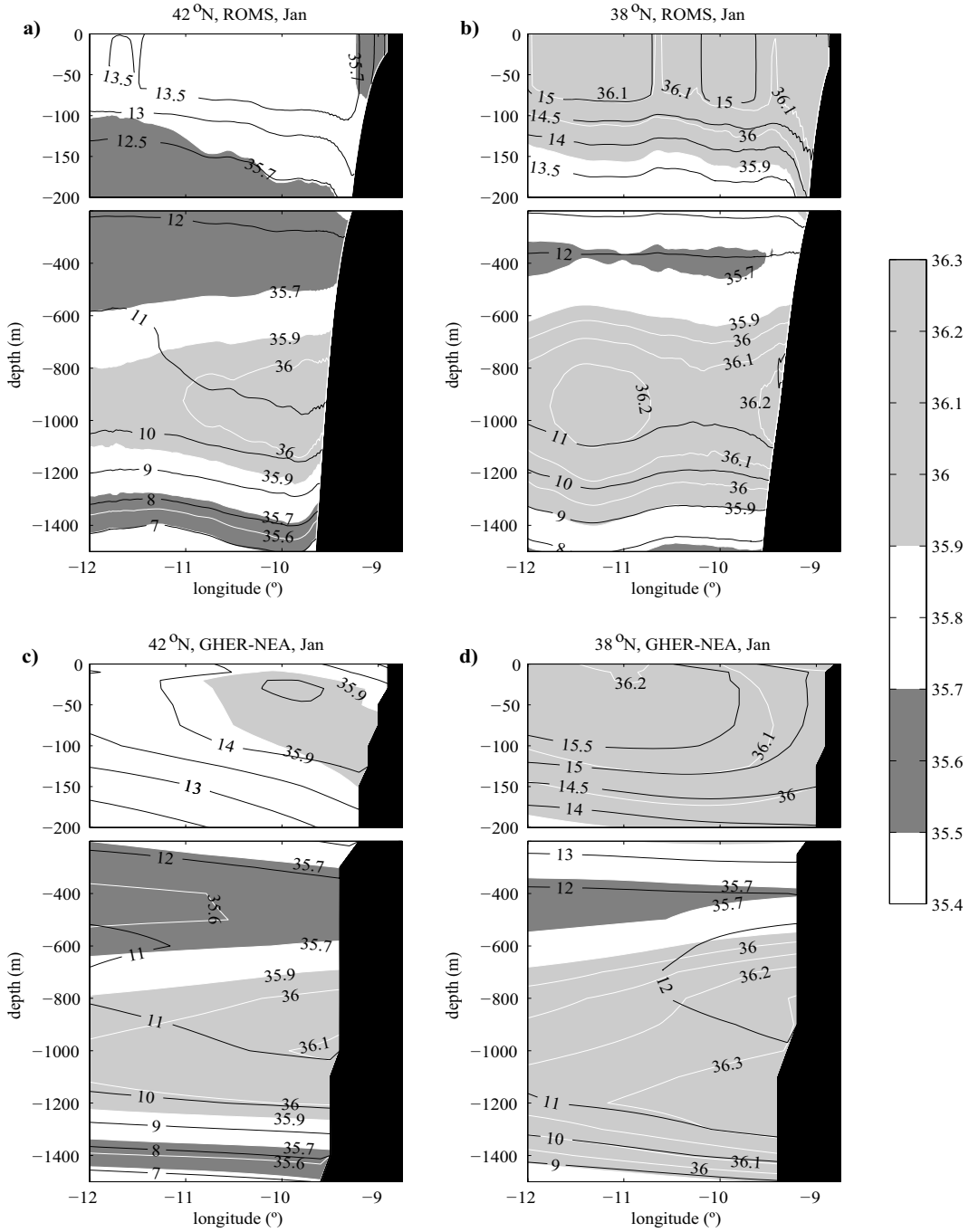

Figure 2.6: Zonal sections of temperature (^oC) and salinity for January: (a,b) 5-year means of ROMS output for 42^{o}N and 38^{o}N, respectively; (c,d) GHER-NEA climatology for 42^{o}N and 38^{o}N, respectively. Sections are down to 1500 m and the first 200 m are enlarged. Temperature is represented in black contours every 0.5^oC in the upper layers and every 1^oC in the deeper layers. Salinity is depicted in white contours every 0.1 and shades of gray for specific values: MW (35.9 to 36.3) is represented in light gray and ENACW (35.5 to 35.7) is represented in dark gray. Bathymetry is colored in black.

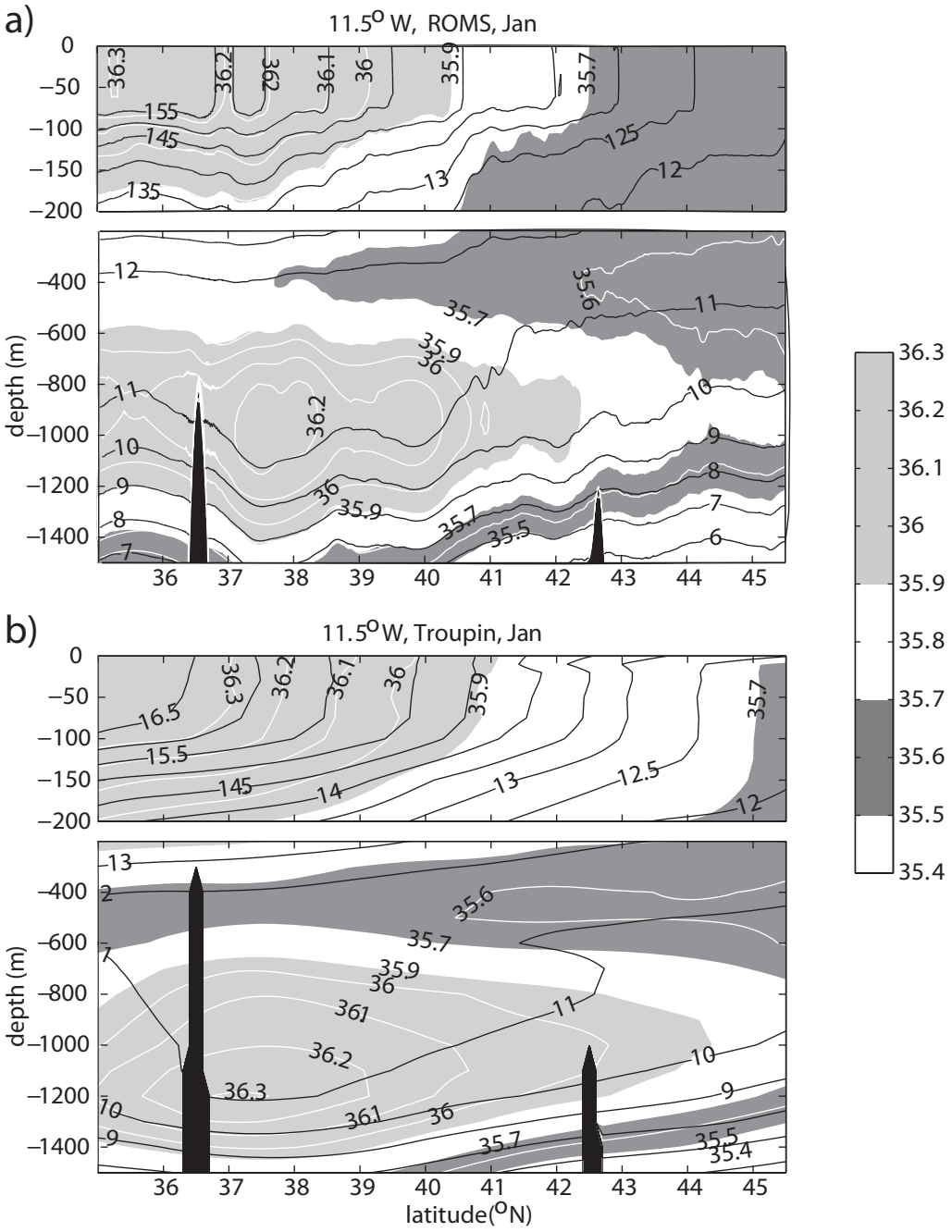

Figure 2.7: Meridional section of temperature (^oC) and salinity for January at 11.5^{o}W: (a) 5-year means of ROMS output; (b) GHER-NEA climatology. Sections are down to 1500 m and the first 200 m are enlarged. Temperature is represented in black contours every 0.5^oC in the upper layers and every 1^oC in the deeper layers. Salinity is depicted in white contours every 0.1 and shades of gray for specific values: MW (35.9 to 36.3) is represented in light gray and ENACW (35.5 to 35.7) is represented in dark gray. Bathymetry is colored in black.

ENACW, the SD temperature maximum ($\sim 12^oC$) does not reach as far offshore as the climatological one (extending to 10.5^{o}W whereas in SD the isotherm is close to the slope), but the depth at which they are found (800 m) is the same. On the other hand, the lower core SD MW salinity maximum, 36.2, is underestimated (-0.1), as is the depth at which this maximum is found (about 1000 m in SD and 1200 m in the climatology). Below the MW, the transition to LSW in SD is located at lower depths than the climatological value.

The upper levels meridional distribution of the temperature and salinity fields along the WIM at 11.5^{o}W (Figure 2.7) shows evidence of a large-scale gradient with southern warmer and saltier waters of subtropical origins and northern colder and fresher waters of subpolar origins. A frontal region, frequently observed between 38 and 40^{o}N and denoted by Western Iberia Winter Front (Peliz et al., 2005) separates both regions.

This meridional density gradient is partly at the origin of the Iberian Poleward current system (Peliz et al., 2003). A proper representation of the meridional distribution of hydrographic fields is needed to obtain a realistic poleward current system along the WIM. Here, we observe similar meridional gradients of temperature and salinity in the upper levels (0-200 m), although ROMS presents lower salinities north of 43^{o}N and south of 37^{o}N (roughly differences of -0.1) and lower temperatures of about -0.5^oC to the north reaching 1^oC to the south. At depth, both the ENACW and the MW signatures are clearly observed, the former at 400-600 m with typical salinities of 35.6- 35.7 and the latter centered at 1000-1200 m with maximum salinities of 35.2-35.3 and a temperature of 11^oC.

b. Summer Hydrography

Similarly to the winter situation, the summer vertical structure is analyzed for zonal sections at 42^{o}N and 38^{o}N. At the northern section (Figure 2.8 a,c) the summer circulation is well characterized by the presence of coastal upwelling, which affects clearly the near-surface temperature field distribution on the continental shelf. The isotherms warmer than 14^oC outcrop on the shelf, generating a front in the numerical configuration. Note that the GHER-NEA climatology shows evidence of upwelling, although the frontal structure is smoothed, as expected from an observational climatological dataset.

The upwelling of the isothermal field extends down to the 13^oC isotherm at approximately 200 m in both SD and climatology. At the surface layers summer salinity is lower than during winter because the signature of ENACW$_{st}$ is not observed, as the upwelled waters have a northern origin. A minimum of salinity is nevertheless observed, similarly to winter, with the 35.6 isohaline located at approximately 400 m.

Concerning the MW distribution in July, at 42^{o}N there are no significant differences with respect to wintertime in the climatology: the same salinity maximum at approximately 1000 m, enclosed by the 35.9 isohalines between 700-800 m and 1200-1300 m. In SD, the MW vein seems to be squeezed and the temperature field is upwelled by about 100 m with respect to the winter equilibrium depth, as observed by Garcia-Lafuente et al. (2008), who related the shallowing of the MW vein with its mesoscale field, and whose origin may be related with the variability of the wind field.

The southern section, 38^{o}N (Figure 2.8 b,d), is also affected by upwelling during sum-

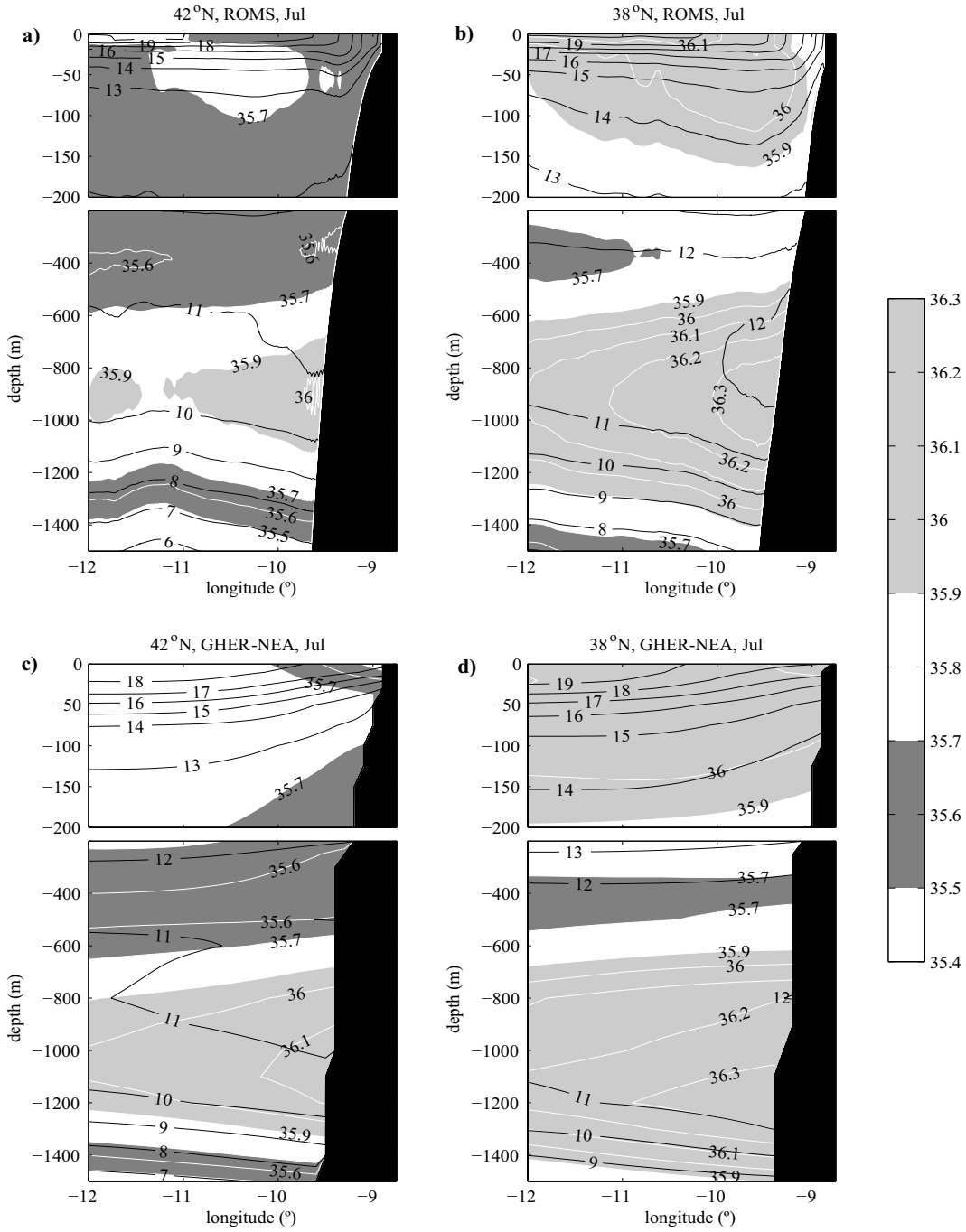

Figure 2.8: Same as Figure 2.6 but for July, except temperature in the upper layers is represented in black contours every 1^oC.

mer. In this case the outcropped isotherm is 15^oC in SD against 17.5^oC in the climatology. At the levels of the MW vein, the main difference between SD and climatology is the 200 m depth difference in the location of the salinity maximum, whereas SD reaches the same climatological maximum of 36.3.

2.5 Mean Flow Structure

The main focus of this section is the analysis of the circulation in the WIM resulting from the process of adjustment of the hydrographic fields. Horizontal slices at 50 m and 1000 m depth showing monthly means for years 10 to 14 of the SD run of the salinity and velocity fields for January and July are displayed in Figure 2.9. In addition, vertical slices of the alongshore circulation at northern (43^oN), central (40^oN) and southern (37.5^oN) locations of the WIM are displayed in Figure 2.10, also for January and July monthly means. Finally, the computation of meridional transport across these same three zonal sections were also carried out.

2.5.1 Winter Circulation

One of the main dynamical features at the western Gulf of Cadiz is the presence of a permanent cyclonic circulation (C1 in Figure 2.9 b), which is part of the usually referred to as topographic β-plume circulation (Kida et al., 2008). Lamas et al. (2010) provided observational evidence of the structure. This cyclonic vortex is stronger at the surface, but has a clear signature in depth as well (Figure 2.9 a,b).

The circulation in the WIM is conditioned by the entrance of the MW vein at the gateway between Cape St Vincent and the Gorringe Bank; furthermore, along its path around the WIM, the current sometimes becomes unstable and separates from the slope at different locations, generating successive anticyclonic structures (Meddies) (Zenk and Armi, 1990). As a consequence of the process of spreading of the MW vein, when the flow turns to the Tagus Basin, the resulting mean flow is observed to generate mean vorticity structures, two of them (anticyclonic and cyclonic) trapped to the slope, denoted A1 and C2 in Figure 2.9 b, and an anticyclonic mean structure offshore, denoted by A2. This complex recirculation system is also evident in Figure 2.10 e. In the northern side of the Estremadura Promontory the flow progresses poleward, giving rise to a partial detachment and an anticyclonic structure, denoted A3, which extend from the MW levels up to the surface (Figures 2.9 b and 2.10 c).

Evidences in the literature of this conspicuous negative vorticity in this region are discussed by Daniault et al. (1994) and Mazé et al. (1997). On the other hand, a region of anticyclonic vorticity is frequently observed near 40^oN in the SST field, separating the southern waters (warmer and saltier) that progress poleward from the northern waters (fresher and colder). Furthermore, a detailed discussion of this anticyclonic region in the framework of the dynamics of the IPC is presented by Peliz et al. (2003a, 2005).

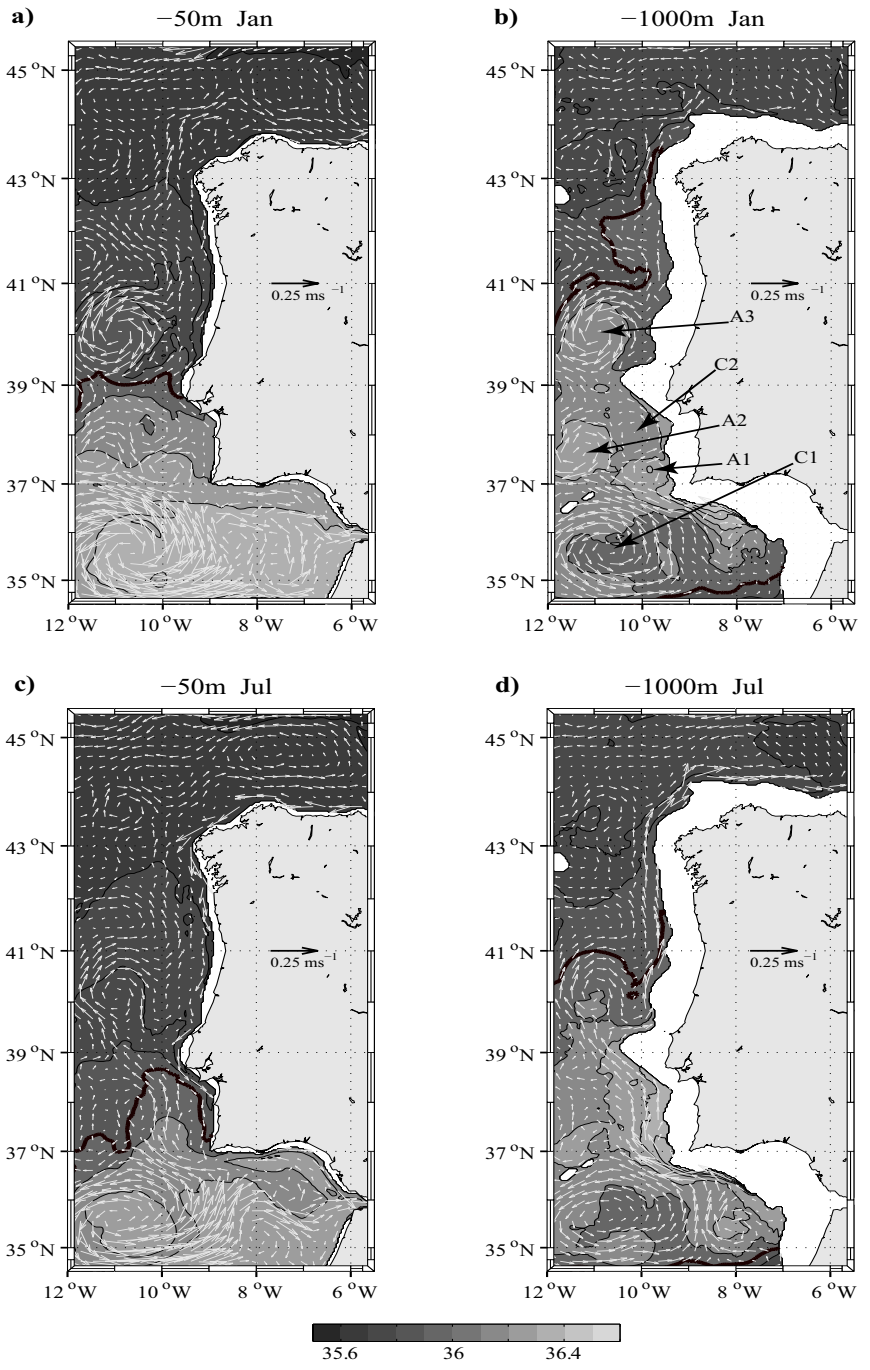

Figure 2.9: Salinity and velocity fields for January (a,b) and July (c,d) at 50 m (a,c) and at 1000 m (b,d). Isohalines are depicted every 0.2 (36 in thick black contours) and the vector scale is indicated on the map. For information regarding the pointing arrows, please refer to the text.

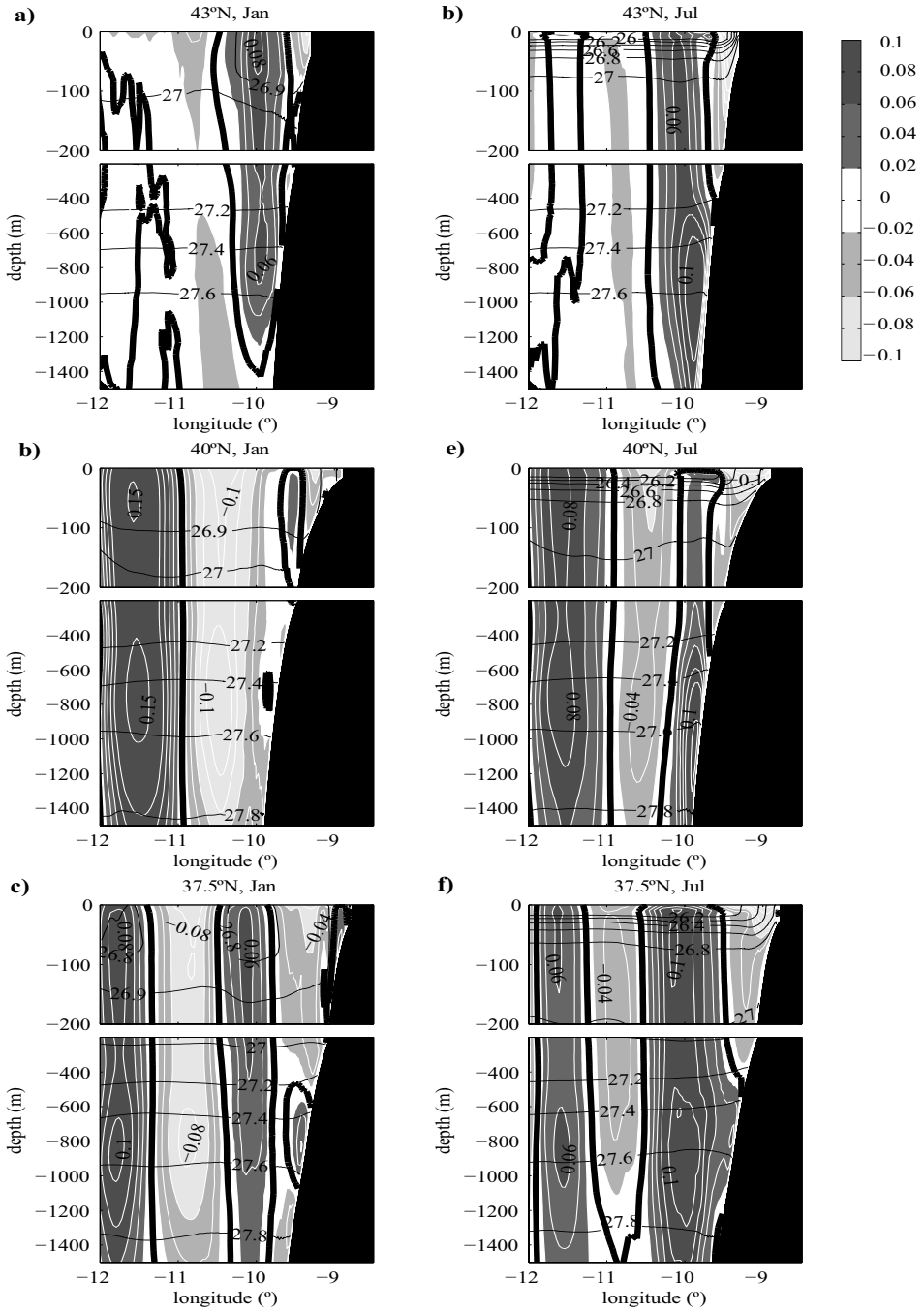

Figure 2.10: Zonal sections of 5-year means of potential density anomalies ($kg\ m^{-3}$) and meridional velocity ($m\ s^{-1}$) for January (left column) and July (right column) down to 1500 m deep. From top to bottom, the latitudes are: 43^{o}N (a,d), 40^{o}N (b,e) and 37.5^{o}N (c,f). σ_θ is depicted every 0.2 $kg\ m^{-3}$. The light shades of gray mark negative values below -0.02 $m\ s^{-1}$ and the dark shades of gray positive values above 0.02 $m\ s^{-1}$. The thick contour is zero and the first 200 m are enlarged.

North of 40^oN, a flow bifurcation is observed (Figure 2.9 b). Part of the flow veers cyclonically and becomes part of a northwestward flow that leaves the domain at 42^oN, 12^oW south of the Galicia Bank; the other part of the flow reattaches to the slope and continues poleward, flowing along Cape Finisterre at 43^oN. At this latitude (Figure 2.10 a), this poleward flow is associated with a downward slope of the isopycnal field centered at about 10^oW and extending upward from the levels of the MW up to the surface, while offshore of 10^oW a weak equatorward flow is dominant.

The 43^oN section in the work of Mazé et al. (1997) shows similar circulation, with maximum poleward tendency at $\sim 9.75^oW$, and equatorward flow from 10.5^oW to 12^oW, which is attributed in part to the recirculation around the Galicia Bank.

The circulation at 50 m (Figure 2.9 a) shows similar patterns to those at 1000 m, showing coupling between the MW and the surface layers as further discussed below.

2.5.2 Summer Circulation

The summer circulation at the MW levels (Figure 2.9 d) presents a similar general behavior to that of winter, discussed above. The inflow in the Tagus Basin occurs more trapped to the slope than in January, with less evidence of southward recirculation (A1 in Figure 2.9 b) and stronger poleward flow between 9.5^oW and 10.5^oW. Offshore (10.5^oW to 12^oW) there is a weakening of both poleward and equatorward signatures (Figure 2.10 f).

The anticyclonic structure centered at 40^oN, 11^oW presents a weaker signature than the one observed in winter, meaning less tendency to detach from the northern flank of the Estremadura Promontory, and hence stronger slope-trapped flow at the levels of the MW, with maximum poleward flow at 1200 m depth (Figure 2.10 d).

North of this latitude, a weaker flow separation tendency south of the Galicia Bank is observed, when compared to the winter case. The tendency for the slope-trapping of the MW vein observed at 40^oN during summer is further confirmed at the 43^oN section (Figure 2.10 b), in which the maximum poleward velocity is 10 $cm\ s^{-1}$ at 1000 m depth and extending up to the surface with some vertical tilting in the poleward flow structure. One of the most striking features in our modeled mean circulation for summer is the existence of conspicuous poleward flow during this season. This issue will be further discussed below. Concerning the surface layers circulation (Figure 2.9 c), a band of equatorward flow along the continental shelf/upper slope is observed associated with the upwelling front, with particular notice to the velocities between Cape Ortegal and Cape Finisterre, replacing part of the northward branch of the poleward flow in winter.

2.5.3 Meridional Transport

In order to obtain some insights about the seasonal and interannual variability of the circulation, series of alongshore transport were computed across the same three zonal sections (43^oN, 40^oN and 37.5^oN) and integrated in the upper 1500 m depth range. As visible in Figure 2.10, there is strong coupling between the circulation at the levels of MW and those of the central waters, as documented by Mazé et al. (1997).

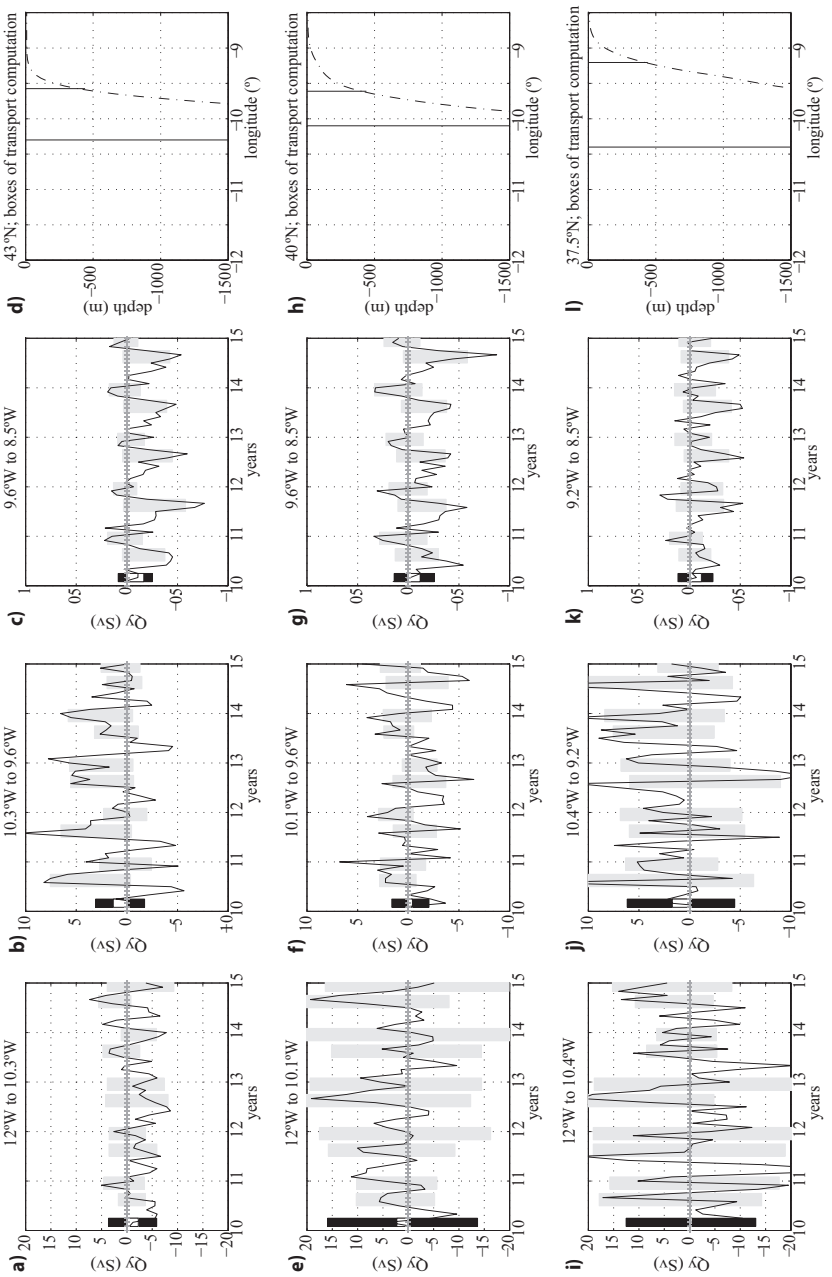

Figure 2.11: Time series of meridional transport (Sv) monthly means across (upper row) 43^oN; (middle row) 40^oN; and (lower row) 37.5^oN. Each column corresponds to a subsection represented in the rightmost column (d,h,l). From left to right: (a,e,i) offshore; (b,f,j) lower slope and adjacent upper layers; (c,g,k) shelf/upper slope (down to 400 m). Seasonal averages (July, August, September — JAS — and November, December, January — NDJ) are plotted in shades of gray for northward and southward transports. To the left of each plot, total northward and southward averages are in black bars and the net average is in white bars.

Results are shown in Figure 2.11. Each zonal section is divided into three sub-sections (hereafter called boxes for simplicity): shelf/upper slope (from the coast to the 400 m isobath), lower slope and offshore box. These boxes will hereafter be designated as onshore, central and offshore boxes, respectively. The boxes are defined individually for each section because the location of both the upper and lower slope circulation varies with latitude, as seen in Figure 2.10. The border of the onshore box was designed to accommodate the shelf circulation, and was therefore defined by setting the depth at the 400 m isobath. The separation between the central and the offshore boxes was carried out by defining the central box as the area of prevailing poleward flow (see Figure 2.10).

Thus, monthly means of meridional net transport, with positive (negative) values corresponding to poleward (equatorward) flow, are shown for 43^{o}N (Figure 2.11 a-c), 40^{o}N (Figure 2.11 e-g) and 37.5^{o}N (Figure 2.11 i-k).

At the onshore boxes (Figure 2.11 c,g,k), the main feature observed is the equatorward flow due to upwelling, which presents one main peak centered in July-August and occasionally one or several minor peaks during spring. In wintertime, a poleward flow associated with the inshore intrusion of the IPC is observed on the upper slope. The equatorward summer transport peak is typically 0.5 Sv independent of the latitude, but the spring peak spans from less than 0.1 Sv to about 0.3 Sv. Although a clear seasonal cycle of the circulation is seen for both upwelling and poleward flow, there is also some interannual variability in the structure of the peaks associated with the upwelling equatorward transport, both in width and intensity. Observing the seasonal cycle, some differences can be remarked regarding the equatorward circulation at different latitudes. In the northern and central sections (43^{o}N and 40^{o}N, respectively — Figure 2.11 c,g), the equatorward flow starts early in the year (February) and lingers on until October, whereas in southern Portugal (37.5^{o}N — Figure 2.11 k) a weak and variable circulation is observed during springtime (February to May), and the clear signal of upwelling appears in June-July. Furthermore, poleward flow along the shelf/upper slope is observed every year for the 43^{o}N and 40^{o}N sections, with typical values of 0.2 to 0.3 Sv, starting recursively at the beginning of autumn and with peaks in December, occasionally with secondary peaks in January. The southern region does not show clear evidences of poleward flow on the upper slope/shelf.

In respect to the central (Figure 2.11 b,f,j) and offshore (Figure 2.11 a,e,i) boxes, the transport patterns are not so clearly defined as in the case of the onshore box. For the northern and central latitudes (43^{o}N and 40^{o}N) at the central box (Figure 2.11 b,f), two peaks of poleward flow are observed throughout the year in almost all simulation years: the first one during summertime (July to September), presenting high transport values, from 3 to 10 Sv; the second peak with smaller amplitudes, 2 to 7 Sv, is observed from November to January. Both transport peaks have strong interannual variability in terms of magnitude. The first peak appears as an offshore poleward flow co-existing with the inshore summer upwelling peak (cf. Figure 2.10 b with Figure 2.10 c and Figure 2.10f with Figure 2.10 g). This offshore shifting of poleward flow during the upwelling season has also been reported in hydrographical cruises (Peliz et al., 2002; Torres and Barton, 2007). The second peak is associated with the winter IPC. Conversely, every year, recurrent peaks of equatorward transport are observed during the late winter-spring months. The southern

region at the central box (Figure 2.11 j) presents a complex pattern, although the tendency for poleward flow with multiple peaks during summer (shaded), late autumn and January is still discernible. The tendency for equatorward flow observed during late winter and spring is only partially met. Recall that this box is strongly influenced by the MW vein and the corresponding shedding of Meddies, which makes it more difficult to interpret than the patterns described for the northern region. Moorings analysis at about 42^oN (from the French project ARCANE, Huthnance et al., 2002, and Colas, 2003) showed that at the depths of ENACW and MW the maximum of poleward flow occurred between August and October, although at the surface this maximum was found in December-January; furthermore, in February-March a direction reversal at those levels was observed, with equatorward flows of 5 to 10 $cm\ s^{-1}$. From float data, the same authors discuss that there is a clear slope current of about 2 $cm\ s^{-1}$ but that the major poleward flow occurs between 600 and 1400 m.

The offshore region (Figure 2.11 a,e,i) is the widest of the three sub-sections, and does not present a clear seasonal pattern as the central and onshore boxes. The northern offshore box (Figure 2.11 a) is characterized by a tendency for equatorward flow, with typical values of less than 5 Sv, as previously discussed (Figure 2.10 a,d). This behavior is opposite to the central box at the same latitude (Figure 2.11 b), meaning that at 43^oN the poleward flow is preferentially attached to the slope (central box), which Figure 2.9 b,d also shows. At 40^oN (Figure 2.11 e), the offshore box is characterized by high values of transport in both directions, resulting from the anticyclonic vorticity structure of the mean circulation (denoted A3 in Figure 2.9 b and visible in Figure 2.10 b,e). Mazé et al. (1997) refer to a circulation of about 6 Sv for the MW levels at this latitude associated with an anticyclonic structure of large dimensions, and Daniault et al. (1994) discuss the existence of anticyclonic vorticity there (see discussion above). However, the net overall contribution (Figure 2.11 e) is poleward during the summer months with strong interannual variability, and presents peaks of poleward flow in February-March. This late winter poleward transport is delayed by two to three months relative to the peaks observed in the central box at 40^oN (Figure 2.11 f), which can be interpreted as the westward IPC migration. On the other hand, the separation of the flow associated with A3 occurring north of the Estremadura Promontory also explains the poleward tendency in this offshore box.

The southern (37.5^oN) offshore region (Figure 2.11 i) is affected by a strong variability, consequence of the spreading of the MW vein and its mesoscale features. However, similarly to the central box, some features can be observed, such as peaks of poleward current during summertime (shaded), and during November-January for most of the years, but also equatorward peaks mainly observed between February and June every year. This equatorward flow is, as discussed above, partially associated with recirculation of the poleward flow across the central box. When comparing this offshore transport to the central box one at the same latitude, transport has a clearer tendency for poleward flow at the central box than the offshore one. This is understandable since most of the MW vein at this latitude tends to circulate poleward by the central box, as shown in Figure 2.10 e,f, where it is also evident that the offshore circulation across 37.5^oN is dominated by the presence of a mean anticyclonic vorticity structure denoted by A2 in Figure 2.9 b.

The meridional transport across the boxes calculated from the results of the model can be compared to those calculated by Mazé et al. (1997) for the Bord-Est 3 cruise during May 1989, for the sections at 37.5^{o}N and 43^{o}N. The authors compute meridional transport through layers defined by density anomalies in order to quantify transport by the North Atlantic Central Waters and by the Mediterranean Water, which corresponds roughly to the layers comprised between the surface and 1500 m depth. Furthermore, the results of the sampled stations provide the transport distribution in longitude ranges, which renders possible a comparison to the modeled results. Table 2.1 displays meridional transport averages through 43^{o}N, 40^{o}N and 37.5^{o}N, both northward (positive — Q_y^+) and southward (negative — Q_y^-), as well as the net transport. Additionally, the transport through the entire section is also computed. The values in the work of Mazé et al. (1997) (hereafter observations) were obtained from their Figures 12 and 13 (a,c). The sub-sections refer to the boxes defined in Figure 2.11 for SD and the most approximate values with respect to the stations presented by Mazé et al. (1997). Absent values in the observations mean no available data. It is important to keep in mind that the observations concern a single month, whereas our results are 5-year averaged transport across every section.

For the northern section at 43^{o}N (first column), similar transport values are reported, which consist in prevailing northward transport in the central box and prevailing southward transport in the offshore box, giving rise to a full net southward transport of about 1 Sv for SD and about 2 Sv for the observations. For the southern region at 37.5^{o}N (last column), transport calculation is more complicated because of the presence of a Meddy in the observations, partially sampled along the western side of the section, that accounts for about 6.6 Sv of southward transport at the MW levels. Therefore, the transport through the offshore box was corrected subtracting this value from the southward total, which would amount to 21.4 instead of the 14.8 Sv presented in Table 2.1, as marked with an asterisk. The southward transports are similar in magnitude. As for the northward transport, in SD at the central box, values are lower than the observations (6.2 Sv against 10.2 Sv, a difference of 4 Sv); however, they are higher at the offshore box with the same difference of 4 Sv (12.5 Sv against 8.5 Sv for the observations), which may mean that the poleward flow crosses 37.5^{o}N at different longitudes. There can be another explanation. Following the interpretation of Mazé et al. (1997), from the 10.2 Sv that flow northward across the central box, approximately half continues northward, and the other half recirculates southward to the west, that is, its contribution adds to the offshore southward transport of 14.8 Sv (as schematically represented in Figure 15 of their work). Then, the exceeding northward transport in SD at the offshore box may be due to the anticyclonic vorticity structure (see Figure 2.9 b and Figure 2.10 c,f), which in the observations is west of 12^{o}W and is therefore not taken into account.

Although Mazé et al. (1997) do not provide data for 40^{o}N, the model results are also shown in Table 2.1 (middle column). Transport is, in terms of balance, northward at the offshore box and southward at the central and inshore boxes. This is due to the separation of the flow that occurs at this latitude, associated with the mean anticyclonic vorticity region discussed in this section (see Figure 2.9 b and Figure 2.10 b,e), which accounts for the strong northward and southward transports at the offshore box.

Latitude		43^{o}N				40^{o}N				37.5^{o}N			
Sub-section		Offshore	Central	Onshore	**Total**	Offshore	Central	Onshore	**Total**	Offshore	Central	Onshore	**Total**
Mazé et al. (1997)	Q_y^+	4.0	5.9	-	**9.9**	-	-	-	-	8.5	10.2	1.2	**19.9**
	Q_y^-	-6.4	-1.4	-	**-7.8**	-	-	-	-	$-14.8*$	-1.2	0	**-16.0**$*$
	Net	**-2.4**	**4.5**	**-**	**-2.1**	**-**	**-**	**-**	**-**	**-6.3**$*$	**9.0**	**1.2**	**3.9**$*$
SD	Q_y^+	3.6	3.1	0.1	**6.8**	15.9	1.6	0.1	**17.6**	12.5	6.2	0.1	**18.8**
	Q_y^-	-5.9	-1.7	-0.3	**-7.9**	-13.7	-2.1	-0.3	**-16.1**	-13.1	-4.5	-0.2	**-17.8**
	Net	**-2.3**	**1.4**	**-0.2**	**-1.1**	**2.2**	**-0.5**	**-0.2**	**1.5**	**-0.6**	**1.7**	**-0.1**	**1.0**

Table 2.1: Mean meridional transports (Sv) across three sections off WIM integrated from 0 to 1500 m, at latitudes 37.5^{o}N, 40^{o}N and 43^{o}N. For each zonal section, three subsections in longitude were defined according to Figure 2.11: Onshore, Central and Offshore. The corresponding transports for the same sections of Mazé et al. (1997) are shown for comparison with modeled transports.

2.6 Lagrangian Considerations

This section addresses the origin of upwelled waters along the Western Iberian Margin during the upwelling season. We apply a Lagrangian particle model run back in time to the climatological run described above, in order to trace the preferential pathways of these waters, as well as the depths of origin and the distances traveled in one month.

2.6.1 Lagrangian Model

The Lagrangian particle model runs offline over the climatological simulation. It consists in an Individual Based Model (IBM), coupled to ROMS using ROFF (Carr et al., 2007). ROFF is a drifter-tracking code that simulates Lagrangian trajectories from stored ROMS velocity and hydrological fields using a high-order predictor corrector scheme to integrate the motion equation $dX/dt = U_{ROMS}(X,t)$, with X being the position vector (x,y,z), and U_{ROMS} being the modeled 3D velocity vector over time, given an initial condition $X(t_0) = X_0$. In addition to the advection generated by the model velocities, the particle movements include random velocities in the vertical direction, which are used to parameterize unresolved turbulent processes.

The particle model allows the trajectories of a cluster of particles to be tracked during a given period. Our purpose is to study the particles arriving at the Western Iberian Margin, but since ROFF runs backward in time, the particles are actually deployed from the coastal region along WIM where upwelling occurs, what we call areas of arrival. We defined four areas of arrival, approximately limited offshore by the 200-m isobath (Figure 2.1): Galician Rias (GR), Northern Portuguese Coast (NC), Estremadura Promontory (EP) and Southern Portuguese Coast (SC). The particles were released in all grid points at three different depths: 20 m, 40 m and 60 m. Furthermore, particles were released on three dates: June 30, July 30 and August 30. Their trajectories were traced backward for one month; therefore their departure points were on June 1, July 1, and August 1, respectively. During that month of travel, we have information on the particles horizontal and vertical displacement. The number of particles depends on the area of arrival and its corresponding grid: 284 at GR; 388 at EP (the largest area); 325 at NC; and 156 at SC (the narrowest). Thus, the total number of particles is three times these values, since the study is carried out for 3 months. The Lagrangian module only runs over the last year of simulation.

Although the configuration has been designed to track particles from the point of arrival back to their point of origin, the discussion refers to the particles as if deployed at their points of origin and terminating at the four arrival areas illustrated in Figure 2.1. For simplification, particles that arrive at 20 m, 40 m and 60 m will be henceforth designated as 20-m, 40-m and 60-m particles, respectively. In addition, the mean SST for June is also shown, as well as the maximum southward meridional velocities. This figure will be used in the interpretation of trajectory maps, as well as in considerations concerning the distance of the particles from the coast, distance traveled and mean depths of origin, discussed in the following sub-section.

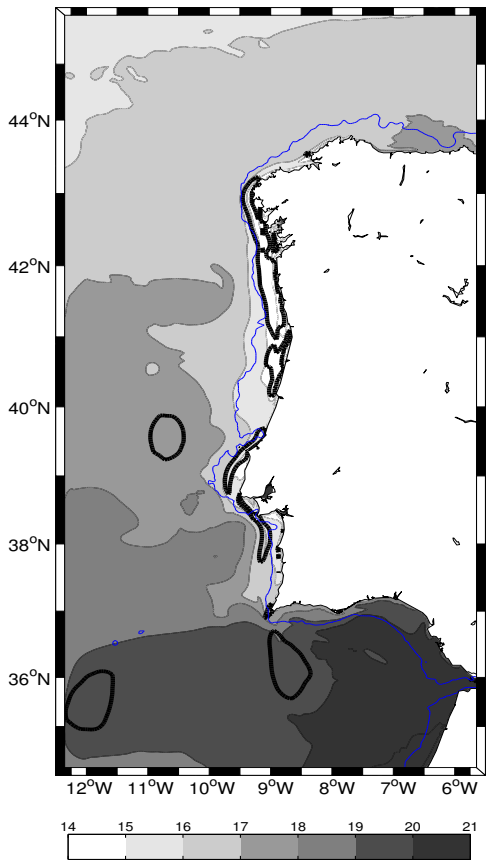

Figure 2.12: Mean field of SST for June of the last year of simulation of SD. The thick black line represents meridional velocities of -25 $cm\ s^{-1}$ for the same month. The 200-m isobath is shown by the blue line.

2.6.2 Trajectories

On a first approach, to avoid overloading the maps, only the preferential pathways of upwelled waters arriving on June 30 were considered, since these were similar to the other months studied. The left column of Figure 2.13 shows the trajectories of particles arriving at 20 m (gray dots), 40 m (black dots) and 60 m (white dots), and the right column shows the origin points of each particle, with the information of its depth on June 1 ($t = 0$) given by the gray shades. In general, the 20-m particles have their origin at farther locations to the north, but mainly at shallow depths. Indeed, the 200-m isobath seems to delimit the particles trajectories, which are mainly alongshore and close to the coast. As for the 40-m and 60-m particles, they appear to have similar trajectory patterns, their origin sometimes located inshore to the north, others from closer offshore regions. The NC and EP locations (Figure 2.13 c,e) show more alongshore pathways, accompanying the shoreline, whereas GR and SC (Figure 2.13 a,g) present some meandering. These results are consistent with the

average signature of the upwelling and associated equatorward jet, shown in Figure 2.12. The coastal cold band is approximately limited by the 200-m isobath, typically at 40 km distant from the coast.

Furthermore, it is evident that, in general, the particles that originated the farthest from their arrival site came from shallower depths. This is most evident at NC (Figure 2.13 d). There are some exceptions, however. In GR and EP (Figure 2.13 b,f), there are some particles whose origin is offshore the WIM at approximately 10^oW and with depths of over 80 m, and also off Estremadura Promontory for particles arriving at SC (Figure 2.13 h). It is apparent that particles originate at shallower depths at the southern coast than at northern locations.

2.6.3 Quantitative Analysis

The following analyses concern the three sets of data, from the Lagrangian simulations of June, July and August. Figure 2.14 shows the distribution of the depths of origin according to region. Histogram bars correspond to depth intervals. The x-axis labels are the maximum depths of each interval, that is: '-50' corresponds to the interval 0-50 m, '-100' corresponds to 50-100 m, and so forth. The first interval of 0-50 m registers the highest occurrences for all regions and for all depths of arrival. Percentages are of 80% for the 20-m particles, 60% to 70% for the 40-m particles from north to south, and between 30% and 50% for the 60-m particles. Regarding the other depth intervals, the behavior is not quite as uniform. At GR (Figure 2.14 a) and EP (Figure 2.14 c), particles originate mainly from depths between 50 and 100 m and between 150 and 200 m, but the other depth intervals still register occurrences. At NC (Figure 2.14 b), preferential depths of origin are 100-150 m, especially for 60-m particles ($\sim$ 25%), and 200-250 m and there are no particles arriving from depths greater than 300 m. At SC (Figure 2.14 d), particles originate preferentially from the 50-100 m interval: 60-m particles register above 40% and 20- and 40-m particles register roughly 20%. Here, there are no particles coming from depths of more than 200 m.

Additionally, Figure 2.15 shows the correspondence between distance traveled by the particles, from their point of origin to the arrival point, and their depth of origin. It is noticeable that the farther the particles have traveled from their origin, the shallower their origin is. The northern locations register the farthest origins, all corresponding to 20-m particles.

Observing Figure 2.12, it is clear that the highest velocities of the equatorward jet are found north of 40^oN, consistent with these results. All regions and particles show a tendency of decrease in distance traveled as the depth of arrival increases except for SC (Figure 2.15 d). Indeed, the southernmost location shows a homogeneous distribution of distance traveled independently of the depth of arrival. According to Figure 2.12, the southward velocities in this area are lower than in all others, that is, conditions are less prone for particles to travel large distances. The deepest points of origin were mainly recorded for the 60-m particles. It is also noticeable that these maximum depths are found at GR and EP (Figure 2.15 a,c).

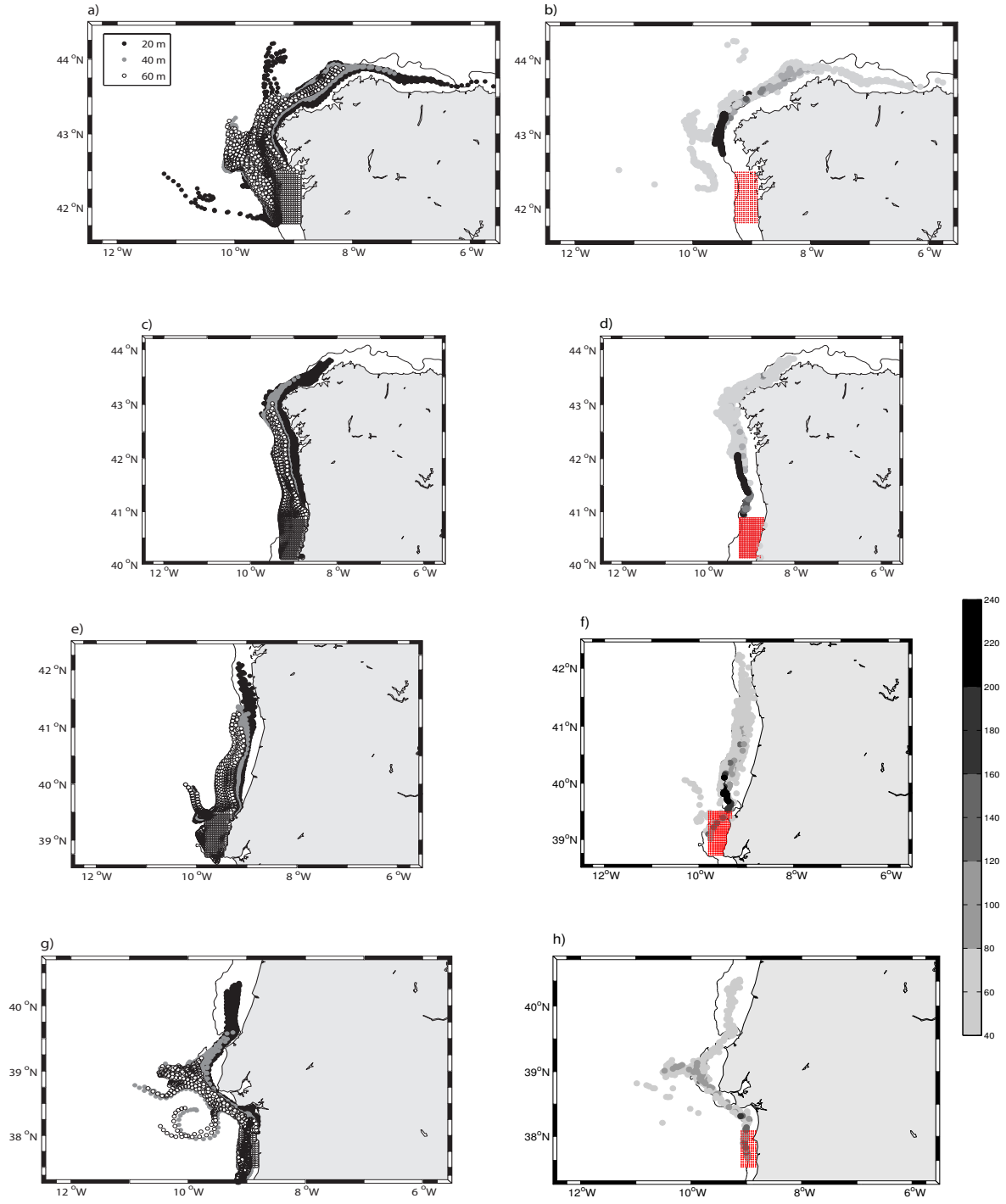

Figure 2.13: (left column) Trajectories of particles arriving on June 30 (20-m particles: black dots; 40-m particles: gray dots; 60-m particles: white dots) and (right column) location and depth of origin of each particle (colorbar in km) for the four arrival locations: (a,b) GR; (c,d) NC; (e,f) EP; (g,h) SC. The 200-m isobath is shown.

Since the trajectory maps reveal a tendency for the particles that travel the greatest distances to trace an alongshore path limited to the upper 200 m of the water column, the mean depth computed for each particle along its trajectory was plotted against its mean distance to the coast (Figure 2.16). For NC and EP (Figure 2.16 b,c) the particles that originate farthest from the coast (on average 80 km) come from the same depths as those from which they later upwell; they essentially have surface/subsurface trajectories. These particles may be influenced by the upwelling-associated mesoscale phenomena. On the other hand, particles whose trajectories were traced, on average, to depths of more than 120 m have never reached distances greater than 20 km from the coast, which is the average distance of the 100-m isobath as discussed in the previous sub-section regarding Figures 2.13 and 2.14. These particles seem to travel mainly through the equatorward jet or come from lower levels directly below their upwelling site, where the associated upward motion of replacement of surface waters with deeper waters takes place.

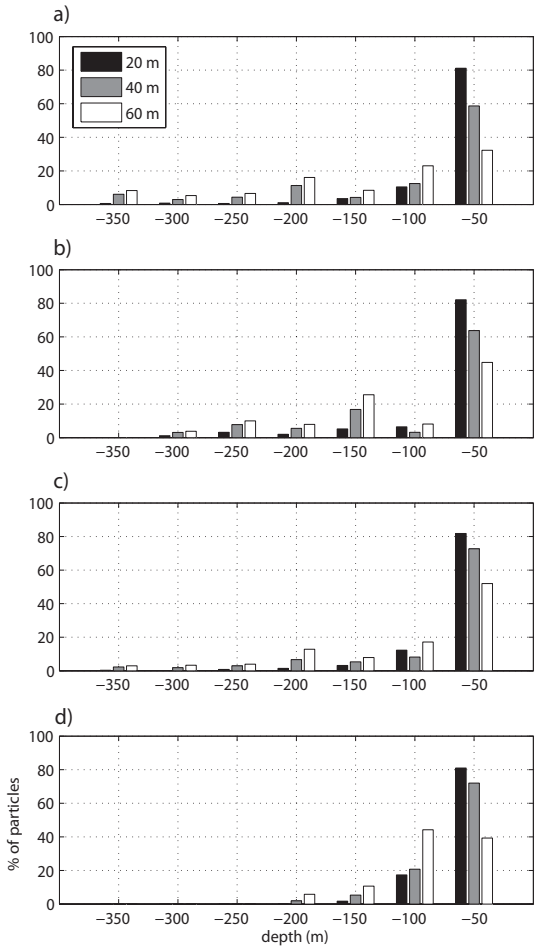

Figure 2.14: Histograms of the origin depth of all particles (3 months) arriving at 20 m (black), 40 m (gray) and 60 m (white), for the four locations of arrival: (a) GR; (b) NC; (c) EP; (d) SC.

It is important to notice that the regions of the Galician Rias and Estremadura Promontory are somewhat different from the others. The GR is characterized by a jagged coastline with several estuaries and bays, and the EP is a prominent topographic feature. Both locations are prone to the development of filaments, that is, detachments of flow from the main alongshore path of the equatorward jet (Torres and Barton, 2007; Oliveira et al., 2009). At these locations, the upwelled waters originate at greater depths and traveled shorter distances, suggesting that their trajectories are dependent on local mesoscale activity. In contrast, at the Portuguese northern and southern coasts, which are roughly meridional coasts, upwelled waters come from larger distances and shallower depths, being mostly dependent on the core alongshore equatorward jet, flowing within 20-40 km of the coast and with velocities that reach 30 $cm\ s^{-1}$, as observed in section 2.4.

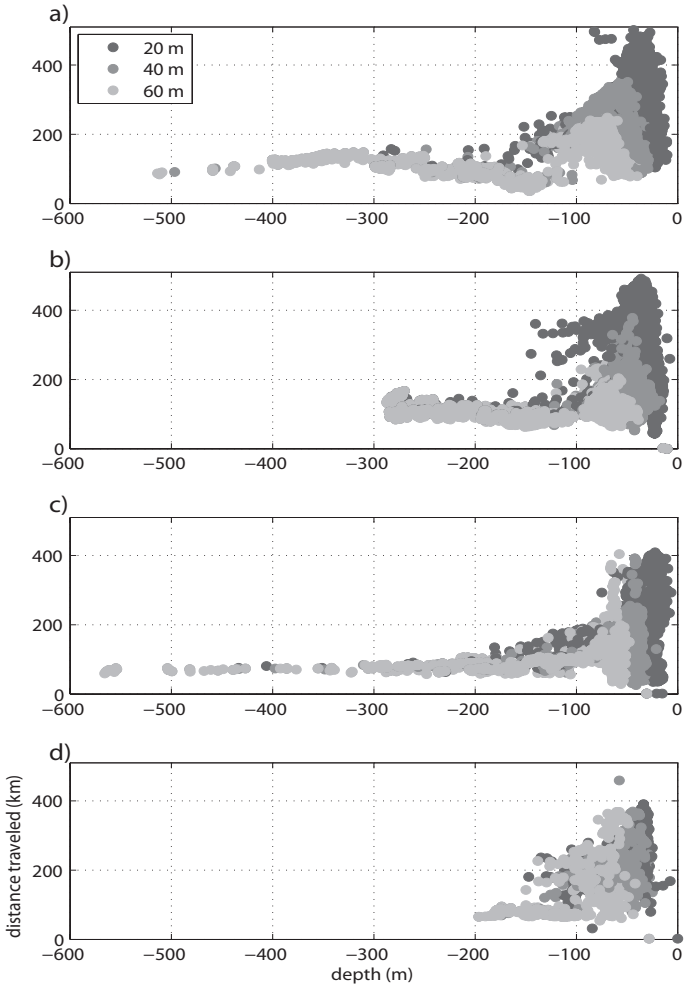

Figure 2.15: Distance traveled according to depth of origin of all particles (3 months), for the four locations of arrival: (a) GR; (b) NC; (c) EP; (d) SC.

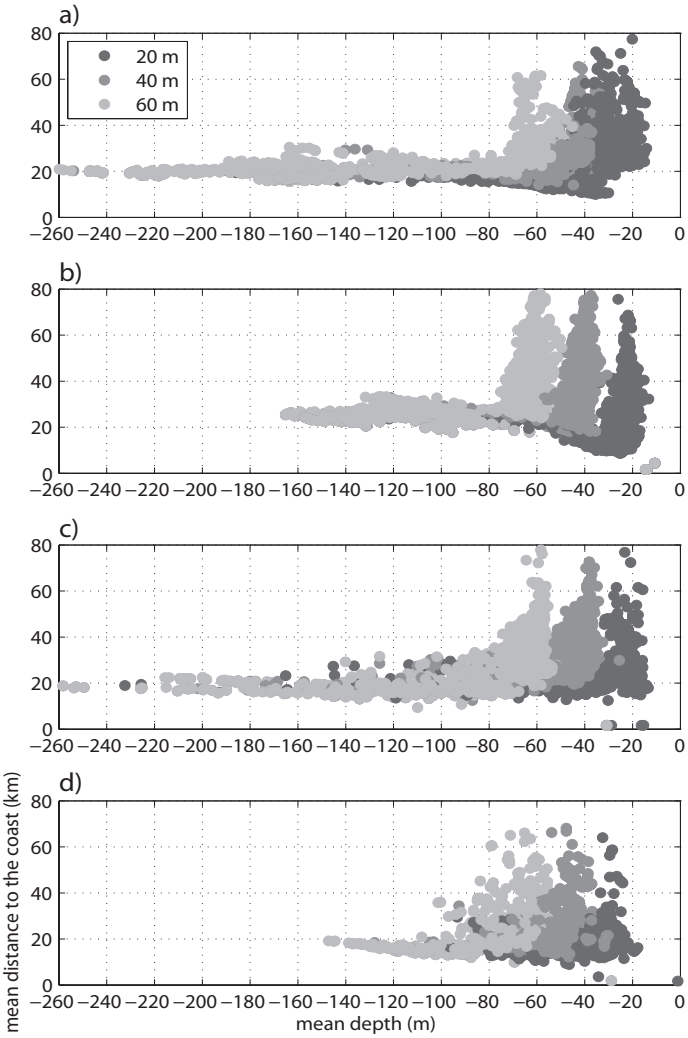

Figure 2.16: Mean distance to the coast of all trajectories (3 months) according to the trajectories mean depth, for the four locations of arrival: (a) GR; (b) NC; (c) EP; (d) SC.

2.7 Discussion

The purpose of this study was to model the mean circulation of the Western Iberian Margin, as well as the seasonal cycle of the hydrographic fields. Three phenomena play the most important roles in setting both hydrography and flow: summer coastal upwelling, the Iberian Poleward Current and the Mediterranean Water outflow through the Strait of Gibraltar. The main focus was to integrate these phenomena into a numerical configuration that takes into account not only the large-scale features such as the Azores Current and the meridional density gradient, but also small-scale features such as the entrance of MW into the Atlantic and river inflow. A thorough characterization of the mean hydrography and flow on the shelf/slope was carried out, as well as the connection between the intermediate circulation (at the MW levels) and the surface layers. The prevalence of the slope poleward flow throughout the year is also explored.

a. Circulation Considerations

The used forcing was the COADS climatology. With this forcing, which contains no interannual variability or synoptic meteorological scale variability, the purpose was to reach a realistic circulation as a result of the adjustment of the hydrographic fields. Concerning this resulting circulation, many of the modeled features have their correspondence in the available observations.

The main pattern of the circulation consists in a poleward flow along the slope during winter and lingering on in summer. The IPC has been regarded as a baroclinic current that results from the isopycnal field adjustment at the upper slope. In addition to this classic view, Torres and Barton (2006) estimated a mean transport of 2 Sv from the surface down to 500 m and postulated that the poleward flow could penetrate down to the levels of MW. The authors hypothesize that a poleward flow at the MW levels would arise from different dynamical reasons, but can form a continuous flow inducing topographic guidance of the surface flow. This behavior is well reproduced by the model results, suggesting that the poleward flow extends downward to the levels of the MW and has a marked barotropic character.

The winter flow patterns obtained by the SD configuration resemble the typical description of poleward flow in the literature. The model results also suggest interannual variability associated with intrinsic variability, that is, not resulting from external forcing. However, this interannual variability does not explain episodes of strong alongshore current observed in particular years only (January 1990, 1996, 1998 as reported in García-Soto et al., 2002, and Peliz et al., 2005). This means that factors other than climatological forcing or large-scale forcing, both imposed seasonally but with no interannual variability, may explain the variability and the years of extreme poleward flow, not described within our simulations.

When considering the mean fields of hydrographic properties and alongshore velocity for several years (5 years in this case), we obtain a picture of a poleward flow extending from the surface down to the levels of the MW, centered at about 10^oW, with weak vertical shear and typical velocities of 6 to 10 $cm\ s^{-1}$ for winter and summer, although with some weakening at the surface in this season (Figure 2.10). This coupling between the MW and the central water layers was already reported by Mazé et al. (1997). Moreover, observations of Huthnance et al. (2002) report maximum poleward flow at moorings near 42^oN, 9.5^oW in September-October for all depths, a secondary peak in December-January at the uppermost currentmeter, and a maximum of equatorward flow in February-April. These features resemble the transport patterns in the central box for section 43^oN (Figure 2.11 b). Likewise, persistent poleward flow at about 250 m depth at a location near 42.3^oN, 10.2^oW is reported by Peliz et al. (2005) based on datasets of the Instituto Español de Oceanografía (Alonso et al., 1995), where the intensity of the poleward current was about 10 $cm\ s^{-1}$ and no correlation between winds and currents was found at this mooring. This tendency to poleward flow at this longitude is comparable to the mean values presented in Figure 2.10.

Concerning the issue related with the presence of poleward flow during the upwelling

season, Peliz et al. (2002) presented evidences of such behavior for central Portugal. Torres and Barton (2007) studied the Galician shelf/slope based on hydrography and ADCP measurements and also showed the coexistence of offshore poleward flow during June 1997 at the starting of the upwelling season. Process studies about the consequences of upwelling-related flow on poleward currents, such as by Peliz et al. (2003b), show that the poleward flow does lose intensity and spreads more offshore while keeping its identity. The presence of poleward flow in summertime is further confirmed by the series of currentmeter moorings discussed in the review by Relvas et al. (2007). The model results suggest that poleward flow is present along the slope and coexist with the upwelling-associated flow along the shelf/upper slope. This is visible not only in the mean alongshore velocities, but also in the transport associated with the central (slope) box.

A schematic view of the annual circulation at 1000 m (which extends its main features up to the surface layers), showing the main paths of the mean circulation, is proposed in Figure 2.17. The MW vein enters through the Cape St Vincent-Gorringe Bank gateway and flows in the northwestward direction, separating from the southwestern slope of the Iberian Peninsula (near Cape St Vincent) through an anticyclonic mean vorticity region (A1). Part of the flow continues poleward along the slope and part recirculates southward through a cyclonic mean vorticity region (C2) and continues poleward offshore due to the presence of another anticyclonic structure (A2). Both poleward branches, at the slope and offshore, give rise to the A3 anticyclonic region north of the Estremadura Promontory, although there is still flow along the slope, contouring the promontory. At the northern flank of this mean vorticity region, results suggest a new separation: part of the flow returns toward the coast and continues as the slope poleward flow, which is linked to the Iberian Poleward Current; the other part circulates poleward in another offshore branch between 11^oW and 12^oW. The slope poleward flow seems to separate south of 42^oN and joins the offshore branch, exiting afterward the domain south of the Galicia Bank. The slope branch continues to flow northward along Cape Finisterre, with evidences of a separation at the northwestern tip of the Iberian Peninsula.

b. Lagrangian Considerations

This work enabled us to draw a general picture of the origin of upwelled waters on the Western Iberian Margin and preferential paths according to location, and trace some relationships between depth of origin and distance traveled by these waters, as well as the trajectories mean distance to the coast and mean depth.

There is a general tendency for the particles that upwell at the WIM to come from the north, following the main pathway of the upwelling-associated equatorward jet, mostly restricted to first 20 km offshore (delimited roughly by the 100-m isobath). From these, the particles arriving at 60 m are more prone to come from deeper levels than particles arriving at 20 m. Moreover, the particles that travel the longest distances (up to 500 km at northern WIM and 400 km at southern WIM) usually originate from the upper 100 m. Conversely, the particles that travel the least ($<$100 km) originate from the deepest levels (up to 500-600 m at GR and EP and 200-300 m at NC and SC). The 20-m particles tend

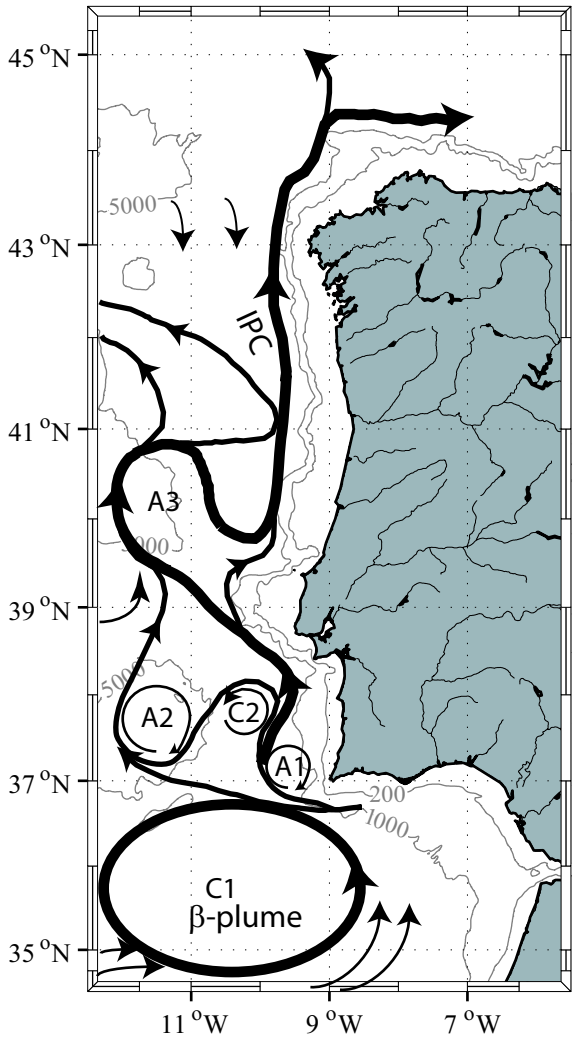

Figure 2.17: Schematic representation of the mean circulation at 1000 m as obtained from the present numerical modeling study, showing the main paths of the obtained circulation structures, and the recirculation vorticity structures.

---

to come from farther distances than 40-m and 60-m particles. On the other hand, the particles that have come from deeper levels are the ones whose trajectories, on average, were always within 20-40 km from the coast, that is, they come from the north and trace alongshore paths until their upwelling site. Also, there is a tendency for particles in some of the regions to travel mostly at the depths at which they afterward upwell.

It is also suggested that particles that have origins the farthest away from their upwelling regions, and hence the shallowest origins and whose trajectories are closest to the coast, are dependent on the equatorward jet, while particles that originate closer to the coast, and hence at deeper levels and sometimes from more offshore locations, are modulated by mesoscale activity.

Chapter 3

Interannual Variability of the Western Iberian Margin Circulation: 2001-2011

Part of the contents of this chapter have been published by Ramos et al. (2013).

3.1 Overview

After portraying the mean state of the region under scope, hydrographically and dynamically, the following chapter focuses on the domain interannual variability. Despite the system very pronounced seasonal variability, it is also very prone to smaller space scale phenomena that are responsible for the differences that are observed from one year to the next. Mesoscale vortices and upwelling-associated filaments are among the dynamical features responsible for non-linear behavior in this current system. The atmospheric interannual variability is also a key factor in determining years with stronger or weaker summer upwelling, or the pathways of the poleward flow.

Due to their importance in the maintenance of the associated marine ecosystems, upwelling regions have been the subject of study for the assessment of significant changes in the past decades. One of the first important works on this matter is the already mentioned work of Bakun (1990), where the four upwelling systems were under scope and, based on observations for period 1946-1988, the author found that all systems showed an alongshore wind stress intensification trend during summer, which would implicate an upwelling intensification. Regarding a more regional scale and for a longer period, Lemos and Pires (2004) found a weakening trend for the longer 1941-2000 period for western Iberian Peninsula when analyzing both meridional wind component and SST datasets, although punctuated by strong interannual variability. The analysis of annual or seasonal signal tendency may hide different behaviors at the monthly scale. In this light, Alvarez et al. (2008) confirmed the negative tendency for period 1967-2006 for months March, April and July to December, but found a positive trend for the remaining months, concluding that

there is no clear seasonal trend in upwelling intensity in the past decades. On the other hand, Santos et al. (2005), based on a shorter satellite-based SST dataset, reported an upwelling regime shift in the early 1990s to stronger upwelling events, after a positive maximum of the North Atlantic Oscillation (NAO) winter index, corroborated by stronger coastal zonal gradients in summer from 1992 onward. Furthermore, Borges et al. (2003) found a higher frequency in northerly wind occurrence during winter, and consequently an increase in winter upwelling events. The difficulty to assess trends of upwelling activity has been summarized recently when Narayan et al. (2010) showed that there can be large discrepancies when analyzing trends derived from upwelling indicators (wind stress and SST), since they depend on the dataset used. Recently, Barton et al. (2013), using different wind datasets, found no wind intensification evidence along the Canary Upwelling System, both off WIM and off northwestern Africa.

This chapter is divided into two parts. The first part makes use of available data concerning the upwelling index (UI) all along the WIM and consists in a description of the interannual variability of upwelling from 1967 to 2011, where possible reasons for this variability are discussed (published in Ramos et al., 2013). The focus of the second part, on the other hand, is a regional numerical modeling study much like the one carried out in chapter 2, with the same configurations, but instead of climatologically-forced, and with the objective of discussing further the interannual variability of this system, the ROMS run was forced with real winds and fluxes for the period 2001-2011, as detailed below.

3.2 Data and Methodology

3.2.1 Upwelling Index

The upwelling index (UI) is a measure of occurrence of upwelling. There are, in general, two ways to compute this quantity, both already used for the WIM: (1) the Ekman transport perpendicular to the coastline, that is, generated by the alongshore wind stress component (e.g. Alvarez et al., 2008); (2) the difference between coastal (10-50 km) and oceanic ($\sim$ 500 km) SST (e.g. Santos et al., 2005). Both methods have advantages and caveats and some of these are discussed here. The first method, despite being based on the known effect of wind stress over the ocean surface and adjacent layers, which is the main driver of upwelling, does not account for the effects of capes and other coastal features, or mesoscale phenomena of which upwelling is also dependent on (Peliz et al., 2002; Relvas et al., 2009). The second approach is more of a proxy for upwelling occurrence, since upwelling is not the only cause for offshore-onshore SST differences; SST is strongly influenced by other phenomena such as river discharge in coastal areas and large-scale circulation offshore (Gómez-Gesteira et al., 2008).

In this study, the UI was provided by the Spanish Institute of Oceanography (IEO — http://www.indicedeafloramiento.ieo.es) and was computed by means of geostrophic winds following the method by Bakun (1973) and adapted later to the Iberian Peninsula by Lavín et al. (1991, 2000) (see formulation used by IEO below). The geostrophic

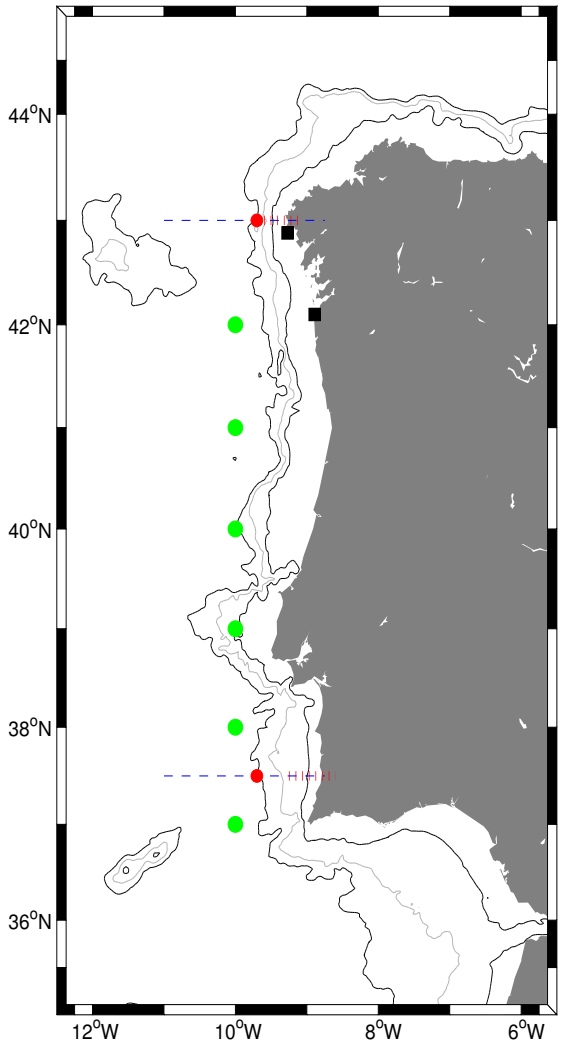

Figure 3.1: SD and the points/sections of analysis in this chapter. Green dots: upwelling index points (Figures 3.2 and 3.3 — from north to south: Rias Baixas; Aveiro; Figueira da Foz; Cabo da Roca; Sines; Sagres). Black squares: location of the HF-radar antennas (Figures 3.6 and 3.7). Red dots: points of measurement for S and v in Figure 3.12 and meridional wind stress in Figures 3.4 and 3.13. Blue dashed lines: S and v sections of Figure 3.11. Red dashed lines: sections of transport computation in Figure 3.13.

---

winds were computed from 6-hourly atmospheric sea level pressure (SLP) fields (at a 1^o resolution) obtained from the U.S. Navy Fleet Numerical Meteorology and Oceanography Center (FNMOC) for the 1967-2011 period. The use of the FNMOC SLP fields to compute the UI index has been used widely in different studies (e.g. Bograd et al., 2009, and namely for western Iberia Alvarez et al., 2011, and Macías et al., 2012).

Given the almost meridional character of the western coast of the Iberian Peninsula (Figure 3.1), UI can be formulated solely taking into account the cross-shore component

of the Ekman transport:

$$UI = -\frac{\tau_y}{\rho_{sw} f} \tag{3.1}$$

where $\tau_y = \rho_a C_D \sqrt{u^2 + v^2} v$ is the meridional wind stress component ($\rho_a \approx 1.22\ kg\ m^{-3}$ is the air density, C_D an adimensional drag coefficient (1.4×10^{-3}), u and v are the zonal and meridional components of the geostrophic wind, respectively, ρ_{sw} is the average density of seawater ($\approx 1025\ kg\ m^{-3}$), and $f = 2\Omega \sin(\theta)$ is the Coriolis parameter (Ω is the angular velocity of the Earth and θ the latitude). The zonal and meridional components of the geostrophic wind were computed as follows:

$$u = \frac{-1}{\rho_a f} \frac{\partial p}{\partial y} \text{ and } v = \frac{1}{\rho_a f} \frac{\partial p}{\partial x} \tag{3.2}$$

A friction correction (30% wind speed reduction and 15^o wind direction shift) was applied by the IEO to these geostrophic winds before the upwelling estimate is computed (Bakun, 1973; Lavín et al., 1991). The UI was multiplied by a factor of 1000, so that the measure translates a displacement of volume for each kilometer of coast ($m^3 s^{-1} km^{-1}$).

UI is positive when the Ekman transport is oriented offshore (i.e. westward) and thus upwelling-favorable, and negative when the Ekman transport is onshore (eastward) and thus downwelling-favorable. The six locations (a-f) at which the UI was computed and analyzed in this study are shown in Figure 3.1. Throughout the analysis, monthly-averaged UI indices were sued, computed from the 6-hourly data available at the IEO database.

Ramos et al. (2013) have validated this UI dataset with wind data from a buoy located at approximately 50 km from the point of Rias Baixas (10^oW, 42^oN). This buoy has data since 1999, and the comparison between the two monthly UI time series for summer (April to September) showed they are significantly correlated (at the 5% level) in all months except in July.

3.2.2 ROMS Forcing

ROMS two-domain nesting configuration has already been described. Both FD and SD forcing is the same, but FD was first initialized from rest using monthly temperature and salinity climatologies from the World Ocean Atlas 2009 at the boundaries (Antonov et al., 2010; Locarnini et al., 2010), and was forced using monthly surface fluxes from Comprehensive Ocean-Atmosphere Data Set (COADS), similarly to the simulation in chapter 2. This FD configuration reached equilibrium solutions after four years. At this stage, the Mediterranean Water (MW) is represented using a nudging term. After that period, and once the ocean reaches equilibrium, realistic forcing at the surface (instead of a climatological one) was used. The forcing consisted of the NCEP2 air-sea fluxes (www.ncep.noaa.gov) and QuikSCAT/ASCAT reanalyzed satellite winds from CERSAT (cersat.ifremer.fr) for the period 2001 to 2011, with a spatial resolution of 0.25^o (QuikSCAT was replaced by ASCAT in 2009). The outputs of FD were used to initialize and provide boundary conditions for SD through offline nesting. The forcing of SD was the same as for the FD, ensuring

consistency for both domains and avoiding problems at the boundaries. For the target domain, the Mediterranean Undercurrent (MU), previously described, is imposed by the same boundary inflow/outflow condition at the Strait of Gibraltar as in chapter 2. The inflow of freshwater to the ocean originated from the main rivers of the region was included in the form of realistic river outflow (provided by INAG, Water Institute of Portugal), when available. When there were no registers of river outflow during a given period of time, a climatological value for seasonal river outflow was imposed.

3.2.3 Satellite and HF-Radar

The SST satellite product is the same as in section 2.2.3, but instead of computing monthly averages for building a climatology, monthly means for each year for period 2001-2011 were used, averaged over the entire SD.

Galician SeaSonde HF radar network provides real time surface currents, wave data and currents forecast information, with a range of up to 200 km offshore. Its operation and exploitation is the responsibility of Puertos del Estado (www.puertos.es), INTECMAR (www.intecmar.org) and MeteoGalicia (www.meteogalicia.es). The two radar antennas are located near Cape Finisterre (42.88^{o}N, 9.27^{o}W) and Cape Silleiro (42.10^{o}N, 8.89^{o}W) (see Figure 3.1). The hourly data was filtered in order to remove the tides.

3.2.4 Argo Floats

Argo is an international collaboration that collects high-quality temperature and salinity profiles from the upper 2000 m of the ice-free global ocean and currents from intermediate depths. The data come from battery-powered autonomous floats that spend most of their life drifting at depth where they are stabilized by being neutrally buoyant at a "parking depth" pressure by having a density equal to the ambient pressure and a compressibility that is less than that of sea water. At typically 10-day intervals, the floats rise to the surface over about 6 hours while measuring temperature and salinity. Satellites determine the position of the floats when they surface, and receive the data transmitted by the floats. The float then returns to its original density and sinks to drift until the cycle is repeated. These data were collected and made freely available by the International Argo Program and the national programs that contribute to it (http://www.argo.ucsd.edu, http://argo.jcommops.org). The Argo Program is part of the Global Ocean Observing System.

3.2.5 EOF Analysis

The spatio-temporal variability of modeled and satellite SST was analyzed by means of Empirical Orthogonal Functions (EOF). The EOF analysis consists in a representation of the data in terms of a reduced set of orthogonal functions or modes, whose outputs are spatial fields and their associated eigenvalues (relative amount of variance) and eigenvectors (temporal weightings for each time step), allowing to study the temporal and spatial

variability of data. The EOF eigenvectors and eigenvalues are obtained via singular value decomposition (SVD) (Preisendorfer, 1988). The contribution of one EOF at any time in a particular point is obtained by multiplying the value at that location times the value of the temporal coefficient at a given instant.

That is, a variable is considered to be a function f of space and time, computed for constant space and time intervals. The EOF method represents the data as a sum of products of functions:

$$f(x, y, z) = \sum F_i(x, y)\ G_i(t) \tag{3.3}$$

where the F_i express the data distribution in space and the G_i give the contribution of the respective space distribution to f at any given time.

This methodology can be applied to vectors (e.g. Torres et al., 2003); hence, modeled and radar surface currents are also compared through EOF analysis.

3.2.6 Root Mean Square Error (RMSE)

Another statistical tool used in this study for the Argo floats data is the root mean square error (RMSE) (Wilks, 2006), which is a computation of the differences between model and observations. RMSE is given by:

$$RMSE = \sqrt{\frac{1}{n}\sum (M_n - D_n)^2} \tag{3.4}$$

where M_n is the model data, D_n the Argo floats data and n the size of both data series and the number of times the comparison is carried out.

3.3 Results Overview

The first part of the results (section 3.4) consists in an analysis of a long upwelling index dataset (1967-2011), already used in the literature (e.g. Alvarez et al., 2008). The purpose of this analysis is to set a background of variability for the model essay in the second part (section 3.5), which is more limited in time (2001-2011). The longer dataset provides a broader look on the interannual variability, namely of upwelling conditions, whereas the model shorter period is intended for trying to identify more specific episodes of variability, which is enabled by the numerical tools.

3.4 Upwelling Index Analysis

The UI mean seasonal and interannual distribution for each location is shown in Figure 3.2. It is evident that the strongest upwelling signal takes place between April and September, i.e. corresponding to the late spring/summer months, as expected from the well-known behavior of mid-latitude upwelling systems, and in particularly the Iberian

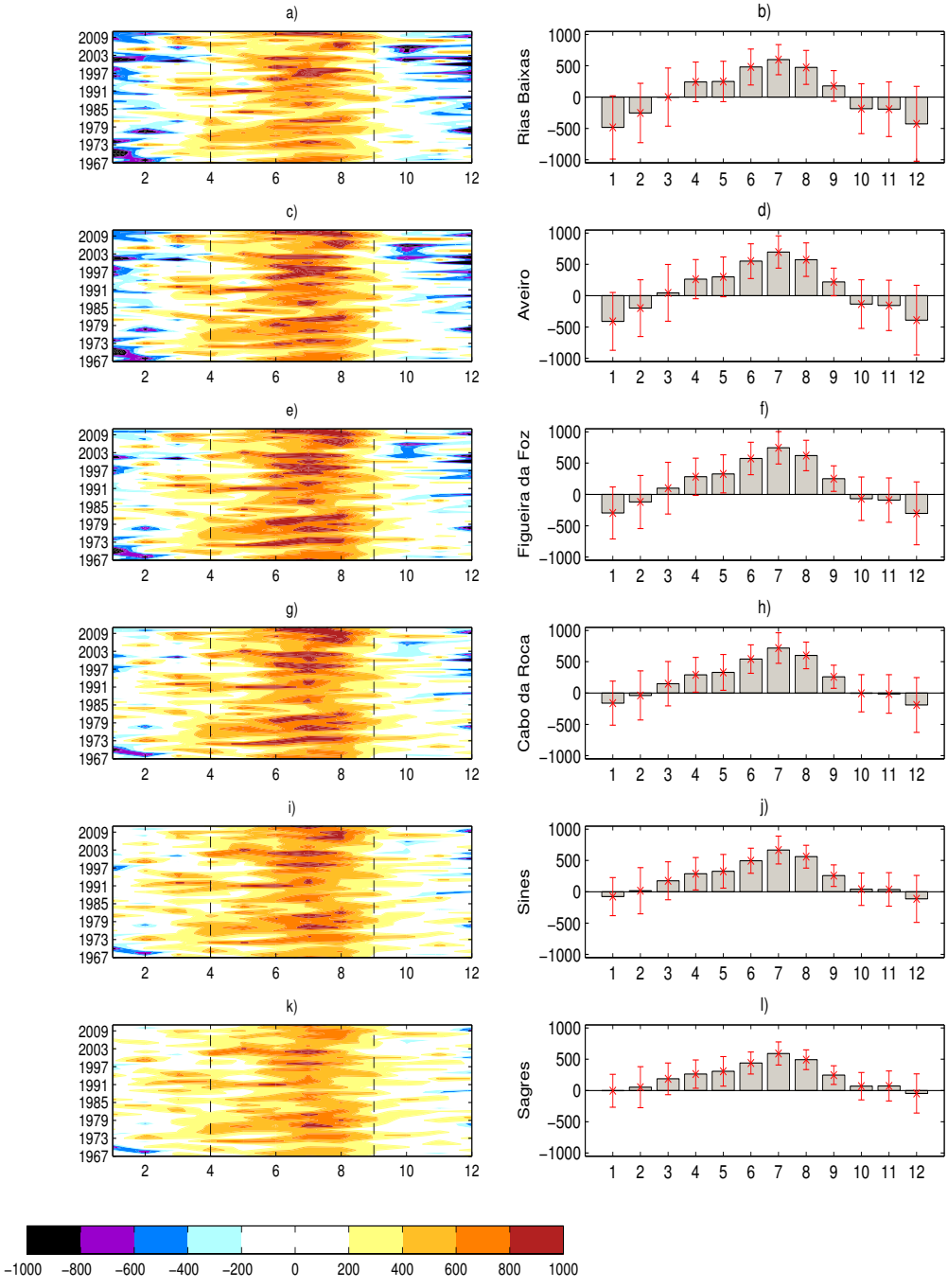

Figure 3.2: Hovmöller diagrams of the monthly UI ($m^3 s^{-1} km^{-1}$) (left column) and monthly distribution of UI intensity with associated errors (right column) for Rias Baixas (a,b); Aveiro (c,d); Figueira da Foz (e,f); Cabo da Roca (g,h); Sines (i,j); and Sagres (k,l).

Upwelling System (Wooster et al., 1976; Fiúza, 1983). Also noteworthy is the similarity between locations of the UI patterns given by the Hovmöller diagrams (left column), although they vary in magnitude. In general, years with early upwelling onset are followed by years with late upwelling onset, seen by the left-to-right slope of the contours in the diagrams. There are some years that register favorable upwelling conditions during winter (February-March), and these are usually the years where the upwelling season lingers on until October (1973, 1983, 1992, 2000, among others). For instances, 2007 was a year with a particularly long upwelling season, which lasted from mid-February to mid-November; however, UI rarely surpassed the magnitudes that characterize strong upwelling events ($>600\ m^3 s^{-1} km^{-1}$). This happens in general for the years of long upwelling seasons, such as the ones mentioned before. Curiously, strong El Niño Southern Oscillation (ENSO) positive events have been registered in the preceding years (1972, 1982 and 1991, according to the Climate Prediction Center of NOAA). ENSO has been known to influence the NW African upwelling region, where warm ENSO events lead to weaker northerly winds and therefore weaker upwelling (Roy and Reason, 2001).

As for years of strong downwelling conditions in winter, one can note the periods 1967-72 and 1977-78, year 1997, and the period 2001-2005. Pérez et al. (2010) also registered low annual mean UI values for these periods in the Rias Baixas location, especially the latter, which corresponds to a negative summer NAO.

This analysis is reinforced by the seasonal average intensity per region and associated error bars (which were computed taking into account monthly UI values) displayed on Figure 3.2, right column. Once again, this seasonal cycle is in agreement with previous studies on the characterization of upwelling seasonality for the western Iberian region (e.g. Wooster et al., 1976; Gómez-Gesteira et al., 2008). In general, UI is positive from March to September, being strongest in July, and negative from November to February, being strongest in January. Standard deviations are larger during winter months, decreasing in summer months, which implies that while in summer (JJA) conditions are always favorable for upwelling, in winter (as well as some of the transient months) some years are upwelling-favorable and others downwelling-favorable, although the latter prevail. Rias Baixas (Figure 3.2 b) presents the lowest positive UI in summer and the highest downwelling conditions in winter. This can be accounted for by the special characteristics of northwestern Iberian Peninsula (Torres et al., 2003), where the wind is more variable than on more southern locations, and the jagged estuaries and closed embayments make the coastline less linear. As we move southward, upwelling-favorable conditions intensify and downwelling-favorable weaken. However, it should be noted that the associated errors vary on the opposite direction, i.e. they tend to decrease when we move southward. In the southernmost location downwelling conditions in winter are almost non-existing and positive UI during summer decreases, with values more similar to the northern locations. From this figure we draw that the preferential period for favorable upwelling conditions is April to September (AMJJAS), as previously described in the literature (e.g. Fiúza, 1983). Therefore, from this point on, results will be analyzed for these months only.

The interannual evolution of the mean summer (April to September) UI since 1967 as a function of latitude is shown on Figure 3.3. Note that, despite the strong variability present,

the color scale is always positive, that is, it is always upwelling-favorable conditions. From this diagram it is evident that UI has strong interannual variability. The UI signal is highly consistent for each year within the latitudinal range. That is, whether UI is high or low, the same is observed at all latitudes. Maximum values are in general observed between 39^oN and 40^oN. At these latitudes the coastline is less meridional than along the rest of the Western Iberian Margin due to the presence of the Estremadura Promontory. This topographic feature may have some influence on the wind direction, usually alongshore. That is why there is recurrent upwelling-associated filament generation, caused by the equatorward advection of the cold and fresh upwelled waters that are sometimes enhanced by the promontory (Haynes et al., 1993; Oliveira et al., 2009). Hence, the UI is recurrently higher in this area.

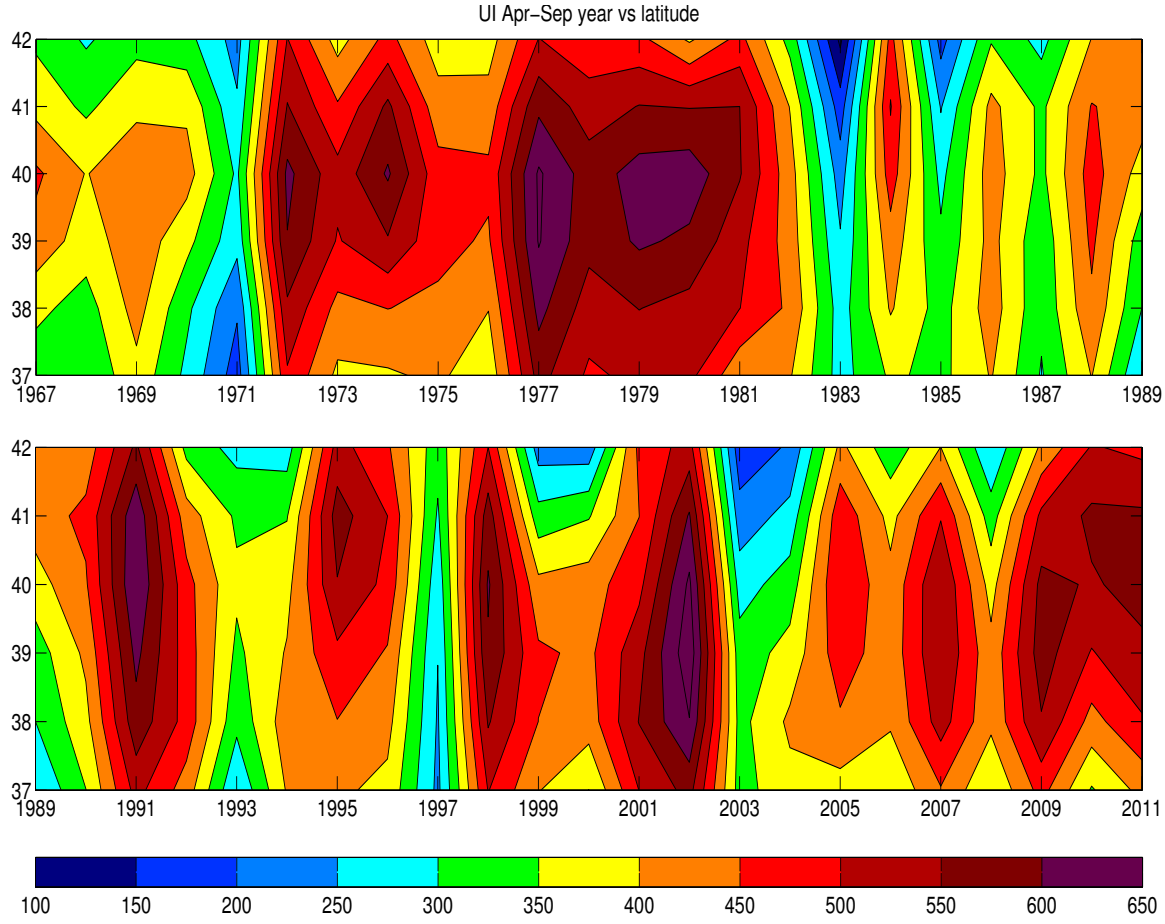

Figure 3.3: Hovmöller diagram of summer UI ($m^3 s^{-1} km^{-1}$) (April-September) as a function of latitude.

There are five years where upwelling occurrence is particularly strong: 1977, 1979, 1991, 1998 and 2002. The 1991 maximum may be related to the early 1990s winter NAO maximum (Santos et al., 2005), which these authors found to be a turning point toward

a period of stronger upwelling occurrence, although such strengthening is not evident in our results. Peliz et al. (2002) report that in August 1998 western Iberian Peninsula was under constant northerly winds for practically the entire month, likely accounting for the strong signal of that year. On the other hand, there are also five years where upwelling episodes are visibly weak, namely: 1971, 1983, 1985, 1997 and 2003. Nykjaer and Van Camp (1994) reported a weak upwelling period in the Canary Upwelling System in 1983-84 due to an exceptional strong El Niño Southern Oscillation (ENSO) in the Pacific Ocean in the previous year. Furthermore, some of these years show rather an increase of UI with increasing latitude instead of maxima at 39-40^{o}N (e.g. 1983, 1985, 1999, and 2003).

3.5 Model Results

The following analysis concerns ROMS output from simulations carried out for period 2001-2011. Before presenting the model results, daily series of the meridional wind at two latitudes are described. Then, model validation and model output analysis is carried out in parallel or simultaneously. First, Argo floats provide comparison through θ-S diagrams. Then, EOF analysis is applied to surface currents and SST. The observational surface currents series comprise one year and a half of data, so this dataset serves only as model validation. Observational SST, on the other hand, obtained from satellite products, is of the same length as that of the model simulations; hence, not only they provide a comparison for the entire study period, but also the SST data is long enough to be valid for analysis. Temperature anomaly episodes are identified.

Afterwards, model results are explored through salinity and meridional velocity Hovmöller diagrams, as a function of longitude and of depth, and through meridional transport series directly compared with wind stress. The meridional transport approach was preferred to EOF analysis of the surface currents, although it has been performed (not shown), so that the first hundreds of meters of the water column could be included. These representations are intended to identify more specifically strong poleward or equatorward events.

3.5.1 Meridional Wind Stress

Figure 3.4 shows daily meridional wind stress for the 11 years under scope, extracted at two latitudes: 43^{o}N and 37.5^{o}N, centered at 9.7^{o}W (for monthly means see Figure 3.13). Wind stress off WIM is quite weak when comparing to other eastern boundary systems such as California, which comprises also an important and strong current system (Di Lorenzo et al., 2005). For the period 2001-2011 there is no clear tendency of increase or decrease of meridional wind stress, nor are there dramatic changes in signal or intensity, although the time series are punctuated by evident interannual variability. From April to September (and in most years also October), equatorward winds prevail, typical of the upwelling season and in agreement with the analysis of section 3.3.

The northern latitude registers more markedly poleward wind events, while in the southern latitude prevails an equatorward signal. In years 2001 and 2002 there are recurrent

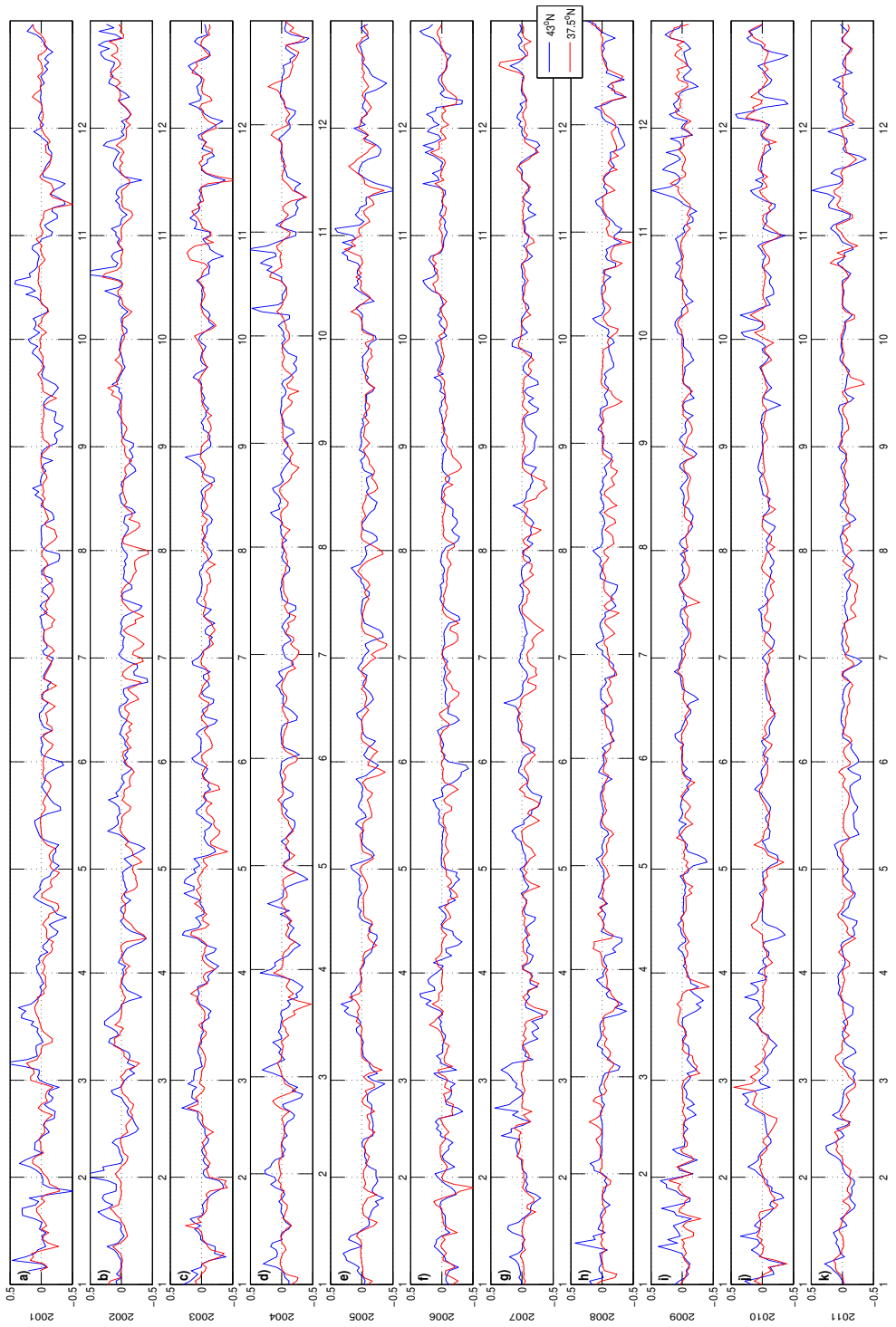

Figure 3.4: Daily meridional wind stress ($N\ m^{-2}$) monthly time series for years 2001 (upper panel) to 2011 (lower panel) at 43^{o}N, 9.7^{o}W and 37.5^{o}N, 9.7^{o}W (see Figure 3.1).

poleward episodes in January-March, as well as in 2004 and 2007. For the remaining years, January seems the month with the most evident northward signal (e.g. 2009, 2010). In autumn (October-December) this tendency is also frequent (e.g. 2002, 2006, 2009, 2010).

3.5.2 θ-S Distribution

In order to assess the model ability to reproduce hydrography, θ-S diagrams (Figure 3.5) were plotted for the data of all available Argo floats profiles during the study period, divided in three regions (Figure 3.5 a). The values of the ENACW, both subpolar and subtropical branches (gray line and black line in the diagrams, respectively) are reasonably well reproduced by ROMS, especially their salinity minimum of about 35.6. Likewise, the deeper, colder waters ($<7^oC$, <35.7) coincide very well with the Argo data. Surface waters, on the other hand, present some discrepancy in terms of salinity, with ROMS minus Argo differences from -0.1 in the northern region to -0.3 in the southern region. Note that the southern region is where there are the fewest Argo floats profile data and the northern region where there is the most. Model and observations also differ at the MW levels in about -0.1 to -0.2. Both these differences are also observed in the RMSE of ROMS in comparison to Argo (Figure 3.5 c), in the upper 100 m and between 1000 and 1400 m depth. Salinity RMSE reaches 0.2 and 0.25 at these depths, respectively, while throughout the water column values remain close to 0.1 or lower, and temperature RMSE reaches 1.15 and 1.3, also respectively at those depths, while at the remaining levels values vary between 0.3 and 0.8. The discrepancy at the MW levels may arise from a displacement of the maximum temperature and salinity associated with MW. This is consistent with the climatological observations of chapter 2. While observations place the MW main core at 1200 m, ROMS places it at about 1000 m.

3.5.3 Surface Currents

EOF analysis was applied to model and observational surface currents for period July 2010 to December 2011 (the period of HF-radar data availability); hence, the following analysis concerns ROMS validation only. Figures 3.6 and 3.7 show the first and the second modes of vector EOF of daily values of surface velocity, respectively, for ROMS and for HF-radar data.

The first mode of the real vector EOF represents basically the current meridional component. For this domain and time frame, the first mode represents roughly 36% of the ROMS variability, while it is 56% of the radar variability. Both spatial modes present south-southwestward vectors (with intensity increasing onshore in ROMS), which means that, for instances, in the case of northerly winds, surface currents are southward with a westward deflection ($\sim 45^o$) due to the wind-induced Ekman dynamics. Conversely, in the case of southerly wind, the deflection is eastward. The temporal mode for both datasets agrees well, except for some overestimation of ROMS.

The second EOF mode (Figure 3.7) represents the zonal current component. For ROMS, 16% of the variability is explained by this mode, whereas for radar the value

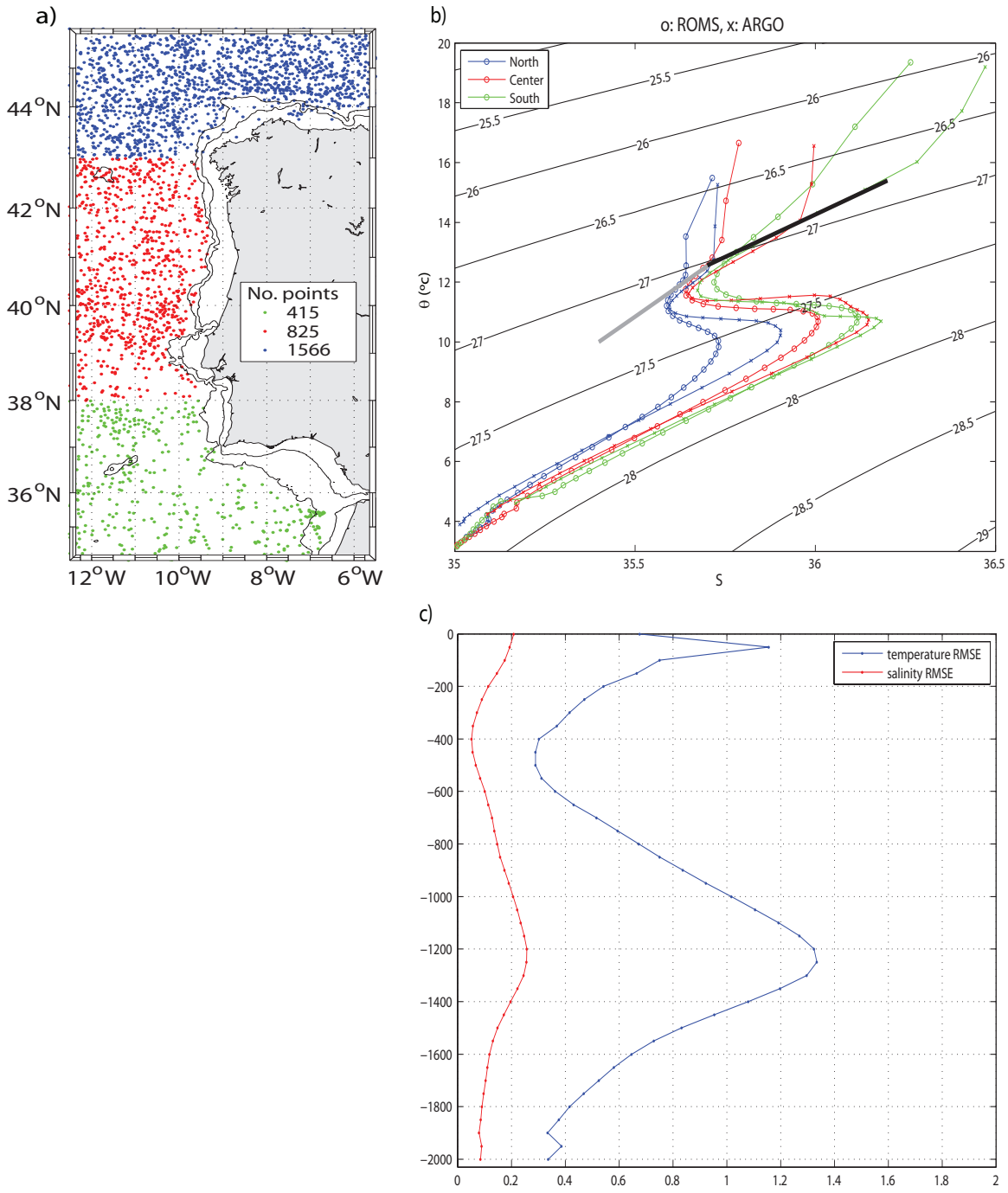

Figure 3.5: (a) Argo float distribution (number of measurements per region indicated). Isobaths 200 m and 1000 m are shown. (b) θ-S diagrams from Argo floats data (crosses) and ROMS output (circles) for the three regions color-coded in (a). (c) Temperature (blue) and salinity (red) RMSE vertical profiles of ROMS output with respect to Argo floats data (depth in m).

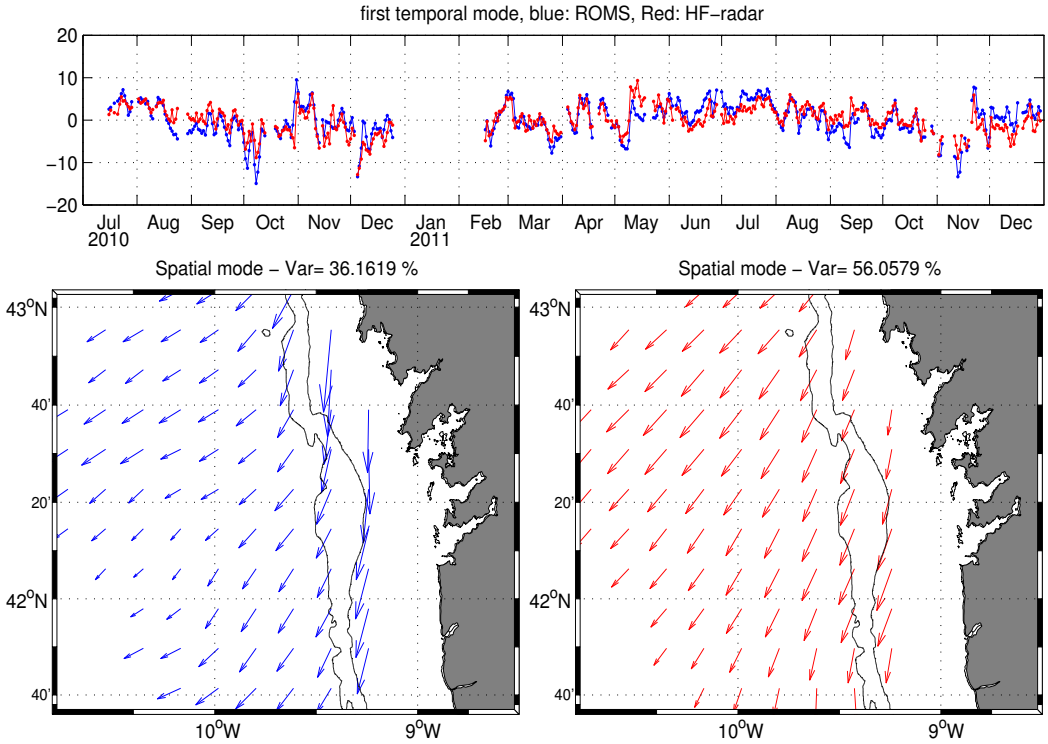

Figure 3.6: Real-vector EOF first temporal (upper graphic) and spatial (lower map) modes for the daily sea surface currents in July 2010 to December 2011. Blue graphics are ROMS outputs and red are HF-radar observations. Isobaths 200 m and 1000 m are shown.

---

is of 18%. The general tendency is for eastward flow, deflected southeastward, reflecting Ekman drift for a zonal wind. There is still reasonably good agreement between the two datasets.

Combining the two modes, we obtain the two components of the Ekman transport, and can thus analyze the preferential direction of the surface flow. When the temporal modes of both EOFs are positive, the spatial modes result in southward vectors, which occur mostly in spring and summer and correspond to the upwelling equatorward jet (June-August 2011). In the second EOF temporal mode, there is another striking positive episode in late October-early November 2010, to which corresponds a weaker and not always positive signal in the first EOF temporal mode; therefore, the direction of the flow oscillated between equatorward or offshore. In September-October and December 2010, both temporal modes are negative, hence indicating poleward flow, also occurring less evidently in March and November 2011. In December 2011 (and early May, although less prominent), the second temporal mode indicates a strong positive event, which counterbalanced by a weak signal in the first temporal mode results in onshore surface flow.

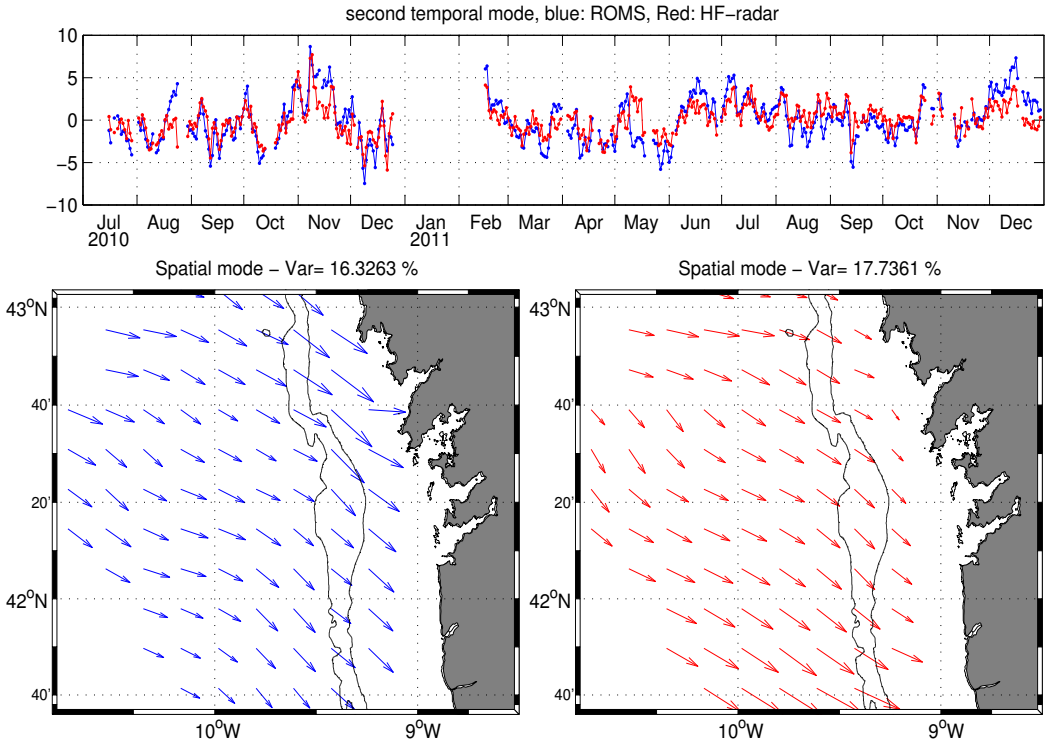

Figure 3.7: Real-vector EOF second temporal (upper graphic) and spatial (lower map) modes for the daily sea surface currents in July 2010 to December 2011. Blue graphics are ROMS outputs and red are HF-radar observations. Isobaths 200 m and 1000 m are shown.

3.5.4 SST

Applying EOF to SST time series, model and satellite, allows not only to evaluate ROMS performance in reproducing SST variability for the study period, but also to give a general portrait of that variability.

EOF were computed for monthly anomalies. The seasonal cycle was removed, otherwise the first mode of variability would be nothing more than SST seasonality. The first mode (Figure 3.8) explains 57% of the variability for the model and approximately 66% for the satellite (without removing the seasonal cycle, this mode would explain $> 90\%$ of the variability — not shown). There is a fairly good agreement between model and observations in the temporal mode, although ROMS tends to overestimate some of the variability peaks, such as in mid-2003, two episodes in 2006 and one at the end of 2008. On the other hand, it achieves a good agreement for the episodes of 2002, 2007 and 2011. The spatial distribution of the first mode shows an offshore gradient, and it is clear that the strongest variability occurs along the coast within the 200-m isobath, the typical band of coastal upwelling.

A strong positive signal on the spatial mode multiplied by negative temporal anomalies in summer can mean intense upwelling events. Regarding positive temporal anoma-

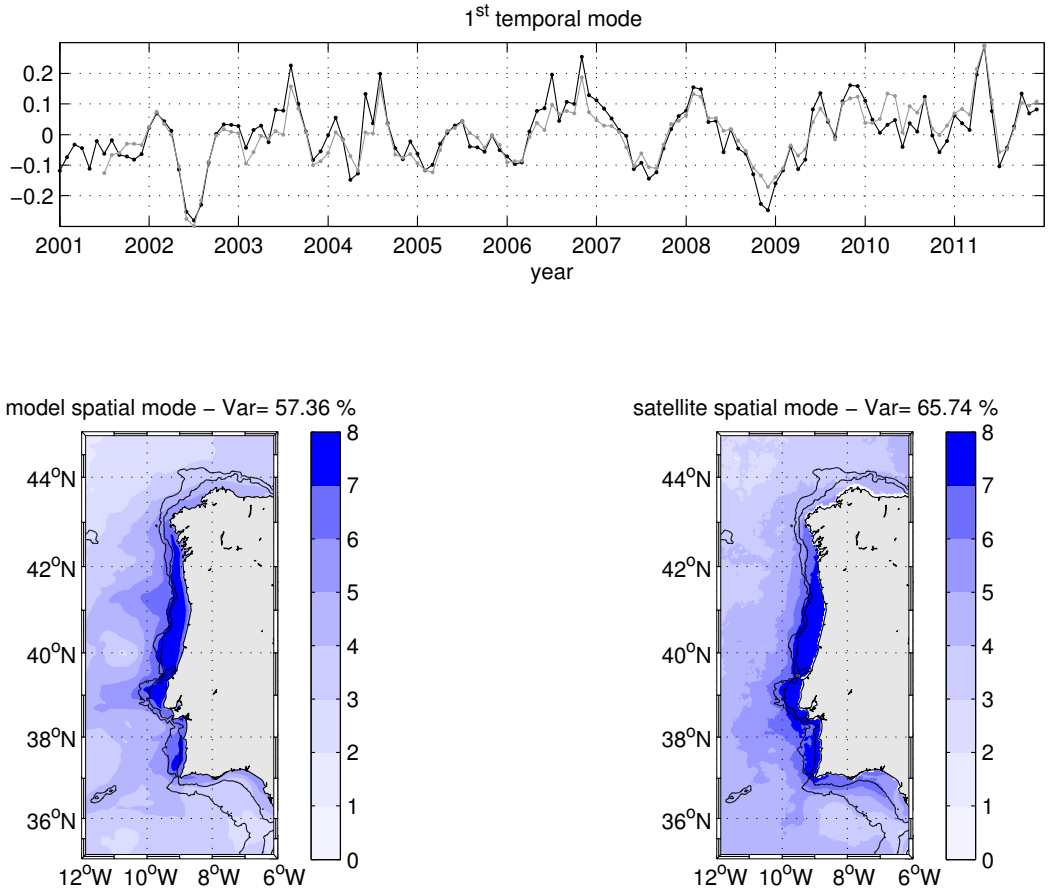

Figure 3.8: EOF first temporal (upper graphic) and spatial (lower maps) modes for the SST monthly anomalies for period 2001-2011. The black line is ROMS temporal mode and the gray line is the satellite temporal mode. Isobaths 200 m and 1000 m are shown.

---

lies, for instances the episode of April 2011, they are usually associated with particularly warm months or, for the summer months, weak upwelling. ROMS spatial mode shows some prominent signals that extend offshore along 39^{o}N, the location of the Estremadura Promontory, and 41^{o}N, off Aveiro. In the satellite spatial mode, there is a more generalized offshore variability south of 40^{o}N, although there is evidence of protuberances located at the latitudes not only of the Estremadura Promontory but also of Cape Finisterre and Cape St Vincent. These signatures may be related to the generation of upwelling-associated filaments.

From the first mode time series, a few strong upwelling signals stand out, e.g. summer 2002, summer 2007 and autumn 2008. Positive anomalies are more frequent and occur in all seasons, sometimes in the same year. In summer (mid-year), there are relevant peaks in 2003, 2004, 2006 and 2009, which correspond to years of less upwelling-favorable winds (Figure 3.4). There are also warm anomalies occurring in other seasons, e.g. early 2002 and 2008, and late 2006.

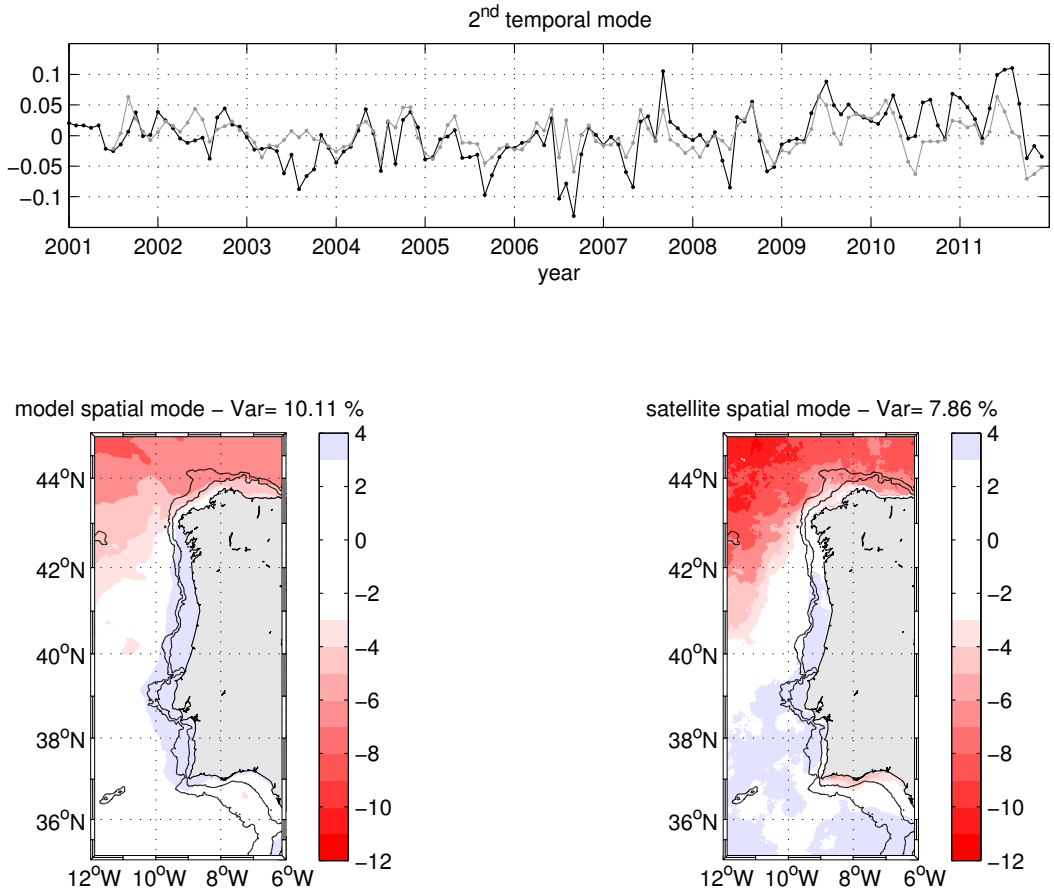

Figure 3.9: EOF second temporal (upper graphic) and spatial (lower maps) modes for the SST monthly anomalies for period 2001-2011. The black line is ROMS temporal mode and the gray line is the satellite temporal mode. Isobaths 200 m and 1000 m are shown.

The EOF second mode (Figure 3.9) presents the strongest variability in the north-western corner of the domain, seen by the negative anomalies in the spatial distribution of both model and satellite. Conversely, anomalies are positive alongshore WIM within roughly the 1000-m isobath. Explained variability is of 10% for ROMS and about 8% for the satellite. The temporal mode shows again some overestimation of variability peaks, for instances the episodes in 2005-2007 and 2011. Negative values of the time series during summer (2003, 2005, 2006-2008) are associated with negative temperature anomalies along the upwelling band, whereas prevailing positive values for e.g. 2009-2011 relate to negative SST anomalies in the northern region.

In the third variability mode (Figure 3.10), explained variability is of 7% for ROMS and 5.5% for the satellite. There is a kind of N-S symmetry in the spatial modes; both ROMS and satellite show negative anomalies along the coast north of 40^{o}N (weaker and extended offshore for the latter) and positive anomalies at the southern coast (stronger in the satellite). For the temporal mode, there is again some overestimation of peaks

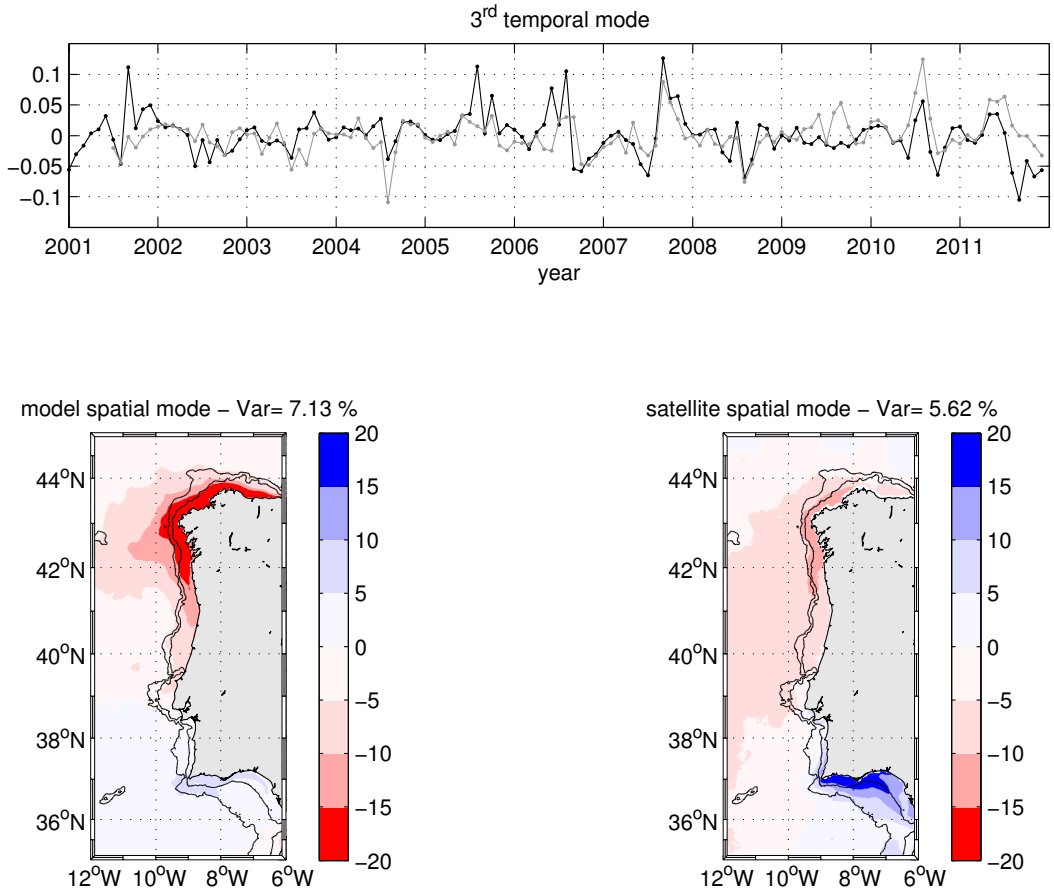

Figure 3.10: EOF third temporal (upper graphic) and spatial (lower maps) modes for the SST monthly anomalies for period 2001-2011. The black line is ROMS temporal mode and the gray line is the satellite temporal mode. Isobaths 200 m and 1000 m are shown.

---

by ROMS (2005-2007); however, there are also instances where the reverse is observed: underestimation of peaks by ROMS (2004, 2010, 2011). In general, the time series seem to agree better than the 2nd mode. Strong positive anomalies can be found in the temporal mode for 2005-2007, 2010 and 2011 (summer and summer/autumn), which brings about negative anomalies along NW Iberian Peninsula and positive anomalies south of Portugal. Summer negative anomalies around the Galician coast may be associated with filament generation, which, as stated before, occurs recurrently in this region due to its bathymetric characteristics (Torres et al., 2003).

3.5.5 Salinity and Meridional Velocity Analysis

From here on the analysis is carried out for ROMS output only. The previous EOF analysis is in itself a good method for identifying particular events of SST anomalies. In addition, we computed Hovmöller diagrams as a function of longitude and of depth (Figures

3.11 and 3.12, respectively), for salinity and meridional velocity, for the entire study period. Note that the salinity color scales are different between latitudes: the southern location is displaced by +0.25 relative to the northern one.

At 43^{o}N (Figure 3.11 a), three strong fresh events are observed near-shore and offshore in early 2001 and 2003, and in late 2006-early 2007, to which correspond poleward velocities nearshore (Figure 3.11 b) and fresh signals at 37.5^{o}N (Figure 3.11 c). These events are related to strong river discharge (not shown), advected offshore through Ekman transport. Fresh water signals nearshore in the beginning of 2004, 2006, 2009, 2010 and 2011 are most likely associated with winter river discharges from the Galician Rias, whose fresh waters usually remain contained within the estuaries. On the other hand, strong episodes of high salinity are observed in the second halves of 2009-2011, with corresponding poleward velocities (especially 2009), which denotes saline water advection from the south. Note that these years presented marked SST positive anomalies (Figure 3.8), which may indicate poleward flow events. Nearshore, equatorward flow prevails in summer at both latitudes, and at 43^{o}N there are punctual strong poleward events, usually associated with moderate high salinity episodes: early and late 2001 (note the very high salinities at 37^{o}N at that period); mid 2002; mid 2006 (with high salinities more offshore); and early 2008. Some of these episodes have also correspondence to SST warm anomalies (Figure 3.8).

At 37.5^{o}N (Figure 3.11 c,d), low salinity values have correspondence with evidence of intense equatorward flow, especially for the summers of 2001 to 2004, and 2007 to 2009. Note that the latter period was characterized by strong UI (Figure 3.3). High salinities and poleward velocities occur more frequently along 11^{o}W, mostly in summer, while in winter both episodes are often registered between 9.5^o and 10^{o}W. This may constitute evidence of offshore displacement of the poleward advection of saline waters during the upwelling season, that in winter occurs closer to the coast. This is apparent, for instances, from 2007 and 2008, for both variables.

In the vertical profiles (Figure 3.12), it is easier to identify particular saline/fresh and poleward/equatorward events. At 43^{o}N (Figure 3.12 a,b), the saline events of 2009-2011 are again striking, also with a poleward velocity signature down to 500 m, as well as the fresh events of early 2001 and 2003, and late 2006-early 2007. There is an episode of subsurface high salinity and poleward velocity, not evident in Figure 3.11: late 2001-early 2002, which corresponds to a very strong salinity signal at 37.5^{o}N, consistent with S-N saline water advection. Equatorward strong signals, reaching down to 400-500 m, can be found in early and mid-2005, the second half of 2008 and mid-2011.

At 37.5^{o}N (Figure 3.12 c,d), salinities above 36 occur at least once a year, mostly centered in winter, consistent with the observations in Figure 3.11 between 9.5^o and 10^{o}W. The years with strongest poleward events were 2002-2003 (autumn-winter), early 2004, early and late 2005, and late 2008. Correspondence with the meridional wind stress distribution is less evident; moreover, the circulation here is more influenced by the Mediterranean flow at deeper levels (below 500 m). On the other hand, equatorward velocities higher than 0.1 $m\ s^{-1}$ are registered in the first halves of 2006, 2009 and 2011, with weaker vertical signatures. At this latitude, this measurement point (centered at 9.7^{o}W) is farther from the coast than at 43^{o}N, hence these episodes may not correspond to strong upwelling

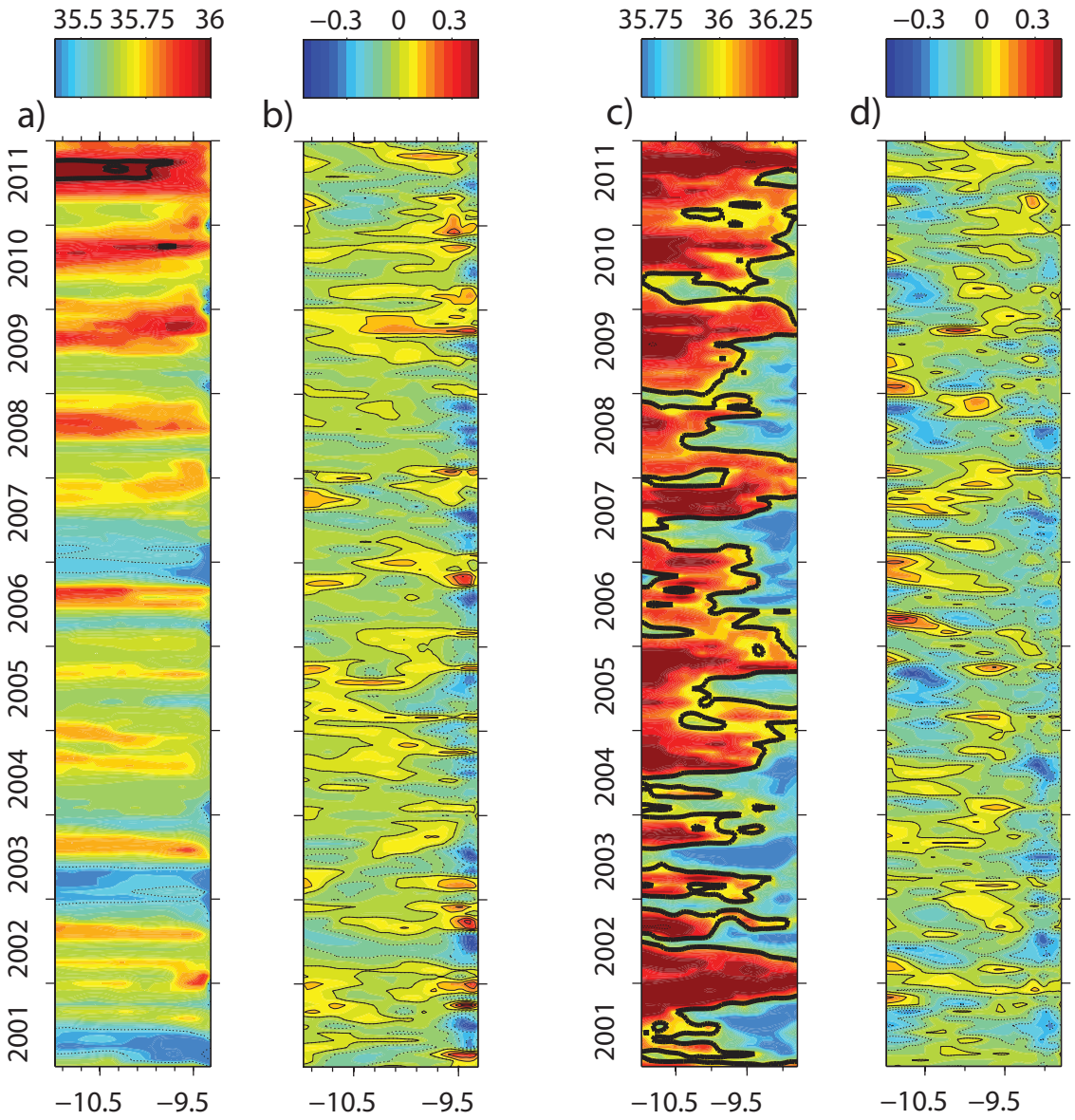

Figure 3.11: Hovmöller diagrams of surface (a,c) salinity; (b,d) and meridional velocity v ($m\ s^{-1}$) as a function of longitude for latitudes 43^{o}N (left columns) and 37.5^{o}N (right columns). Thick line in S corresponds to the 36 isohaline and dashed line to 35.5. Solid (dashed) line in v corresponds to positive (negative) velocities every 0.05 $m\ s^{-1}$.

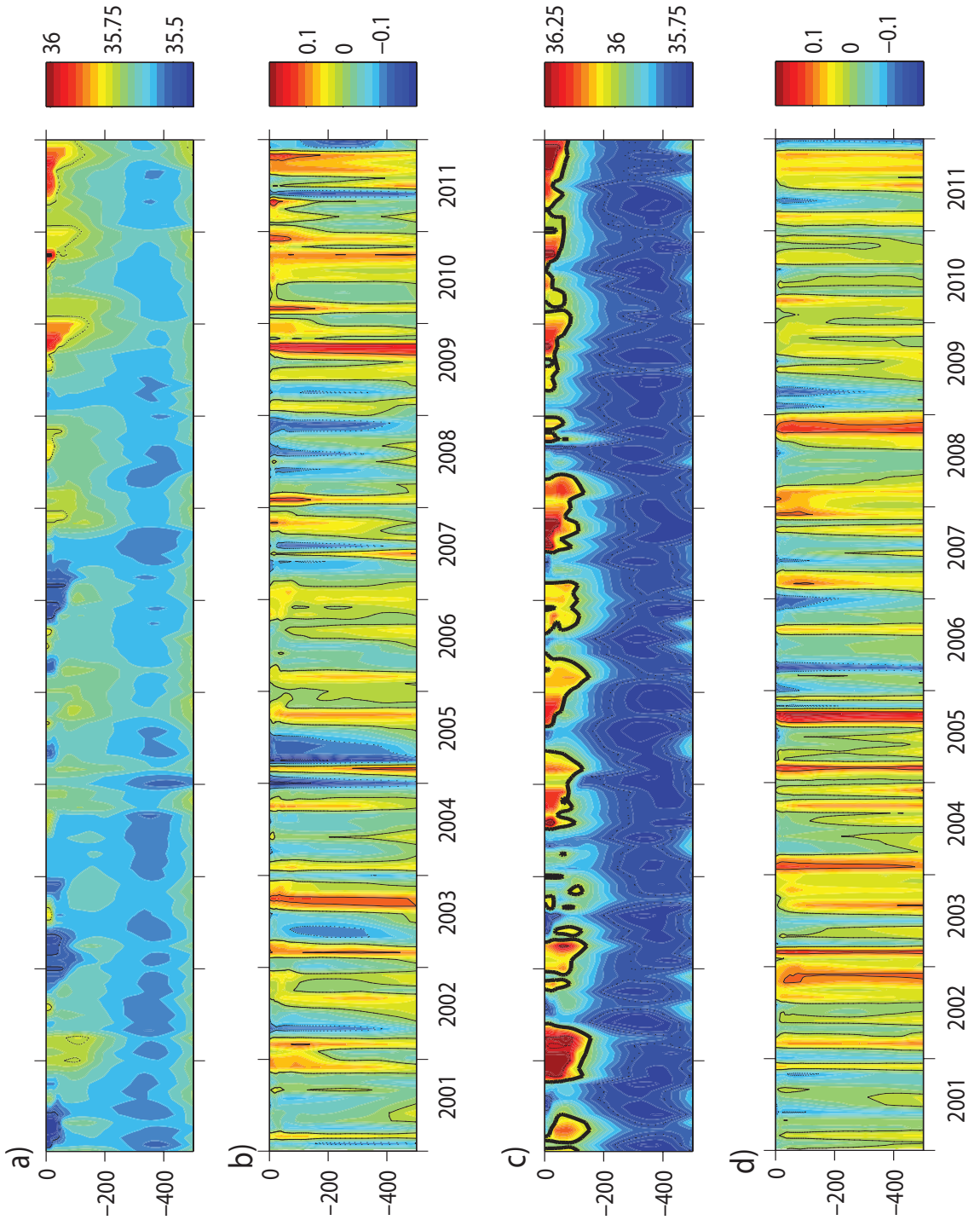

Figure 3.12: Hovmöller diagrams of (a,c) salinity and (b,d) meridional velocity v ($m\ s^{-1}$) as a function of depth at 9.7^{o}W for latitudes 43^{o}N (left columns) and 37.5^{o}N (right columns). Thick line in S corresponds to the 36 isohaline and dashed lines to 35.75 and 36.25. Solid (dashed) line in v corresponds to positive (negative) velocities every 0.05 $m\ s^{-1}$.

events; they could rather be associated with vortex structures as seen in chapter 2. Note the salinity minima between 300 and 400 m at both latitudes, the signature of ENACW. Also noteworthy is the barotropic character of the flow, which has also been observed in chapter 2.

3.5.6 Meridional Transport

Figure 3.13 presents the wind stress meridional component time series for two points off WIM and the meridional transport integrated from the coast to the upper slope down to 400 m. In the northern section (Figure 3.13 a), 2001 and 2002 were years with relatively strong southerly wind episodes in autumn-winter, partially in agreement with the Hovmöller diagrams. The strong saline episodes observed in Figures 3.11 and 3.12 in 2009-2011 have transport correspondence, since for those years it is mostly poleward, but not in the meridional wind stress, which indicates these poleward flows are not wind-driven. Other years that have episodes with poleward wind stress $> 0.05\ N\ m^{-2}$ are March 2003, October 2006, and February 2008, all of which were observed in Figure 3.11 and/or Figure 3.12 in the velocity profiles. In the remaining years, there is in general equatorward transport in summer, coincident with average northerly winds. For the three intense fresh water events (2001, 2003, and 2006-2007), they have correspondence with prevailing poleward winds for those periods.

At 37.5^oN (Figure 3.13 b), both the meridional wind stress and transport time series are preferentially equatorward. Among the few exceptions are years 2009-2011, the saline and poleward events of the Hovmöller diagrams. Strongest equatorward winds ($> 0.1\ N\ m^{-2}$) occur in 2001-2003, 2007, 2008 and 2011, partly consistent with the high UI of Figure 3.3 and the coastal equatorward velocities (and low salinities) seen in Figure 3.11.

3.6 Discussion

a. Upwelling Index

An initial brief study of the intra- and interannual variability of Upwelling Index off western Iberian Peninsula was performed taking into account six locations (Rias Baixas, Aveiro, Figueira da Foz, Cabo da Roca, Sines and Sagres — Figure 3.1). The data is characterized by a strong seasonal cycle and a superimposed strong interannual variability, in agreement with previous works that have thoroughly described the Iberian Upwelling System (e.g. Relvas et al., 2007). UI is quite homogeneous along the western coast of the Iberian Peninsula; strong and weak upwelling signals in different years are observed at all latitudes, although with different intensities.

These results indicate that large-scale meteorological conditions can explain the largest fraction of the variability of upwelling processes in the western coast of Iberia. However, it is evident that mesoscale processes also play a significant role in this variability. It is suggested that mesoscale processes are rather important in mid-summer, seen by the significant UI differences from year to year. Hoinka and Castro (2003) observed that July

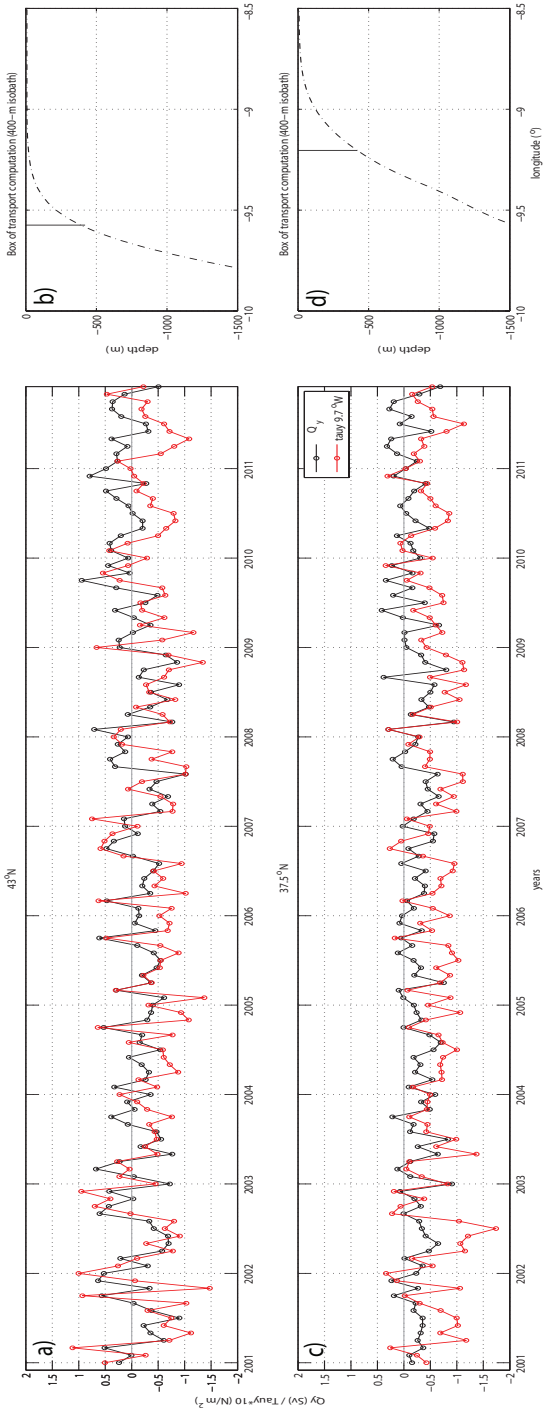

Figure 3.13: Meridional volume transport in Sv (black) across (a,b) 43^oN and (c,d) 37.5^oN (delimited by the 400-m isobath — right column) and the corresponding meridional wind stress in $N\ m^{-2}$ at 9.7^oW (red) (note the $10\times$ scale).

is usually the month with the highest frequency of thermal low patterns. The question of the role of mesoscale on upwelling systems has been addressed by previous authors such as Di Lorenzo et al. (2005) for the California Current System and by Relvas et al. (2009) for western Iberian Peninsula. The former found, for period 1949-2000, a warming trend attributed to surface heating and a strengthening of upwelling-favorable winds, which in turn increase current velocities and associated variance. This extra eddy activity, the authors postulate, may have implications in the decadal variability of the system. The latter, considering the different SST trends in the northern and southern coasts of Western Iberian Peninsula since 1985, attribute the differences to mesoscale activity associated with upwelling. This difference is higher for the core summer months (JJA).

Taking into consideration studies in the above-cited literature of interannual variability and upwelling trends, the data presented here does not show any clear increase or decrease of UI from 1967 to 2011. Figure 3.3 indicates that the 70's (80's) were a decade of generally strong (weak) upwelling events, and that from 1990 on the intensity of UI alternates roughly every two years. Bakun (1990) observed similar behavior off Iberian Peninsula at 43^oN, with general high UI in the 70's and oscillating UI in the 80's. Even Narayan et al. (2010), who have found both strengthening and weakening UI tendencies by analyzing several yearly-averaged UI time series, observed, for a similar period for a region off NW Africa, more accentuated UI variability after 1990.

b. Model Results

ROMS showed a good performance in reproducing both the hydrography and the surface dynamics, according to the validation analysis that comprised radar surface currents, satellite SST and Argo floats temperature and salinity profiles. There are T and S biases in depth similar to those observed in chapter 2, which arise from the differences in the depths where the properties of the Mediterranean Water are found rather than from the inability of ROMS to reproduce them. The interannual variability of SST reflected in the EOF analysis was well captured, particularly the warm and cold anomaly events given by the first mode.

From these short time series of either SST, salinity or meridional wind stress there is no evidence of trends. Longer series are necessary to assess the time scales of that variability. Ruiz-Villarreal et al. (2008) analyzed SST long time series (1900-2006) for the Galician coast and found an increase of roughly $0.1^oC\ decade^{-1}$; for a shorter period (1967-2006), the authors report decrease in upwelling-favorable winds in summer. They also trace a correlation between the variations of the upper layers temperature and salinity and decadal variability, namely the North Atlantic Oscillation (NAO). In this study, preliminary tests concerning the NAO did not show any evidence of correlation between that index and either SST or meridional wind stress times series (including with month lagging).

From the combined analysis of salinity and meridional velocity zonal and vertical profiles, together with coastal meridional transport and the meridional wind stress, it was possible to identify several episodes of saline water northward advection. Years 2009 to 2011 showed SST warm anomalies, and strong salinity and meridional flow signals, as well

as some tendency for northward transport, which may indicate that there were episodes of poleward flow. These events also suggest that salinity has been increasing for the last ten years, although the time series is not long enough, nor is it possible to validate. Nevertheless, Reboreda et al. (in revision) compared ROMS salinity profiles for period May 2001-April 2002 with data retrieved at two points along 42^oN between 9^o and 9.5^oW, and found good agreement between results, particularly the salinity event in the beginning of 2002 that is reported here. Moreover, Amorim et al. (2012) reported high salinities for summer 2010 and 2011 from measurements carried out off Aveiro, at about 41^oN.

Other high salinity and poleward flow events have correspondence in the literature: Otero et al. (2008) registered strong poleward currents measured by a buoy at approximately (42^oN, 9.4^oW) in November and December 2002; Gago et al. (2011) registered an episode of temperatures above 18^oC at the surface on the second half of 2002, and generalized high salinities throughout 2006 in the upper 100 m. Furthermore, Le Cann and Serpette (2009) observed evidences of strong poleward flow in late 2006 and early 2007 in the northern coast of the Iberian Peninsula, with surface temperatures of 17^oC, which is consistent with the EOF SST anomalies, although not with the salinity and meridional flow profiles.

In the previous chapter it became evident that the poleward flow is likely a permanent feature of the WIM circulation system, co-existing with upwelling during summer, which means that it is not driven solely by wind stress, although it can be strengthened by intense poleward events. The notion that poleward flow shifts offshore during the upwelling season was further suggested by these results, particularly from Figure 3.11.

In what concerns upwelling events, there is relatively good agreement between the vertical Hovmöller diagrams (Figure 3.12), the UI time series (Figure 3.3) and in the monthly-averaged wind stress (Figure 3.13). This is expectable, since UI is computed from wind stress, and upwelling is strongly dependent on wind. Furthermore, ROMS was able to reproduce the strong fresh water input of particularly intense river discharge events in 2001, 2003 and 2006-2007.

Chapter 4

Model-derived Connectivity Patterns along the Western Iberian Margin: a Lagrangian Approach

4.1 Overview

The study of larval connectivity allows for a better understanding of marine species dynamics, in particular in such coastal ecosystems as the WIM. Coastal ocean processes play a fundamental role in the life cycle of numerous marine species, from crustaceans to small pelagic fish. Hence, it is important to understand how their variability and/or long-term changes affect(s) and/or bound(s) the development and survival of larvae. Larval dispersal is crucial in the life cycle of these species, since it dictates the supply of larvae from one location to the next, the ability of retention of a given location, and even the mortality and the migration success. Understanding these patterns is also important in terms of coastal management and biodiversity conservation measures. Among the factors that contribute for the offshore transport of larvae are upwelling filaments and other mesoscale phenomena, the upwelling front itself, the dynamics of the WIBP and species-specific larval behavior (Nolasco et al., 2013b).

Larval dispersal and supply may be quantified to a certain degree through connectivity. Connectivity of marine populations consists in assessing the connection between spawning locations and settlement locations, the traveling distance for settlement and the fraction of settled larvae at given locations (Kim and Barth, 2011). This successful settlement of larvae is called recruitment, which usually means that when larvae arrive at a given location conditions are prone for that larvae to develop and reach the adult stage (Domingues et al., 2011).

Numerical models have helped to overcome the inherent difficulties of monitoring such complex dynamics, in particular Lagrangian models coupled to regional ocean configurations (Marta-Almeida et al., 2006; Peliz et al., 2007). Taking advantage of this work high-resolution domain configuration for the WIM, this chapter comprises an effort to

study these different quantities (supply, accumulation, connectivity) for this region, following the work of Nolasco et al. (2013b). While these authors performed a study focused on a specific species, and where the larvae supply locations were set at the main estuaries along the WIM, this approach is more generic in the sense that larvae are treated more as Lagrangian particles, and recruitment is allowed to occur at any location along the WIM, not only in estuaries. Two simulations were carried out: one with no imposed vertical migration or travel distance limitations, either horizontal or in depth, much like the Lagrangian application in section 2.6; the other where particles have diel vertical motion (DVM), that is, they migrate down to 60 m during the day, for protection against predators, and up to the surface/subsurface during the night, for feeding (Santos et al., 2008). In this light, for the case of DVM, larvae are restricted to the upper 60 m.

Hence, this chapter describes connectivity along the WIM of generic larvae for adjacent locations with equal areas. This is carried out numerically for years 2001 to 2011, that is, the Lagrangian model runs over the ROMS simulations forced by real data for that period, described in chapter 3. The purpose of this application is not only to assess the influence of vertical displacement on dispersal distances and accumulation rates, but also to relate the patterns of dispersal/accumulation and connectivity with strong/weak wind episodes and upwelling events, the presence of topographic or bathymetric features, estuaries, etc.

4.2 Data and Methodology

As previously mentioned, the adopted methodology is built from that of Nolasco et al. (2013b), whose approach was already validated in the work of Domingues et al. (2012). However, mortality and growth rates dependent on temperature and salinity were not taken into account, since they are specific of specific species. Recruitment is assumed to occur when a larva enters one of the defined areas, which means that conditions such as the larval stage or other information that may influence successful settlement of larvae are not considered.

4.2.1 ROMS Configuration

The ROMS configuration used for this study is the same as in chapter 3, described in section 3.2.2. The real forcing for period 2001-2011 was retrieved from the NCEP2 air-sea fluxes (www.ncep.noaa.gov) and QuikSCAT/ASCAT reanalysis satellite winds from CERSAT (cersat.ifremer.fr). Boundary conditions were provided by the World Ocean Atlas (Antonov et al., 2010; Locarnini et al., 2010).

4.2.2 Lagrangian Model

The Lagrangian model, IBM (Individual Based Model), used in this chapter is the same as the one used in section 2.6, and is described therein (subsection 2.6.1). However, while in section 2.6 IBM ran over ROMS climatological run (described throughout chapter 2),

here it runs over the ROMS simulation forced by realistic winds, which period spans from 2001 to 2011, as described in chapter 3.

4.2.3 Methodology

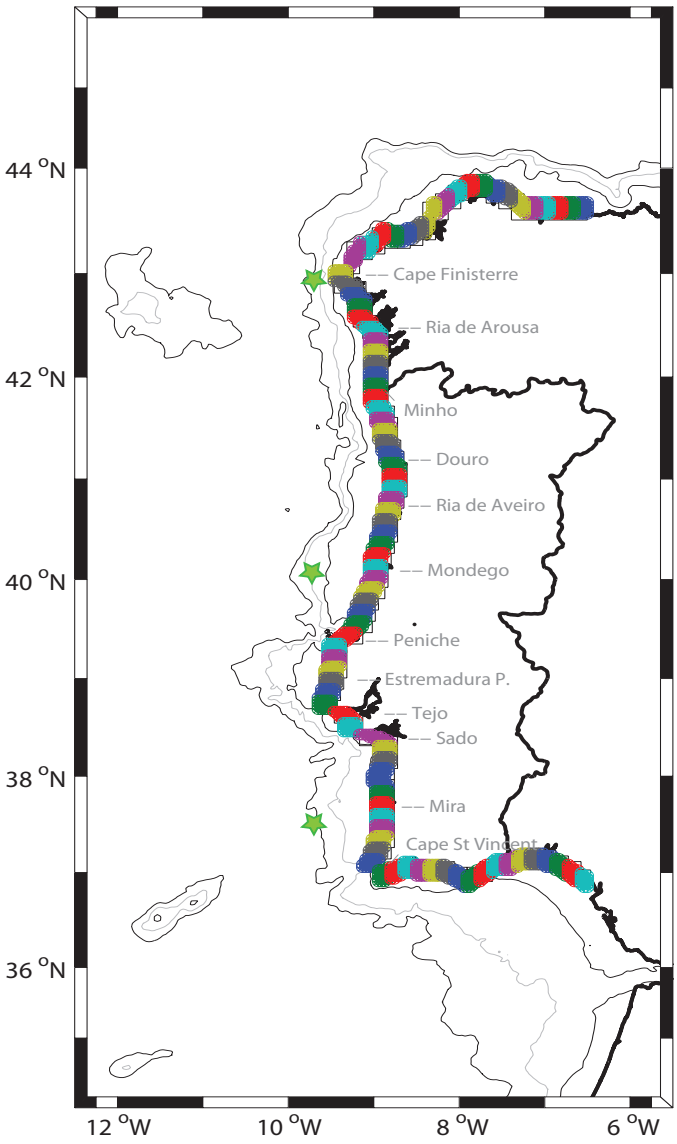

Figure 4.1: SD and larvae deployment areas. Some of the major topography features and rivers are indicated. Isobaths 200 m and 2000 m are shown in black and 1000 m in gray. Green stars indicate wind stress measurement points of Figure 4.2.

Figure 4.1 shows the 89 areas where the Lagrangian particles simulating larvae are measured, in terms of supply sources and sinks (the term "source" and "sink" will be properly defined in the following subsection). Some prominent regions of the WIM (capes,

estuaries, ...) are indicated for an easier identification when interpreting. Each area is defined taking 5 grid points cross-shore, seaward from the land mask, and 4 grid points alongshore, which means that each area is approximately 15 $km \times 12$ km. This area corresponds approximately to the area of influence of a typical river plume (Nolasco et al., 2013b). For computational viability, and each area having 4 alongshore points by 5 offshore points, larvae emission is done in only 2 out of each 4 sets of 5 points, which means 10 out of 20 grid points. Recruitment, on the other hand, is measured in the total area. Deployment is done at 3 different levels — 3 m, 5 m and 7 m — every 5 days during 3 months: February, March and April, which is the beginning of larval season for many marine species, and before the beginning of the upwelling season. Trajectories are registered every 3 hours for 40 days; however, the analysis is carried out after 30 days of travel, that is, for the last 10 days of the trajectory. Thirty is the typical number of days that takes some marine species (e.g. shore crabs) to reach the next stage of development, and after which they are known to recruit (Domingues et al., 2011). This means that, for instances, for the particles that are deployed March 31, their source/sink capabilities are analyzed for the first 10 days of May. The total number of particles deployed is 89 areas $\times$ 10 grid points $\times$ 3 levels $\times$ 19 time steps = 50,730.

Although these areas are defined west of 6.5^{o}W, which means that there is also emission/retention at part of the northern and southern coasts of the Iberian Peninsula (see Figure 4.1), the analysis carried out in terms of supply from source and to sink in the following section concerns the western coast only. The reason for this is that the focus of this work is the WIM alone. On the other hand, the WIM cannot be looked at in terms of departure and arrival of particles without taking into account these neighboring areas, as if it were detached completely. Thus, the northern and southern coasts are allowed to supply and to recruit larvae; they are merely not computed when quantifying for the WIM. Furthermore, Nolasco et al. (2013b) estimated that the contribution of larvae supplying outside the domain to the north and south through the eastern boundaries is negligible, as should be the contribution of larvae supplying at the WIM with origin at the same boundaries. This is valid for the entire set of analyses except for the connectivity matrix, described below.

4.2.4 Data Analysis

In order to describe the dispersal and connectivity process, some concepts related to dispersal and accumulation of larvae must be introduced. Dispersal kernel, dispersal from source or supply from source refers to the process of transport of larvae away from each defined area along the coast. Conversely, accumulation kernel, accumulation to sink or supply to sink refers to the process of transport of larvae recruiting into an area.

Dispersal/accumulation kernels convey the frequency distribution of distances of dispersal/accumulation. Idealistically (homogeneous ocean, linear coast, symmetrical currents, ...), dispersal kernels would obey the Gaussian distribution, supplying the most to or from near itself or adjacent locations, and this supply decreasing as the distances increase. Another way to measure supply to and from a location is to represent the percentage of larvae

recruited as a function of distance between sources/sinks. In this study, source and sink are operational terms that designate whether an area is "emitting" or "receiving" larvae, and competent larvae refers to larvae that successfully recruit into any area.

In the present study, one of the aims was to study the inter-annual and spatial patterns of connectivity. To this end, square connectivity matrices were computed. A connectivity matrix is defined as the probability matrix of exchange of individuals between sites (Cowen et al., 2006). These matrices describe the annual accumulated supply of competent larvae from source area i ($i = 1$ to k) to sink area j ($j = 1$ to l):

$$C_y = \begin{pmatrix} C_{1,1} & \cdots & C_{1,l} \\ \vdots & \ddots & \vdots \\ C_{k,1} & \cdots & C_{k,l} \end{pmatrix} \tag{4.1}$$

In matrices C_y, each element was normalized by the total number of larvae that originated from all areas. These matrices formed the basis to calculate a series of descriptors of the dispersal and connectivity processes.

Annual supply from each source area was defined as the number of larvae originating in that area that successfully recruited into any area, normalized by the total number of larvae deployed. This was calculated as the sum of the respective i line of matrix C_y:

$$Ssource(y_i) = \sum_{j=1}^{l} C_{i,j} \tag{4.2}$$

Similarly, annual supply to each sink area was defined as the number of larvae that recruit into that area independently of the source area, also normalized by the total number of larvae deployed, and calculated as the sum of the respective j column of matrix C_y:

$$Ssink(y_j) = \sum_{i=1}^{k} C_{i,j} \tag{4.3}$$

Additionally, net supply to each area was computed as the difference between supply from and supply to that area:

$$Netsupply(y_i) = Ssource(y_i) - Ssink(y_i) \tag{4.4}$$

Positive values of net supply for position y_i mean that y_i is predominantly a source (it supplies more than it recruits), and for negative values y_i is a better sink (it recruits more than it supplies).

The dispersal kernels describe particle dispersal as the probability density function [P(x)] of the number of particles that recruit as a function of distance from the source. They were standardized by dividing each element by the total number of larvae that were produced by that area and that recruited subsequently. This resulted in an annual dispersal kernel for each source area centered on 0 km and describing the probabilities of supply for the other equally spaced areas. Finally, the ensemble of source areas was averaged in order

to obtain annual coast-wide dispersal kernels. Since flow along the coast is not stationary, leading to non-uniform dispersal along the coast, and because each area receives larvae from multiple sources, it was also interesting to describe the dispersal distances travelled by larvae that were supplied to each population. Therefore, accumulation kernels were also calculated as the distribution of these dispersal distances, in a similar way to the dispersal kernels but standardizing by dividing each element of the kernel by the total number of larvae that recruited into that area.

In the above calculations, distances travelled northward were always defined as positive distances, and distances travelled southward as negative distances. Connectivity matrices, dispersal and accumulation kernels and supply from source and to sink areas were calculated for the 11-year period by averaging the annual values.

4.3 Results

4.3.1 Wind Stress Patterns

Figure 4.2 presents the wind stress meridional component for all years under scope at three points off WIM (43^oN, 40^oN and 37.5^oN, at longitude 9.7^oW, marked in Figure 4.1), for the months where larvae is deployed and/or supply is computed — February to June. The average of all years is also shown.

Besides the evident interannual variability, it is interesting to remark that depending on the latitude, meridional wind episodes are different, especially in what concerns point 40^oN in comparison with the other two. For instances, in 2004 there is a positive peak in early April that is much stronger at 40^oN; the same occurs for a negative peak in early March 2008. On the other hand, in 2011, in late February there is a positive maximum at 40^oN, whereas for the other latitudes the meridional wind stress is negative and not particularly strong. Another noteworthy aspect is the fact that in June there are not well-defined equatorward winds yet, although they are in general negative.

In general, equatorward winds prevail over poleward winds; however, the more sporadic poleward events tend to be stronger than the recurrent equatorward patterns. The strongest poleward episodes occur usually in February (2001-2003, 2007, 2010, 2011), but may also occur in March and April (2001, 2003, 2004-2006). The years with less relevant poleward peaks are 2008 and 2009. Important equatorward episodes can occur roughly in every considered month, depending on the year.

4.3.2 Dispersal and Accumulation Kernels

Figures 4.3 and 4.4 present dispersal and accumulation kernels (annual averages), for both runs (with and without DVM). For the dispersal kernels, positive distances mean supply to the north, and for the accumulation kernels positive distances mean supply from the south. That is, the south-north direction is always positive. Furthermore, the sink distributions are very similar to those of the source, as it should be, since if in average a

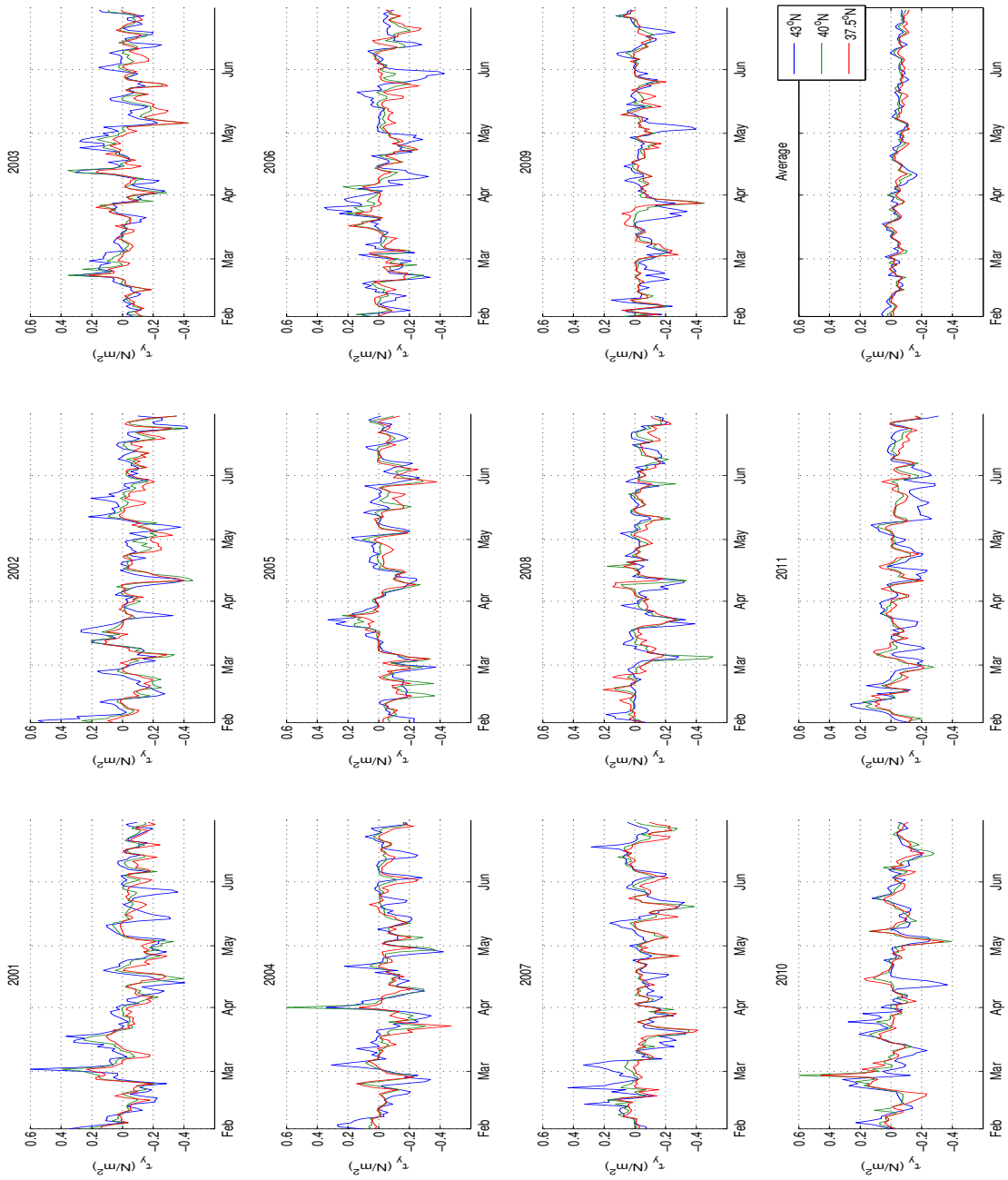

Figure 4.2: Daily wind stress meridional component ($N\ m^{-2}$) time series for years 2001-2011 and period February-June at three points off WIM marked in green stars in Figure 4.1.

source supplies, for instances, to a northern (southern) location 10 km away, it is supplied in average from a southern (northern) location 10 km away. The strong interannual variability is striking.

In some years supply is done mostly to the south (2002, 2004, 2009, and also 2006 and 2007, discussed further below) and from short distances, and we see that 2009 was a year where winds were predominantly equatorward and with few strong episodes (Figure 4.2 i), consistent with short displacements. In other years, particles travel longer distances (2001, 2008, 2010). In these years there are long periods of consistent winds: in 2001, after a month and a half of strong poleward winds, equatorward winds prevail between April and June, hence the long distances travelled in both directions; in 2008, there are rarely poleward episodes, thus promoting generalized southward transport; in 2010, there are mostly poleward winds, at least at 43^{o}N and 40^oN, accounting for the marked northward dispersal.

The cases of 2006 and 2007 are quite interesting, with an abrupt change at distance zero. Observing the dispersal (accumulation) kernels — Figure 4.3 f,g (Figure 4.4 f,g) — , on one hand there is a higher supply to the south (from the north) at shorter distances, and on the other supply to the north (from the south), although lower, reaches farther locations. In terms of winds (Figure 4.2 f,g), 2006 has an important poleward episode in March, while in 2007 several poleward peaks take place throughout February, promoting northward transport, both followed by consistent equatorward winds, lasting several months, which explains the large distribution to the south (from the north).

The most evident difference between distributions with and without DVM is the shift toward supply to the south (from the north). This shift is visible in almost all years, clearly in 2004, 2007 and 2009, but also in 2003, 2005 and 2011, where the protuberance toward supplies to the north (from the south) are softened and the distribution becomes more symmetric around zero. The shift is also visible from the mean and standard deviation of the distributions (indicated in black and red at each side of the plot).

In the end, the mean distribution is mostly symmetrical (Figure 4.3, 4.4 last subplot), with a central peak that suggests self-recruitment (or in adjacent areas) and an exponential decrease toward farther distances. Nolasco et al. (2013b) results were more consistent with this kind of distribution for each year, which means that there was higher self-recruitment and that populations tended to supply to/from adjacent locations. Furthermore, the imposition of DVM does not mean higher self-recruitment as could be expected, since the vertical migration of larvae could inhibit advection offshore and promote retention near their origin.

4.3.3 Supply from Source and to Sink

Figures 4.5 and 4.6 show the total annual supply from each source and to each sink, respectively (the last subplot is the 11-year mean), for DVM and no DVM simulations. There is some interannual variability, but overall all areas are able to supply. However, it seems that Tejo and Sado are systematically the "worst" sources, particularly seen in years 2007 to 2009. Note that the extremities of the western Iberian coast are also weak

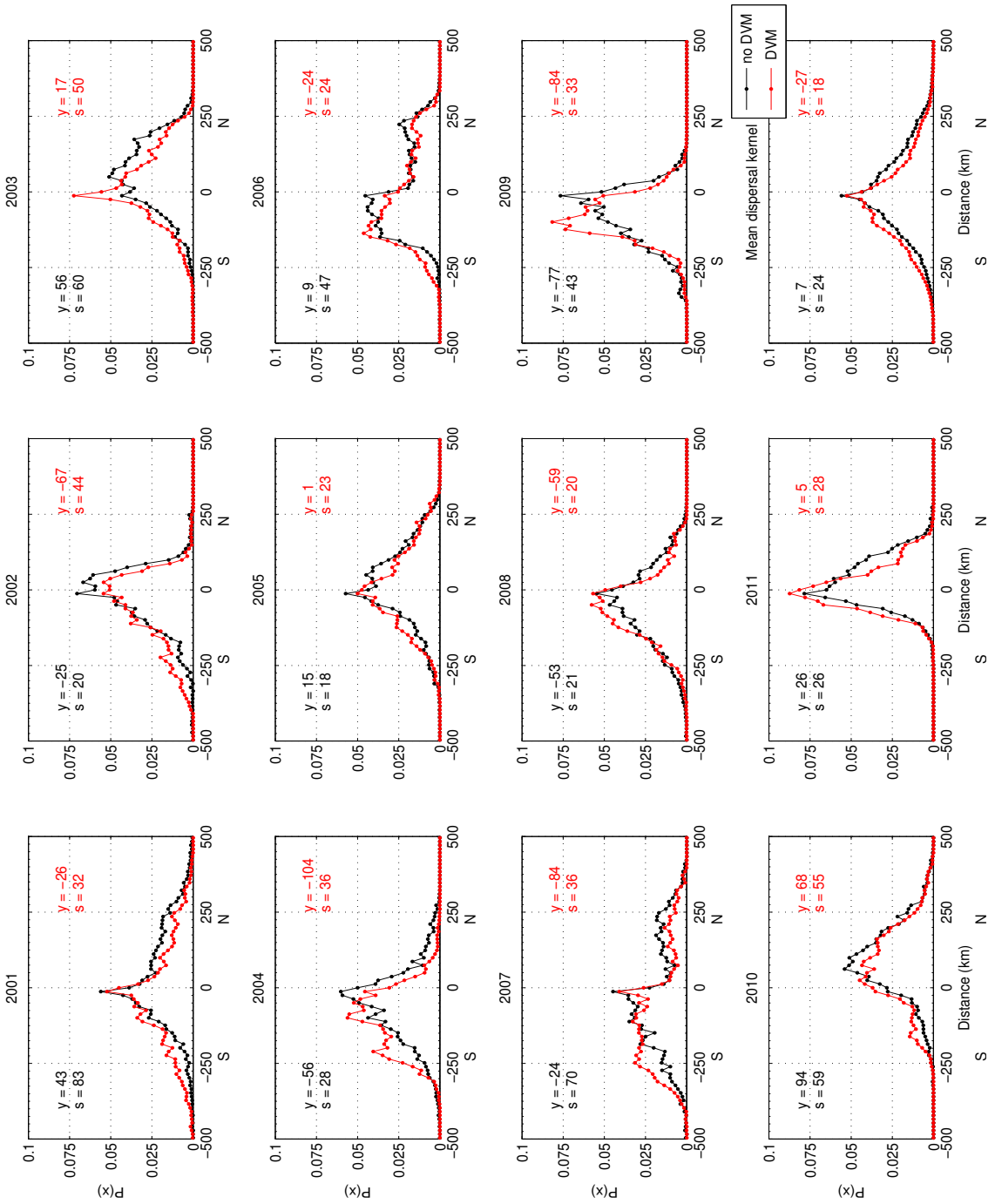

Figure 4.3: Dispersal kernels (the mean and standard deviation are shown). The black distribution corresponds to the case of no DVM, and the red distribution to the case of DVM.

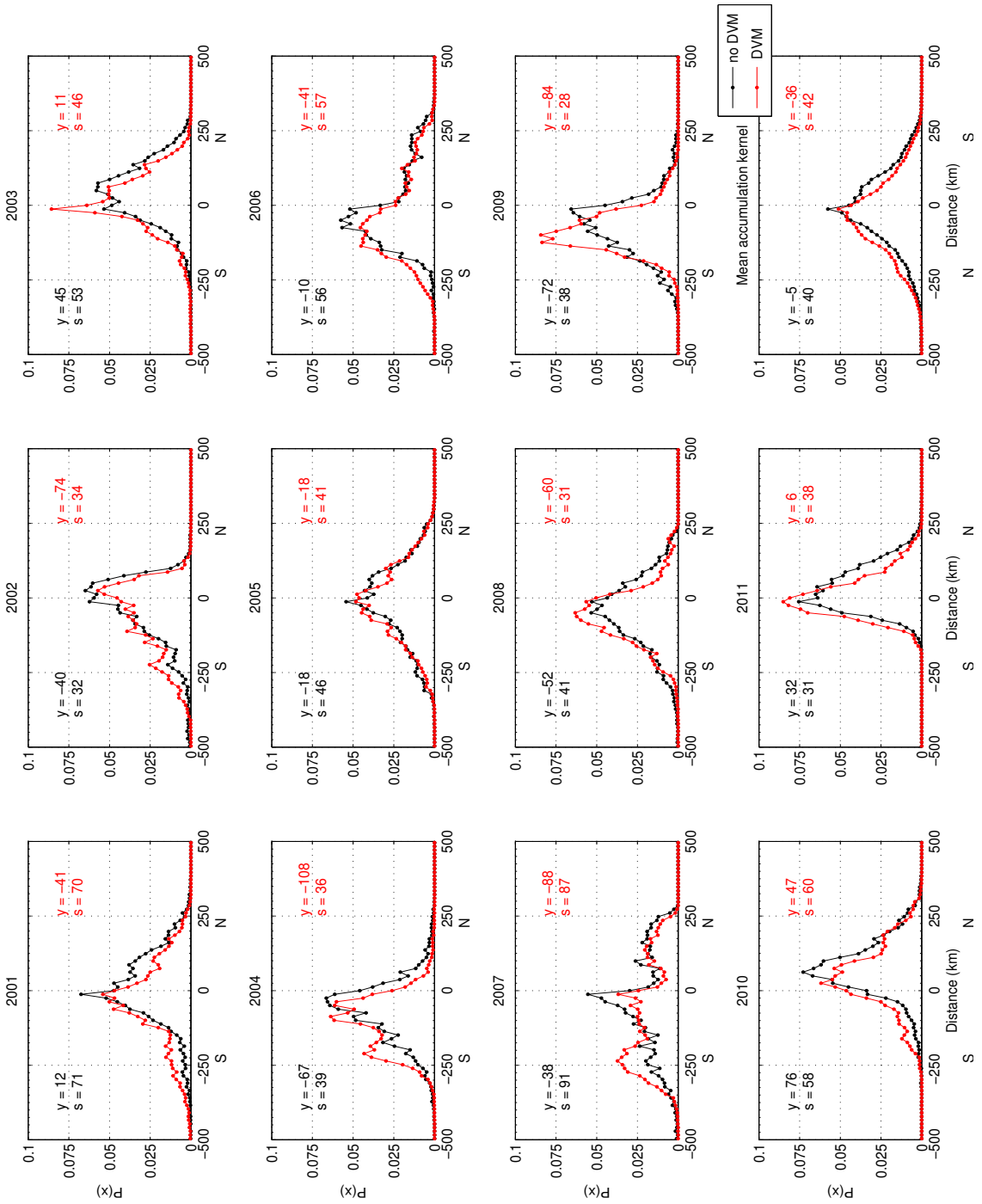

Figure 4.4: Accumulation kernels (the mean and standard deviation are shown). The black distribution corresponds to the case of no DVM, and the red distribution to the case of DVM.

sources. In the case of DVM, the supply increases throughout, especially north of Peniche. With the introduction of vertical migration, particles spend more time below the surface Ekman layer, avoiding offshore dispersion during upwelling, and thus improving the ability of successful recruitment.

In what concerns supply to sinks, there are more marked differences between locations. The areas that seem to retain more are Peniche, Tejo, and Sado, and once again the extremities of the western Iberian coast. The reason for these regions to be good sinks may be the fact that they are all located adjacent to capes or promontories, which may enable them to retain arriving particles. On the other hand, they were observed to be weak sources, likely due to the same reason. In the case of DVM, the tendency for good retention is enhanced, particularly near pronounced topography features.

Figure 4.7 shows the balance between supply to and from each location. Positive values mean that supply is greater than accumulation and negative values mean that accumulation is greater than supply. Therefore, zero balance does not usually mean that there is neither supply nor accumulation; rather that supply is equal to accumulation. The general tendency indicates that the areas between capes Finisterre and Corrubedo (the northernmost regions, see Figure 4.1) are good sinks, whereas the northwest from ria da Arousa to north of the Estremadura Promontory (that is, where the coastline is mostly meridional), holds the best sources. Between Peniche and Tejo there is also a tendency for more supplying than accumulation (the coastline is again mostly meridional), but at Tejo and Sado there is preferentially accumulation, as previously seen. South of Sado there is again more tendency for supplying, with the exception of the two southernmost locations near Cape St Vincent. Therefore, we conclude that there are better conditions for larvae sources in regions where the coastline is smoother and straight, and better conditions for larvae sinks where the coastline is more jagged and protuberant. Once again, the introduction of vertical displacement of larvae tends to enhance both supply and accumulation. The locations where the differences between DVM and no DVM are the extremities: north of ria de Arousa and south of Mira.

It is interesting to remark that Nolasco et al. (2013b) found that for instances Aveiro was a good sink and a weak source, conversely to these results. However, since in that study the locations for recruitment were limited to the estuaries, a possible explanation for this difference is the fact that in order for Aveiro to successfully supply southward was if that recruitment were done in Mondego or Tejo, with no sink in between, over the 150 km that separate these two locations. In this approach, Aveiro can supply to much closer locations, becoming a more successful source than sink.

4.3.4 Dispersal Distances

Figure 4.8 (4.9) presents the dispersal distance of particles supplied to (from) each area according to the alongshore location of all areas when functioning as sources (sinks). In Figure 4.8, positive (negative) distances indicate particles being supplied to the north (south), while in Figure 4.9 positive (negative) distances mean that particles are being supplied from the south (north). Figure 4.10 is a source/sink balance where the average

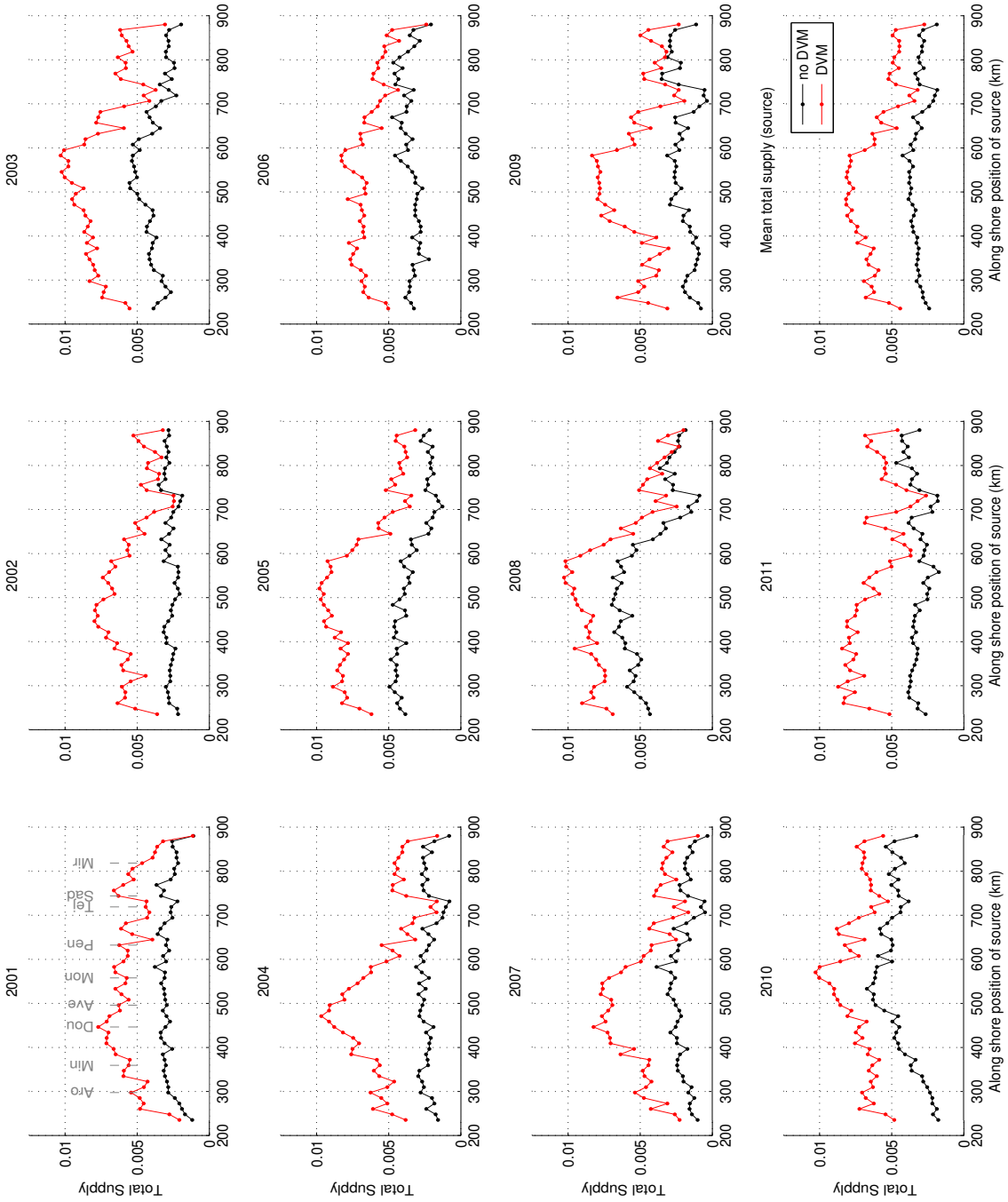

Figure 4.5: Total annual supply from each source according to its alongshore position. The black distribution corresponds to the case of no DVM, and the red distribution to the case of DVM. Labels in gray in the first plot correspond to the regions identified in Figure 4.1.

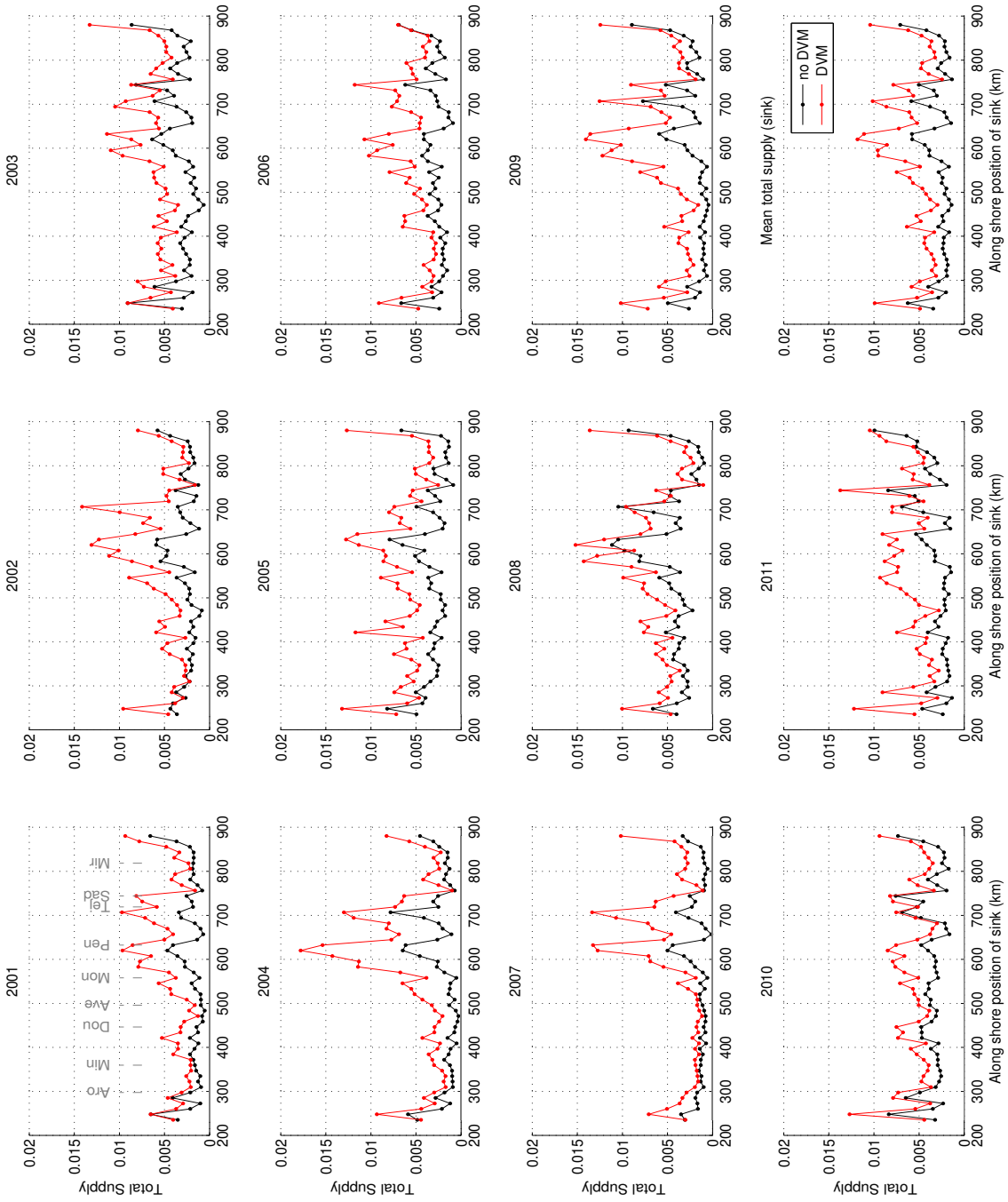

Figure 4.6: Total annual supply from each sink according to its alongshore position. The black distribution corresponds to the case of no DVM, and the red distribution to the case of DVM. Labels in gray in the first plot correspond to the regions identified in Figure 4.1.

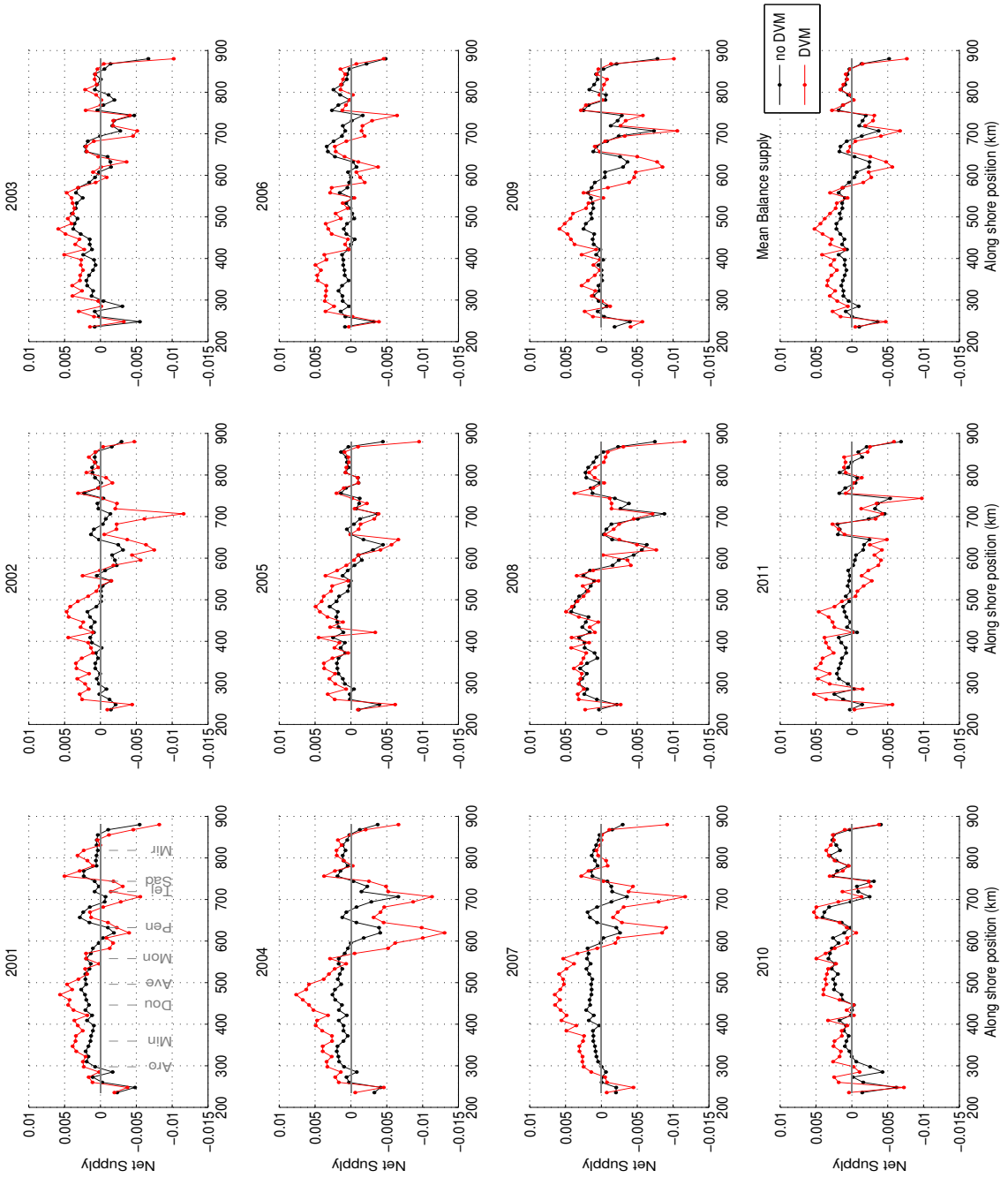

Figure 4.7: Balance supply. The black distribution corresponds to the case of no DVM, and the red distribution to the case of DVM. The black distribution corresponds to the case of no DVM, and the red distribution to the case of DVM. Labels in gray in the first plot correspond to the regions identified in Figure 4.1.

is computed in time. The last subplot is the 11-year mean. In all these figures, there is a crucial area for change in behavior, which is the region between Peniche and Tejo (between approximately 630 and 730 km in terms of alongshore position of source/sink) — the Estremadura Promontory (EP).

Like in the supply analysis, dispersal distance undergoes strong interannual variability. Analyzing the case with no DVM, in terms of source location (Figure 4.8), there are several years where north of Peniche/Tejo particles are supplied to the north, and south of Peniche/Tejo they are supplied to the south (2001, 2003, 2010, and less evidently in 2006 and 2007), and this is reflected on the 11-year mean, while in other years it is not so clear. In some years, the particle dispersal is mostly southward (2004, with the exception of Tejo and Sado, 2008 and 2009, also visible in 2002, but very close to zero, with the exception of the EP region); in others it is preferentially northward (2005, 2011). In 2005, however, dispersal distances are near zero, except in the EP, while in 2011 distances to the north down to Aveiro are positive, near zero from Aveiro to Sado, and positive again to the south, although much weaker. As suggested in the previous figures, DVM enhances supply to the south in the region north of Peniche (e.g. 2001, 2002, 2004, 2007), as seen in the average (last subplot). In the southern WIM differences between DVM and no DVM are negligible. A possible explanation for this follows. DVM increases southward recruitment in general. North of Peniche, since recruitment was carried out preferentially northward, the difference is more evident than south of Peniche, where recruitment was already preferentially to the south.

When observing dispersal distances according to the sink (Figure 4.9), there is more agreement interannually, and also between the cases with and without DVM: particles are supplied from the south in northern WIM and from the north in southern WIM. Here, the transition between supply origin (the geographical gap) is north of the Estremadura Promontory, between Mondego and Peniche (and sometimes even farther north). The more evident exceptions are years 2002, 2004, 2008 and 2009, where the particles retained were supplied mostly from the north. However, in average (last subplot), tendencies are for positive retention north of Aveiro, negative retention south of Aveiro, and close to zero south of Sado. Differences between the cases with and without DVM are not significant because, although dispersal distances are greater, they increase in both directions, and so the balance remains similar to the case without DVM (only slightly enhanced southward, as expected). Since there are few larvae supplied from south of Tejo that go northward, the regions between Aveiro and Tejo are not much supplied from the south. Even in years where particle dispersal is mostly northward, there is a decrease between Peniche and Tejo.

As previously observed in Figures 4.3 and 4.4, the existence of DVM enhances southward transport. From these figures it can be drawn that this happens mostly north of the EP. The EP is an evident geographical obstacle for larvae transport. It is interesting to note that, from the source point of view, the gap takes place between Peniche and Tejo, whereas from the sink point of view it occurs between Mondego and Peniche. That is, generally speaking, for years where dispersal occurs on opposite directions relative to the EP, supply north of Peniche (north of Mondego) is carried out to the north (from the south), and vice-versa. When introducing DVM, supply is carried out farther to the south in northern

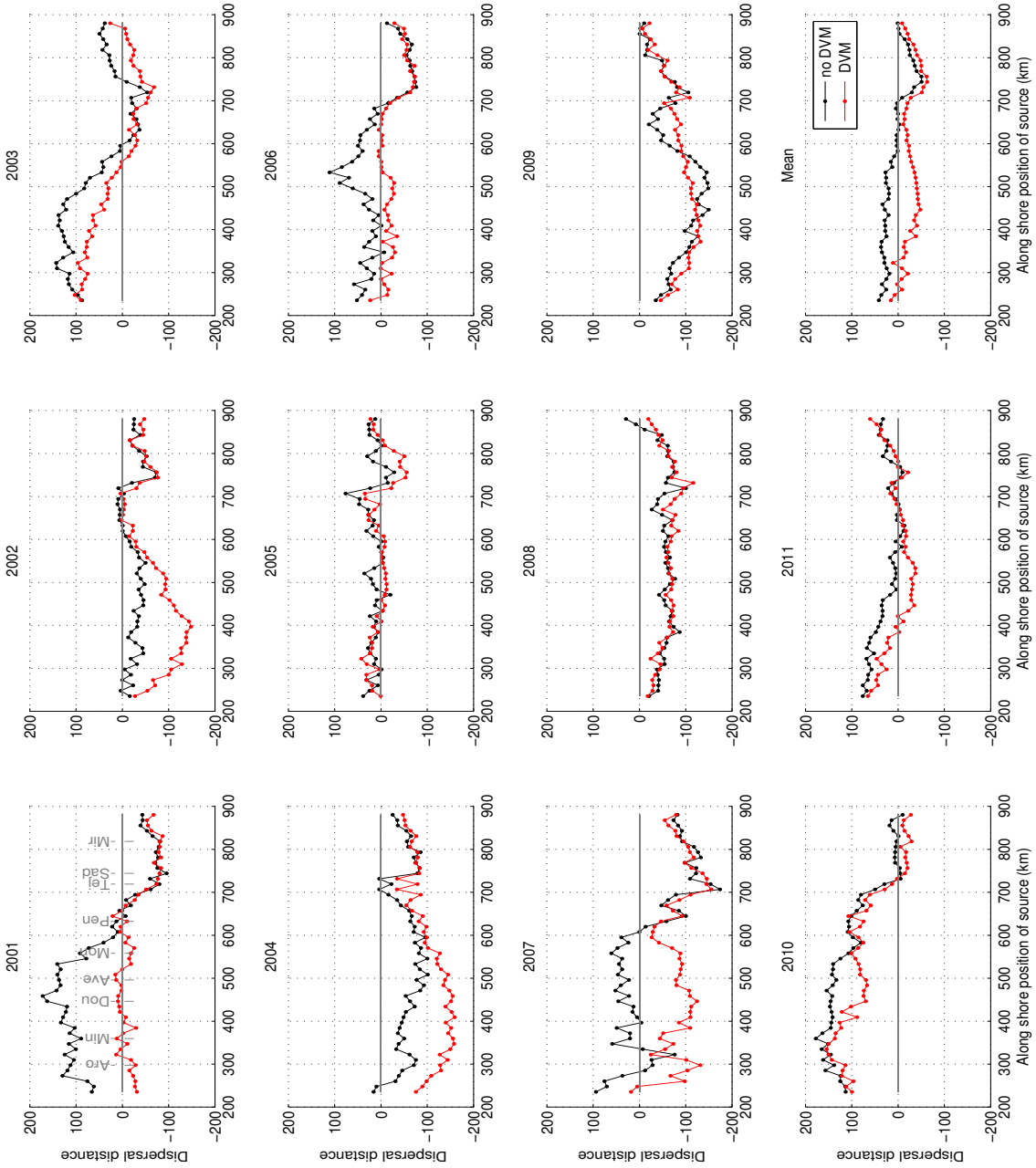

Figure 4.8: Dispersal distance of particles supplied to each area according to the alongshore location of all areas when functioning as sources. The black distribution corresponds to the case of no DVM, and the red distribution to the case of DVM. Labels in gray in the first plot correspond to the regions identified in Figure 4.1.

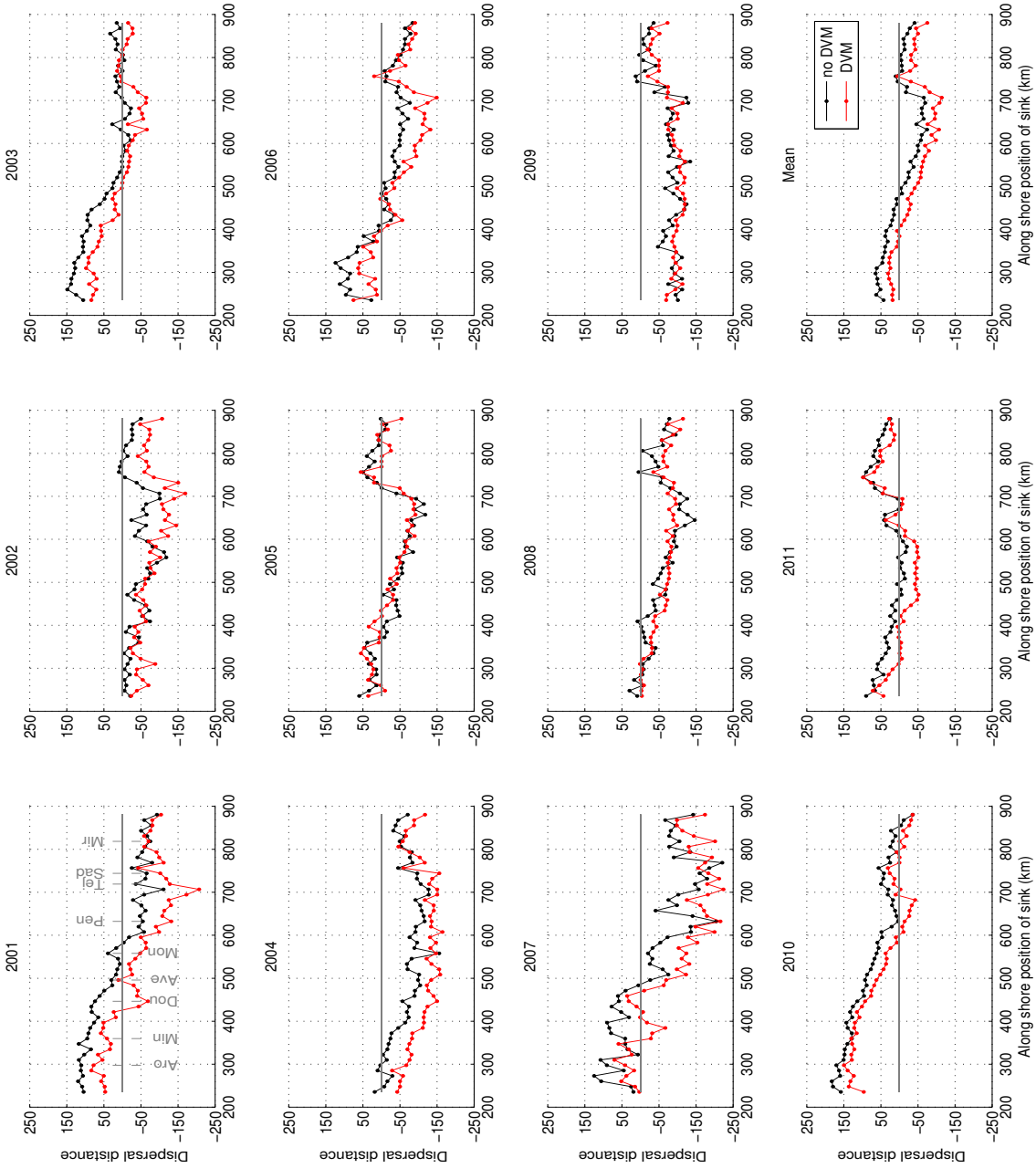

Figure 4.9: Dispersal distance of particles supplied from each area according to the alongshore location of all areas when functioning as sinks. The black distribution corresponds to the case of no DVM, and the red distribution to the case of DVM. Labels in gray in the first plot correspond to the regions identified in Figure 4.1.

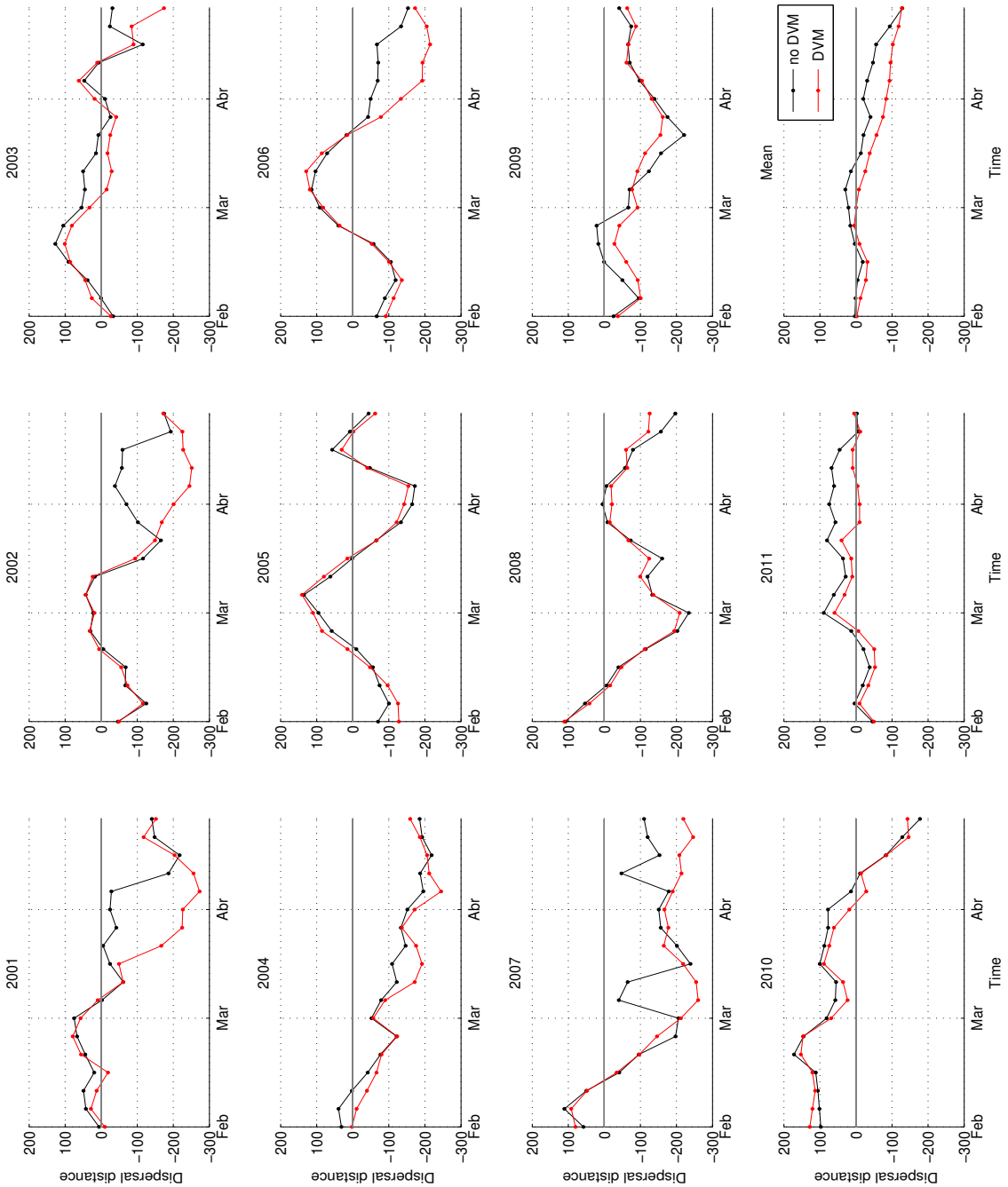

Figure 4.10: Dispersal distance according to time (annually-averaged for the months of deployment). The black distribution corresponds to the case of no DVM, and the red distribution to the case of DVM.

WIM (Figure 4.8) because there is less offshore advection due to Ekman transport. On the other hand, supply is carried out from farther north all along the WIM.

Taking in consideration the dispersal distance averaged in time (Figure 4.10), its analysis is less evident because positive (negative) values may indicate either supply to the north (south) or supply from the south (north). But it is interesting to remark the interannual variability. To years with marked poleward events early in the period of supply, such as 2001, 2005, 2007 and 2010 (see Figure 4.2), correspond preferential northward dispersal during February and sometimes mid-March. In average (last subplot) the balance is practically zero, with southward tendency from April on for the case with no DVM and from March on in the case of DVM. Note that the time period is relative to the deployment of larvae, and not the analysis period (after 30 days, and for 10 days), which means that the larvae supplied in April were recruited already during the upwelling season. The DVM case shows more clearly southward dispersal prevailing over northward dispersal.

4.3.5 Connectivity Matrix

Figures 4.11 and 4.12 present the connectivity matrices for the case without and with DVM, respectively, for the all the areas along the WIM, including the ones located in the northern and southern coasts. Each line of the matrix represents the distribution of larvae originating from each area (y-axis) that successfully recruit to the different areas along the coast (x-axis). That is, following the diagonal, which means self-recruitment, the upper triangular matrix indicates where areas are supplied from the north (equartorward dispersal), and the lower triangular matrix where they are supplied from the south (poleward dispersal).

With respect to the case of no DVM, the most striking differences in relation to the connectivity matrix of Nolasco et al. (2013b) are less accumulation, seen by the differences in the order of magnitude (colorbar), and less self-recruitment. To the north of Douro, supply is carried out mostly from the south, most evident for Finisterre. Between Douro and Peniche, particles are supplied preferentially from the north, recruiting larvae from almost as far as Arousa. Furthermore, we observe again a gap in the Tejo-Sado region: larvae originated here do not travel north, and between Peniche and Tejo supply is carried out strictly from the north (mostly south of Aveiro). This was also observed by Nolasco et al. (2013b). Between Sado and Cape St Vincent, recruitment is done in both directions, although Cape St Vincent is strongly supplied by the region south of Mira.

In what concerns the case of DVM, the diagonal band is wider, indicating larger dispersal, and general higher recruitment, seen by the lighter blues. Higher recruitment, whether supply is done northward or southward, is enabled by the fact that larvae, is less advected offshore in case of northerly winds and less retained onshore in case of southerly winds, allowing the particles to travel longer distances. Also, there is higher dispersal to the south, seen by the displacement of the diagonal band toward the "upper" triangle; hence, there is a tendency for recruitment to happen in the N-S direction. This is consistent with the analysis of the dispersal/accumulation kernels (Figures 4.3 and 4.4), where the same southward displacement was observed. The difference is more evident between Douro

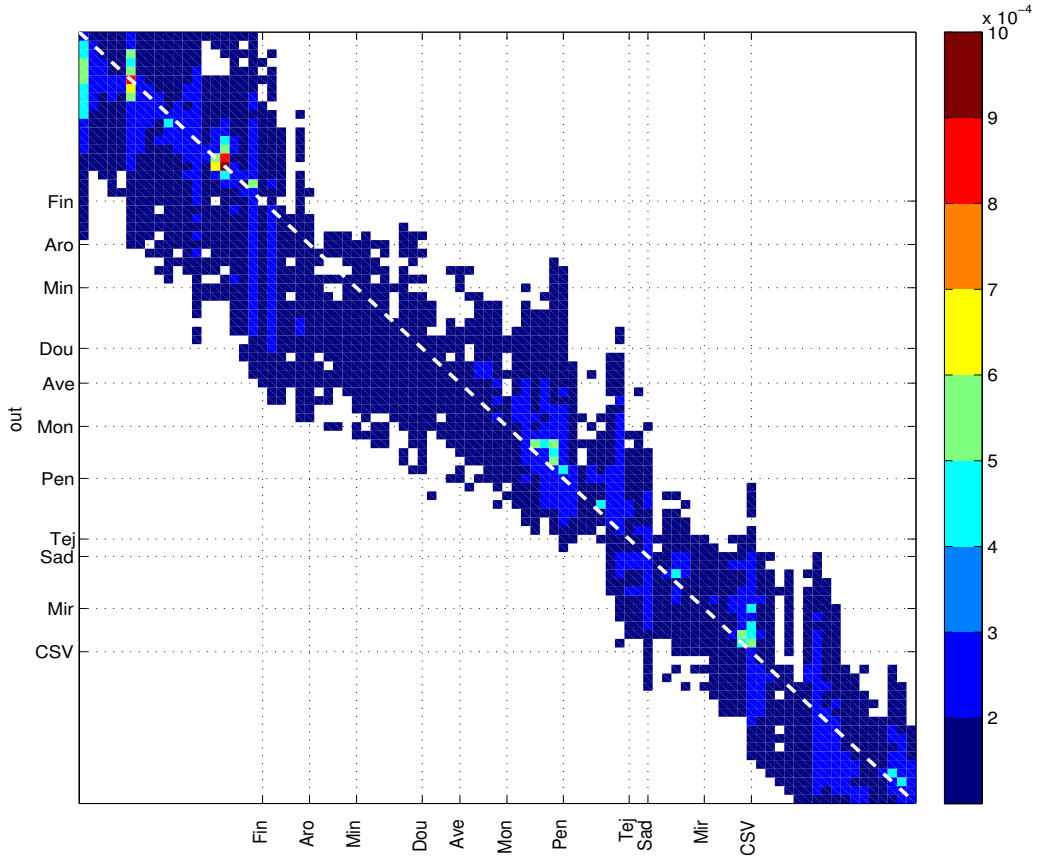

Figure 4.11: Connectivity matrix without DVM.

and Peniche, where the colors are more vivid, which was also made clear in the dispersal distance plots (Figures 4.8 and 4.9).

4.4 Discussion

This chapter consists in an idealized study where Lagrangian particles deployed in equally spaced and equally sized areas serve as means to infer about a generic type of larvae and to allow tracing average behaviors such as supply, accumulation and connectivity. This Lagrangian study is applied to the interannual ROMS run described in chapter 3.

An experiment including diel vertical migration are analyzed in parallel with the ones in the absence of DVM in order to assess the differences between both. Indeed, low accumulation is a consequence of the absence of vertical migration. By not allowing the particles to descend periodically in the water column, they remain in the surface Ekman layer and are thus constantly transported offshore in the presence of upweeling and away from their origin, contributing to lower probability of recruitment.

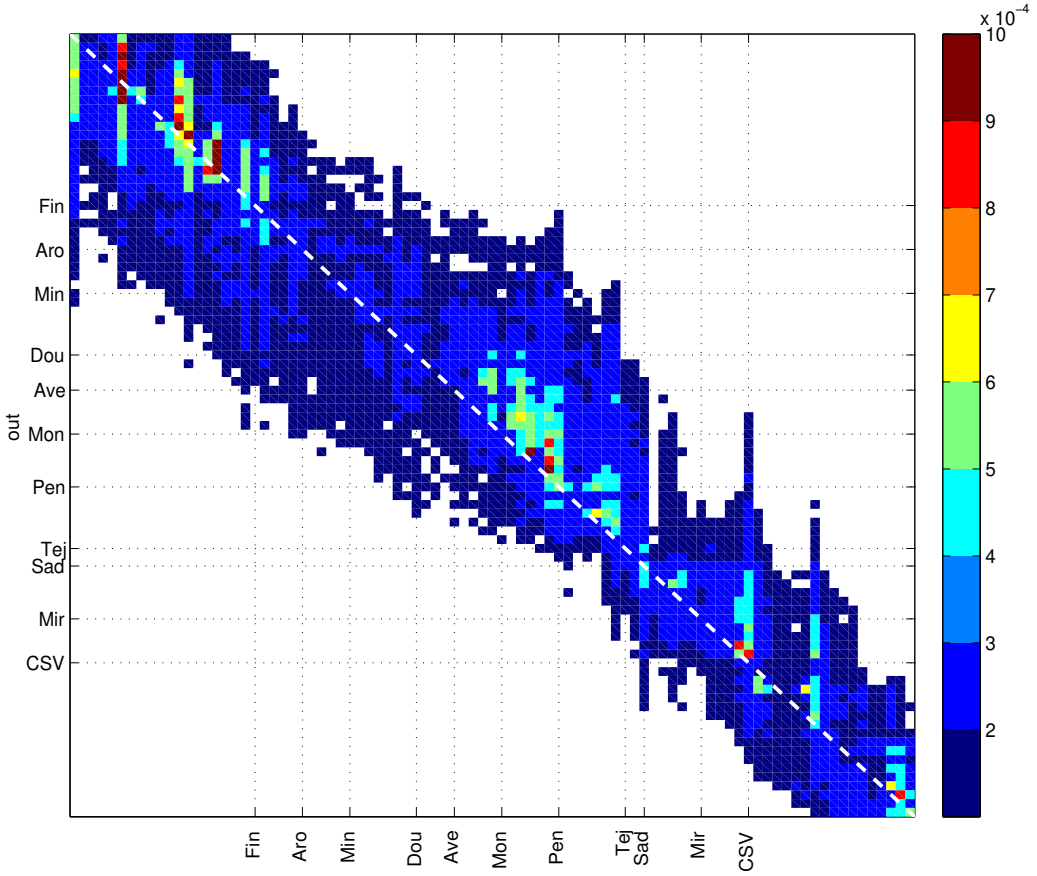

Figure 4.12: Connectivity matrix with DVM.

One of the major factors influencing these processes and patterns is wind stress, and particularly meridional wind stress, which, as seen throughout this work in the previous chapters, regulates the upper level circulation off WIM in the shelf region. During the months that were taken into account, which are mainly winter and spring, winds are very variable, with some years witnessing strong poleward episodes, especially in February (2001, 2002, 2007, 2010), and a few equatorward and generally weaker episodes, occurring most frequently in April (2001, 2002, 2004, 2006, 2008, 2011), although equatorward winds exist every year.

In spite of the fact that particles should preferentially supply to and be supplied from closer areas, the dispersal and accumulation kernels (Figures 4.3 and 4.4) show that this is not necessarily the case and that it varies greatly from year to year. Equatorward winds prevail from April to June, although punctuated by poleward episodes. Long periods of equatorward winds and particularly strong poleward episodes occurring for at least a month originate dispersal/accumulation at great distances. The years with fewer poleward events seem to be the ones where supply is carried out in both directions.

The supply from source and to sink images reveal that the ability to supply to or ac-

cumulate depend strongly on topography. The WIM northern extremity areas are poor sources but good sinks, likely due to the Galician Rias embayments and jagged coastline that are prone for the retention of particles. Tejo and Sado, being located directly south of the Estremadura Promontory, are observed to be poor sources, although with good abilities to retain, alongside Peniche, which is located between two capes. And the WIM southern extremity, the southwest-oriented Cape St Vincent, presents tendency to accumulation. The best sources are located in the areas with the smoothest coastlines, promoting alongshore transport of the particles. The connectivity matrices also confirm the Estremadura Promontory as an obstacle for the supply from the south, in both simulations.

The absence of vertical migration promotes larger advection, as seen in Figures 4.8-4.10. On the other hand, self-recruitment does not greatly increase when introducing DVM. Hence, it must be due to the continuous distribution of sources and sinks along the coast, instead of just taking into account the major estuaries as in the work of Nolasco et al. (2013b). Furthermore, those authors report, for instances, Aveiro and Mondego as good sinks, which is not the case in the present study; rather the reverse. The difference must be attributed to the evenly distributed areas alongshore that makes it easier for the supply to be done farther away rather than in its point of origin. In their work, there were no areas of recruitment between Aveiro and Mondego, hence larvae would either disperse or return to their own estuary; here, they can easily be recruited into adjacent areas that are only 12 km apart.

There is another striking difference between the cases with and without DVM: in the former, supply increases significantly, especially in the southern locations, which is a direct consequence of the particles not being subject to offshore advection associated with Ekman transport in the presence of equatorward winds. An increase in retention is also evident when observing the connectivity matrices with and without DVM, and although self-recruitment does not clearly increase, retention between adjacent areas is more noticeable.

Chapter 5

A Future Climate Scenario, part 1: Global Climate Models as forcing for regional ocean modeling

Part of the contents of this chapter have been submitted to Climate Dynamics (Cordeiro Pires et al., in review).

5.1 Overview

Global climate models (GCMs) have been one of the most important tools of the past three decades for studying climate, whether past variability or future scenarios in the context of global change. The increasing need for realistic assessments of climate change from a policymaker and social-economical point of view calls for the minimization of uncertainties, not only of the models themselves but also of the future scenarios the climate simulations are based on.

The Intergovernmental Panel for Climate Change (IPCC) has played a major role in providing a large database of state-of-the-art GCM simulations from numerous research institutes around the world, open to the scientific community, comprising not only past simulations but also simulations forced by scenarios of future climate (Nakićenović et al., 2000). Consequently, several multi-model inter-comparison studies were carried out (e.g. Collins et al., 2006; Fyfe et al., 2010; Lorenzo et al., 2011) to assess the models ability to simulate a given phenomenon or variable, and allow the conjugation of different models in a specific study. The Coupled Model Inter-comparison Project (CMIP) was created with this intent (Lambert and Boer, 2001), making it possible to evaluate the strengths and weaknesses of the GCMs. A way to minimize the individual model biases is to use the multi-model ensemble mean, that is, the combination of output from different models (Tebaldi and Knutti, 2007). This approach has been increasingly considered the most suitable in climate projections because, assuming that simulation errors in different GCMs are independent, the mean of all the models can be expected to present lower uncertainties

than each model individually (Lambert and Boer, 2001). Compared against historical observed gridded data, the ensemble mean shows good results in replicating historical climate, from which we can infer that it is also a valid approach in the representation of future climate conditions (Räisänen and Palmer, 2001). Pierce et al. (2009) and Annan and Hargreaves (2010) carried out statistical analyses of the CMIP3 model set and showed that, in general, the best results are obtained with the multi-model ensemble of a selection of models.

The atmospheric regimes simulated by GCMs have been thoroughly explored. With respect to ocean studies based on atmosphere-ocean coupled GCMs (CGCMs), there are several underlying difficulties: (a) there are by far fewer observation data than for the atmosphere, rendering model validation more difficult; (b) the air-sea interactions and feedbacks are strongly non-linear and therefore more difficult to predict and simulate; (c) CGCMs, especially in deeper layers, usually fail to properly represent the ocean mean state due to their coarse resolution (Russell et al., 2005); (d) assessments of future global ocean regimes, which must take into account the ocean distinct time of response and the role of mesoscale phenomena, have limited reliability. Ocean modeling studies where one or several CGCMs of the CMIP database have been used include that of Stouffer et al. (2006) to study the thermohaline circulation variability and that of Karnauskas et al. (2009) where sea surface temperature tendencies were focused on. However, to date, there have been no studies with the purpose of assessing if these global climate models were able to properly represent the mean hydrography of the ocean, whether global or regional, and which ones were more accurate.

Due to their seasonality nature, upwelling systems are very sensitive to climate change (Holt et al., 2010). It is of high interest to try to assess the impacts of climate change on the hydrography and circulation of these areas, because such changes may have consequences on the respective ecosystem (Pauly and Christensen, 1995). In order to do so, one needs an ocean model with a good horizontal and vertical resolution, and reliable atmospheric conditions to use as forcing. In what concerns the latter, with the IPCC future scenarios and the several CGCM simulations at our disposal, if we are able to obtain good results regarding the present climate, we can postulate that the same configuration and forcing must be reasonable for applying climate scenarios. One of the most recent works under this scope and for this region is that of Miranda et al. (2012), who used a regional climate model to force a ROMS configuration, and assessed the impacts on the hydrography of the coastal waters and offshore the Iberian Peninsula. Our approach is different in the sense that, before applying a future climate scenario to the ocean model (chapter 6), we first evaluate the performance of several CGCMs for the present climate and assess their differences, rather than choosing only one CGCM as forcing for the ocean model. In this way, we are aiming at finding the most adequate regional atmospheric forcing, both present and future simulations.

Hence, the present work consists in a sensitivity study aiming at the evaluation CGCMs as forcing in regional ocean simulations, with focus on FD (although sometimes extending to the Eastern North Atlantic Basin or the North Atlantic), for the present climate. To achieve this, the study is divided into two distinct parts. In the first part (section 5.3), the

output of nine CGCMs is analyzed regarding the variables needed to force ROMS. This is carried out in two ways: an analysis of difference fields between every CGCM and COADS, for every variable; and through the computation of the RMSE between each CGCM and COADS, for every variable (section 5.3.9). In the second part (section 5.4), two of the CGCMs with the highest RMSE relative to COADS are set as surface forcing for two ROMS runs, with the purpose of assessing the range of uncertainty comprised in this set of CGCMs. In addition, two other ROMS simulations are carried out: one forced with COADS, which serves as the control run; the other forced with the average of the nine CGCMs — the ensemble mean. The ultimate goal of the sensitivity study is to find the most suitable forcing for this region and, hence, the one that should be used to evaluate ocean climate change based on future climate scenarios.

5.2 Data and Methodology

5.2.1 Forcing variables

The variables needed to force ROMS, which comprise the COADS climatology and which will be compared for each CGCM, are the following: sea level pressure (SLP, in Pa); surface air temperature (SAT, in ^oC), radiation fluxes (longwave, shortwave and net heat balance, the latter including latent and sensible heat transfer — SW, LW and NH, respectively, in $W\ m^{-2}$), water flux into ocean (evaporation minus precipitation — E-P, in $mm\ d^{-1}$ — including the discharge of the world main rivers), sea surface temperature (SST, in ^oC), sea surface salinity (SSS), wind stress (zonal and meridional components — Tx and Ty, in $N\ m^{-2}$); and specific humidity (SH, in $g\ kg^{-1}$), which will only be analyzed in the RMSE study. These variables are inter-compared through difference fields between each CGCM and COADS, and through the RMSE computed for FD, also between each CGCM and COADS.

5.2.2 Climatologies

The climatology used for both the CGCM inter-comparison and the ROMS control run is the Comprehensive Ocean and Atmosphere Data Set (COADS). COADS has been, by excellence, the used climatology for such regional ocean modeling studies (e.g. Marchesiello et al., 2001) and this data set is described in section 2.2.1.

The CGCM sea level pressure is compared with the National Center for Environmental Prediction (NCEP/NCAR) Reanalysis. The NCEP/NCAR Reanalysis project uses a state-of-the-art analysis/forecast system to perform data assimilation using past data from 1948 to the present (Kalnay et al., 1996).

5.2.3 CGCMs

The IPCC model data for this study were retrieved from the World Climate Research Programme (WCRP — http://www.wcrp-climate.org/) through the Coupled Model Intercomparison Project phase 3 (CMIP3) archived at the Program for Climate Model Diagnosis and Inter-comparison (PCMDI) (http://www-pcmdi.llnl.gov/ipcc/about_ipcc.php). This program has made available a multi-model dataset of outputs from over 20 GCMs, for every IPCC future climate change scenario, as well as the past and present climate, plus several runs for each model that started from different initial conditions (Meehl et al., 2007).

From the large PCMDI database, we selected nine models, chosen because they included not only an atmospheric model but also an ocean module to provide ocean forcing variables (coupled models — CGCMs). CGCMs also have ocean temperature and salinity vertical profiles, but preliminary analyses have shown that values were very far from the World Ocean Atlas 2009 (Antonov et al., 2010; Locarnini et al., 2010) and, therefore, not suited as vertical initial and boundary conditions. Instead, the WOA09 is used in the CGCM-forced runs, as it is in the control run. The models are listed in Table 5.1, where their name, origin and spatial resolution are presented. The CGCM output is monthly averaged for each variable (described in section 5.2.1), and for the same period of COADS (1945-1989) (see section 2.2.1). The approach is to run climatological simulations; hence, the daily values of all variables for period 1945-1989 are averaged into a data set of monthly means. Therefore, each ROMS run year is forced with the same monthly values.

For the computation of the ensemble mean, which consists in the average of all the CGCMs considered in this study, each CGCM climatology is gridded to $2.5^o \times 2.5^o$ ($1.25^o \times 1.25^o$ for the ocean) by means of bicubic interpolation, after the application of a land mask. Finally, a plain averaging of the nine CGCMs is computed for every variable.

5.2.4 ROMS Configuration

ROMS setup is similar to that of chapter 2, that is, a climatological run, and the domain is FD. All runs have WOA09 as initial and boundary conditions, and each of the four runs has the respective surface forcing, as described in the previous section. SST and SSS undergo the same heat correction as in the climatological run to take into account thermal feedback at the ocean surface and to avoid numerical drift, using the CGCM monthly means. Each run final 5 years of output is averaged and we thus obtain climatological values.

5.2.5 Error Computation

As previously carried out in chapter 3, in the evaluation of the CGCMs the root mean square error (RMSE) (Wilks, 2006) is computed in order to quantify how close the CGCM

Institution	Model designation	Country	Land Resolution	Ocean Resolution	Reference
Canadian Centre for Climate Modelling and Analysis (CCCMA)	CGCM version 3 (t47)	Canada	$3.75^o \times 3.71^o$	$1.88^o \times 1.86^o$	Flato et al. (2000)
Centre National de Recherches Météorologiques (CNRM)	CM version 3	France	$2.81^o \times 2.79^o$	$2^o \times 1^o$	Salas-Mélia et al. (2005)
Center for Climate System Research, University of Tokyo (CCSR), the National Institute for Environmental Studies (NIES) and the Frontier Research Center for Global Change (FRCGC)	Model for Interdisciplinary Research On Climate — medium resolution (MIROC medres)	Japan	$2.81^o \times 2.79^o$	$1.41^o \times 1^o$	Hasumi and Emori (2004)
Commonwealth Scientific and Industrial Research Organisation (CSIRO)	Mark 3.5 (Mk3.5)	Australia	$1.88^o \times 1.87^o$	$1.88^o \times 0.93^o$	Gordon et al. (2002)
Geophysical Fluids Dynamics Laboratory (GFDL-NOAA)	CM version 2.0	USA	$2.5^o \times 2^o$	$1^o \times 1^o$	Delworth et al. (2006)
Goddard Institute for Space Studies (GISS-NASA)	E-R model	USA	$5^o \times 4^o$	$5^o \times 4^o$	Russell et al. (1995)
Meteorological Research Institute (MRI)	CGCM version 2.3.2	Japan	$3.75^o \times 2.5^o$	$1.25^o \times 1.25^o$	Yukimoto et al. (2001)
Met Office (UKMO)	Hadley Center for Climate Prediction and Research climate model version 3 (HadCM3)	UK	$1.88^o \times 1.87^o$	$1^o \times 1^o$	Pope et al. (2000)
Max Planck Institute (MPI)	European Centre / Hamburg Model version 5 (ECHAM5)	Germany	$2.81^o \times 2.79^o$	$2.5^o \times 2^o$	Roeckner et al. (2003)

Table 5.1: CGCM designation, institution, country of origin, horizontal resolution and literature reference.

output is to COADS (the considered reference) as forcing:

$$RMSE = \sqrt{\frac{1}{N}\sum_{i}(M_i - C_i)^2} \tag{5.1}$$

where i is each grid point, M_i is CGCM output for grid point i, C_i is COADS output for grid point i and N is the number of grid points.

5.3 CGCM Inter-comparison

The CGCM inter-comparison is carried out in two complementary ways: first, winter and summer difference fields between each variable and the climatological correspondent, for each CGCM, are presented. Most fields concern the entire North Atlantic (Figure 1.1 a), to enable the analysis of the complete patterns, others concern an enlarged area around FD, that is called in this work Eastern North Atlantic Basin (ENAB) (Figure 1.1 b) for simplification. This domain is used when a more detailed analysis of the mean field is justified. Second, the seasonal cycle of each variable, averaged over FD (Figure 1.1 c), as well as the respective RMSE, are analyzed.

5.3.1 Climatological Mean Fields

Figures 5.1 and 5.2 show the climatological mean fields of each variable for winter and summer, respectively (NCEP for the case of SLP, COADS for all the others). The typical winter and summer patterns are evident in these fields: in SLP (Figures 5.1,5.2 a), the typical winter dipole between the Iceland Low and the Azores High, as well as the northward migration of the former in summer; the northward summer warming in SAT (Figures 5.1,5.2 b); prevailing precipitation in winter and evaporation in summer (Figures 5.1,5.2 e); the Earth's heat loss in winter and heat gain in summer (Figures 5.1,5.2 g-i); and the less seasonal varying in the ocean (Figures 5.1,5.2 c,d). Finally, close to the coast, the winds show prevailing northerly flow in summer, consistent with the presence of the Azores High, while in winter winds are in general weak and often with no meridional component, contrary to what could be expected from the SLP winter conditions, prone for the passage of low-pressure systems that are characterized by southerly/southwesterly winds. This is an important aspect of COADS, that is discussed throughout this work.

5.3.2 Sea Level Pressure (SLP)

The pressure fields are the main driving mechanisms of the entire climate system. Figure 5.3 shows the differences between each model and the NCEP/NCAR reanalysis for winter. Figure 5.4 presents the same but for summer. In winter, all models overestimate SLP over Greenland and the majority does so also at midlatitudes (30-40^{o}N), with CCCMA, CNRM and CSIRO (Figure 5.3 a,b,d) presenting this positive difference up to the

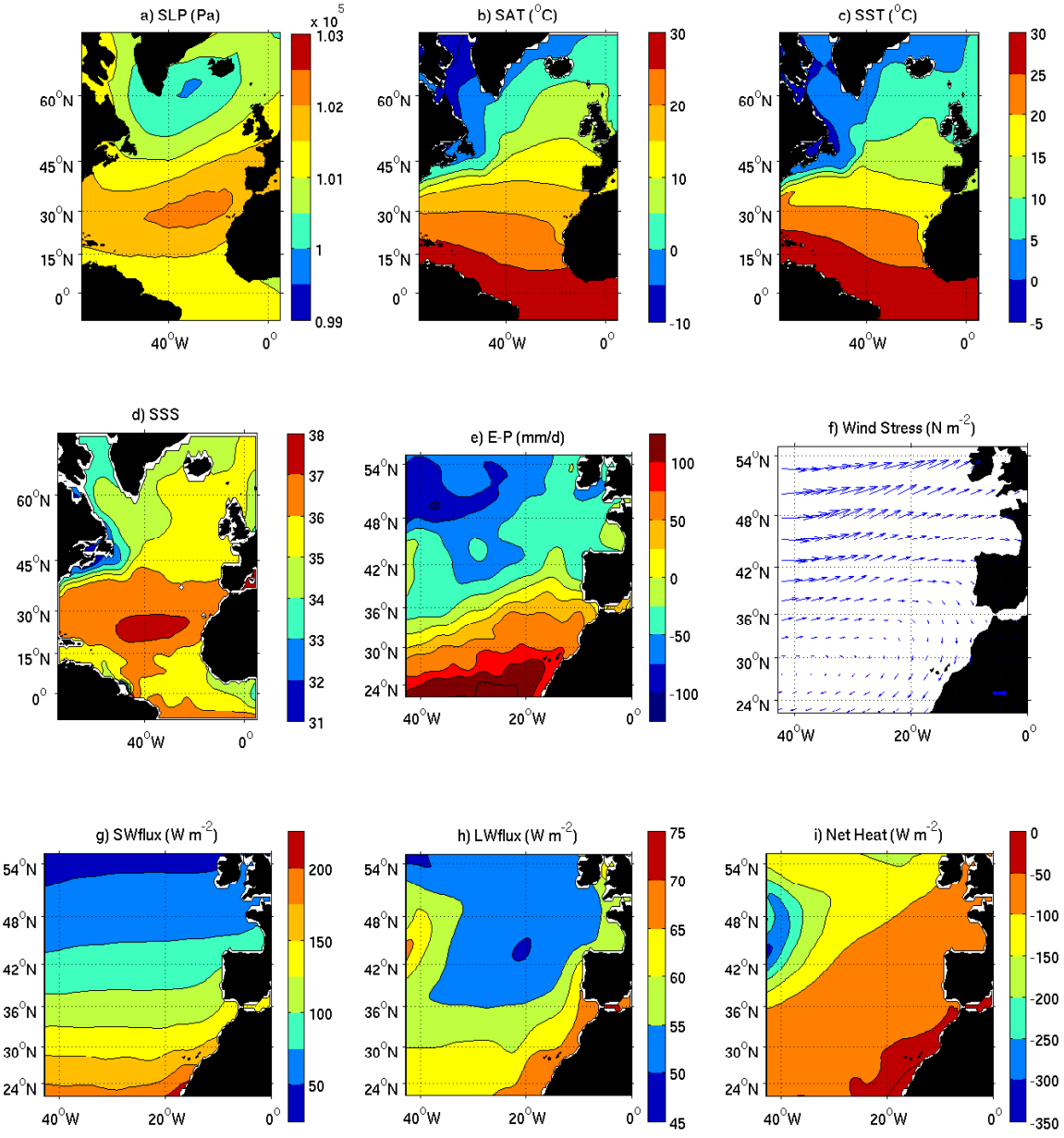

Figure 5.1: Winter COADS mean fields for forcing ROMS: (a) SLP (Pa); (b) SAT (^oC); (c) SST (^oC); d) SSS; e) E-P ($mm\ d^{-1}$); f) Wind Stress ($N\ m^{-2}$) (arrow scale indicates 0.1 $N\ m^{-2}$); (g) SW Flux ($W\ m^{-2}$); (h) LW Flux ($W\ m^{-2}$); (i) Net Heat Flux ($W\ m^{-2}$).

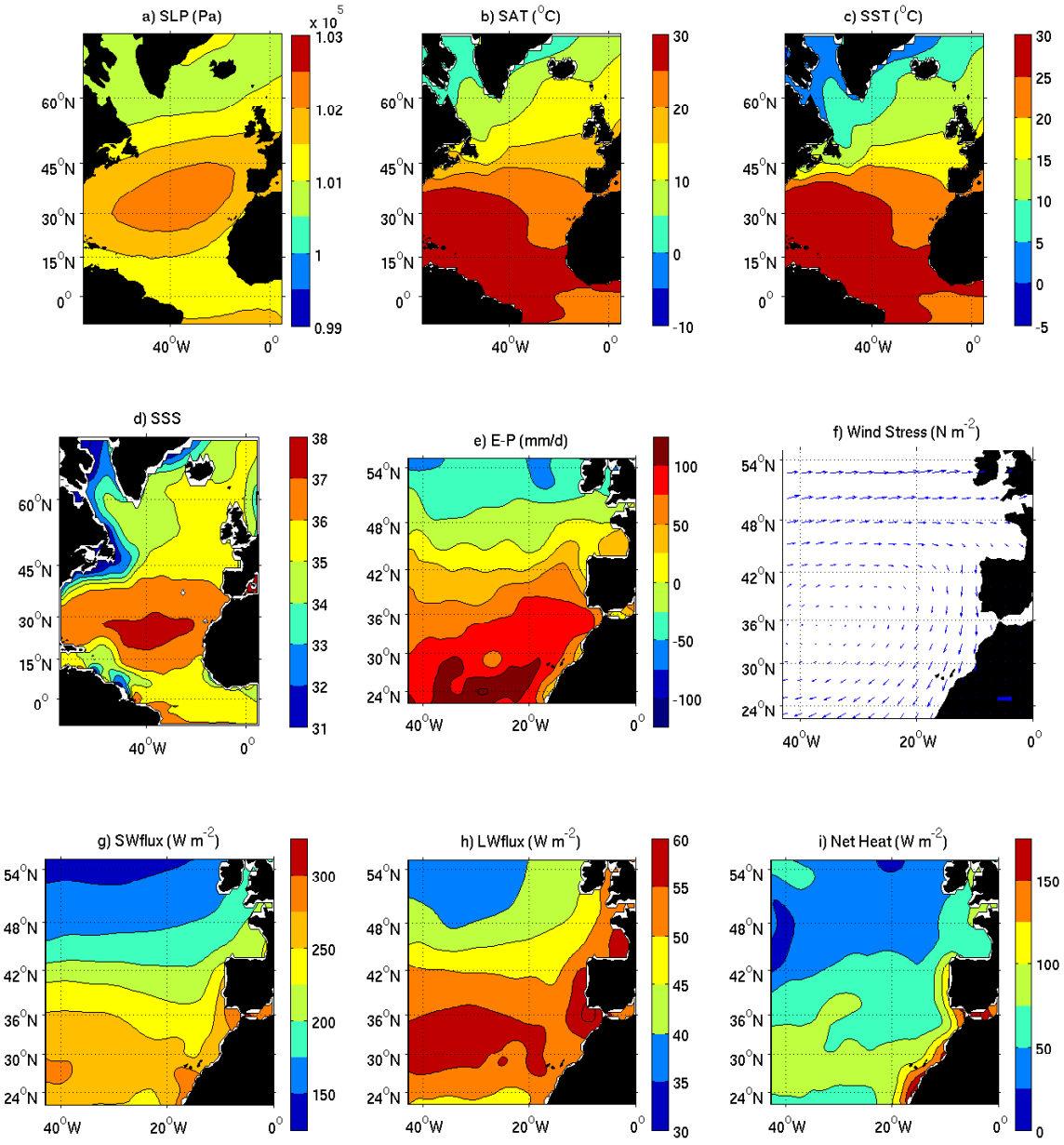

Figure 5.2: Same as Figure 5.1 but for summer.

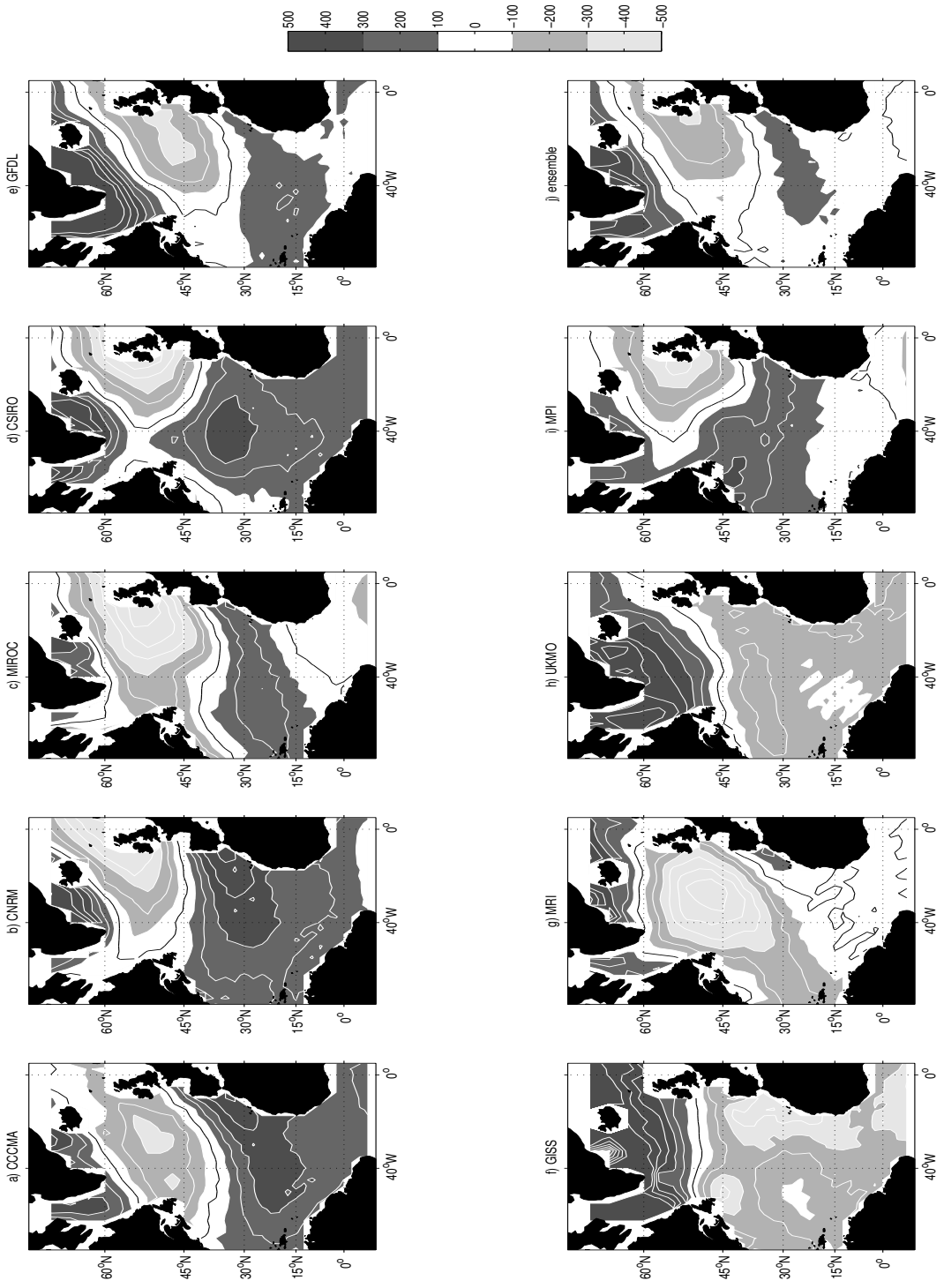

Figure 5.3: Differences of SLP (Pa) between each CGCM, including the ensemble mean, and the NCEP reanalysis for winter in the North Atlantic.

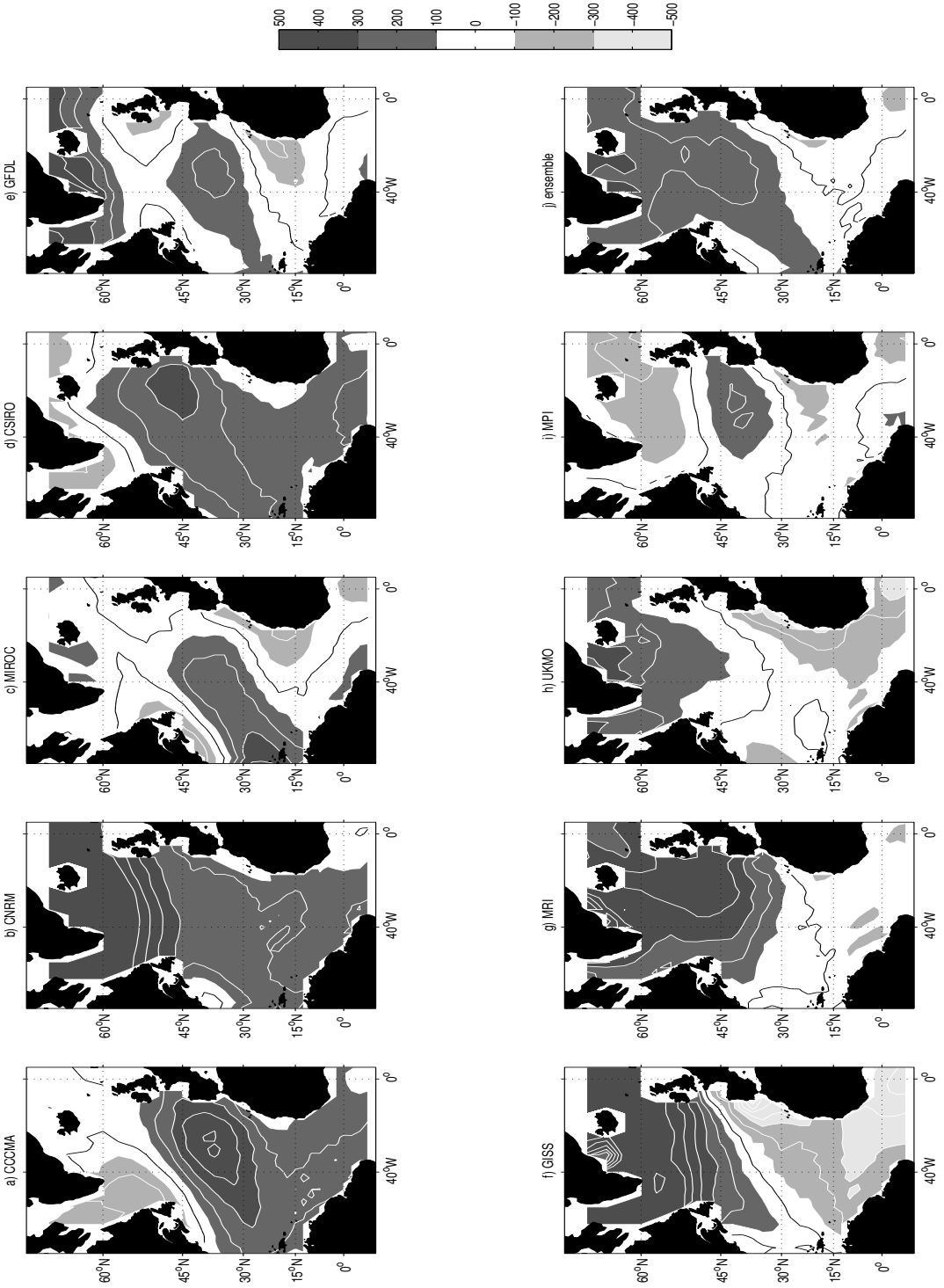

Figure 5.4: Same as Figure 5.3 but for summer.

equator. The exceptions are GISS, MRI and UKMO (Figure 5.3 f-h), which present negative differences for this region, the typical location of the Azores High. There is also a general underestimation of pressure over Great Britain. Even for a variable that presents a more or less steady seasonal behavior such as SLP, the results vary greatly from model to model. In the end, the ensemble (Figure 5.3 j) presents the lowest differences when comparing to observations, with a tendency to intensify the high-pressure centers and attenuate the low-pressure centers in relation to the observed values. In summer (Figure 5.4), the positive differences are displaced northward, as is the Azores High center; therefore the models overestimation remains related to the same phenomenon. This general positive difference is the main feature of the multi-model ensemble mean (Figure 5.4 j). In the area delimited by the coasts of Europe, Africa and South America, the general signal is negative, especially in GISS and UKMO (Figure 5.4 f,h), with the exception of CCCMA, CNRM and CSIRO (Figure 5.4 a,b,d), which roughly overestimate SLP throughout the North Atlantic. These models were already the exception in winter.

5.3.3 Surface Air Temperature (SAT)

SAT is also a variable of consequence to the ocean surface in terms of air-sea interaction. In addition, it is the parameter on which climate change is most strikingly reflected. Figure 5.5 shows the differences between each model and COADS for winter, Figure 5.6 the same for summer. It is interesting to notice that the majority of models overestimates SAT over the Gulf Stream and most of these all along the North Atlantic Current path. This is accompanied by an underestimation of SAT around Greenland. Moreover, SAT within the subtropical gyre tends to be lower than COADS (Figure 5.5 c,e,i). These are the main features that are reflected in the ensemble (Figure 5.5 j). CSIRO and UKMO (Figure 5.5 d,h) show warmer SATs along the western coasts of Europe and Africa, while GISS and MPI (Figure 5.5 f,i) overestimate SAT near the equator. In summer (Figure 5.6), the overestimation over the Gulf Stream and the North Atlantic Current is less evident; on the contrary, there are some models that present lower SATs than the observations. There is higher discrepancy between models in this season. The main differences, reflected on the corresponding ensemble, are, again, an underestimation in the region of the subtropical gyre and an overestimation near the equator off the African coast. As far as the Iberian Peninsula coast is concerned, SAT is less than 1^oC lower in winter and less than 1^oC higher in summer, which may be due to the influence of the SAT overland.

5.3.4 Sea Surface Temperature (SST)

The differences of SST between climatology and models (Figures 5.7 and 5.8) present some similarities to those of surface air temperature, namely the tendency of the models to underestimate SST in the region of the subtropical gyre. However, the models are less coincidental. In general, in winter (Figure 5.7) there is overestimation of SST in the Gulf Stream and underestimation in the region of the subtropical gyre. SST around Greenland is underestimated by the majority of models, and some of them extend this

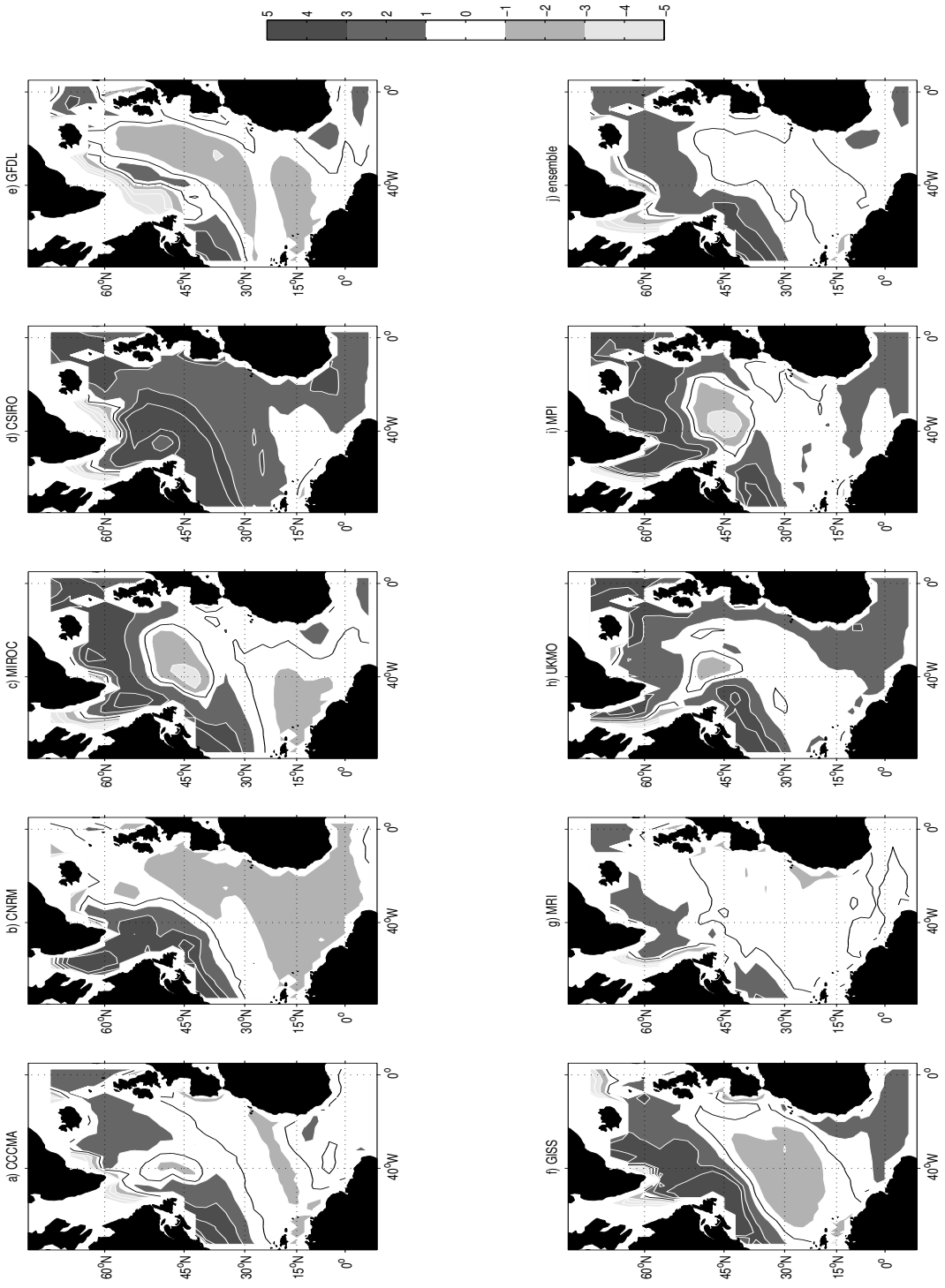

Figure 5.5: Differences of SAT (^oC) between each CGCM, including the ensemble mean, and COADS for winter in the North Atlantic.

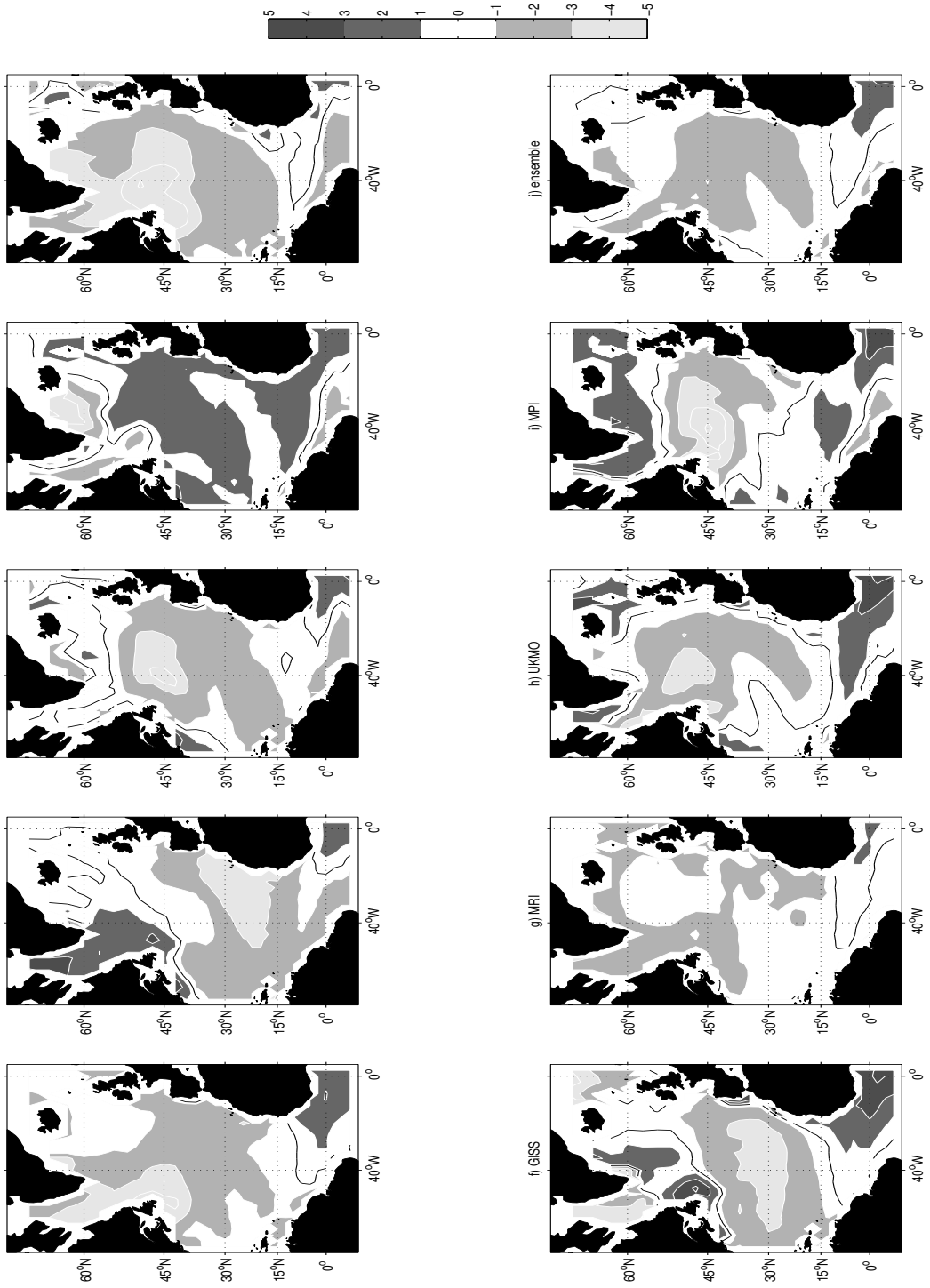

Figure 5.6: Same as Figure 5.5 but for summer.

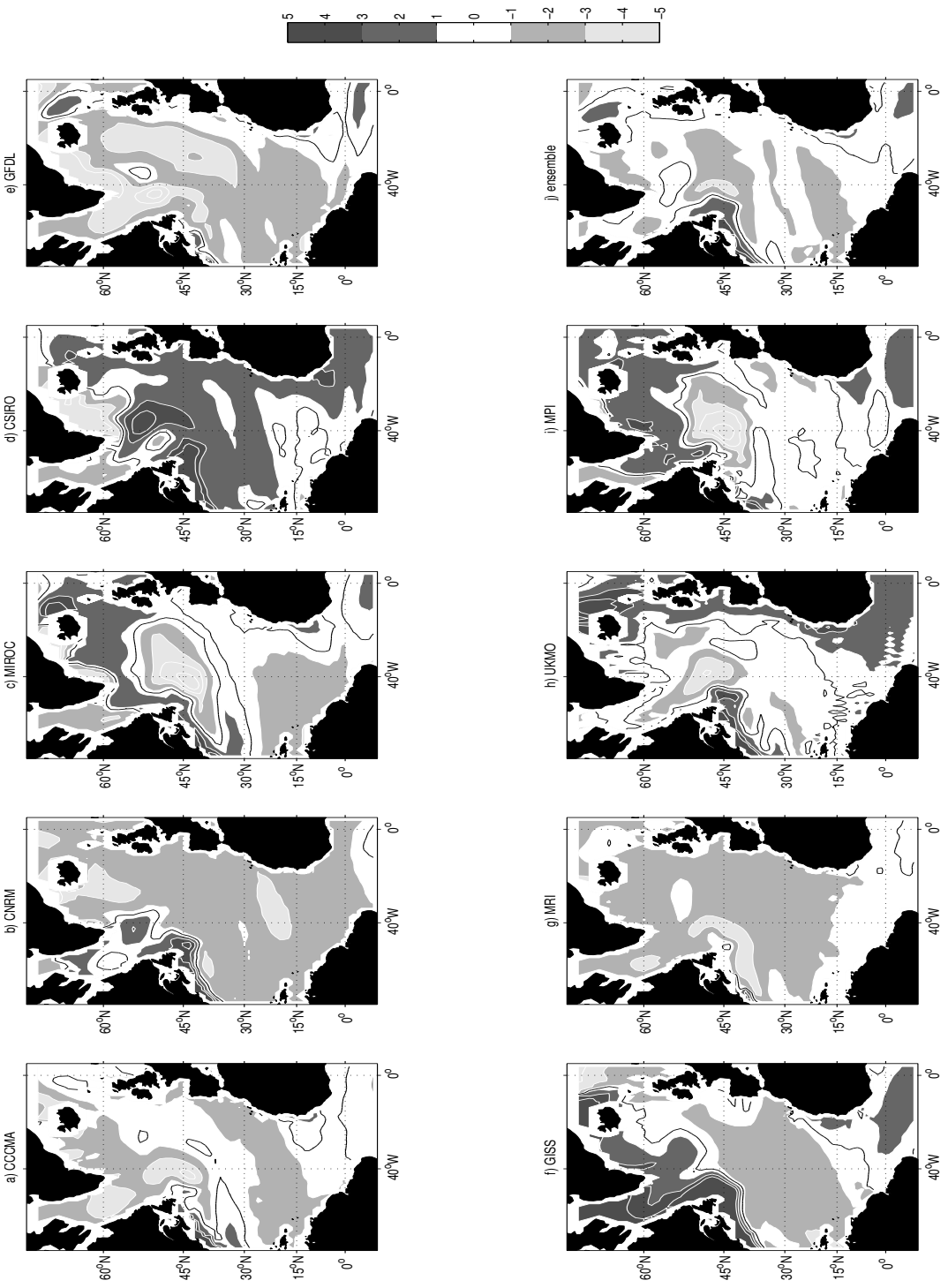

Figure 5.7: Differences of SST (^oC) between each CGCM, including the ensemble mean, and COADS for winter in the North Atlantic.

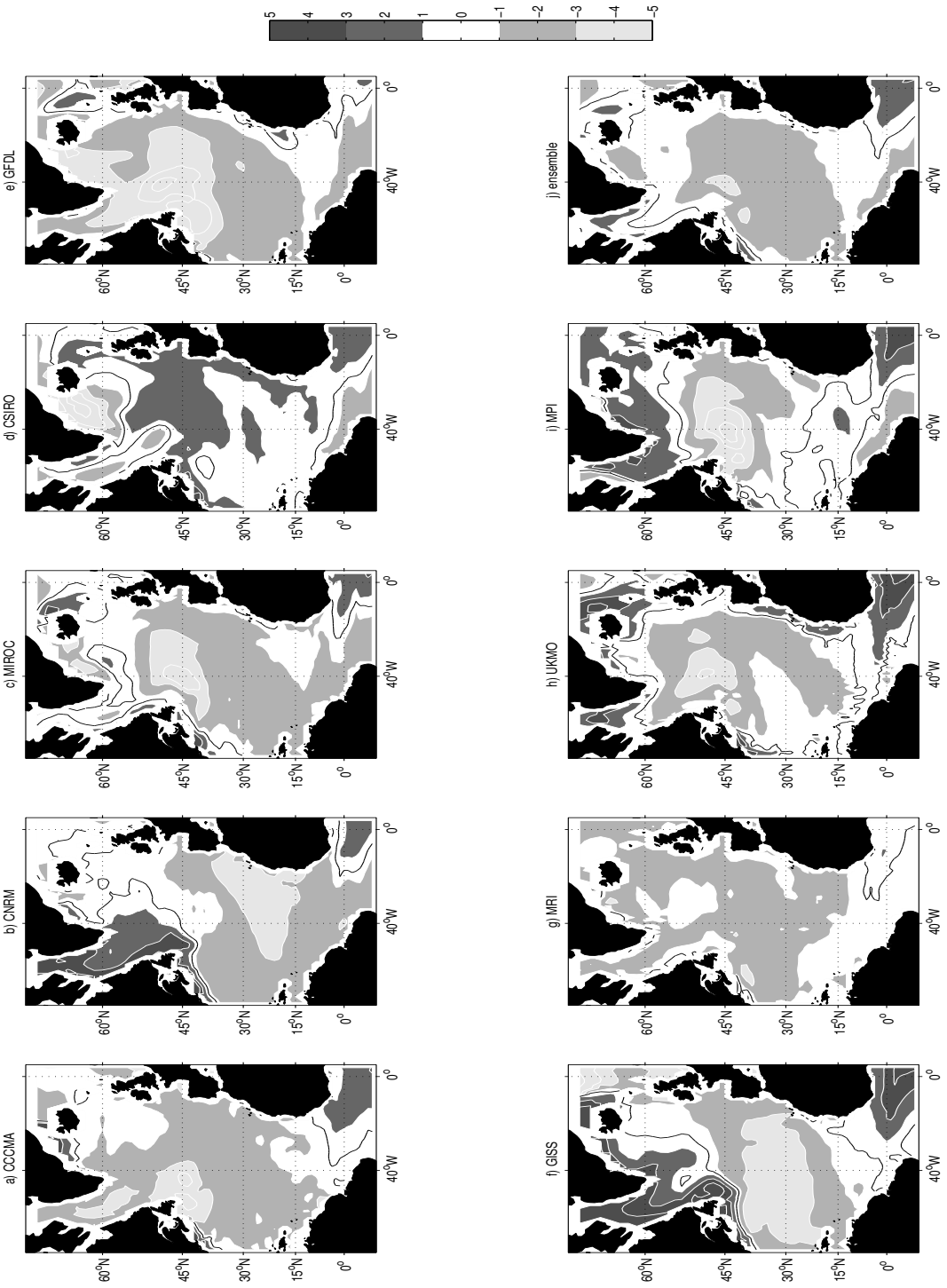

Figure 5.8: Same as Figure 5.7 but for summer.

negative difference along the coast of America, contouring the positive anomaly of the Gulf Stream (Figure 5.7 a-c,e,g). The differences change signal around the equator. The ensemble (Figure 5.7 j) shows a general negative difference of 1-3^oC, with the exception of the area of the Gulf Stream. In summer (Figure 5.8), this pattern is even more generalized and fewer models present the overestimation over the Gulf Stream. Observing the eastern basin, the ensemble results are better for winter than for summer: the differences in relation to COADS are of less than 1^oC in winter and 1 to 2^oC in summer.

5.3.5 Sea Surface Salinity (SSS)

Salinity is the variable that models find the hardest to reproduce. It is a parameter harder to calibrate, since there are no satellite products on which to validate. It is rapidly influenced by the precipitation-evaporation balance and river discharge and it depends strongly on density. Due to the SSS weak seasonality (salinity distribution does not vary substantially throughout the year), we present results for winter only (Figure 5.9). The discrepancy between models is very high, although the differences of between models and COADS are somewhat similar to those of SST (Figures 5.7 and 5.8): overestimation of SSS in the Gulf Stream, underestimations along the North Atlantic Current (Figure 5.9 a,c,h,i), in the region of the subtropical gyre (Figure 5.9 a,f,g) and around Greenland (Figure 5.9 a,d,e). There is also an overall lower SSS near the equator as reproduced by the models, reflected on the ensemble (Figure 5.9 j). Once again, the ensemble succeeds in minimizing the differences of individual models in relation to observed data, as it presents the lowest differences when comparing to COADS. Off the Iberian Peninsula, differences are less than 0.5.

5.3.6 Evaporation Minus Precipitation (E-P)

Before entering further into this variable, it is necessary to properly define it. Evaporation minus precipitation is a water flux input measurement. When positive, evaporation is higher than precipitation (negative water flux into ocean), and vice-versa for negative values. In what COADS is concerned, it consists only of an atmospheric water flux, but for the CGCMs, the river input is also taken into account. Furthermore, the differences between models and climatology do not have a straightforward meaning. Positive differences, for instances, can mean the model shows stronger evaporation than COADS or that the fluxes at that point are reversed. Therefore, we choose to present results for the eastern basin only (Figures 5.10 and 5.11). There is no river making the difference in water flux; here the differences reflect essentially the ability of the models to well reproduce the precipitation/evaporation cycle. Models vary greatly between them. The highest differences are in winter (Figure 5.10), in the northwestern corner, typically the location of the North Atlantic Current, and also in the Bay of Biscay and off Great Britain, a region of strong and constant rains. In summer (Figure 5.11), there is a general low negative difference throughout the domain and the ensemble once again is able to minimize individual model differences.

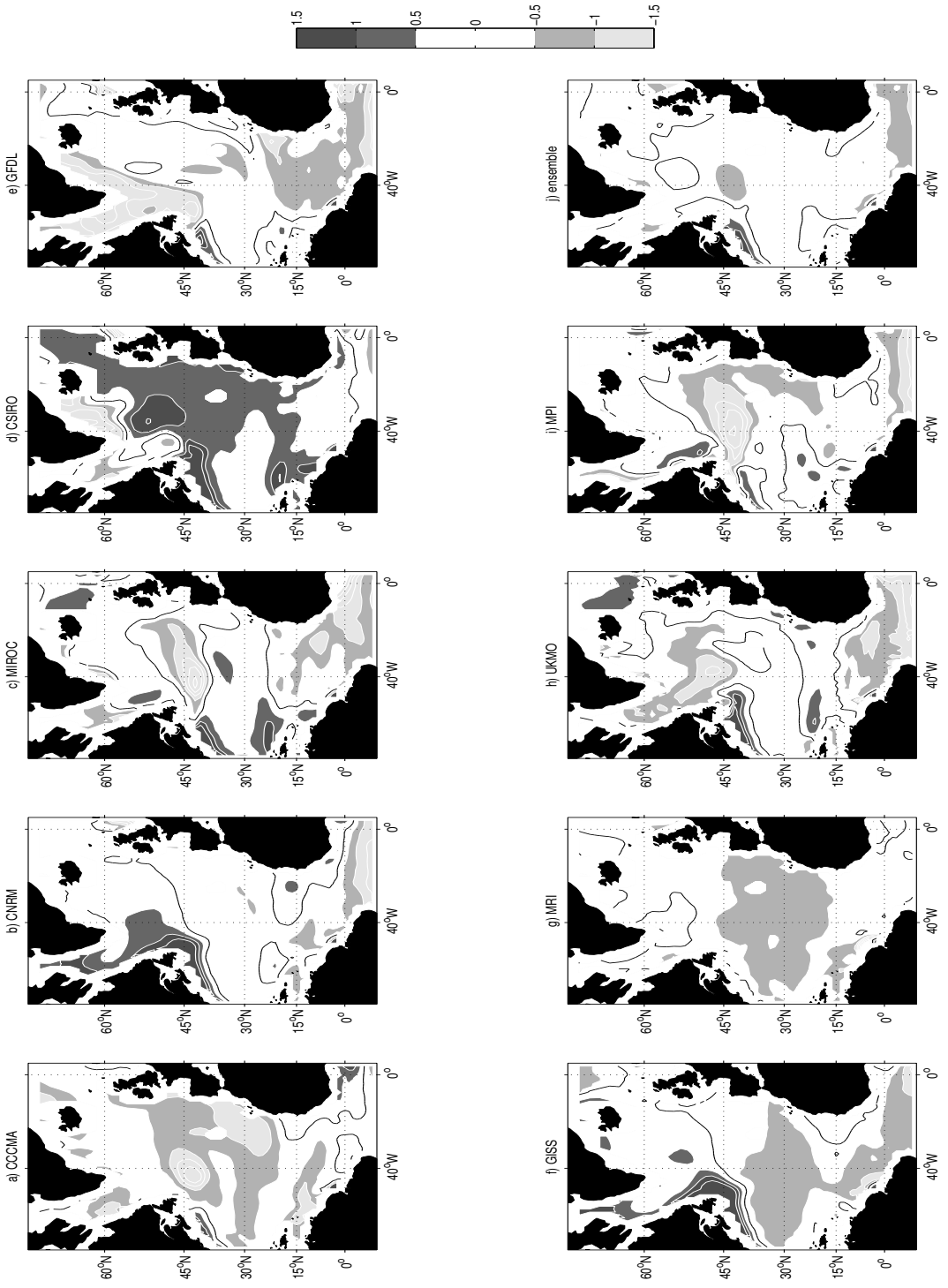

Figure 5.9: Differences of SSS between each CGCM, including the ensemble mean, and COADS for winter in the North Atlantic.

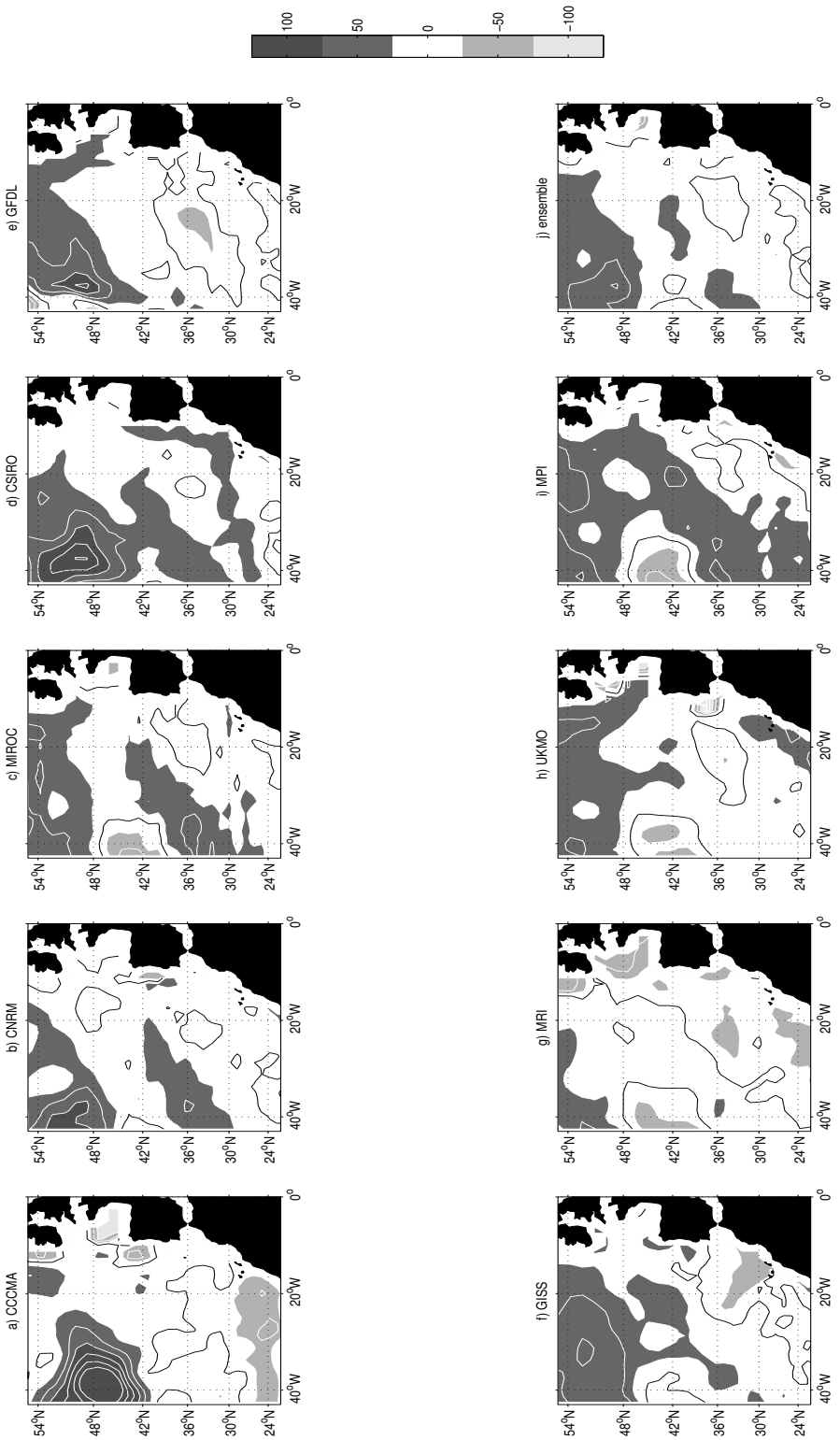

Figure 5.10: Differences of E-P ($mm\ d^{-1}$between each CGCM, including the ensemble mean, and COADS for winter in the ENAB.

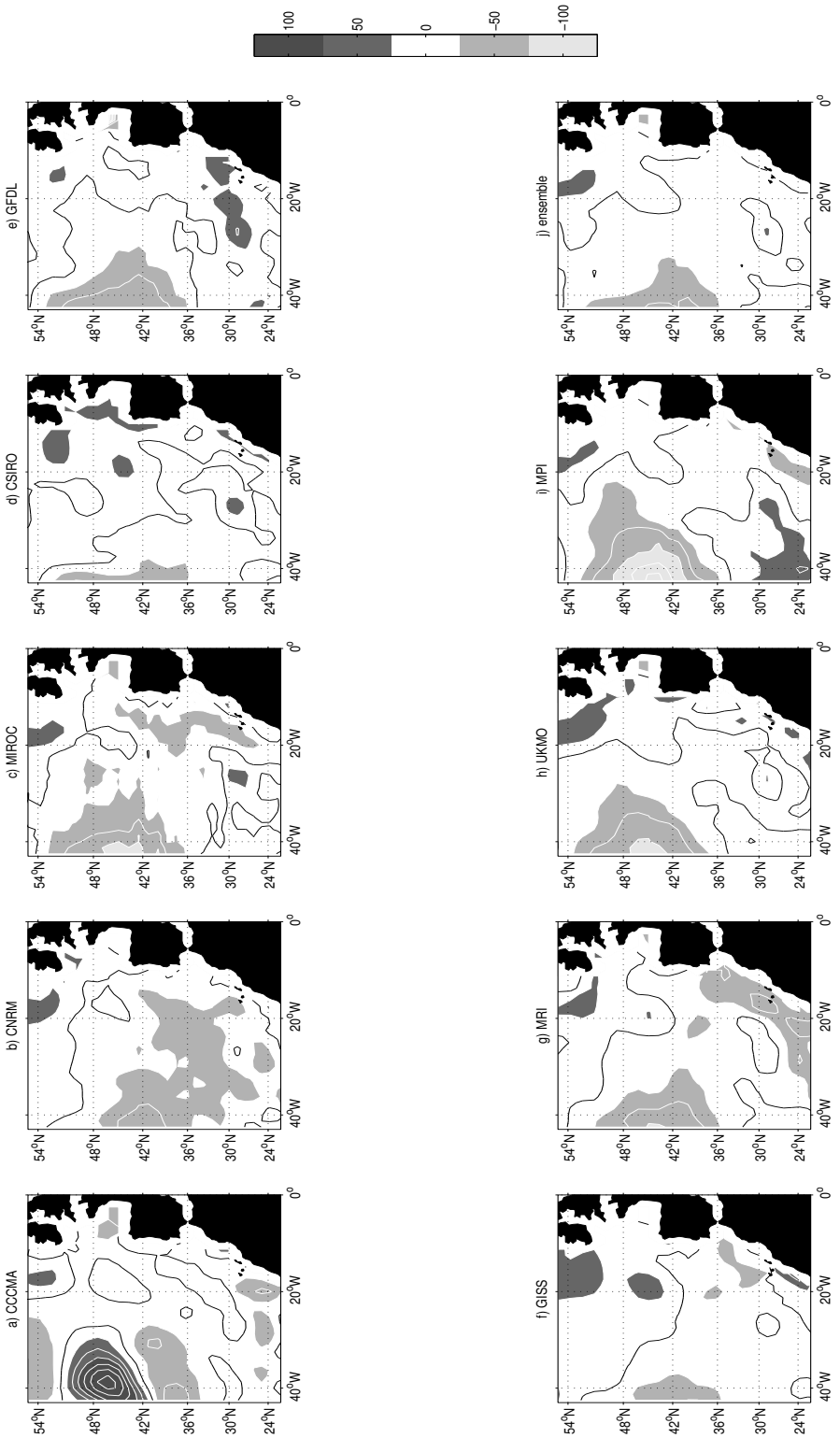

Figure 5.11: Same as Figure 5.10 but for summer.

5.3.7 Wind Stress

Figures 5.12 and 5.13 show the vectorial differences of wind stress between each model and COADS for winter and summer, respectively, once more for the eastern basin rather than the North Atlantic. Several models present strong differences near the coast (Figure 5.12 a,e,f; Figure 5.13 a,b,h) that can be accounted for by the vicinity of land and the land-sea shear due to thermal wind. In general, in winter (Figure 5.12), models show stronger northeastward winds north and west of the Iberian Peninsula than COADS. This difference is due to the fact that the COADS winds in winter, rather than being essentially southerly as expected from typical low-pressure systems in this season, are southward or with no meridional component. As for summer (Figure 5.13), the overall wind stress pattern is very similar to COADS, especially in the ensemble mean (Figure 5.13 j). In general, all models slightly overestimate southward wind stress along both coasts of the Iberian Peninsula and North Africa. Some models (Figure 5.13 a,c,e,i) intensify the Azores High circulation, seen in the northeastward difference to the north and the southwestward difference to the south.

5.3.8 Radiation Fluxes

Radiation fluxes are an important surface forcing and a relevant aspect to look at. Figure 5.14 shows the radiation fluxes difference fields between COADS and the multi-model ensemble mean for winter (upper row) and summer (lower row) in the ENAB. Radiation fluxes differ greatly from model to model and season to season. We chose to show for the basin and for the ensemble only because for these parameters the large-scale patterns are not so important as the local input. The left column concerns the incoming shortwave radiation flux (SW), the middle column the outgoing longwave radiation flux (LW) and the right column the net heat balance (NH). This balance is computed taking into account not only the SW and LW fluxes but also the latent and sensible heat fluxes, and the result is the downward minus upward balance. SW and LW fluxes (Figure 5.14 a,b,d,e) are fairly well represented by the ensemble mean in relation to COADS, with the exception of summer SW flux (Figure 5.14 d), underestimated by the ensemble in the entire domain. In respect to NH (Figure 5.14 c,f), the concordance between datasets is less agreeable. In winter, the ensemble overestimates NH up to 60 $W\ m^{-2}$ while in summer it presents lower values than COADS south of 36^{o}N and off the Iberian Peninsula by about 30-40 $W\ m^{-2}$. The much coarser model resolution and consequently the aggravated difficulty in reproducing latent and sensible heat may be a reason for this discrepancy.

5.3.9 CGCM Forcing Seasonal Cycles

The seasonal cycles of all variables, averaged over FD (Figure 1.1 c), are presented in Figure 5.15, superimposed to the COADS (control) cycle and the ensemble mean cycle. For each variable, the CGCM set covers a range of values; in some cases this range is wider (e.g. LW, SSS) than others (e.g. SW, NH). The performance of each CGCM relative to COADS

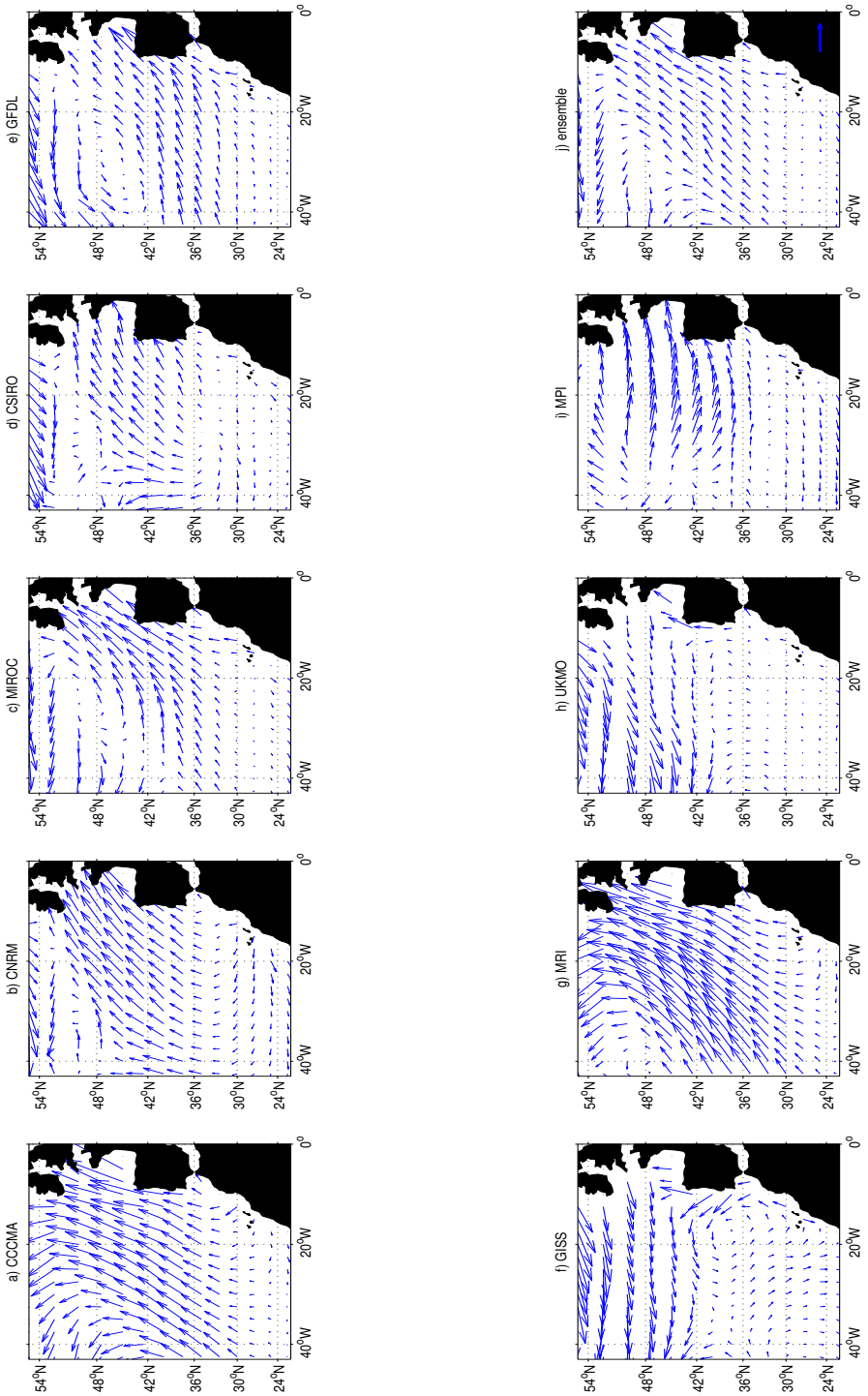

Figure 5.12: Differences of wind stress ($N\ m^{-2}$) between each CGCM, including the ensemble mean, and COADS for winter in the ENAB (arrow scale indicates 0.1 $N\ m^{-2}$).

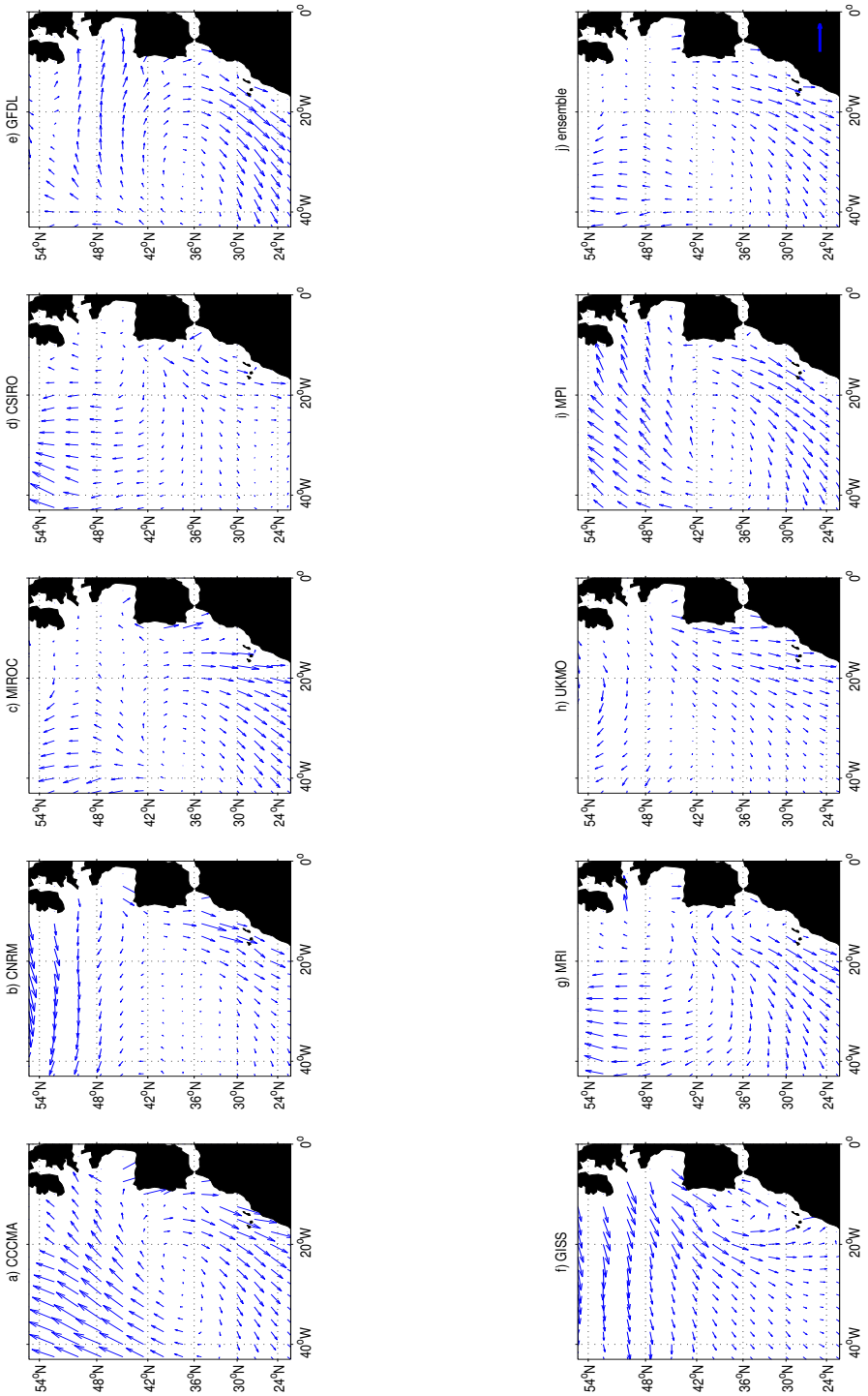

Figure 5.13: Same as Figure 5.12 but for summer.

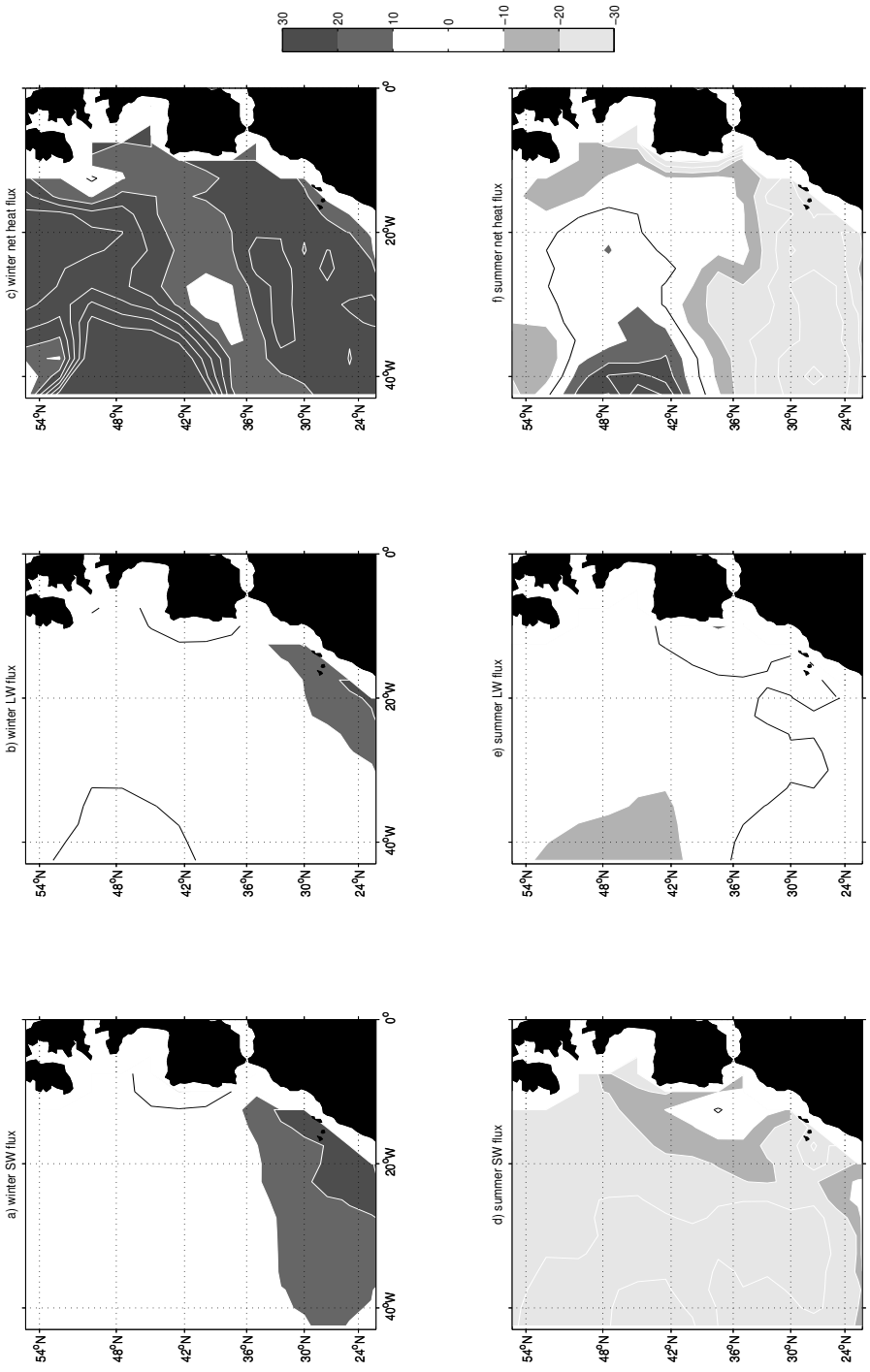

Figure 5.14: Differences of radiation flux between the ensemble mean and COADS for winter (a-c) and summer (d-f) in the ENAB. (a,d) Shortwave flux; (b,e) Longwave flux; (c,f) Net heat flux ($W\ m^{-2}$).

depends on the variable. For instances: CNRM overestimates SLP and underestimates LW, but compares well in Ty and E-P; GFDL underestimates SAT and SST, but agrees well in SW and NH; GISS underestimates Tx and overestimates E-P, but is adequate in SSS. Overall, we cannot state from a first observation which model is the closest to COADS.

Figure 5.16 presents the RMSE of each CGCM relative to COADS, for every variable. RMSE varies strongly seasonally, and we confirm the observations of Figure 5.15, that is, the good or bad performance of a CGCM depends on the variable. It is not possible to draw a best and a worst model in comparison to COADS. Yet, the ensemble mean presents consistently low errors for all variables, although it is rarely the one with the lowest RMSE. A few CGCMs stand out as having high RMSEs for several variables. For instances: CSIRO and GFDL for SAT and E-P; CNRM for SLP and LW; CCCMA and MRI for Tx and Ty.

This inter-comparison does not allow us to clearly identify one CGCM as the best for all variables and disregard all the others. This is why we choose to force ROMS with

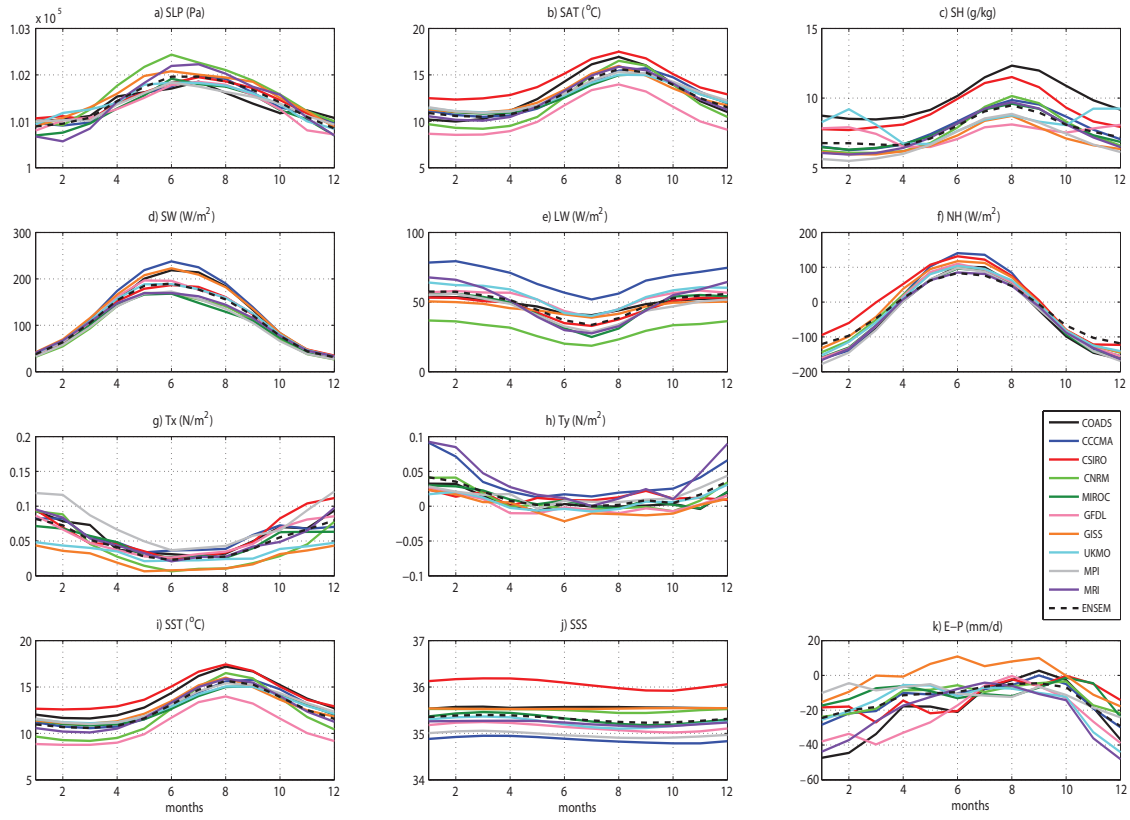

Figure 5.15: Seasonal evolution of (a) SLP (Pa); (b) SAT (^oC); (c) SH ($g\ kg^{-1}$); (d) SW ($W\ m^{-2}$); (e) LW ($W\ m^{-2}$); (f) NH ($W\ m^{-2}$); (g) Tx ($N\ m^{-2}$); (h) Ty ($N\ m^{-2}$); (i) SST (^oC); (j) SSS; (k) E-P ($mm\ d^{-1}$) (see text for the acronyms) for each considered CGCM (see Table 5.1), as well as their mean (ENSEM) and the control run forcing (COADS), averaged over the entire domain.

two CGCMs that will encompass all the others in terms of the variability range of the ensemble. Bearing this in mind, and given the differences among CGCMs from variable to variable, we focus on one of the ocean variables: SSS (Figures 5.15, 5.16 j), which is difficult to reproduce in coarse resolution models. The two models that stand out in terms of overestimation and underestimation are CSIRO and CCCMA, respectively. Differences between CSIRO and COADS are about +0.5 to +0.8 (Figure 5.15 j), with a RMSE of approximately 0.28 (Figure 5.16 j), and CSIRO differences from the ensemble mean are roughly +0.7 throughout the year. CCCMA, on the other hand, differs from COADS by -0.5 to -0.8 and from the ensemble mean by approximately -0.5, while RMSE ranges from 0.19 to 0.25. The choice of CCCMA instead of, for instances, MPI, which also presents a high RMSE regarding SSS, is based on the relatively high RMSE that CCCMA also presents for LW, Tx and Ty; moreover, for SW and NH it also differs substantially from the ensemble mean.

Thus, the following section is an analysis of four ROMS runs with similar configurations

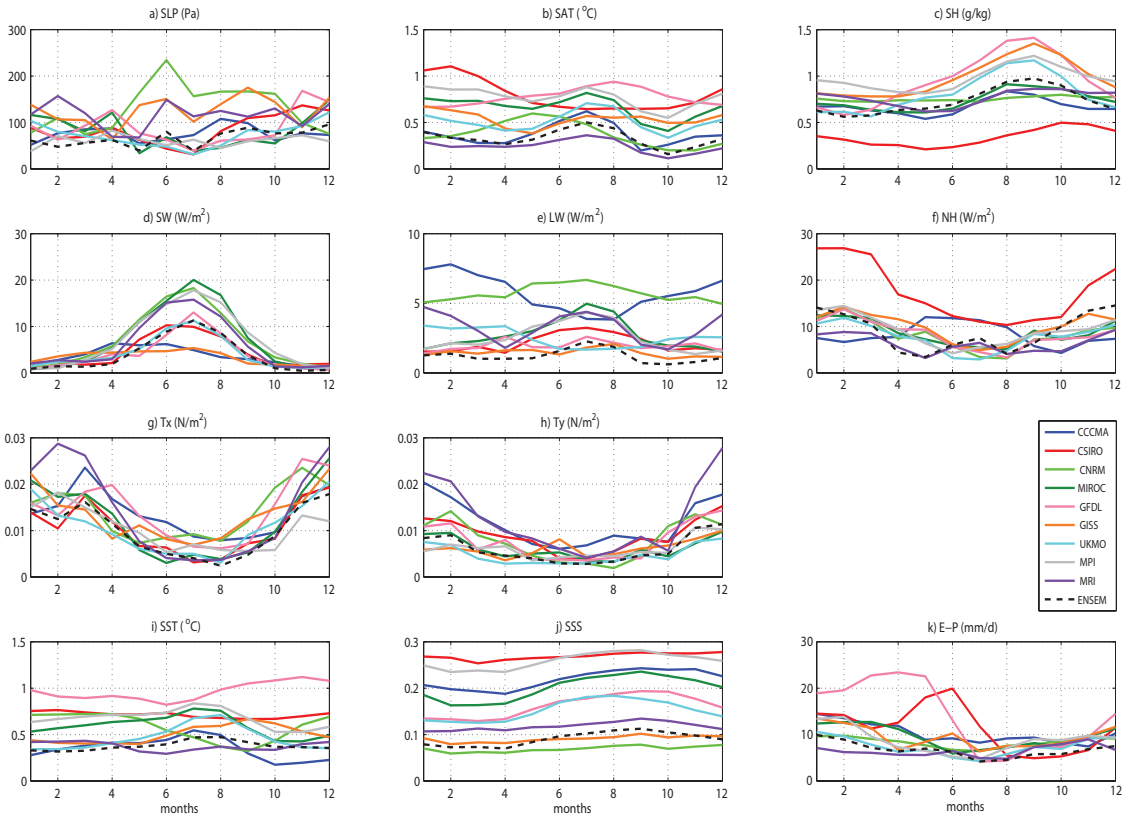

Figure 5.16: Monthly RMSE of (a) SLP (Pa); (b) SAT (^oC); (c) SH ($g\ kg^{-1}$); (d) SW ($W\ m^{-2}$); (e) LW ($W\ m^{-2}$); (f) NH ($W\ m^{-2}$); (g) Tx ($N\ m^{-2}$); (h) Ty ($N\ m^{-2}$); (i) SST (^oC); (j) SSS; (k) E-P ($mm\ d^{-1}$) (see text for the acronyms) between each considered CGCM and the control run forcing (COADS), including their mean (ENSEM), averaged over the entire domain.

and applied to the same domain, but each forced at the surface with a different dataset: (a) COADS, which will be the control run; (b) CCCMA; (c) CSIRO; and (d) the ensemble mean, henceforth ENSEM.

5.4 ROMS Runs

ROMS output of the four simulations is analyzed by means of surface fields and vertical slices of the ocean upper levels at key regions in the domain, focusing on the hydrography and circulation. Some seasonal characterization is also carried out through Hovmöller diagrams. For a better assessment, some of the results are presented as differences between each CGCM-forced run and the COADS-forced (control) run. Results will be shown as monthly means of the last 5 years of simulation. For simplification, ROMS runs will be identified as follow: the COADS-forced run will be referred to as R_COADS, and similarly R_CCCMA, R_CSIRO, R_ENSEM.

The analysis will be focused on FD. Less attention will be paid to the regions near the boundaries, namely the Bay of Biscay and the Morocco northwestern coast.

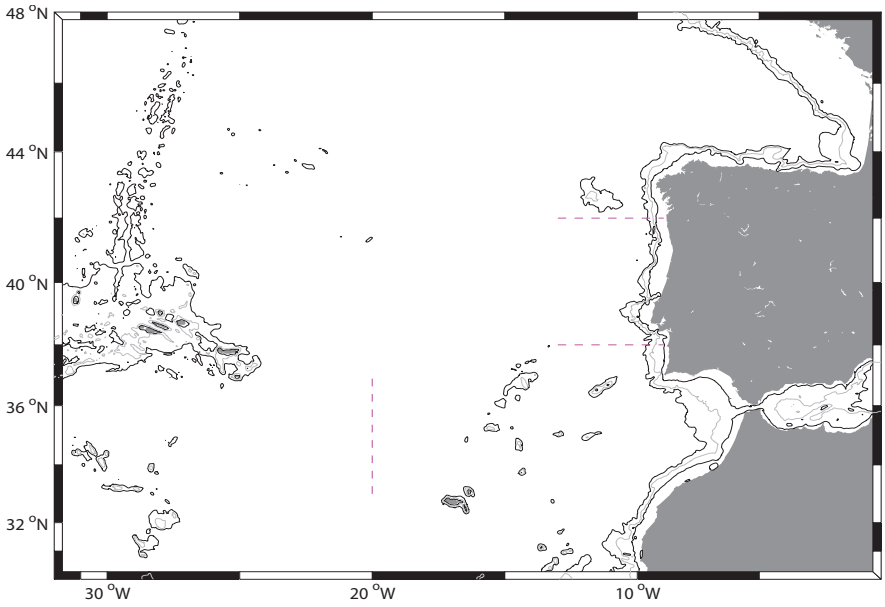

Figure 5.17: Map of the region under study (FD). Isobaths are shown for 200 m and 2000 m in black and 1000 m in gray. The meridional line across the AzC denotes the meridional section of Figure 5.22 and the zonal lines off the WIM denote the zonal sections of Figures 5.23 and 5.24.

5.4.1 Surface Fields

The January mean fields of SST and SSS (Figure 5.18 a,b) have a zonal distribution, except close to the coast north of 40^{o}N, where a warmer (14^oC) and saltier (35.8) tongue of water contours the northwest tip of the Iberian Peninsula — the signature of the IPC. R_CCCMA (Figure 5.18 c,d) presents SST differences in general lower than 1^oC, except in coastal areas. Regarding SSS, differences are always negative and vary from about 0.4-0.8 offshore to 0.8-1.2 close to the coast, and in general to the east of the Azores. R_CSIRO (Figure 5.18 e,f) overestimates temperature in general between 1 and 2^oC, and by more than 2^oC in the northwestern corner of the domain. SSS differences are mostly between 0.4 and 0.8, higher along the coast. As for R_ENSEM (Figure 5.18 g,h), SST differences are mostly within $\pm$1^oC throughout the domain, and SSS differences are almost always lower than 0.4 in module.

For July (Figure 5.19), the surface mean fields show the signature of coastal upwelling, with a narrow band of cold water (<18^oC, Figure 5.19 a) off the entire WIM and a southward deflection of isohalines (Figure 5.19 b) in the same region. Observing the differences, all runs present strong negative differences (greater than -5^oC) in the Gulf of Cadiz, meaning that all CGCM-forced runs overestimate coastal upwelling in that area with respect to the control run. This happens because, unlike the COADS-forced run, they represent upwelling as a continuous band of cold coastal water in the Gulf of Cadiz, as if there were no gap at the Strait of Gibraltar. Most CGCMs, given their general coarse resolution, have a single grid point over the Gulf of Cadiz. Over-land air temperature is always higher than over-ocean in summer; hence, although a land mask was applied to all CGCM output, and given that the Gulf of Cadiz grid point is surrounded by land from three sides (and thus under some influence of land temperatures), this land-ocean temperature gradient intensifies alongshore winds. Indeed, observing the mean wind stress fields for July (Figure 5.13), it is clear that at the Gulf of Cadiz, and for all CGCMs, including the ensemble mean, the alongshore wind stress is higher than in COADS.

R_CCCMA (Figure 5.19 c,d) tends to underestimate temperature relative to R_COADS near coastal areas by values higher than 1^oC in module, and in the rest of the domain the range in temperature differences is approximately $\pm$1^oC. Salinity differences vary mostly between 0.4 and 1.2. R_CSIRO (Figure 5.19 e,f) strongly overestimates SST, especially to the north/northwest, reaching a difference of up to 5^oC. At the WIM, however, differences vary between -1^oC and 1^oC. In terms of SSS, differences are always positive, mostly between 0.4 and 1.2. As for R_ENSEM (Figure 5.19 g,h), SST differences are mostly between -2 and 0^oC. SSS differences on the other hand are lower than 0.4 in module, except in the northwestern corner of the domain, the Gulf of Cadiz and north of the Iberian Peninsula.

Figure 5.20 shows the zonally-averaged seasonal cycle of SST and SSS for the four runs. The SST cycle (Figure 5.20, left column) is well reproduced by both R_CCCMA and R_ENSEM, although in the former temperatures south of 35^{o}N are warmer in winter and cooler in summer by $\sim$ 1^oC, and in the latter temperatures south of 34^{o}N are warmer in winter and colder in summer south of 40^{o}N. Also, there is a phase lag of about one month

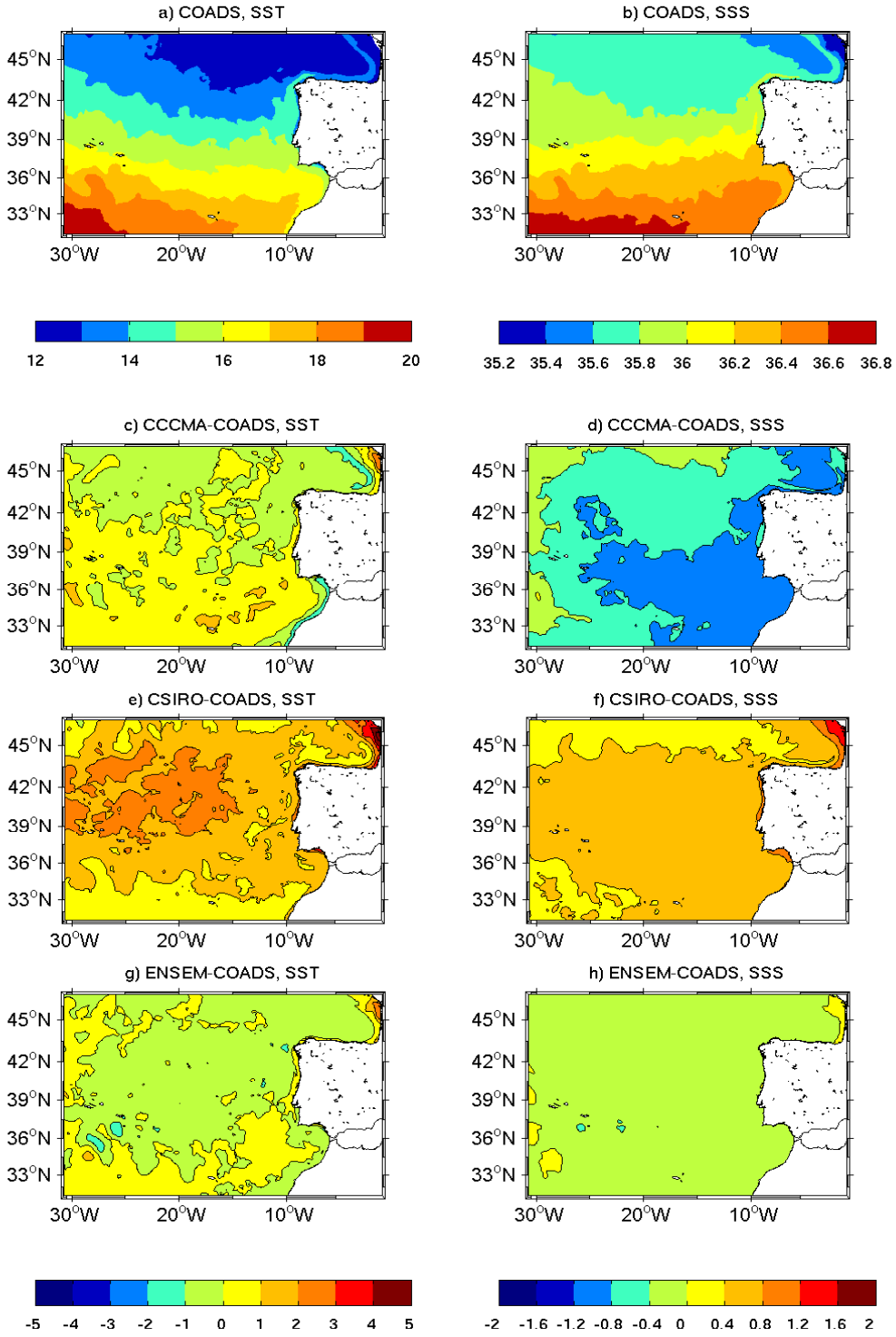

Figure 5.18: (a,b) Mean SST (^oC) and SSS January fields for R_COADS; (c-h) Mean difference fields for January of SST (^oC) (left column) and SSS (right column) between runs: (c,d) R_CCCMA minus R_COADS; (e,f) R_CSIRO minus R_COADS; (g,h) R_ENSEM minus R_COADS.

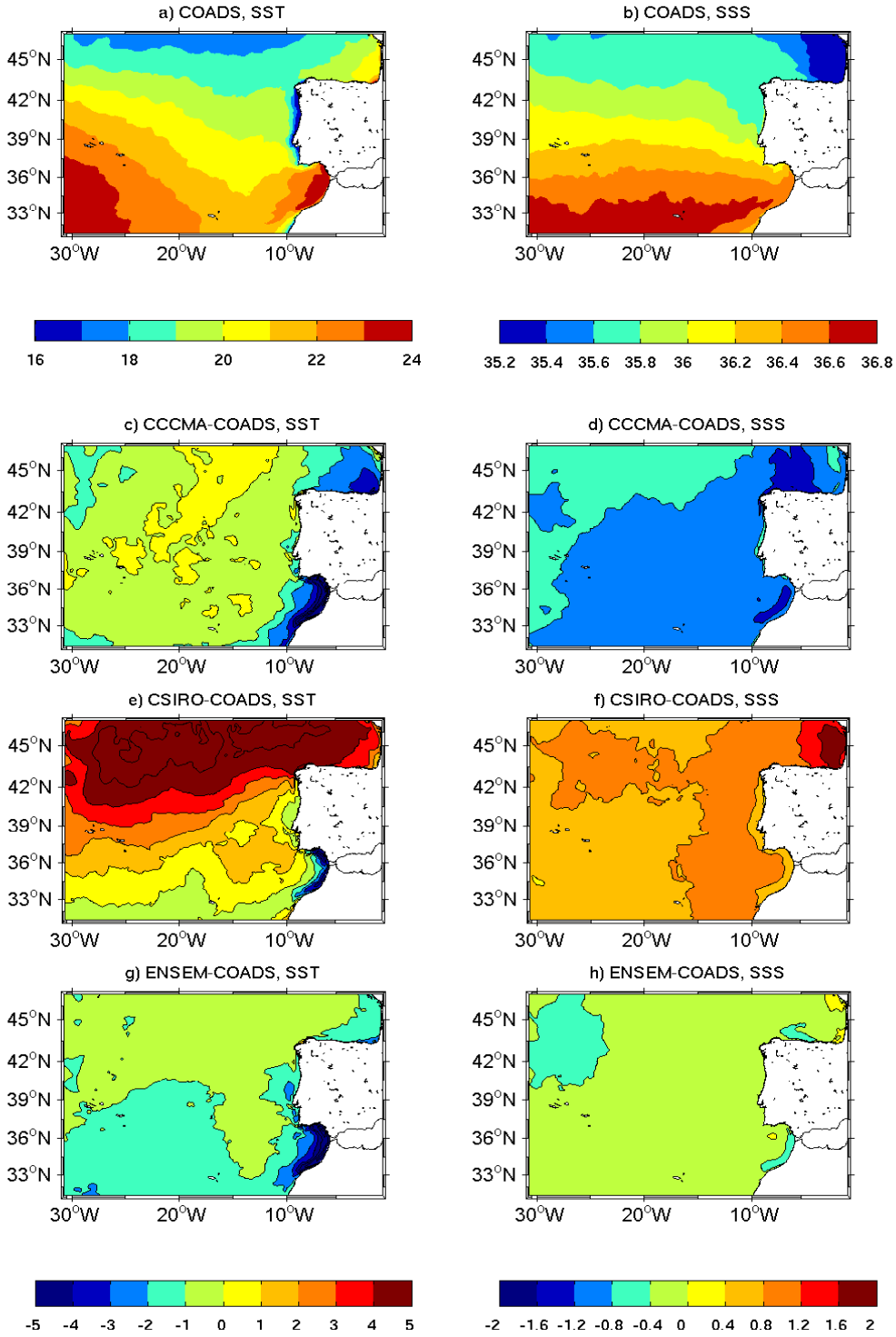

Figure 5.19: Same as Figure 5.18 but for July.

in the temperature cycle. On the other hand, R_CSIRO is always warmer, independently of the latitude. In winter, temperature differences are $\sim 1^oC$ in the southern part and $\sim 2^oC$ in the northern part, and there is a sudden increase in temperature in spring, seen by the vertical N-S orientation of the isotherms especially between May and July: 2^oC (3^oC) to the south (north) in one month. Also, there is no meridional temperature gradient during summer, and the highest temperature is found at 42^oN and not to the south. In respect to the average SSS cycle (Figure 5.20, right column), R_CCCMA does not represent it properly, with differences from 0.8 in winter to 1 in summer. CSIRO overestimates salinities by 0.6 (0.4) in the northern (southern) part but the seasonal cycle is well reproduced. R_ENSEM presents lower values than R_COADS, with differences of -0.2 in summer/autumn to the south and up to -0.4 to the north, whereas in winter differences are mostly -0.2.

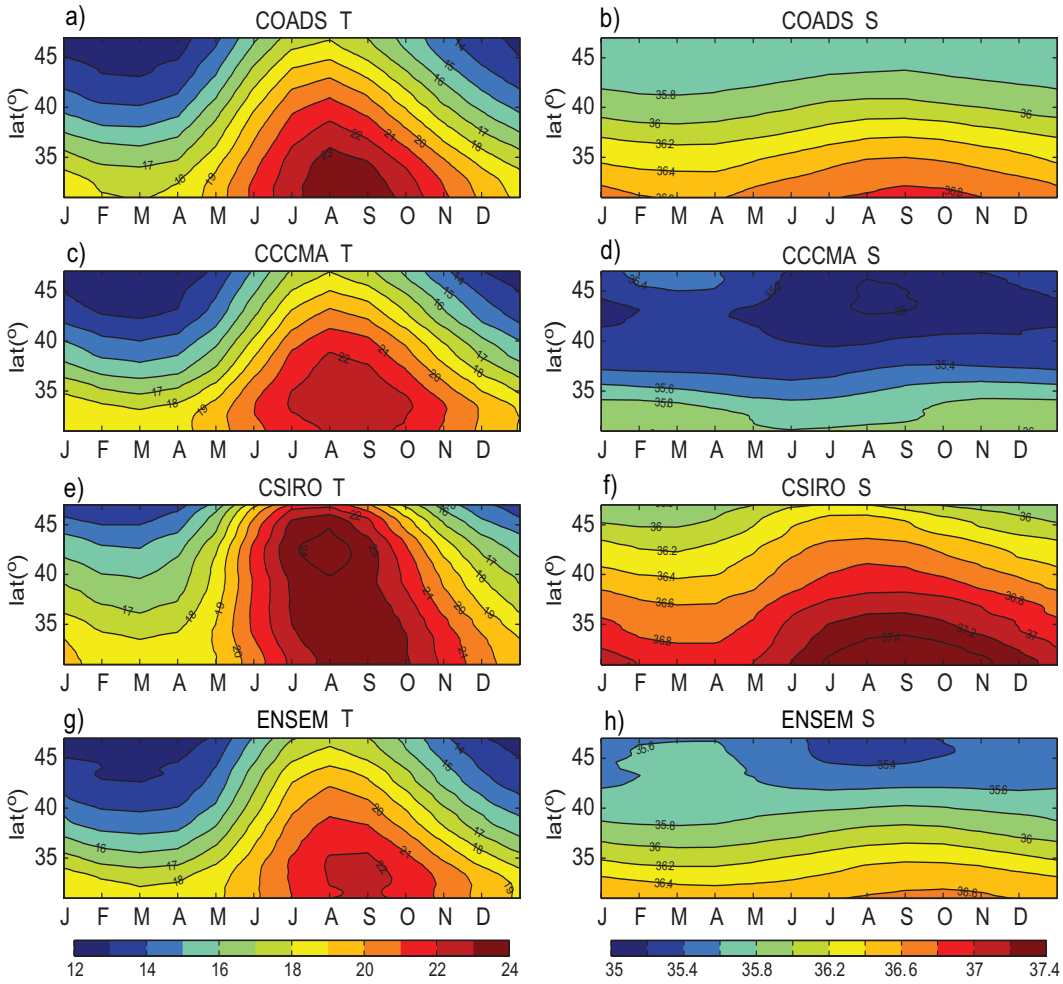

Figure 5.20: Zonally-averaged seasonal cycle of SST (^oC) (left column) and SSS (right column) to the west of 11^oW for run (a,b) R_COADS; (c,d) R_CCCMA; (e,f) R_CSIRO; (g,h) R_ENSEM.

5.4.2 Azores Current

As stated before, the Azores Current (AzC) is an important dynamical features of the region, and therefore it is important to achieve a good numerical representation. For the evaluation of the ability of the CGCMs under study, we choose to show, for all ROMS runs, Eddy Kinetic Energy (EKE) surface mean fields (Figure 5.21) and a meridional section of the zonal (u) component of the velocity, superimposed by temperature (Figure 5.22 a-d) to explore the thermohaline front typical of the AzC. The u variance is also shown (Figure 5.22 e-h). These profiles are represented along 20^{o}W between 33^{o}N and 37^{o}N (the mean location of the AzC) from the surface down to 1000 m deep.

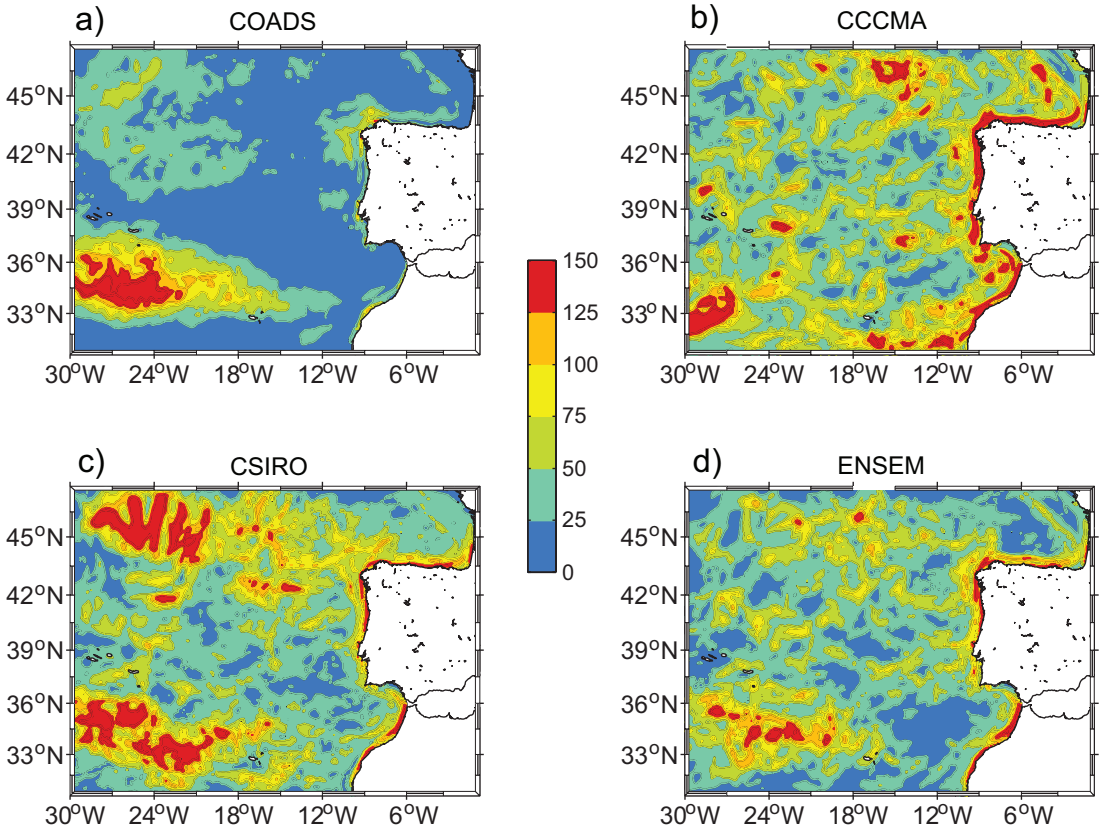

Figure 5.21: Mean annual EKE fields for run (a) R_COADS; (b) R_CCCMA; (c) R_CSIRO; (d) R_ENSEM.

R_COADS EKE shows a strong signal around the average location of the AzC. A comparison between R_COADS EKE and altimetry-based EKE was presented in chapter 2 (Figure 2.3), with very good agreement on the main dynamical patterns. On the other hand, R_CCCMA does not present clear signals, having strong EKE small regions spread throughout the domain. R_CSIRO has two main regions of strong EKE, again between 32^{o}N and 36^{o}N and another to the northwest of the domain. R_ENSEM also shows an

EKE maximum around AzC and alongshore the eastern boundary, as did the other models, associated with coastal circulation instabilities such as filaments and eddies.

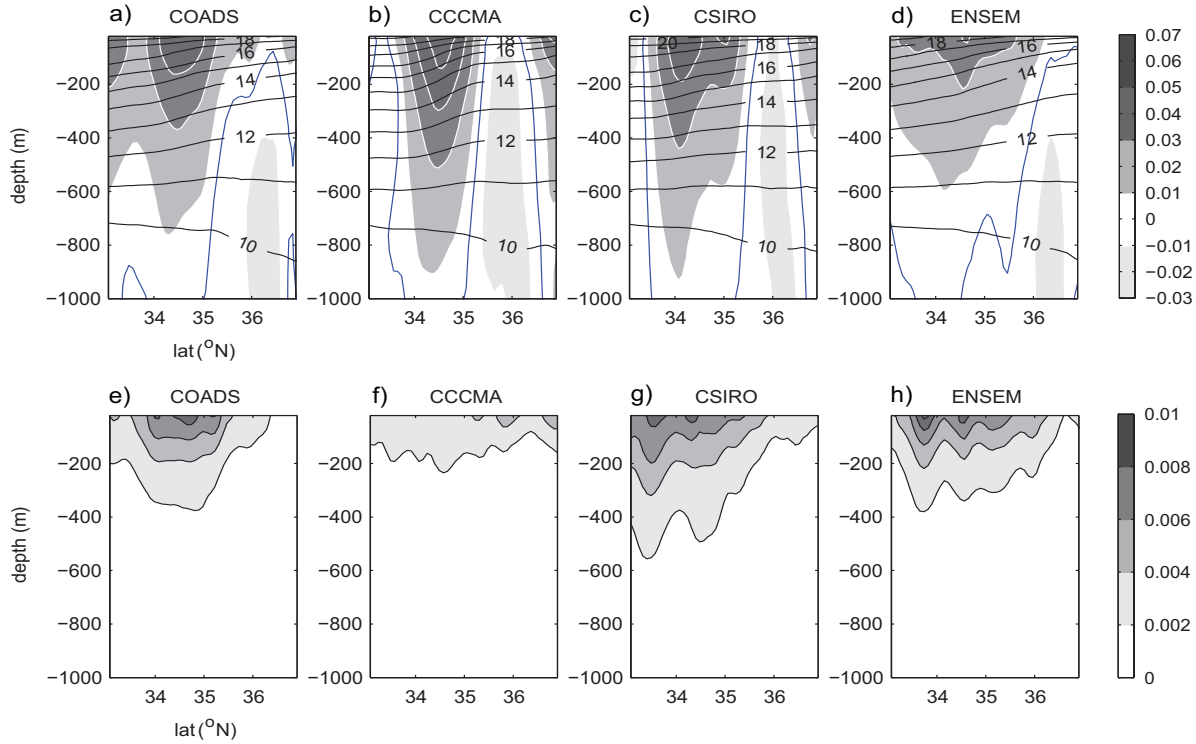

Figure 5.22: (upper row) Meridional sections of mean annual zonal velocity u ($m\ s^{-1}$) (gray shades) and temperature (^oC) (black lines) across 20^{o}W (see Figure 5.17) and (lower row) u variance ($m^2\ s^{-2}$) for run (a,e) R_COADS; (b,f) R_CCCMA; (c,g) R_CSIRO; (d,h) R_ENSEM. The blue lines denote zero u.

Concerning the across section (see Figure 5.17), the associated thermohaline front is in general reproduced by ROMS, no matter which surface forcing is applied. R_COADS (Figure 5.22 a,e) shows a primary core centered approximately at 34-34.5^{o}N and a secondary one south of 33^{o}N. The current is stronger in the upper 350 m but reaches down to 1000 m, and its maximum is roughly 6 $cm\ s^{-1}$. The variance maximum is mostly between 34 and 35^{o}N in the upper 100 m, with maximum values of $8 \times 10^{-3}\ m^2 s^{-2}$. R_CCCMA (Figure 5.22 b,f) presents a strengthened AzC, reaching 7 $cm\ s^{-1}$ at the surface and down to 500 m, due to the stronger temperature gradient. On the other hand, the variance indicates that the AzC does not greatly vary either in latitude or in depth. R_CSIRO (Figure 5.22 c,g) reproduces a wider AzC from 33.5^{o}N to 35.5^{o}N, reaching the depths of R_CCCMA and the velocity surface values of R_COADS. Surface temperature is overestimated by about 1^oC. Its variance suggests that the AzC core can also be found southward. Finally, R_ENSEM (Figure 5.22 d,h) apparently presents a less concordant comparison with R_COADS concerning u, with velocities barely reaching 5 $cm\ s^{-1}$ in the upper 200 m and a more disperse signature along the section. However, variance shows the strongest variability of the cur-

rent in latitude, and presents the strongest values ($10^{-2}\ m^2 s^{-2}$) of the four runs centered at the surface at about 33.5^{o}N and 34.5^{o}N. This value in variance means a standard deviation of $\pm 0.1\ m\ s^{-1}$, reflecting a strong seasonal variability of the modeled current. Thus, it is possible that the AzC cores are present all the same, but varying strongly in location. R_ENSEM also presents the best comparison in terms of the temperature distribution in depth.

5.4.3 WIM Cross-shore Sections

For the cross-shore profiles, we discuss the section along 42^{o}N for January (Figure 5.23) and the section along 38^{o}N for July (Figure 5.24) of the ROMS runs. (see Figure 5.17 for the location of the sections). These sections and these months were thus chosen because the Iberian Poleward Current usually associated with wintertime is stronger at northern latitudes. On the other hand, upwelling is fairly similar in intensity along the coast; in choosing a more southern latitude we aim at a complete WIM representation.

For January (Figure 5.23), the main fields of R_COADS show a temperature and salinity signal consistent with the IPC over the slope in the upper layers ($\sim 15^oC$ and ~ 36), and a low salinity minimum is also visible between 400 and 500 m deep (~ 35.6), attributed to the ENACW signature. In what concerns temperature (Figure 5.23, left column), the model that shows the most striking difference is R_CSIRO (Figure 5.23 e), where temperatures are higher than any of the other simulations, reaching up to 2^oC in the upper slope. On the other hand, R_CCCMA (Figure 5.23 c) presents a -0.5^oC at the upper slope, as does R_ENSEM (Figure 5.23 d) at some points in the upper layers. Concerning salinity (Figure 5.23, right column), R_CCCMA (Figure 5.23 d) underestimates salinity up to 1 in the upper 100 m and down to 200 m when approaching the coast, and R_CSIRO (Figure 5.23 f) overestimates it in the same order close to the coast and reaching deeper near the slope ($\sim 350\ m$). On the contrary, R_ENSEM (Figure 5.23 h) shows differences mostly lower than -0.2 on the entire section.

For July, at latitude 38^{o}N (Figure 5.24), the rising of the isotherms and isohalines is observed near the coast, typical of upwelling, along again with the fresh signature of the ENACW. There is the same tendency of R_CCCMA and R_ENSEM to underestimate and R_CSIRO to overestimate values. In what concerns temperature, R_CCCMA (Figure 5.24 d) presents negative differences in the upper 300 m, strongest at the continental shelf/upper slope where they are greater than -2^oC. This suggests an overestimation of the upwelling strength. The same behavior is observed for R_ENSEM (Figure 5.24 h), although the differences are less prominent ($\sim 1.5^oC$ at the shelf/slope and lower than 1^oC mostly elsewhere). On the other hand, R_CSIRO (Figure 5.24 f) overestimates strongly not at the upper levels, but rather between 200 and 400 m (500 m close to the slope). The maximum difference of 2^oC occurs along roughly 300 m. This suggests that CSIRO does not reproduce well the typical temperatures of the ENACW, which round 12-13^oC, thus exceeding them by 1 to 2^oC.

Salinity shows similar differences to those of January at 42^{o}N: R_CCCMA (Figure 5.24 d) underestimates it by roughly 1 at the surface down to 0.2 at about 300 m; R_CSIRO

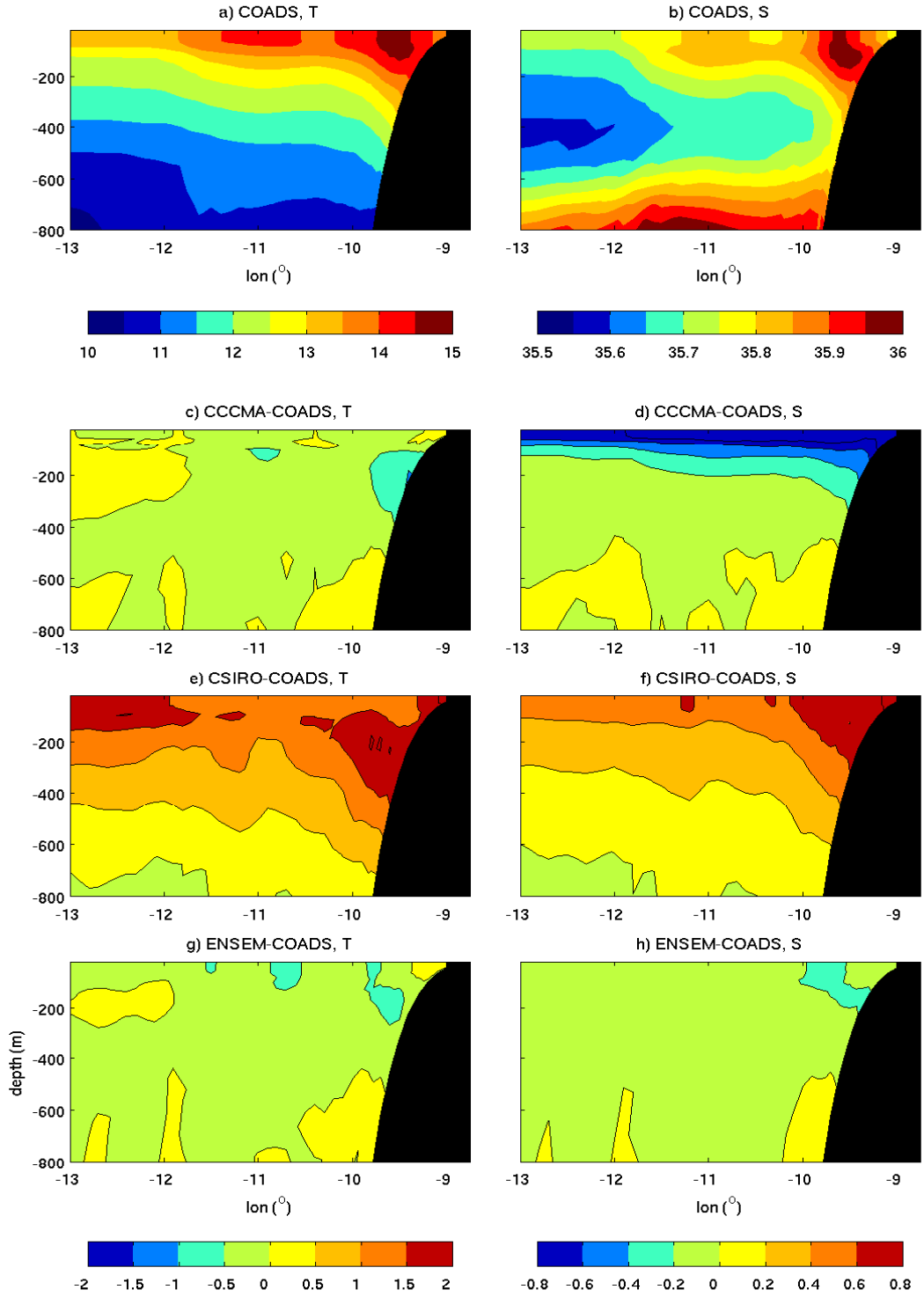

Figure 5.23: (a,b) Zonal sections of mean temperature (^oC) and salinity across 42^{o}N (see Figure 5.17) for January for R_COADS; (c-h) Sections of mean differences of temperature (^oC) (left column) and salinity (right column) across 42^{o}N for January between runs: (c,d) R_CCCMA minus R_COADS; (e,f) R_CSIRO minus R_COADS; (g,h) R_ENSEM minus R_COADS.

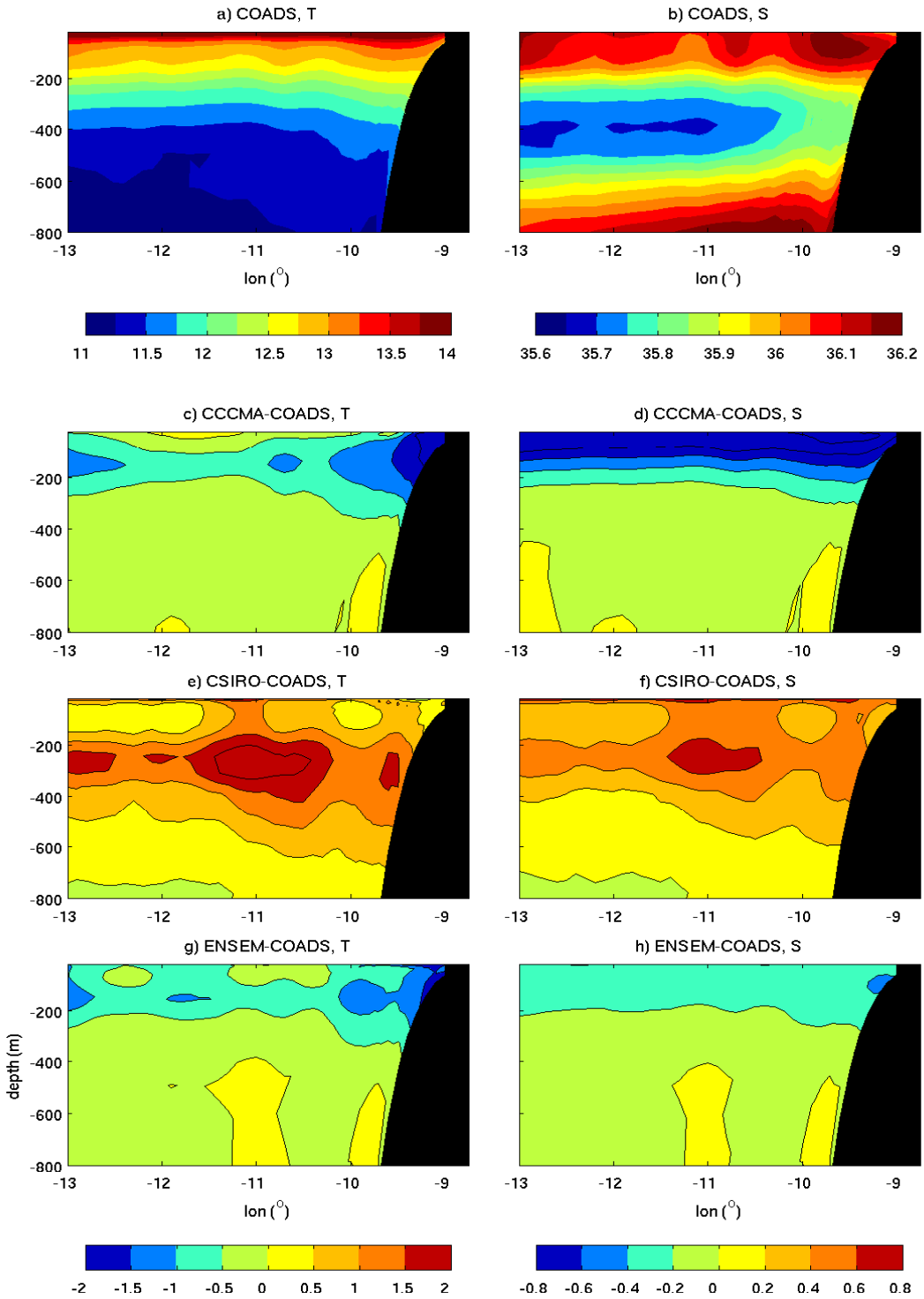

Figure 5.24: Same as Figure 5.23 but for July and across 38^{o}N (see Figure 5.17).

(Figure 5.24 f) presents differences of up to 0.8 in the area between 200 and 300 m, the same region where the temperature difference was the highest; R_ENSEM (Figure 5.24 h) shows more spread negative differences of about 0.2 in the upper 200 m.

From the analysis of these sections, we conclude that the difficulties the CGCM-forced runs have in reproducing the hydrography, at least in this particular area, are verified mostly in the upper 500 m, down to the basis of the central waters. It is also clear that R_ENSEM is the simulation that presents the lowest differences relative to the control run (R_COADS).

In a different approach, we look at horizontal fields of the velocity meridional component (v), averaged between the depths of 50 and 100 m (excluding the Ekman layer). At 42^{o}N (Figure 5.25), note the all-negative v close to the coast (east of 9.5^{o}W) in R_COADS. Velocities in the control run associated with the upwelling equatorward jet do not surpass 10 $cm\ s^{-1}$ and occur in average between March and September. As far as the other runs are concerned, in late autumn/winter (from October to March) velocities are positive (about 5 $cm\ s^{-1}$ in R_CSIRO — Figure 5.25 c — and between 5 and 10 $cm\ s^{-1}$ in R_CCCMA and R_ENSEM — Figure 5.25 b,d) and in summer southward velocities reach 20 $cm\ s^{-1}$ for R_CCCMA and 15 $cm\ s^{-1}$ for R_CSIRO and R_ENSEM. These differences arise from the different wind fields between forcing datasets. A comparison between the average seasonal wind fields of COADS and of each CGCM including the ensemble (see Figures 5.12 and 5.13, and also 5.1, 5.2 f) showed that COADS winter winds have nearly zero zonal components, whereas model winds frequently have a westerly/southwesterly component. On the other hand, summer northerly winds are slightly weaker in COADS than in the CGCMs. CGCMs capture the v seasonality such that ROMS simulates northward circulation in winter and stronger southward circulation during summer relative to COADS.

Offshore (between 9.5 and 10.5^{o}W) all runs show an almost constant poleward flow, which reaches its maximum value of 20 $cm\ s^{-1}$ in August. Typical of eastern boundary current systems, upper slope poleward flows are usually associated with winter circulation due to the presence of summer coastal upwelling. However, as seen in chapter 2, the Iberian Poleward Current may exist throughout the year, although occurring more offshore in summer. This westward displacement in spring is clear in the R_ENSEM field (Figure 5.9 d), with velocities almost always above 5 $cm\ s^{-1}$.

At 38^{o}N (Figure 5.26), the general patterns are similar to those at 42^{o}N, except that the poleward flow is weaker, both coastal and more offshore during summer, barely reaching 15 $cm\ s^{-1}$ in August around 10^{o}W. On the other hand, in R_CCCMA (Figure 5.26 b) and R_ENSEM (Figure 5.26 d) the upwelling-associated equatorward jet is stronger, the first being always higher than 20 $cm\ s^{-1}$ from April to November, and the second reaching 20 $cm\ s^{-1}$ in August. R_COADS (Figure 5.26 a), however, simulates a weaker upwelling relative to 42^{o}N, and with an inversion of flow direction near the coast in winter, with velocities below 5 $cm\ s^{-1}$. R_CSIRO (Figure 5.26 c) presents also southward velocities lower than at 42^{o}N. The differences in winds as discussed regarding Figure 5.9 also account for these observations.

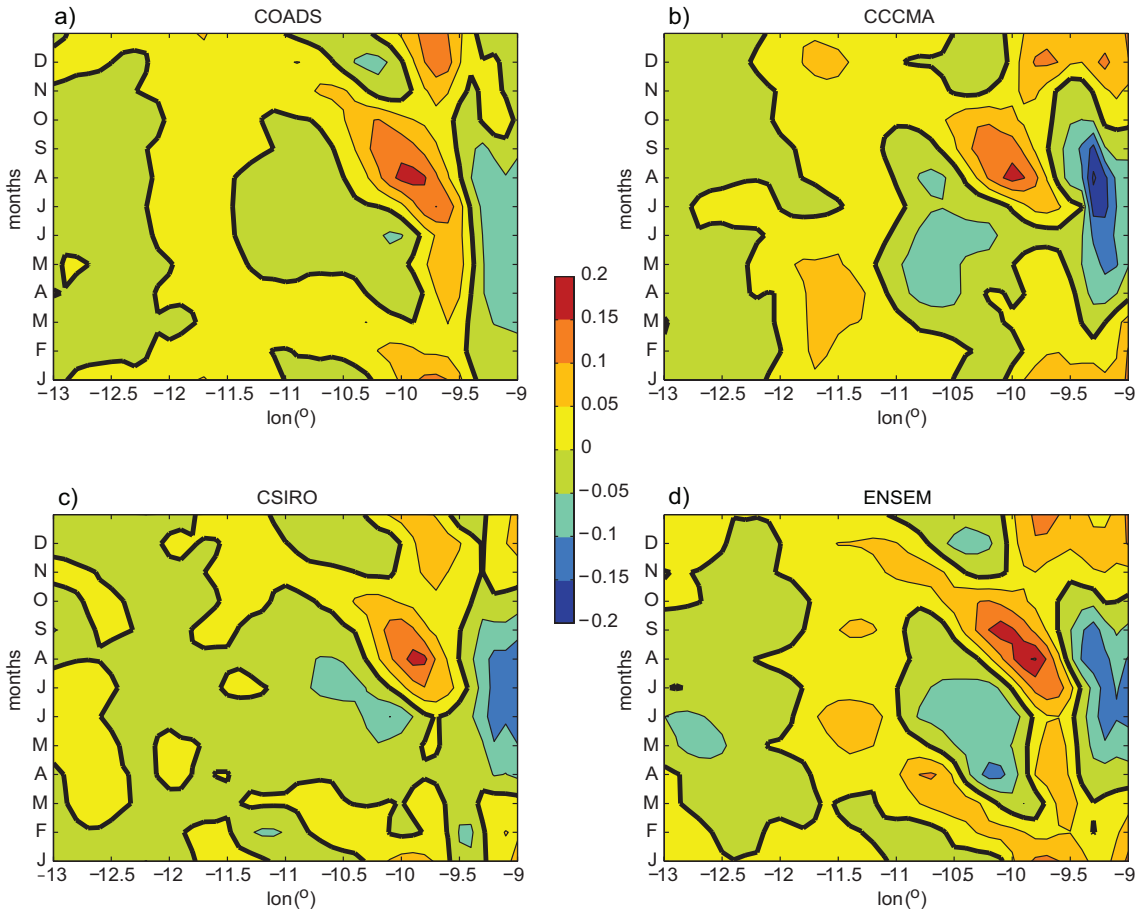

Figure 5.25: Seasonal evolution of mean annual meridional velocity v ($m\ s^{-1}$), averaged at 42^oN between 50 m and 100 m depth for run (a) R_COADS; (b) R_CCCMA; (c) R_CSIRO; (d) R_ENSEM.

5.5 Discussion

The purpose of this work was to evaluate the ability of available CGCM output to force a regional ocean model configuration. A preliminary inter-comparison was carried out for all variables, and an RMSE analysis was performed for each CGCM against the COADS climatology, our control data set. It was clear that there was no consensus in determining the best or the worst model to reproduce climatological values. Different models compared better with COADS regarding different variables. The ensemble of CGCMs encompasses a set of values for each variable, and for most variables COADS lies within that range, which means that the ensemble mean is often very close to the climatological value. Out of the nine CGCMs, two were selected to be used as forcing in ROMS simulations. The objective was to choose one that overestimated values in relation to COADS, and another that would underestimate them. In the end we selected CSIRO and CCCMA. The former frequently presents the highest RMSE, while the latter was chosen based on the fact that

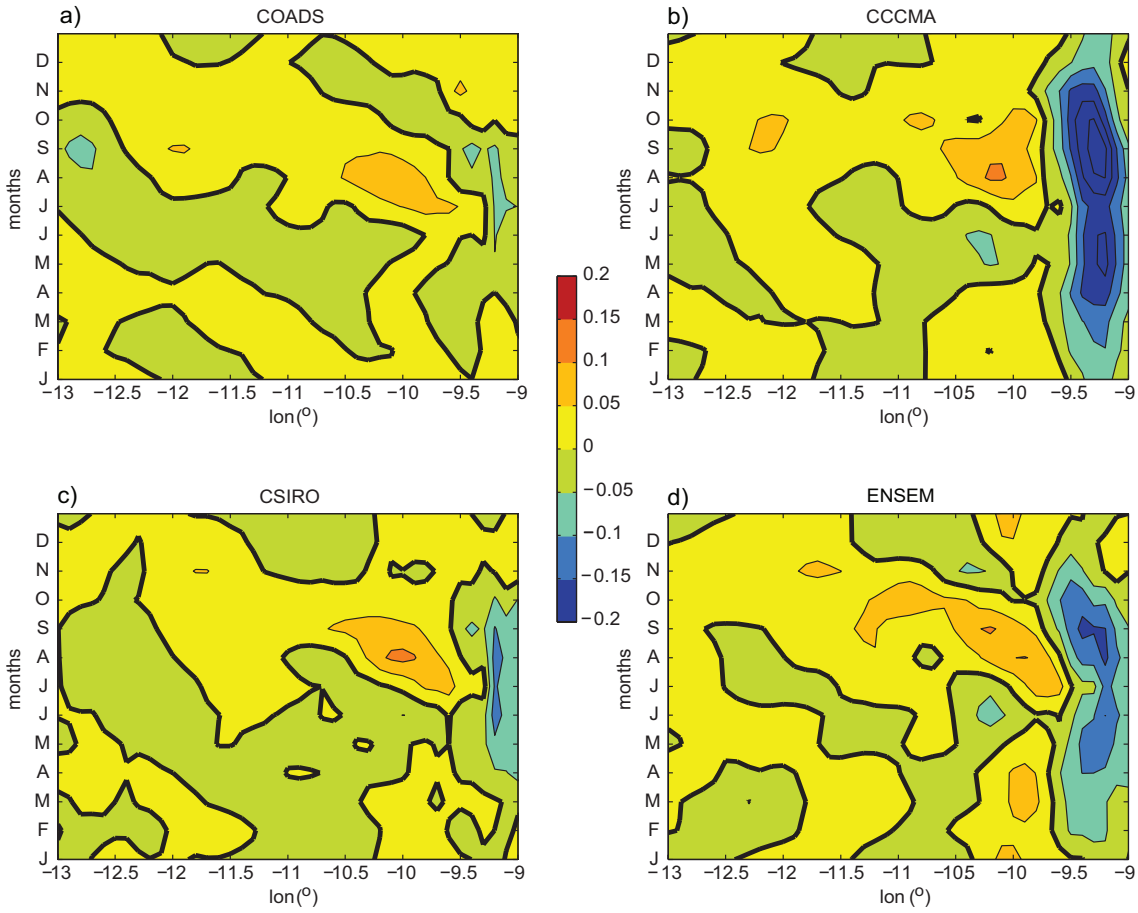

Figure 5.26: Same as Figure 5.25 but for 38^{o}N.

it underestimated SSS the most.

ROMS was forced with these two CGCMs, as well as with the ensemble mean (ENSEM), and finally with COADS, which represented the control run. With these four runs we aim at illustrating the entire CGCM range of values. In terms of thermohaline properties (Figures 5.19-5.21), it is clear from the ROMS surface fields of temperature and salinity that the ocean model results are strongly dependent on the respective forcing. The overestimation of CSIRO and underestimation of CCCMA, particularly of SST and SSS, are fed into ROMS, such that the ocean simulations present the same tendencies in the upper layers. On this matter, the ensemble mean proves to be the most suitable, as would be expected from the forcing inter-comparison of sections 5.3, in the sense that R_ENSEM is the run that presents the most similar hydrographical and dynamical fields with respect to R_COADS (the control run). This is evident in the zonally averaged seasonal signal of SST and SSS for the entire domain (Figure 5.21). This result agrees with numerous works in the literature, e.g. Pierce et al. (2009), and is attributed to the fact that averaging multiple models may reduce their individual uncertainties and result in an intermediate solution that compares better with climatological values.

These conclusions also apply to the deeper layers, namely at coastal locations off WIM (Figure 5.23-5.26), as far down as 500 m, especially in the case of the CSIRO-forced run. As stated in section 5.3, in this case, the wind stress plays the most important role in the intensity variations of the upwelling-associated equatorward jet, as well as the seasonal-varying poleward flow. However, it is worth mentioning the influence that surface forcing in regional ocean modeling has on the proper reproduction of intermediate level water properties. Inadequate values of surface input leads not only to incorrect modeled ocean surface patterns / seasonal cycles, but also incorrect intermediate water values, and hence wrong derived dynamics.

The Azores Current is reproduced in all four runs. Although in terms of its mean location they all resemble, in terms of intensity and vertical profile they differ greatly. The reason for this may lie with the thermohaline distribution in depth. The CCCMA-forced run presents a steeper front, with lower temperatures/salinities north of 34.5^{o}N and higher temperatures/salinities to the south of 34.5^{o}N, enabling a stronger flow. The CSIRO-forced run, on the other hand, is uniformly warmer/saltier on the whole, as the ensemble-forced run is colder/fresher, thus producing weaker associated currents. Nevertheless, the variance of the results allows to postulate that all ROMS runs represent well the AzC, but the location of the current varies more throughout the year, which means that its signal is not as strong when computing the yearly average. Despite this observation, the importance of having proper temperature and salinity (and thus density) vertical distributions is reinforced. And since initial and boundary conditions are the same for the four runs, as well as the same numerical configuration, these distributions depend solely on the different surface input provided by each forcing.

With the CCCMA- and the CSIRO-forced runs we intended to illustrate the range of possible ROMS output that the ensemble of nine CGCMs could provide without actually carrying out the nine ROMS simulations. The first conclusion we may draw is that the use of forcing obtained from a particular CGCM in an ocean simulation should be considered with caution. Secondly, in light of all considerations, both regarding the CGCM intercomparison and the ROMS runs, the ensemble mean stands out as the most adequate forcing for FD with respect to any other individual CGCM, particularly supported by the results of the R_ENSEM simulation, which we have shown that provides the most realistic physical results concerning the hydrography and circulation fields when compared to the control run (R_COADS) for the present climate. As such, one may postulate that simulations to evaluate future ocean climate change may also legitimately be forced with the ensemble mean; that is, in using the ensemble mean for a future period, we would be aiming at minimizing the uncertainties associated with every individual CGCM. This application is carried out in chapter 6.

Chapter 6

A Future Climate Scenario, part 2: Climate Change on the Western Iberian Margin using ROMS

Part of the contents of this chapter has been published by Cordeiro Pires et al. (2013b).

6.1 Overview

This chapter consists in a case study of the impacts of a global climate change scenario on the hydrography and dynamics of the Iberian Upwelling System through numerical modeling.

As previously stated, given that upwelling systems undergo strong seasonal and interannual variability, it is also likely they are very sensitive to climate change (Holt et al., 2010). The work of Bakun (1990) was one of the earliest studies on the effects of climate change on upwelling systems. The author postulated that a global increase in surface air temperature over land would intensify the land-sea pressure gradient at coastal regions, which in turn would cause an intensification of alongshore winds and subsequently upwelling. Upwelling intensification would mean cooling of the sea surface temperature (SST), which would result in a positive feedback in the land-sea pressure gradient. Since then, several studies have been carried out, based either on SST or wind stress time series from the last decades. Some of them confirm the Bakun hypothesis while others found a weakening of the upwelling signal, depending on the dataset the results are based on and the periods of computation (Narayan et al., 2010). Demarcq (2009) points out that one of the main reasons of uncertainty in what concerns upwelling systems is the unknown behavior of wind patterns in the future, which is the main driver of eastern boundary coastal dynamics. Analyzing satellite data, the author found both SST warming and equatorward wind strengthening trends in upwelling systems. Particularly for the Iberian Peninsula, increases were estimated to be $0.15^oC\ decade^{-1}$ ($0.44^oC\ decade^{-1}$) in SST for period 1998-2007 (2000-2007) and 1 $m\ s^{-1}\ decade^{-1}$ in equatorward wind for period 2000-2007.

In what concerns the WIM, the work of Relvas et al. (2009) based on SST data, provides evidence of upwelling enhancement since 1960 based on climatological *in situ* data, corroborated by satellite data since 1985. However, Santos et al. (2005) (whose study extends to the entire Eastern North Atlantic Upwelling System) hypothesize a long-term variability behind the strengthening of upwelling from 1990 on. Conversely, Lemos and Pires (2004) found a weakening trend for 1941-2000 when analyzing both meridional wind component and SST datasets, although punctuated by strong interannual variability. A general weakening for both Iberian and Canary upwelling regions was also found by Pardo et al. (2011) from the NCEP/NCAR reanalysis data of SST and wind.

With the numerical modeling tools improvement of the past few years, providing good performances on the reproduction of the dynamics of both the atmosphere and ocean, in addition to the Intergovernmental Panel for Climate Change (IPCC) climate studies, it became possible to carry out future scenarios in the scope of climate change (Nakićenović et al., 2000). However, the general circulation models (GCMs) used in this international effort are global and therefore have very coarse resolution. Recently, the increased challenge has been to assess global change at a regional scale (Woolings, 2010). Therefore, climate studies have been aiming at the improvement of GCM simulations and the development of downscaling techniques toward regional, and thus more realistic, simulations (Hewitson and Crane, 1996).

From the studies that focus on ocean circulation in a context of future climate change scenarios by means of Coupled GCMs (CGCMs), there is a large number that focuses on the thermohaline circulation and the impact of increases in temperature and CO_2 concentration and consequent fresh water input (e.g. Gregory et al., 2005; Stouffer et al., 2006). Furthermore, using a set of IPCC CGCMs, Diffenbaugh (2005) assessed the sensitivity of large-scale eastern boundary currents to increased greenhouse gas concentrations, discussing the limited ability of global climate models to predict more than the general patterns and distribution of atmospheric pressure and surface winds, namely in what concerns trends and interannual variability. Particularly regarding upwelling systems, Mote and Mantua (2002) used two CGCMs to see how the seasonality and intensity of coastal upwelling change in the four world systems, whereas Snyder et al. (2003) assessed future changes in upwelling intensity for the California Current System based on CO2 concentration increase. However, while the former found no significant change in future years for any of the world upwelling systems, the latter obtained results in agreement with Bakun (1990) for California, that is, increasing of upwelling intensity and frequency. More recently, Wang et al. (2010) evaluated the ability of several IPCC CGCMs in reproducing upwelling seasonality and what future changes in atmospheric patterns would bring to the Canary, the California and the Humboldt upwelling systems, and found the results differed greatly from model to model, with some presenting a weakening of upwelling and others showing intensification. For the WIM, Miranda et al. (2012) carried out a regional ocean modeling study, using a regional atmospheric model as surface forcing, for the A2 IPCC scenario and for period 2071-2100, and also found results in agreement with Bakun (1990).

Following these works, and the sensitivity study carried out in the previous chapter, the present chapter consists in a comparison between the present mean circulation features of

the upper levels along the western coast of the Iberian Peninsula described in chapter 2 and the dynamics imposed by a set of atmospheric conditions dictated by a future circulation regime; in this case, based on the multi-model ensemble mean.

6.2 Data and Methodology

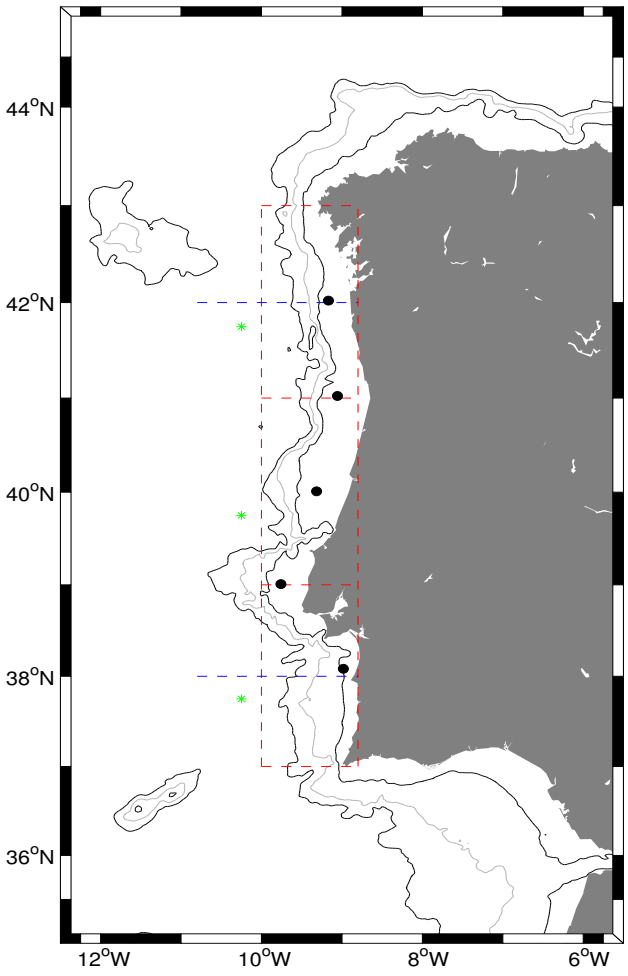

Figure 6.1: SD, with the several study locations of this chapter. Dashed blue lines: zonal sections of Figures 6.5-6.8. Black dots: measurement points of SST and SSS in Figure 6.9 (along 100 m). Dashed red lines: delimitation of the areas of Figure 6.10. Green dots: UI measurement locations (Figure 6.11). Isobaths 200 m and 2000 m are shown in black and 1000 m in gray.

The choice of forcing for this study underwent several steps. In the first approach, the goal was to find one global climate model that would compare well with our climatological run of chapter 2, and which would consequently provide reasonable future forcing for the

scenario study. However, when we started to analyze the nine CGCM forcing (as described in chapter 5), we soon realized that there was not one that outstood from the others, one that would solely provide the best comparisons to the climatology when all variables were taken into account. One would better represent radiation fluxes but be poor in E-P, the other would be better in SST and SSS but be poor in SLP. That is why, in the end, the multi-model ensemble mean was the selected future forcing; because in averaging the input from all CGCMs we believe we are minimizing their uncertainties.

The results are presented first showing the differences between the ensemble present-forced run and the COADS-forced run, and then between the ensemble future-forced run and the ensemble present-forced run, which will be addressed as a possible future ocean scenario, having validated first the present ensemble as adequate forcing.

For this study, ROMS is setup using the same configuration of chapter 2: offline nesting, climatologically-forced, with FD providing initial and boundary conditions for SD. Three runs are taken into consideration: the one described in chapter 2, with COADS as surface forcing, which consists in the control run; one forced with a climatology constructed for the same period as COADS, that it, 1945-1989, from the multi-model ensemble mean; and one forced with a future climatology (2071-2100), also constructed from the ensemble mean. The methodology used to obtain these climatologies is the same as described in the previous chapter (section 5.2). The CGCMs that compose the multi-model ensemble mean are listed in Table 5.1. As mentioned in chapter 5, the ensemble-forced FD runs are fed with the same initial and boundary conditions as the COADS-forced run, since the vertical hydrographical fields provided by the CGCMs were not realistic (not shown).

The chosen emission scenario from the IPCC future climate projections assessment report from 2007 (AR4) was the Special Report on Emissions Scenarios (SRES) A2 scenario (Nakićenović et al., 2000). The SRES scenarios are grouped into four scenario families (A1, A2, B1 and B2) that explore alternative development pathways, covering a wide range of demographic, economic and technological driving forces and resulting greenhouse gas emissions. The SRES scenarios do not include additional climate policies above current ones. They can be summarized as follows:

- A1: assumes a world of very rapid economic growth, a global population that peaks in mid-century and rapid introduction of new and more efficient technologies. A1 is divided into three groups that describe alternative directions of technological change: fossil intensive (A1FI), non-fossil energy resources (A1T) and a balance across all sources (A1B).

- B1: describes a convergent world, with the same global population as A1, but with more rapid changes in economic structures toward a service and information economy.

- B2: describes a world with intermediate population and economic growth, emphasizing local solutions to economic, social, and environmental sustainability.

- A2: describes a very heterogeneous world with high population growth, slow economic development and slow technological change.

The A2 scenario is the most "business-as-usual" approach, where the basic social, economical and technological behavior is maintained throughout the period under study (2001-2100). There is not a scenario more likely than the other; the four encompass equally possible changes in society. This choice was based on two factors. First, in the beginning of this study, we had no idea what to expect either from the CGCM output or from the ROMS simulations. Hence, the tendency was to choose a scenario where changes would be marked; that is, one of the "worst" scenarios. Secondly, A2 along with A1B seem to be the scenarios which are most frequently applied, based on the literature.

6.3 Results

For the analysis of the mean hydrography of the region, the following sub-sections present: seasonal maps of wind stress; monthly-mean fields of SST and SSS; cross-shore sections of temperature, salinity and meridional velocity along the WIM; the seasonal cycle of SST, SSS and the upwelling index. This is carried out for the three runs. For the horizontal and vertical slices, ROMS output was processed for January and July as monthly averages from the last 5 years of a 10-year simulation.

6.3.1 Seasonal Wind Stress

Wind stress is one of the most important variables that must be well modeled for a good reproduction of both hydrography and circulation. That is why it is described first of all. Observing Figure 6.2, the ensemble presents roughly a meridional gradient, whereas in COADS wind stress varies along a NW-SE axis in winter and autumn and along a NE-SW axis in spring and summer. Furthermore, while in winter the ensemble shows a clear south/southwesterly wind stress component, COADS wind stress is mostly eastward and southeastward. That is, there are never downwelling-favorable conditions according to COADS, which means that this forcing does not comprise e.g. strong storm conditions associated with low-pressure systems, typical of winter. In spring, COADS already presents a clear tendency for equatorward winds, whereas the ensemble wind, although showing a southward component, is mostly directed onshore. In summer, the ensemble presents stronger wind stress, especially south of 42^oN, and in autumn COADS and present ensemble have similar patterns as during wintertime, that is, an eastward and southeastward tendency in COADS and relatively strong north/northeastward winds in the ensemble. In the future, wind stress distribution remains mostly zonal, but enhanced, especially to the north in winter and autumn and to the south in spring and summer. In winter and autumn, south of 40^oN, wind stress has a stronger southward component, particularly noticeable in the Gulf of Cadiz. In summer, the strengthening is striking south of 41^oN, with an increase of wind stress intensity of $>0.02\ N\ m^{-2}$.

The absence of a clear inversion on the wind direction in COADS as opposed to the present ensemble will strongly influence the differences between the two runs, since the wind stress plays a key role in dictating the thermohaline structure of the coastal ocean

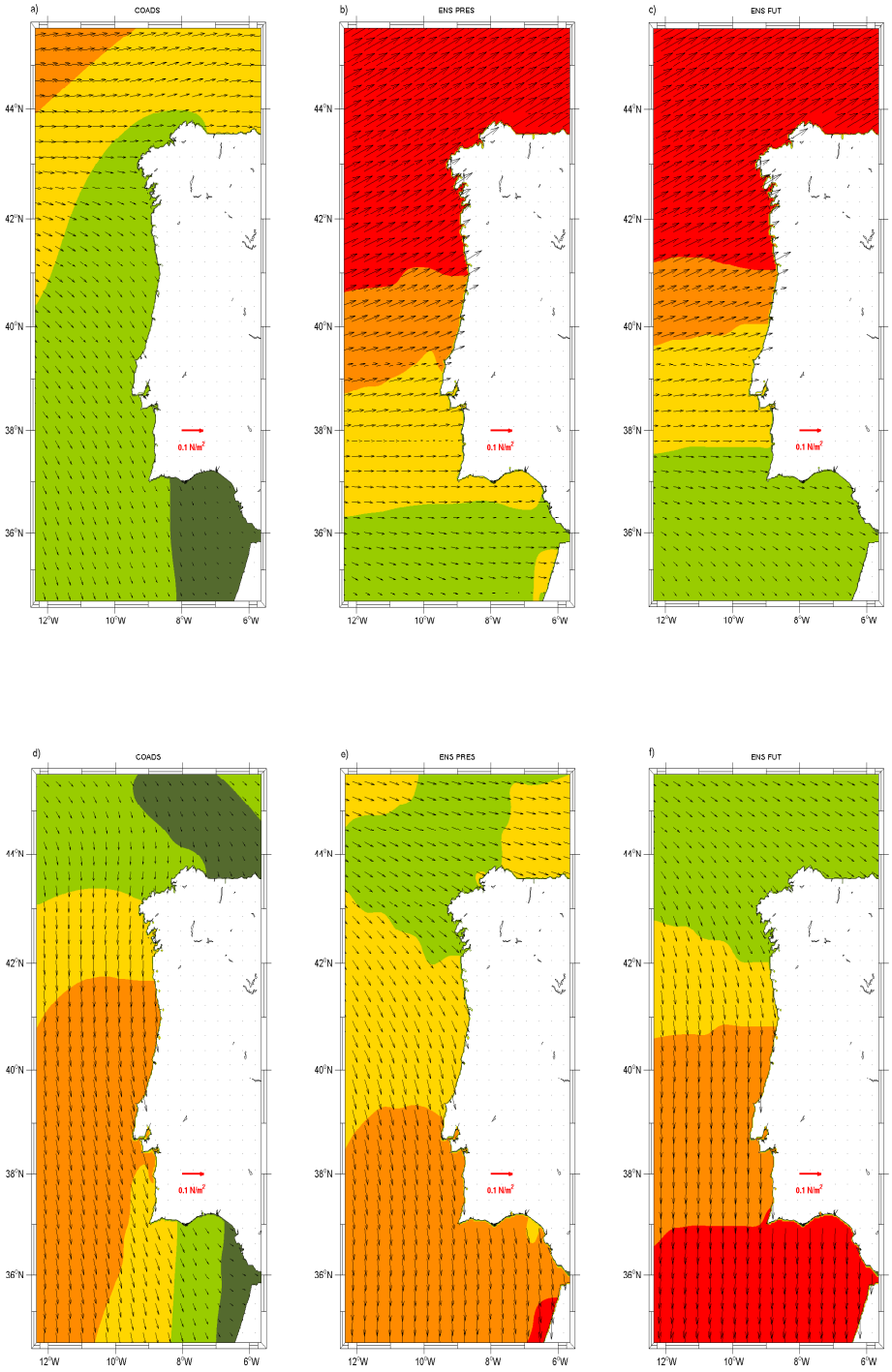

Figure 6.2: Wind stress ($N\ m^{-2}$) seasonal fields for COADS (left column), present ensemble (middle column), and future ensemble (right column). (a-c) Winter; (d-f) Spring; (g-i) Summer; (j-l) Autumn.

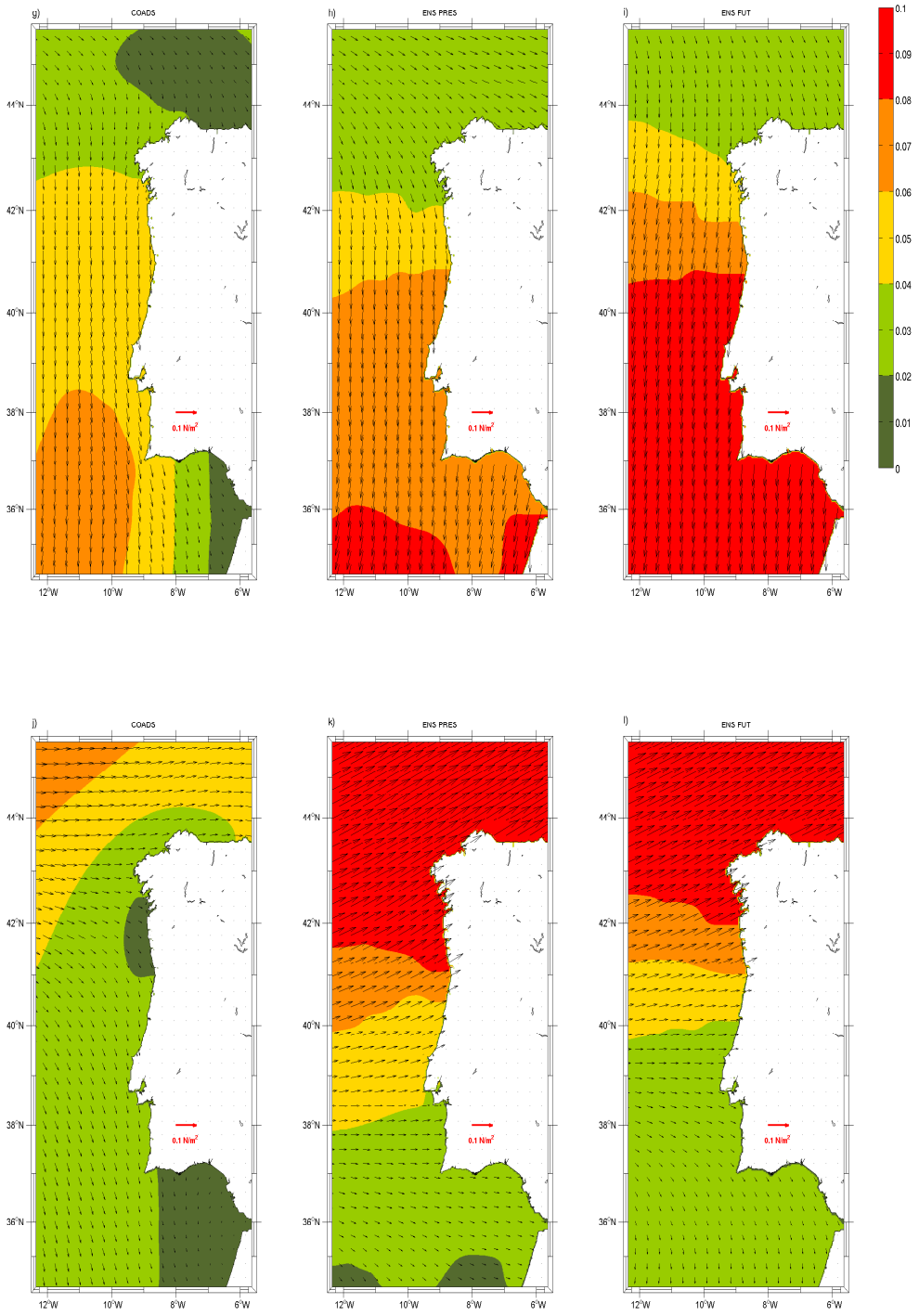

Figure 6.2: Continued.

and hence its circulation. Nevertheless, it is important to have a "control run" against which to test our hypothesis, and as described in chapter 2 the COADS-forced SD run traces a reasonably accurate portrait of the WIM hydrography and dynamics.

6.3.2 Surface Fields

Figure 6.3 presents SST (upper row) and SSS (lower row) fields for January, from the three runs: COADS (Figure 6.3 a,f), present ensemble (Figure 6.3 b,g) and future ensemble (Figure 6.3 c,h). Also represented are the difference fields between the ensemble and COADS (Figure 6.3 d,i) and between future and present of the ensemble (Figure 6.3 e,j). Figure 6.4 shows the same but for July. The differences between the control run and the present ensemble will be addressed first, and then the differences between present ensemble and future ensemble. Note the different color scale in the difference fields.

In winter (Figure 6.3), the present ensemble reproduces well the coastal warm and saline tongue typical of the slope poleward flow, with the 13^oC isotherm and the 35.7 isohaline following the bathymetry along the northern coast of the WIM. On the other hand, COADS shows more clearly the low temperature ($<12.5^oC$) and low salinity (<35.7) band along the coast north of the Estremadura Promontory. While low salinities are usually attributed to winter river discharge, these low temperatures nearshore are due to winter cooling in the continental shelf. This is also observed in the ensemble, but along a much narrower coastal band, perhaps more restricted to the coast due to the presence of the stronger and well defined poleward flow, that can partially overcome these lower temperatures and salinities. That is why the alongshore differences (Figure 6.3 d,i) are positive. Furthermore, there are generalized SSS negative differences offshore (-0.15 to -0.25).

In summer, both SST (Figure 6.4 a,b) and SSS (Figure 6.4 f,g) distributions are similar when comparing present ensemble and COADS. Coastal upwelling is overestimated by the former in SST with a clearly wider cold-water band along the western coast, most likely due to the stronger equatorward winds (see Figure 6.2). In the ensemble runs, upwelling occurs as if there were no land interruption at the Strait of Gibraltar. This has been discussed in the previous chapter: most CGCMs, given their general coarse resolution, have a single grid point over the Gulf of Cadiz, and hence do not reproduce well the winds at this location. This accounts for the SST and SSS differences in the Gulf of Cadiz, including along the southern coast of Portugal. Note that in the northwestern tip of the Iberian Peninsula upwelling is enhanced in SSS and weakened in SST by the ensemble.

For the future, the general tendency is for warming and for freshening of the ocean surface. In winter (Figure 6.3), the SST increase is stronger near the coast ($+2^oC$ in northern WIM and $+2.5^oC$ in southern WIM) and the SSS decrease is stronger offshore (-0.2 in the northern quadrant, reaching -0.4 in the Gulf of Cadiz). The temperature and salinity anomalies associated with the poleward flow surface signature are still visible, although with higher temperatures and lower salinities along its path, relative to the present ensemble. Note that both temperature and salinity onshore-offshore anomalies are similar to the present, although the absolute values increase (decrease) in temperature (salinity).

In summer (Figure 6.4), the opposite occurs in SST: differences are greater offshore (up

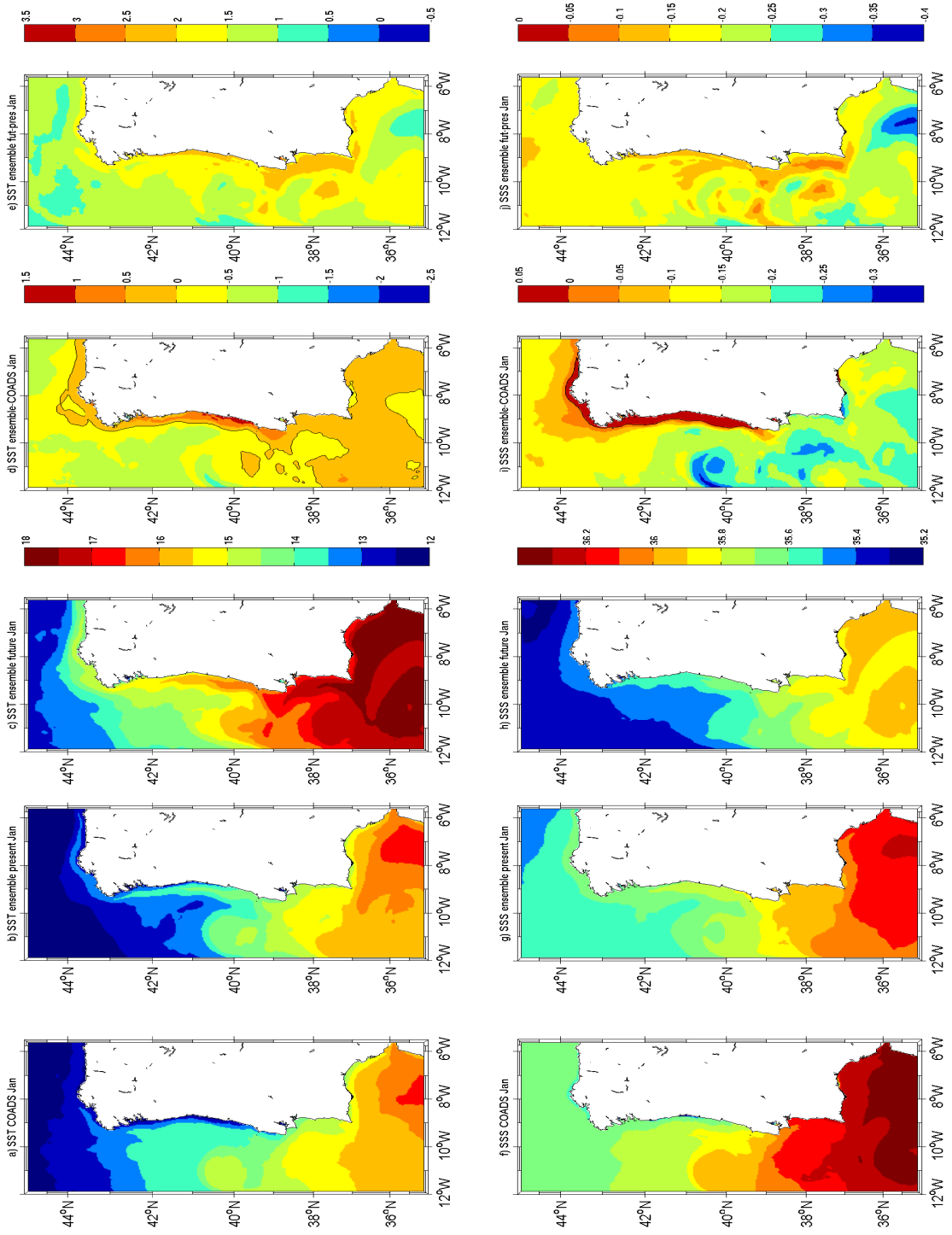

Figure 6.3: SST (upper row, ^oC) and SSS (lower row) mean fields for January, from the three runs: COADS (a,f), present ensemble (b,g) and future ensemble (c,h). Difference fields between the ensemble and COADS (d,i) and between future and present of the ensemble (e,j).

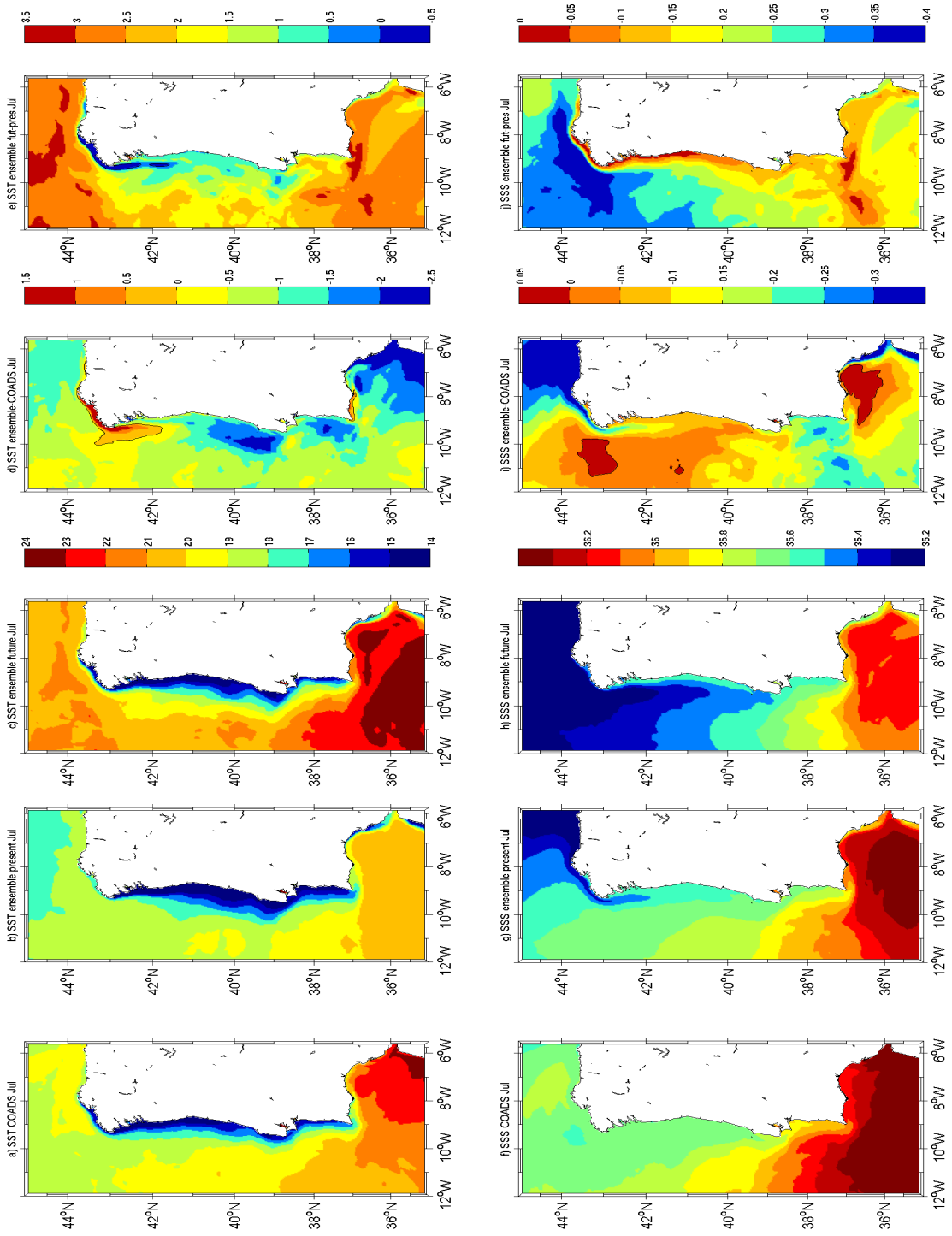

Figure 6.4: Same as Figure 6.3 but for July.

to $+3.5^oC$), than onshore ($+1^oC$ in northern WIM and $+1.5^oC$ in southern WIM). For SSS, the strongest differences remain offshore, up to -0.4 to the north and -0.2 to the south, and are lower onshore (lower than -0.1 along northern WIM and about -0.15 along southern WIM). The cross-shore gradient associated with coastal upwelling is enhanced and wider, due to the higher warming rate of temperatures offshore than onshore. Nevertheless, note that the width of the upwelling band has not increased, as could be expected from the strengthening of upwelling-favorable winds observed in Figure 6.2. It has even decreased in the southern WIM. This will be further discussed in the following section.

These results are expectable, since the basis of the IPCC A2 scenario is a global rise in surface air temperatures, which has as consequence among many others freshwater input from melting icecaps in the poles (Huybrechts et al., 2004). Furthermore, the higher warming rate along the southern WIM than along the northern WIM is consistent with the trends found by Relvas et al. (2009) when analyzing SST time series for period 1960-2005, as well as satellite data from 1985 to 2008 and buoy data from 1960 to 2003.

6.3.3 WIM Cross-shore Sections

The following analysis concerns cross-shore sections at two latitudes off WIM: 42^oN and 38^oN, where temperature, salinity and meridional velocity mean fields for January and July are analyzed for each of the runs: COADS, present ensemble and future ensemble. As before, the present runs are compared first, and then follows the comparison between future and present of the ensemble.

The vertical hydrographical fields are presented in Figure 6.5 for January and in Figure 6.6 for July. Analyzing first the northern section in winter, COADS (Figure 6.5 a) presents a tendency for low temperatures and salinities nearshore (note the upward of the isotherms), consistent with the coastal narrow band of low temperatures and salinities observed in Figure 6.3 attributed to winter cooling and river discharge, respectively. The ensemble (Figure 6.5 b) shows in part lower salinities, and a warmer core that is formed nearshore (closed isotherm 13.5^oC centered at 9.2^oW), the signature of the poleward flow seen also in Figure 6.3. Onshore, temperatures are again 13^oC.

At 38^oN, for the upper 200 m, the surface coastal waters in the ensemble are warmer by 0.5^oC and isotherms are less steep at the upper slope, although an upward of isotherms is visible in both runs. With respect to salinity, at the upper 200 m, it is generally underestimated by the ensemble by 0.1-0.2.

Below 200 m, for both latitudes, the present ensemble (Figure 6.5 b,e) represents the well temperature field. At 42^oN, the salinity general distribution is well captured, although the ensemble underestimates values by ~ 0.1 at 42^oN, especially noticeable at the MW levels (800-1200 m). At these levels for section 38^oN, on the other hand, the ensemble shows good results in the reproduction of the MW salinity.

In summer (Figure 6.6), below 200 m, the differences between the two present simulations are similar to those of winter: the temperature distribution compares well and salinity is underestimated by the ensemble by about 0.1, especially striking at the depths of the MW (800-1200 m). In the upper 200 m, while at 42^oN temperature in the ensemble still

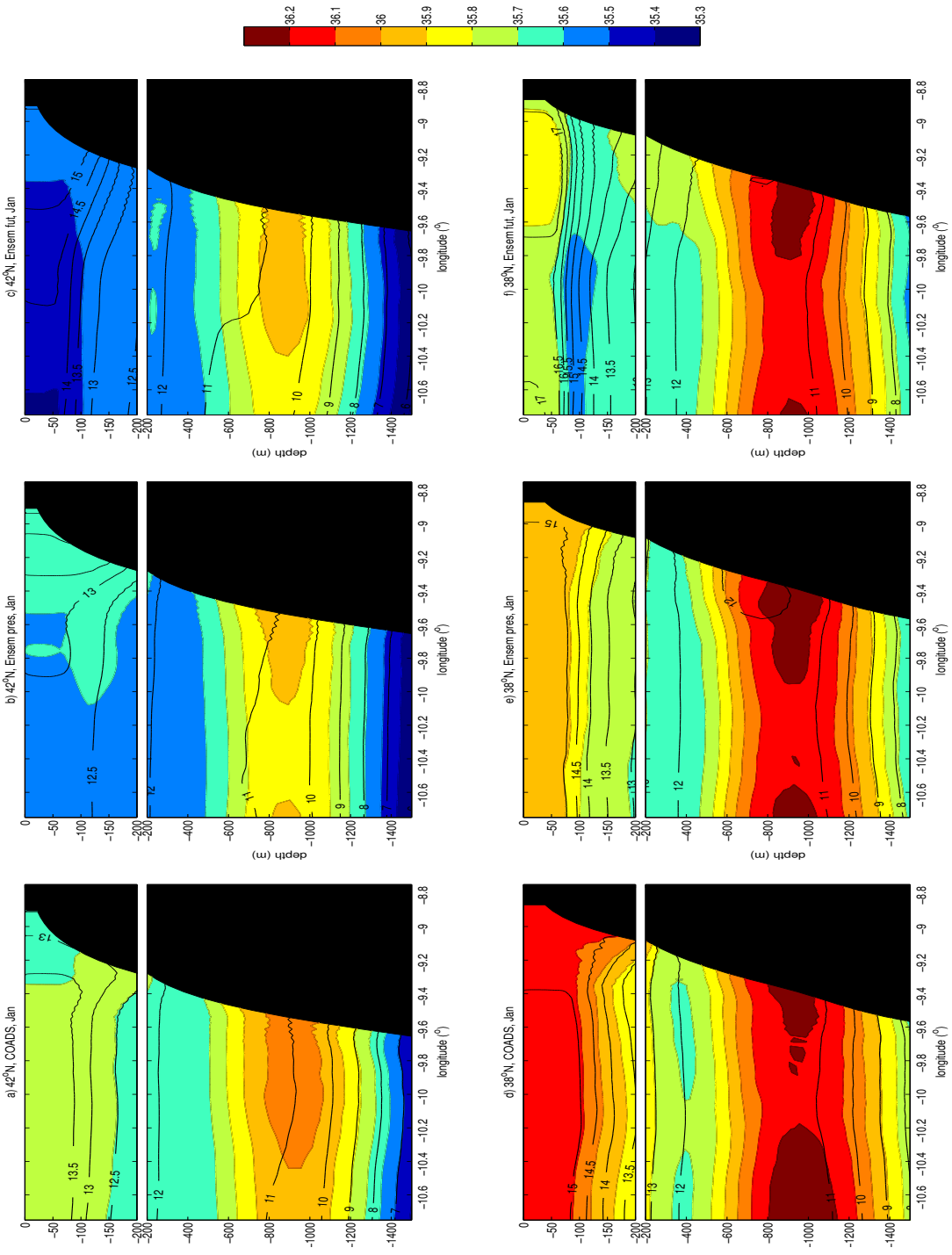

Figure 6.5: Zonal sections at 42^oN (upper row) and 38^oN (lower row) of mean temperature (^oC) and salinity for January, from the three runs: COADS (a,f), present ensemble (b,g) and future ensemble (c,h).

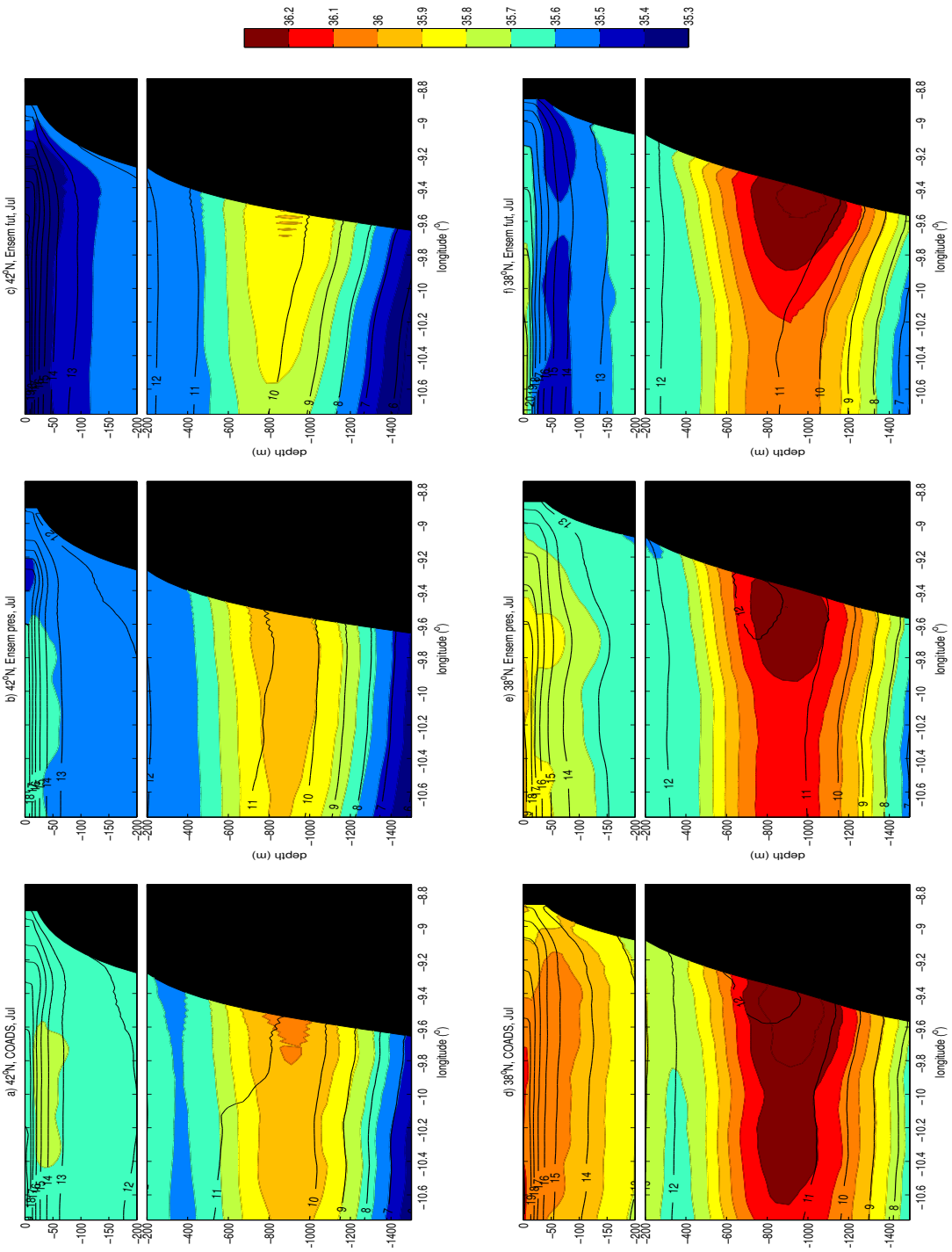

Figure 6.6: Same as Figure 6.5 but for July.

compares well with COADS and salinity maintains a -0.1 difference, at 38^{o}N temperature is lower by about 1^oC and salinity differences can reach 0.3, consistent with a stronger and wider upwelling observed in Figure 6.4.

For the future (Figures 6.5,6.6 c,f), below 300 m, in January there are no significant changes neither in temperature nor in salinity; but in July, although overall the same vertical structure of T and S over the slope is observed, there is a difference of roughly 0.1 in salinity at the depths of the MW. In the upper 300 m, in winter, temperatures are 0.5^oC higher at deeper levels and the difference increases up to +1.5^oC at the surface and near the coast. In summer, near the coast the cross-shore gradient is clearly stronger, and offshore in the upper 100 m temperatures are up to +2^oC warmer. In what concerns salinity, differences are more striking, from about -0.1 in winter to -0.3-0.4 in summer. Note that at 38^{o}N the highest negative anomalies are at the subsurface, while a saltier lens is placed at the surface. We have observed in Figure 6.4 that at the southern WIM the upwelling band was considerably narrower in the future.

Figures 6.7 and 6.8 present zonal vertical slices at the same sections of meridional velocity for January and July, respectively, again for the three runs. For the present in January, at 42^{o}N (Figure 6.7 a,b), the ensemble shows stronger poleward flow than COADS, consistent with what was observed in both surface fields and zonal sections of T and S. There is also an offshore reverse in flow direction.

At 38^{o}N (Figure 6.7 d,e), the flow patterns are similar, with weak poleward flow tendency at the upper slope, some equatorward flow throughout the water column at the 400 m isobath (weaker in the ensemble than in COADS), and then poleward flow at mid-depths corresponding to the MW flow and equatorward flow offshore, both enhanced in the ensemble. In July (Figure 6.8), at both latitudes, the ensemble shows stronger and wider upwelling, with velocities higher than 5 $cm\ s^{-1}$ reaching deeper levels (400 m as opposed to 100 m in COADS). The poleward flow from the surface down to the slope between 9.5^{o}W and 10^{o}W is equally strong at 38^{o}N, but weaker at 42^{o}N.

The differences between present and future in winter (Figure 6.7 c,f) are not very striking. There is a more generalized tendency for poleward flow at 42^{o}N, and at 38^{o}N there is a shift of the poleward flow maximum from mid-depths to the subsurface ($\sim$ 10 $cm\ s^{-1}$). In summer (Figure 6.8 c,f), although upwelling intensifies at the surface by about $5-10\ cm\ s^{-1}$, its width and depth decrease, seen by the more restricted equatorward jet, reaching down to 300 m at 42^{o}N and 100 m at 38^{o}N in depth instead of 600 m in the present, and also much closer to the coast. To compensate, the poleward flow occupies most of the slope and is wider at the surface.

As suggested by Figures 6.4 and 6.6, the upwelling band is narrower and shallower in the future, although with stronger equatorward velocities, likely due to the intensification of the equatorward winds (Figure 6.2). This limitation in width and depth of upwelling may be explained by the different offshore-onshore warming rates (lower temperature rise near the coast than in the open ocean) and the consequent strengthening of the upper level stratification. On the other hand, there is an intensification of poleward flow adjacent to the upwelling band, especially at 42^{o}N.

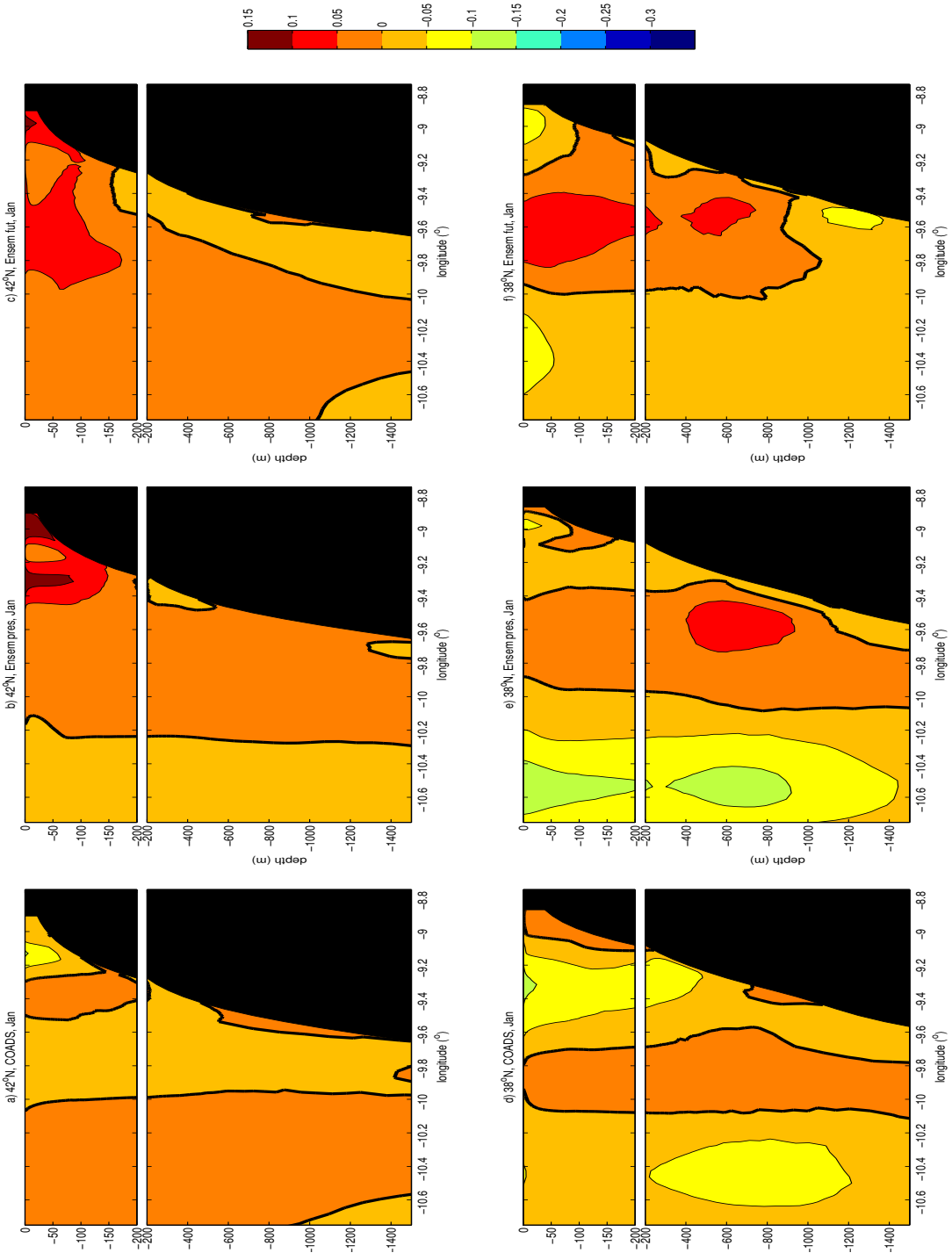

Figure 6.7: Zonal vertical sections at 42^{o}N (upper row) and 38^{o}N (lower row) of the mean meridional velocity component ($m\ s^{-1}$) for January, from the three runs: COADS (a,f), present ensemble (b,g) and future ensemble (c,h).

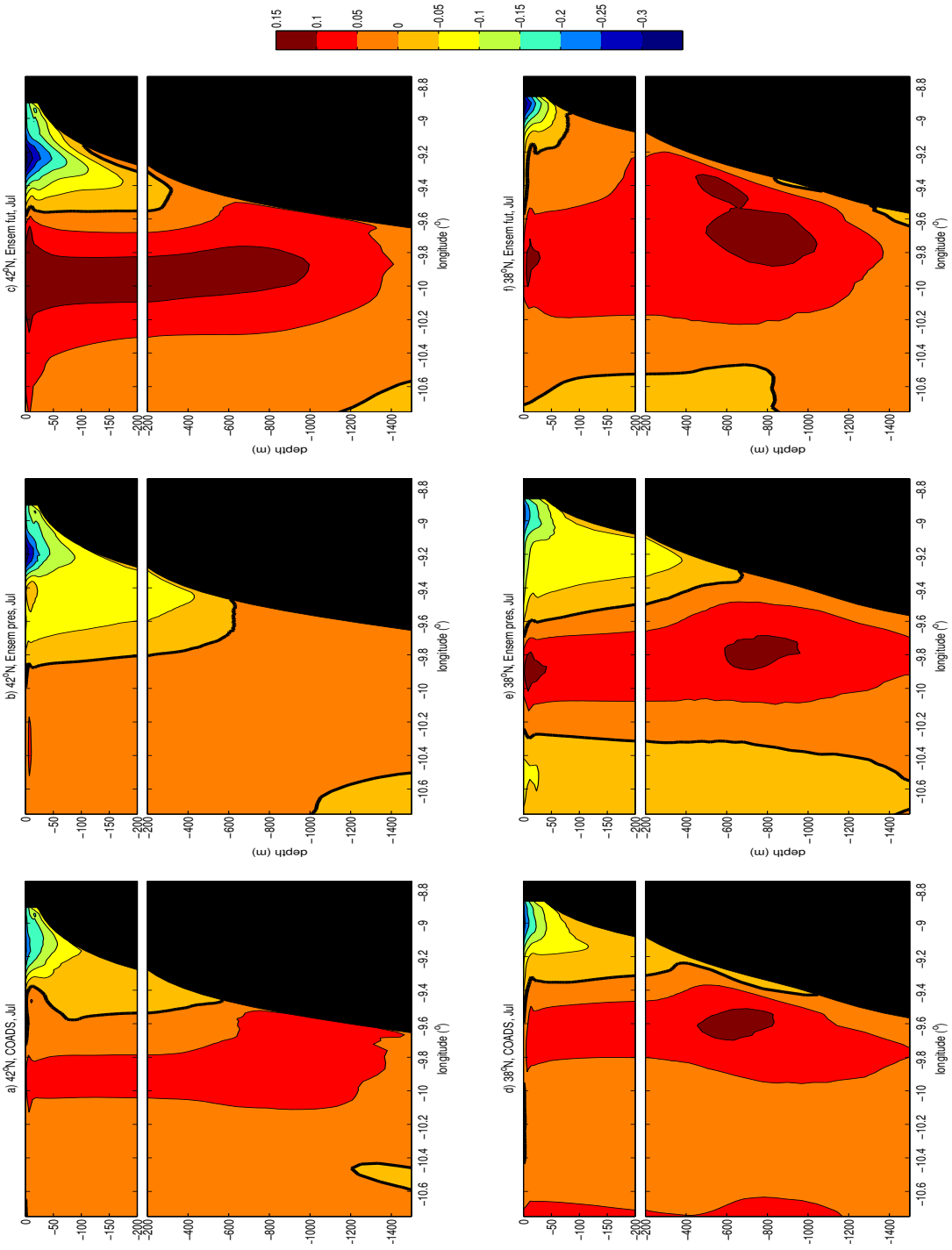

Figure 6.8: Same as Figure 6.7 but for July.

6.3.4 Seasonal Analysis

From the previous sections it becomes clear that future changes depend on the month and also on the distance from the coast. In this section, these differences are analyzed from a seasonal point of view, as well as a function of longitude.

Figure 6.9 presents the seasonal evolution of sea surface temperature (SST — left column) and salinity (SSS — right column) for present and future at the five points marked on Figure 6.1, located at the 100-m isobath. The strongest differences are observed in winter and autumn, and the lowest during spring and summer. SST does not present a sinusoidal-like evolution such as would be expected offshore. On the contrary, at these points, minimum temperatures are registered between February and April, and a second minimum is reached between June and August. The highest temperatures are observed in autumn, when the northerly winds begin to relax after the upwelling season. These peaks also occur in the future, although enhanced. The SST difference for months May to August is of $+1^oC$, while for the remaining months the difference is about $+2^oC$. In October at 40^oN, differences reach $+2.5^oC$, whereas at 41^oN and 42^oN the lowest differences are found in August and September (0-0.5^oC). Concerning SSS, the general difference between present and future is of -0.2. Moreover, while at present the SSS minimum is reached in July (with the exception of the 42^oN section, where this minimum is observed in September), in the future the lowest SSS is found in May for the southern sections and also in September for the northern sections. May is the month where the future-present difference is the highest, reaching -0.3. The May and September double low peak results in a summer increase of salinity, which, being absent in the present series, means a lower difference (about -0.1) between present and future for these months.

From Figure 6.9 it is evident that the temperature and salinity seasonal evolution depend on latitude, but these variables may also depend on longitude. Hence, monthly mean plots of SST and SSS future minus present differences along longitude are shown on Figure 6.10, averaged along three latitudinal bands: 41-43^{o}N, 39-41^{o}N and 37-39^{o}N.

In what concerns temperature, from a first observation, there is not a striking difference between offshore/near shore locations. At the northern band (Figure 6.10 a), the general difference is of +1 to $+1.5^oC$. The exception is between July and September, where a difference as low as zero can be found centered at 9.3^{o}W, the average location of the 100-m isobath at that latitudinal band (see Figure 6.1), where the upwelling jet is the strongest (as discussed further on). Onshore, differences reach the highest ($+2^oC$) difference in winter and the lowest ($+0.5^oC$) in summer. At the central band (Figure 6.10 c), differences are of mostly $+1.5^oC$ except for the upwelling season (May to September), where they are in general lower, being the lowest ($<0.5^oC$) close to the coast. Concerning the southernmost band (Figure 6.10 e), the strongest differences are again around 9.2-9.3^{o}W, with differences reaching +2-3^oC between August and October. The early summer interval (May-July) is once more the one that presents the lowest SST differences (+1-1.5^oC).

In what concerns salinity (Figure 6.10 b,d,f), the northern band shows strong negative differences offshore between May and November (from -0.25 to -0.35), while near shore during summer differences are again the lowest. At the central band, SSS differences vary

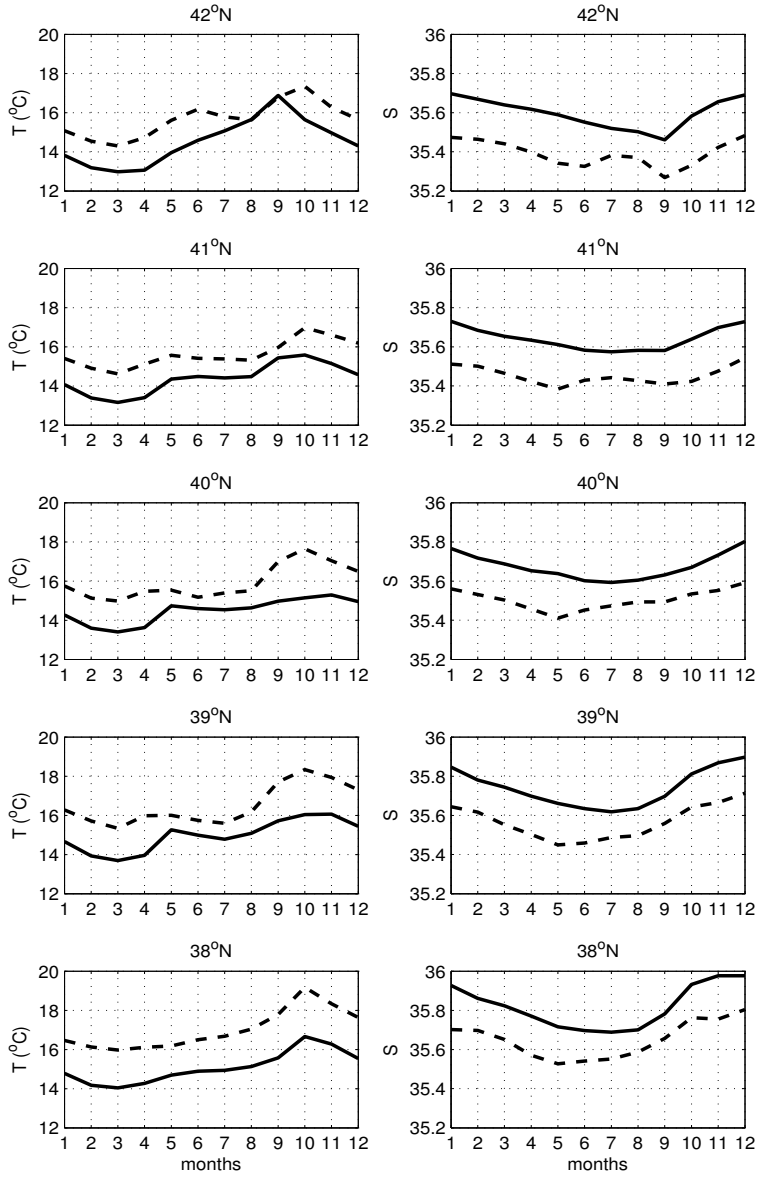

Figure 6.9: Seasonal evolution of SST (^oC) (left column) and SSS (right column) for present (solid line) and future (dashed line) at the five points marked on Figure 6.1, located at the 100-m isobath.

in general between -0.15 and -0.2, with differences of less than -0.1 near the coast between June and September. Finally, at the southern band, the coastal summer low differences of about -0.1 are displaced toward offshore longitudes.

From these observations we can draw that, despite the warmer temperatures in about 2^oC and fresher waters in about 0.2 in the future, these differences are smaller near the coast and during the upwelling season. This confirms the different SST increase between coastal and offshore locations, responsible for strengthening of the upper layer stratification. Nevertheless, the surface mean fields and WIM cross-sections revealed that upwelling did not weaken, which could be expected from this increase in stratification. Furthermore, it is interesting to note that SST and SSS strong/weak differences do not exactly correspond in time. For instances, the coastal SST minimum differences occur in May-June, while coastal SSS minimum differences occur in July-August.

Given these previous SST and SSS considerations concerning upwelling, and since the latter is strongly dependent of wind stress, we look now at the upwelling index (UI). As defined in section 3.2.1, UI is a measure of favorable or unfavorable upwelling conditions. One of its formulations is based on the cross-shore Ekman transport derived from wind stress (Bakun, 1973), which given the quasi-meridional orientation of the WIM, can be considered to be solely the Ekman transport zonal component Q_x, which is given by the following equation:

$$Q_x = \frac{\tau_y}{\rho_w f} \tag{6.1}$$

where $\tau_y = \rho_a C_D |W| W_y$ is the meridional wind stress component ($\rho_a \approx 1.22\ kg\ m^{-3}$ is the air density, C_D an adimensional drag coefficient (variable, dependent on the wind intensity — Large and Pond, 1981), $|W|$ is the module of the wind at 10 m, and W_y its meridional component), ρ_w is the average density of seawater ($\approx 1025\ kg\ m^{-3}$), and $f = 2\Omega \sin(\theta)$ is the Coriolis parameter (Ω is the angular velocity of the Earth and θ the latitude). $UI = -Q_x$ is multiplied by a factor of 1000, so that the measure translates a displacement of volume for each kilometer of coast ($m^3 s^{-1} km^{-1}$). UI is positive when the Ekman transport is oriented offshore (i.e. westward) and thus upwelling-favorable, and negative when the Ekman transport is onshore (eastward) and thus downwelling-favorable.

Figure 6.11 shows the seasonal upwelling index computed at three points along the WIM (see Figure 6.1) for the three runs: COADS, present ensemble and future ensemble. First of all, there is a striking difference between COADS and ensemble, with the former presenting a double peak in April and July and the latter in July only. Also, the COADS UI is always positive, that is, upwelling-favorable throughout the year, whereas the ensemble shows a stronger seasonality, with downwelling-favorable conditions from November to April. This was already observed in the seasonal wind stress fields (Figure 6.2). The differences between present and future are basically an enhancement toward upwelling-favorable conditions: in autumn/winter UI is less negative, that is, less downwelling-favorable, and in spring/summer is higher. Also, the upwelling season seems to start earlier (April instead of May) and end later (October instead of September), at least in the southernmost point. Note that in the northernmost point future UI equals the COADS peak for June and July

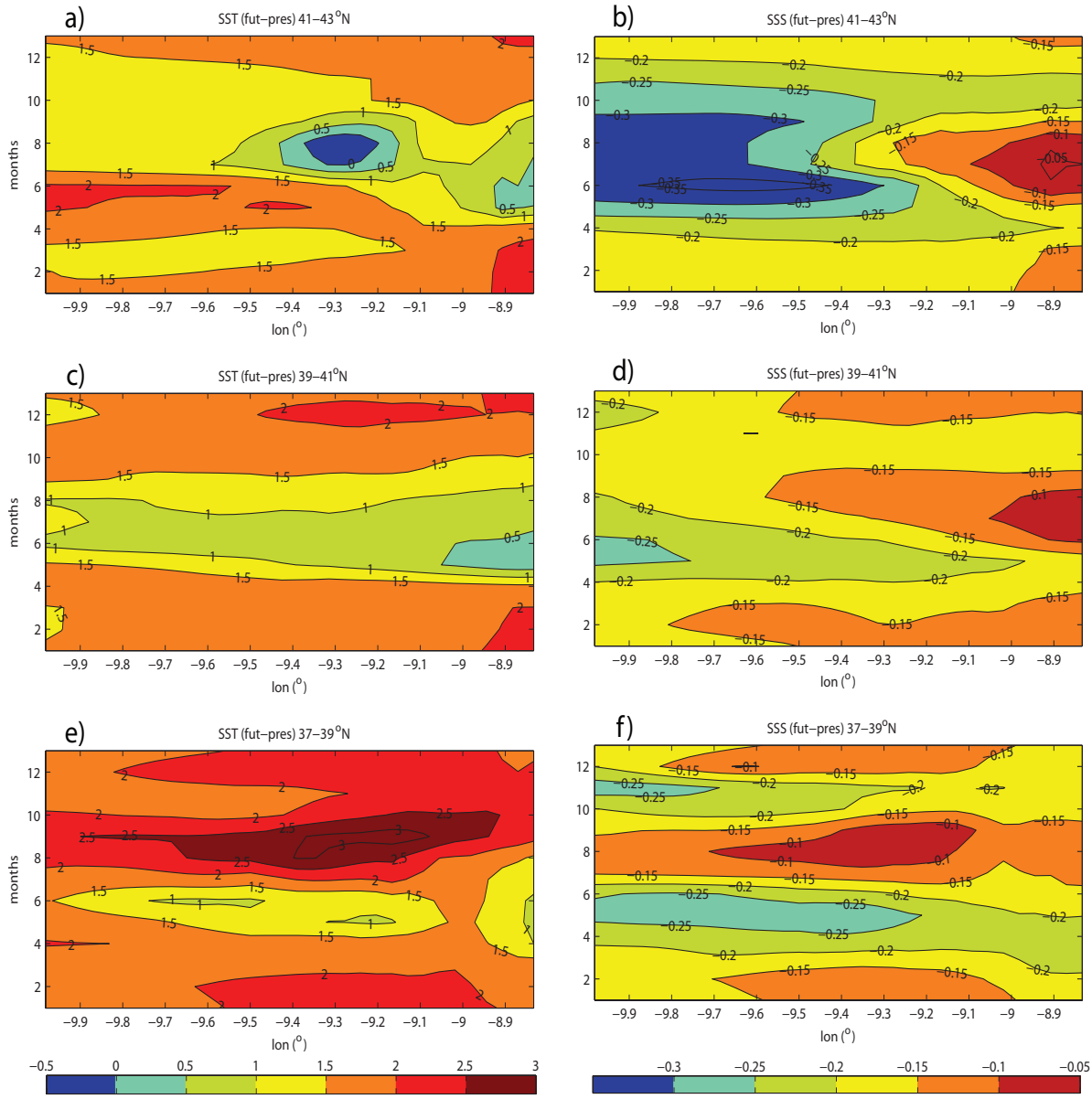

Figure 6.10: Monthly mean plots of SST (^oC) and SSS future minus present differences as a function of longitude for three latitudinal bands: (a,b) 41-43^{o}N; (c,d) 39-41^{o}N; (e,f) 37-39^{o}N.

(the present ensemble UI is lower than COADS for those months), whereas in the other points present ensemble overestimates UI in relation to COADS.

The reason for these changes is evident in the wind stress seasonal maps (Figure 6.2). Regarding the WIM, in winter and autumn the ensemble, both present and future, show similar patterns: southwesterly wind stress north of 39^{o}N and westerly wind stress south of 39^{o}N. Thus, in these seasons UI is negative. As seen before, COADS wind stress has always a southward component, independently of the season; hence, UI is always positive. In summer, the increase in UI is similar for all latitudes and reflects the intensification of the northerly wind stress seen in the seasonal fields.

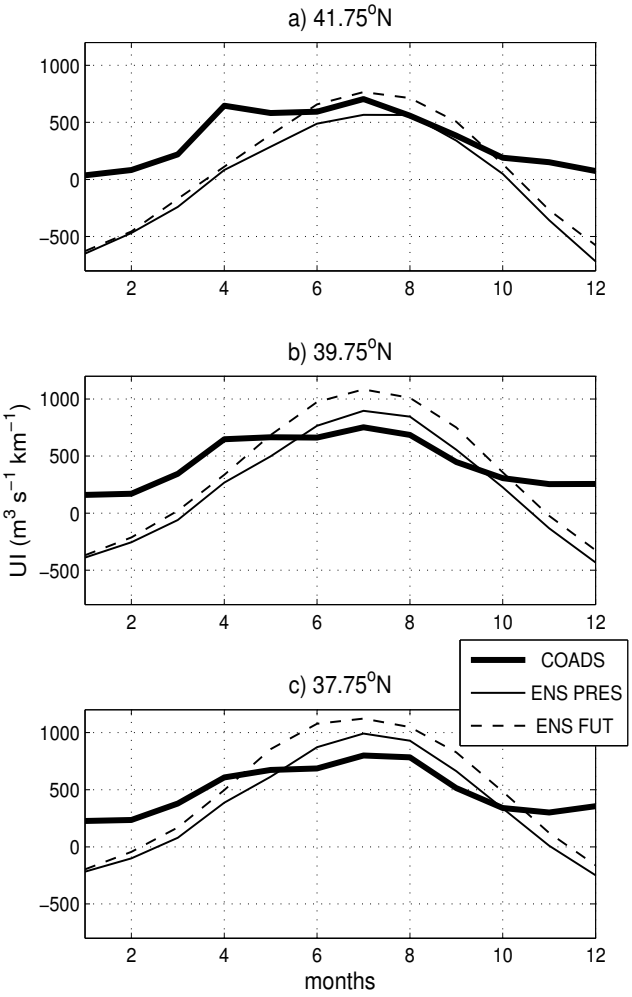

Figure 6.11: Seasonal upwelling index ($m^3 s^{-1} km^{-1}$) computed at three points along the WIM (see Figure 6.1) for the three runs: COADS (bold line), present ensemble (solid line) and future ensemble (dashed line).

6.4 Discussion

The work comprised in this chapter aimed at taking advantage of state-of-the-art climate projections and applied it to regional ocean modeling. Due to the coarse resolution of global climate models, selecting the best model or method with respect to forcing is difficult and debatable. Based on the sensitivity study of chapter 5, the ensemble mean of a set of CGCMs was selected as the most adequate, because not only did it compare best with climatological values, but also does it minimize individual uncertainties of the global models, in spite of the loss of horizontal resolution relative to some of the CGCMs.

In agreement with the general tendencies of future climate scenarios, and in particular in what concerns A2, the ocean off the WIM under increased greenhouse gas concentration is found to warm as expected (e.g. Casey and Cornillon, 2001). Likewise, given the tendency for the polar icecaps to melt or at least to become absent during the warm seasons, a freshwater input is associated to future climate, and consequently a general decrease in the salinity field (Gregory et al., 2005; Stouffer et al., 2006). However, in the coastal ocean, more regional phenomena are at play and future assessments become more difficult.

Sea surface temperature and salinity change differently, depending on season, latitude and distance to the coast. In winter, SST changes are higher at more coastal locations than in the open ocean, especially in southwestern WIM, in agreement with the tendency observed by Relvas et al. (2009). Conversely, SSS changes are lower onshore than offshore.

In summer, offshore waters undergo a stronger increase in temperature than coastal waters, including the regions associated with filament generation (Cape Finisterre and the Estremadura Promontory). Again, the southwestern coast is the onshore region with the highest temperature increase. On the other hand, SSS maintains its winter tendency: it presents the lowest decrease alongshore, especially around Galicia and northern WIM. That is, SST differences tend to be higher to the south and SSS differences higher to the north. Furthermore, nearshore, SST and SSS differences are lower during the upwelling season than in the remaining months.

Concerning specifically the phenomenon of upwelling, there are two factors that need to be considered when evaluating climate change impacts on these systems: the change in wind stress and the change in the offshore-onshore SST gradient. First of all, they are not independent from one another. Second, for a reliable assessment of wind stress change we would need reliable future prediction of pressure systems, which have still much uncertainty as far as numerical models are concerned (e.g. Seidel et al., 2008).

There are two possible consequences of climate change, particularly the surface air warming, on eastern boundaries:

1) The summer over-land thermal low intensifies as a consequence of the more rapid temperature increase over land than over ocean; hence, equatorward winds also intensify, as well as upwelling (Bakun, 1990);

2) The general warming of the ocean increases the offshore-onshore SST gradient, typical of upwelling, thus weakening the upwelling itself.

Di Lorenzo et al. (2005) found in observations of the California Current System, for period 1949-2000, that although upwelling-favorable winds had intensified in average during

summer, a general warming had also taken place in the upper 200 m. This warming, in conjunction with the redistribution of heat carried out by the southward currents, brings about a deepening of the thermocline and a stronger stratification. This increase in stratification reduces the vertical transport associated with upwelling and counteracts the strengthened upwelling-favorable winds, with the result of upwelling intensity and frequency decrease. So, in fact, the two factors are at play, but one prevails over the other.

This might be the case of our modeling results: while a general increase in equatorward wind stress is predicted, it is also true that, although upwelling does not undergo weakening, it undergoes narrowing and shallowing of its jet, most likely due to the increase in stratification.

Furthermore, this two-factor dynamics is possibly why observations seem contradictory, at least for the Iberian Upwelling System, as previously mentioned. There seems to be concordance in what concerns a general warming trend in the past decades (e.g. Ruiz-Villarreal et al., 2008), regardless if upwelling intensity is increasing or decreasing. However, it is not possible to draw definite conclusions on whether this warming is the cause for the weakening of upwelling through the increase in stratification.

Moreover, there are also contradictory observations concerning wind stress in the past decades, with some works reporting intensification of upwelling-favorable wind stress (Narayan et al., 2010), which is in agreement with our results, others reporting the opposite, especially in the northwestern coast of the Iberian Peninsula (e.g. Ruiz-Villarreal et al., 2008), and others yet finding no change in wind stress whatsoever (Barton et al., 2013).

In this case, although we register an increase in UI, our modeling study seems to agree with the view in which the warming of coastal waters inhibits vertical transport, thus leading to a narrowing of the upwelling jet. However, given the coarse resolution of the ensemble forcing and associated uncertainties, we cannot ascertain which of the factors prevail over the other.

Previous similar modeling studies on the different upwelling systems reveal intensified alongshore equatorward winds (Snyder et al., 2003 for the California system; Garreaud and Falvey, 2009 for the Chilean coast; Miranda et al., 2012 for the Iberian system). These studies conclude, from this increase, that it is very likely that upwelling will also increase in intensity and frequency. In spite of this, our in-depth results indicate that it may not be as direct as the latter authors postulate; as previously discussed, the warming of coastal waters and consequent increment in stratification may in fact cause net weakening of upwelling.

Global climate models still have much uncertainty. In this study we have tried to put to use these state-of-the-art tools, along with a high-resolution ocean model configuration, and build a consistent evaluation study of a future scenario applied to an upwelling system. However, there are clear handicaps of CGCMs in reproducing the dynamics of these systems, and in particular the Iberian Upwelling System. The most striking evidence of this is the continuous upwelling signal along the Strait of Gibraltar reproduced by both ensemble-forced runs, as if there were no geographic interruption. This is due to CGCM low resolution, which also inhibits a more thorough analysis of, for instances, the wind stress fields and wind stress curl, crucial in dictating upwelling variability.

Chapter 7

Conclusions

The purpose of this work was to develop a study of the Western Iberian Margin upper ocean hydrography and dynamics, and to carry out not only a seasonal characterization but also an interannual variability analysis, and to explore what the future could hold.

The basis for this study was a regional model configuration that consisted on a two-domain nesting, designed such that the larger domain would resolve the large-scale flow and properly introduce water masses and fluxes into the smaller, high-resolution domain through the boundaries. The high-resolution domain would then be able to reproduce, at once, the circulation at the shelf and at the slope, and the MW spreading, taking into account the open ocean circulation and the strong bathymetric irregularities. This configuration, along with a proper advection scheme that allows to avoid diapycnal mixing errors associated with σ-coordinate models, was found suitable to achieve the proposed objectives, and allowed to study the WIM mean circulation (chapter 2), its interannual variability (chapter 3), larvae connectivity patterns (chapter 4), and finally possible future implications in the context of a climate change scenario (chapter 6), as well as the sensitivity of global climate models in forcing such a scenario (chapter 5).

From chapter 2 it became clear that the WIM is characterized by a complex oceanic system, with both strong interannual variability and marked seasonal cycles. The mean circulation results from the interaction of three main phenomena: coastal upwelling, the Iberian Poleward Current and Mediterranean Water outflow through the Strait of Gibraltar. The region dynamics is also influenced by large-scale phenomena such as the eastward extension of the Azores Current, the structure of the meridional density gradients, or the less energetic offshore, equatorward Portugal Current. Furthermore, small-scale localized phenomena such as the exchange of waters through the Strait of Gibraltar, which spreads throughout the Eastern North Atlantic, or river inflow, particularly at the surface layers and along the continental shelf, also play a role in the system's dynamics. The most important results drawn from this chapter are the following:

- The WIM mean circulation presents a tendency for poleward flow along the slope of the WIM, although with some evidences of equatorward flow mostly in spring;
- Wind-forced upwelling-driven equatorward flow is observed along the continental

shelf in summer, in coexistence with poleward flow offshore;

- The main paths of poleward flow appear to be linked to the MW vein along the WIM (barotropic character);

Furthermore, a Lagrangian application was carried out over this climatological run with the purpose of assessing the origin of the waters that upwell along the WIM during summer. The experimental set was a back-in-time deployment of Lagrangian particles, that is, the points of departure were four bands along the WIM at the ocean subsurface (upwelling region) and particles travelled back 30 days to see where they had originated from. Here are some remarks in what concerns the origin of upwelled waters along the WIM:

- There is a higher number of upwelling particles coming from the north and from the upper 100 m (the main pathway of the upwelling equatorward jet);
- The shallower they upwell, the shallower their origin is;
- The particles that travel the longest distances originate at the shallowest depths, and vice-versa;
- The particles that come from the deepest levels trace trajectories the closest to the coast;
- The particles that have origins the farthest away from their upwelling spots (and hence the shallowest origins and trajectories closest to the coast) seem more dependent on the equatorward jet, while particles that originate closer to the coast (and hence at deeper levels and from offshore) seem modulated by mesoscale activity.

With chapter 3, the intention was to broaden the climatological view of chapter 2 and extend it to an interannual study of the WIM dynamics. First, a description of a 45-year long (1967-2011) upwelling index dataset was carried out, in an attempt to characterize the mean wind conditions and their variability. Then, using an 11-year (2001-2011) ROMS simulation, an analysis of anomalous years was attempted, based on SST, wind stress, and salinity and surface velocity profiles. First of all, ROMS was able to reproduce reasonably well the SST anomalies for the entire study period, as well as temperature and salinity profiles given by Argo floats and surface currents for the one year and a half period available in observations. Secondly, a characterization of particular events of high/low salinities and/or strong alongshore velocities was carried out. We successfully identified episodes of S-N saline water advection, and found evidence of the poleward flow offshore shift during summer, in the presence of upwelling. Furthermore, many of these modeled events have correspondence with observational studies in the literature.

Making use of this interannual study, chapter 4 was a Lagrangian application over the same ROMS run for period 2001-2011 with realistic forcing, in order to compute some generic larvae connectivity aspects of SD. Two simulations were carried out: one with diel vertical motion (DVM), and one without. In doing so, the purpose was to check the role of

this diurnal/nocturnal migration of larvae in the supply and recruitment along the WIM, in equally-spaced adjacent regions with equal areas. These were the main conclusions reached:

- Wind stress direction plays an important role: in the occurrence of poleward events, the direction of supply is mainly to the north, whereas when equatorward wind prevails supply is carried out in both directions;
- The Estremadura Promontory works as a geographical gap between northern and southern WIM, consisting in a natural obstacle for supply from the south.
- Supply is strongly influenced by topography: in the presence of pronounced features such as capes, promontories and general uneven coastline, retention is higher, whereas in regions where the coastline is roughly linear it is where the most successful sources are located;
- In the simulation with DVM, retention increases throughout the domain (dispersal distances are greater) and supply to the south increases significantly, due to the lesser offshore advection once the particles are not subject to Ekman transport.

Having in mind an ocean modeling essay applied to a future climate scenario, chapter 5 comprised an evaluation of several global climate models (GCM) as forcing for ROMS for present conditions. The chapter was divided in two parts: the first consisted in a GCM inter-comparison regarding all variables needed to force ROMS, where difference fields were analyzed, as well as seasonal averages and RMSEs; in the second part, two of these GCMs served as forcing for two ROMS runs aiming at a sensitivity assessment. The ultimate goal was to find the most suitable GCM to reproduce the present climatological atmospheric and ocean conditions at the surface. No GCM was found to be perfect in what concerns every variable; they all had strengths and weaknesses. The main conclusion was that the multi-model ensemble mean (GCM climatological average) would be the most appropriate forcing among the GCM dataset.

After this assessment on the uncertainties of global climate models in reproducing the present hydrography and dynamics of the WIM, and based on that conclusion, in chapter 6 SD was forced with a future climatology. Besides the general warming of the ocean surface and subsurface (although varying in longitude and latitude) due to the increase in the surface air temperature, expected by every future climate scenario, a general decrease in salinity brought about by melting of ice in the poles was also found. Furthermore, although global climate models typically expect, for eastern boundary systems, strengthening of the alongshore equatorward winds and hence upwelling, the results do not show such a clear outcome. Indeed, as a consequence of a higher warming rate of the ocean temperature offshore than onshore, the SST cross-shore gradient intensifies, strengthening stratification, which inhibits vertical motion. As a result, the upwelling-associated equatorward jet intensifies, but the upwelling coastal band of colder and fresher waters is more restricted in width and depth, suggesting that both mechanisms are at play. The following main conclusions were drawn from this study:

- There is a general temperature increase and salinity decrease, particularly in the upper 100-200 m;
- Winter: SST increase is higher onshore and SSS decrease is higher offshore;
- Summer: SST increase is higher offshore and SSS decrease is higher offshore;
- There is strengthening of the SST offshore-onshore gradient, and thus of stratification;
- In spite of meridional wind stress intensification in summer, there is narrowing and shallowing of the upwelling jet, although at the surface there may be an equatorward velocity increase.

These high-resolution ROMS configurations, which have also been successfully implemented in operational mode (http://climetua.fis.ua.pt/fields/oceanoAtlantic/templ1) and in biogeochemical studies (Reboreda et al., submitted, in review), enabled a study encompassing seasonality, mean behavior, interannual variability, future changes, and larval dispersion considerations. Overall, I believe this work constitutes a relevant contribution in the understanding of the Iberian Upwelling System, addressing important physical aspects of the coastal transition zone.

Bibliography

Albert, A., Echevin, V., Lévy, M., and Aumont, O., 2010. Impact of nearshore wind stress curl on coastal circulation and primary productivity in the Peru upwelling system. *Journal of Geophysical Research*, 115, C12033.

Alonso, J., de Castillejo, F.F., Diaz del Rio, G., Marcote, D., and Casas, G., 1995. Preliminary Results of Current Measurements in the North West of the Iberian Peninsula. *MORENA Scientific and Technological Report no. 15*, Instituto Español de Oceanografía C.O., La Coruña, Spain.

Alvarez, I., Gómez-Gesteira, M., deCastro, M., and Dias, J.M., 2008. Spatiotemporal evolution of upwelling regime along the western coast of the Iberian Peninsula. *Journal of Geophysical Research*, 113, C07020, doi:10.1029/2008JC004744.

Alvarez, I., Gómez-Gesteira, M., de Castro, M., Lorenzo, M.N., Crespo, A.J.C., and Dias, J.M., 2011. Comparative analysis of upwelling influence between the western and northern coast of the Iberian Peninsula. *Continental Shelf Research*, 31, 388-99.

Álvarez-Salgado, X.A., Figueiras, F.G., Pérez, F.F., Groom, S., Nogueira, E., Borges, A.V., Chou, L., Castro, C.G., Moncoiffé, G., Ríos, A.F., Miller, A.E.J., Frankignoulle, M., Savidge, G., and Wollast, R., 2003. The Portugal coastal counter current off NW Spain: new insights on its biogeochemical variability. *Progress in Oceanography*, 56, 2, 281-321, doi:10.1016/S0079-6611(03)00007-7.

Álvarez-Salgado, X.A., Rosón, G., Pérez, F.F., and Pazos, Y., 1993. Hydrographic variability off the Rías Baixas (NW Spain) during the upwelling season. *Journal of Geophysical Research*, 98 (C8), doi:10.1029/93JC00458.

Amante, C., and Eakins, B.W., 2009. ETOPO1 1 Arc-Minute Global Relief Model: Procedures, Data Sources and Analysis. *NOAA Tech. Memorandum NESDIS NGDC-24*, 19 pp.

Ambar, I., and Howe, M.R., 1979a. Observations of the Mediterranean outflow I — Mixing in the Mediterranean outflow. *Deep-Sea Research Part A*, 26, 5, 535-554.

Ambar, I., and Howe, M.R., 1979b. Observations of the Mediterranean outflow II — The deep circulation in the vicinity of the Gulf of Cadiz. *Deep-Sea Research Part A*, 26, 5, 555-568.

Amorim, F.N., Dubert, J., Nolasco, R., Oliveira, P., and Moita, T., 2012. Estudo dos processos físicos subjacentes à dinâmica de blooms de algas tóxicas na região adjacente à costa central de Portugal. *Encontro de Oceanografia Física*, Quiaios, Portugal, personal communication.

Annan, J.D., and Hargreaves, J.C., 2010. Reliability of the CMIP3 ensemble. *Geophysical Research Letters*, 37, L02703, doi:10.1029/2009GL041994.

Antonov, J.I., Seidov, D., Boyer, T.P., Locarnini, R.A., Mishonov, A.V., Garcia, H.E., Baranova, O.K., Zweng, M.M., and Johnson, D.R., 2010. World Ocean Atlas 2009, Volume 2: Salinity. S. Levitus, Ed. *NOAA Atlas NESDIS 69*, U.S. Government Printing Office, Washington, D.C., 184 pp.

Arístegui, J., Barton, E.D., Álvarez-Salgado, X.A., Santos, A.M.P., Figueiras, F.G., Kifani, S., Hernández-León, S., Mason, E., Machú, E., and Demarcq, H., 2009. Sub-regional ecosystem variability in the Canary Current upwelling. *Progress in Oceanography*, 83, 33-48.

Bakun, A., 1973. Coastal upwelling indices, west coast of North America, 1946-71. *U.S. Department of Commerce*, National Oceanic and Atmospheric Administration, National Marine Fisheries Service.

Bakun, A., 1990. Global Climate Change and Intensification of Coastal Ocean Upwelling. *Science*.

Bakun, A., Field, D.B., Redondo-Rodriguez, A., and Weeks, J.W., 2010, Greenhouse gas, upwelling-favorable winds, and the future of coastal ocean upwelling ecosystems. *Global Change Biology*, 16, 1213-1228.

Barja, F.J.R., and Lestegás, F.R., 1992. Os Ríos Galegos — Morfoloxía e Réxime, *Consello da Cultura Galega*, Ponencia de Patrimonio Natural, Santiago de Compostela, Spain.

Barton, E.D., Arístegui, J., Tett, P., Canton, M., Garcia-Braun, J., Hernández-León, S., Nykjaer, L., Almeida, C., Almunia, J., Ballesteros, S., Basterretxea, G., Escanez, J., Garcia-Weill, L., Hernandez-Guerra, A., Lopez-Laatzen, F., Molina, R., Montero, M.F., Navarro-Perez, E., Rodriguez, J.M., van Lenning, K., Vélez, H., and Wild K., 1998. The transition zone of the Canary Current upwelling region. *Progress in*

Oceanography, 41, 455-504.

Barton, E.D., Field, D.B., and Roy, C., 2013. Canary current upwelling: More or less?. *Progress in Oceanography*, 116, 167-178.

Batteen, M.L., Martinez, J.R., Bryan, D.W., and Buch, E.J., 2000. A modeling study of the coastal eastern boundary current system off Iberia and Morocco. *Journal of Geophysical Research*, 105 (C6), 14173-14195.

Batteen, M.L., Martinho, A.S., Miller, H.A., and McClean, J.L., 2007. A process-oriented modelling study of the coastal Canary and Iberian Current system. *Ocean Modelling*, 18, 1-36.

Blanke, B., Penven, P., Roy, C., Chang, N. and Kokoszka, F., 2009. Ocean variability over the Agulhas Bank and its dynamical connection with the southern Benguela upwelling system. *Journal of Geophysical Research*, 114, C12028.

Bograd, S.J., Schroeder, I., Sarkar, N., Qiu, X., Sydeman, W.J., and Schwing, F.B., 2009. Phenology of coastal upwelling in the California Current. *Geophysical Research Letters*, 36, L01602.

Borges, M.F., Santos, A.M.P., Crato, N., Mendes, H., and Mota, B., 2003. Sardine regime shifts off Portugal: a time series analysis of catches and wind conditions. *Scientia Marina*, 67, S1, doi:10.3989/scimar.2003.67s1235.

Bower, A.S., Armi, L., and Ambar, I., 1995. Direct evidence of meddy formation off the southwestern coast of Portugal. *Deep-Sea Research I*, 42, 9, 1621-1630.

Carr, S.D., Capet, X.J., McWilliams, J.C., Pennington, J.T. and Chavez, F.P., 2007. The influence of diel vertical migration on zooplankton transport and recruitment in an upwelling region: estimates from a coupled behavioral-physical model. *Fisheries Oceanography*, 17, 1-15.

Casey, K.S., and Cornillon, P., 2001. Global and Regional Sea Surface Temperature Trends. *Journal of Climate*, 14, 3801-3818.

Chavez, F.P., and Messié, M., 2009. A comparison of Eastern Boundary Upwelling Ecosystems. *Progress in Oceanography*, 83, 80-96, doi: 10.1016/j.pocean.2009.07.032.

Chhak, K., and Di Lorenzo, E., 2007. Decadal variations in the California Current upwelling cells. *Geophysical Research Letters*, 34, L14604.

Coelho, H.S., R.J.J. Neves, M. White, P.C. Leito, and A.J. Santos, 2002. A

model for ocean circulation on the Iberian coast. *Journal of Marine Systems*, 32, 1-3, 153-179, doi:10.1016/S0924-7963(02)00032-5.

Colas, F., 2003. Circulation et dispersion lagrangiennes en Atlantique Nord-Est. *PhD Thesis*, Université de Bretagne Occidentale, 246 pp.

Collins, W.D., Ramaswamy, V., Schwarzkopf, M.D., Sun, Y., Portmann, R.W., Fu, Q., Casanova, S.E.B., Dufresne, J.L., Fillmore, D.W., Forster, P.M.D., Galin, V.Y., Gohar, L.K., Ingram, W.J., Kratz, D.P., Lefebvre, M.P., Li, J., Marquet, P., Oinas, V., Tsushima, Y., Uchiyama, T., and Zhong, W.Y., 2006. Radiative forcing by well-mixed greenhouse gases: Estimates from climate models in the Intergovernmental Panel on Climate Change (IPCC) Fourth Assessment Report (AR4). *Journal of Geophysical Research*, 111, D14317, doi:10.1029/2005JD006713.

Cordeiro Pires, A., Nolasco, R., and Dubert, J., 2013a. On the origin of summer upwelled waters on the Western Iberian Margin. *Journal of Coastal Research*, Special Issue 65, 1993-1998, doi:10.2112/SI65-337.1

Cordeiro Pires, A., Nolasco, R., Rocha, A., and Dubert, J., 2013b. Assessing future climate change in the Iberian Upwelling System. *Journal of Coastal Research*, Special Issue 65, 1909-1914, doi:10.2112/SI65-323.1

Cordeiro Pires, A., Nolasco, R., Rocha, A., Ramos, A.M., and Dubert, J., in review. Global Climate Models as forcing for regional ocean modeling: A sensitivity study in the Iberian Basin (Eastern North Atlantic). *Climate Dynamics*.

Cowen, R.K., Paris, C.B., and Srinivasan, A., 2006. Scaling of connectivity in marine populations. *Science*, 311, 522-527.

da Silva, A.M., Young, C.C., and Levitus, S., 1994. Atlas of Surface Marine Data 1994. *NOAA Atlas NESDIS 10*. U.S. Department of Commerce, NOAA, NESDIS.

Daniault, N., Mazé, J.P., and Arhan, M., 1994. Circulation and Mixing of Mediterranean Water West of the Iberian Peninsula. *Deep-Sea Research I*, 41, 11-12, 1685-1714, doi:10.1016/0967-0637(94)90068-X.

Delworth, T.L., Broccoli, A.J., Rosati, A., Stouffer, R.J., Balaji, V., Beesley, J.A., Cooke, W.F., Dixon, K.W., Dunne, J., Dunne, K.A., Durachta, J.W., Findell, K.L., Ginoux, P., Gnanadesikan, A., Gordon, C.T., Griffies, S.M., Gudgel, R., Harrison, M.J., Held, I.M., Hemler, R.S., Horowitz, L.W., Klein, S.A., Knutson, T.R., Kushner, P.J., Langenhorst, A.R., Lee, H.C., Lin, S.J., Lu, J., Malyshev, S.L., Milly, P.C.D., Ramaswamy, V., Russell, J., Schwarzkopf, M.D., Shevliakova, E.,

Sirutis, J.J., Spelman, M.J., Stern, W.F., Winton, M., Wittenberg, A.T., Wyman, B., Zeng, F., and Zhang, R., 2006. GFDL's CM2 Global Coupled Climate Models. Part I: Formulation and Simulation Characteristics. *Journal of Climate*, 19, 643-674. doi:10.1175/JCLI3629.1.

Demarcq, H., 2009. Trends in primary production, sea surface temperature and wind in upwelling systems (1998-2007). *Progress in Oceanography*, 1-4, 376-385.

Di Lorenzo, E., Miller, A.J., Schneider, N., and McWilliams, J.C., 2005. The Warming of the California Current System: Dynamics and Ecosystem Implications. *Journal of Physical Oceanography*, 35, 336-362.

Diffenbaugh, N.S., 2005. Response of large-scale eastern boundary current forcing in the 21st century. *Geophysical Research Letters*, 32, L19718, doi:10.1029/2005GL023905.

Domingues, C.M., Church, J.A., White N.J., Gleckler, P.J., Wijffels, S.E., Barker, P.M., and Dunn, J.R., 2008. Improved estimates of upper-ocean warming and multi-decadal sea-level rise. *Nature*, 453, 1090-1094, doi:10.1038/nature07080.

Domingues, C.P., Nolasco, R., Dubert, J. and Queiroga, H., 2012. Model-Derived Dispersal Pathways from Multiple Source Populations Explain Variability of Invertebrate Larval Supply. *PLoS ONE*, 7, 4, e35794.

dos Santos, A., Santos, A.M.P., Conway, D.V.P., Bartilotti, C., Lourenço, P., and Queiroga, H., 2008. Diel vertical migration of decapod larvae in the Portuguese coastal upwelling ecosystem: implications for offshore transport. *Marine Ecology Progress Series*, 359, 171-183, doi:10.3354/meps07341.

Fiúza, A.F.G., 1983. Upwelling patterns off Portugal. In: Suess, J., Thiede, E. (eds), *Coastal upwelling: its sediment record. Part A*, Plenum, New York, 85-98

Flato, G.M., Boer, G.J., Lee, W.G., McFarlane, N.A., Ramsden, D., Reader, M.C., and Weaver, A.J., 2000. The Canadian Centre for Climate Modelling and Analysis global coupled model and its climate. *Climate Dynamics*, 16, 6, 451-467, doi: 10.1007/s003820050339

Friocourt, Y., Levier, B., Speich, S., Blanke, B., and Drijfhout, S., 2007. A regional numerical ocean model of the circulation in the Bay of Biscay. *Journal of Geophysical Research*, 112, C09008, doi:10.1029/2006JC003935.

Frouin, R., Fiúza, A.F.G., Ambar, I., and Boyd, T.J., 1990. Observations of a poleward surface current off the coasts of Portugal and Spain during winter. *Journal*

of Geophysical Research, 95, C1, 679-691.

Fyfe, J.C., Gillett, N.P., and Thompson, D.W.J., 2010. Comparing variability and trends in observed and modelled global mean surface temperature. *Geophysical Research Letters*, 37, L16802, doi:10.1029/2010GL044255.

Gago, J., Cabanas, J.M., Casas, G., and Miranda, A., 2011. Thermohaline measurements in the continental shelf zone of the NW Iberian Peninsula, 1994-2006. *Climate Research*, 48, 219-229, doi:10.33547cr00943.

García-Lafuente, J., Sánchez Garrido, J.C., Díaz del Río, G., Criado Aldeanueva, F., Marcote, D., and Sánchez Román, A., 2008. Low frequency variability of the Mediterranean undercurrent off Galicia, northwestern Iberian Peninsula. *Journal of Marine Systems*, 74 (1-2), 351-363, doi:10.1016/j.jmarsys.2008.02.007.

Garreaud, R.D., and Falvey, M., 2009. The coastal winds off western tropical South America in future climate scenarios. *International Journal of Climatology*, 29, 543-554.

Gómez-Gesteira, M., deCastro, M., Alvarez, I., Lorenzo, M.N., Gesteira, J.L.G., and Crespo, A.J.C., 2008. Spatio-temporal Upwelling Trends along the Canary Upwelling System (1967-2006). *Trends and Directions in Climate Research: Annals of the New York Academy of Sciences*, 1146, 320-337, doi: 10.1196/annals.1446.004.

Gordon, H.B., Rotstayn, L.D., McGregor, J.L., Dix, M.R., Kowalczyk, E.A., OFarrell, S.P., Waterman, L.J., Hirst, A.C., Wilson, S.G., Collier, M.A., Watterson, I.G., and Elliott, T.I., 2002. The CSIRO Mk3 Climate System Model. *CSIRO Atmospheric Research Tech Report*, 60.

Gregory, J.M., Dixon, K.W., Stouffer, R.J., Weaver, A.J., Driesschaert, E., Eby, M., Fichefet, T., Hasumi, H., Hu, A., Jungclaus, J.H., Kamenkovich, I.V., Levermann, A., Montoya, M., Murakami, S., Nawrath, S., Oka, A., Sokolov, A.P., and Thorpe, R.B., 2005. A model inter-comparison of changes in the Atlantic thermohaline circulation in response to increasing atmospheric CO2 concentration. *Geophysical Research Letters*, 32, L12703, doi:10.1029/2005GL023209.

Haidvogel, D.B., and Beckmann, A., 1999. Numerical ocean circulation modeling. *Series on Environmental Science and Management*, 2, Imperial College Press.

Hansen, J., Ruedy, R., Sato, M., and Lo, K., 2010. Global surface temperature change. *Reviews of Geophysics*, 48, RG4004, doi:10.1029/2010RG000345.

Hasumi, H., and Emori, S., 2004. K-1 coupled GCM (MIROC) description.

Center for Climate System Research, University of Tokyo, National Institute for Environmental Studies, Frontier Research Center for Global Change, 38.

Haynes, R., and Barton, E.D., 1990. A poleward flow along the Atlantic coast of the Iberian Peninsula. *Journal of Geophysical Research*, 95 (C7), 11425-11441, doi:0.1029/JC095iC07p11425.

Haynes, R., Barton, E.D., and Pilling, I., 1993. Development, Persistence, and Variability of Upwelling Filaments off the Atlantic Coast of the Iberian Peninsula. *Journal of Geophysical Research*, 98(C12), 681-692.

Hewitson B.C., and Crane, R.G., 1996. Climate downscaling: techniques and application. *Climate Research*, 7, 85-95.

Hoinka, K.P., and Castro, M., 2003. The Iberian Peninsula thermal low. *Quarterly Journal of the Royal Meteorological Society*, 129 (590), 1491-1511, doi: 10.1256/qj.01.189.

Holt, J., Wakelin, S., Lowe, J., and Tinker, J., 2010. The potential impacts of climate change on the hydrography of the northwest European continental shelf. *Progress in Oceanography*, 86, 3-4, 361-379, doi: 10.1016/j.pocean.2010.05.003.

Huthnance, J.M., Van Aken, H.M., White, M., Barton, E.D., Le Cann, B., Ferreira Coelho, E., Alvarez Fanjul, E., Miller, P., and Vitorino, J., 2002. Ocean margin exchange — water flux estimates. *Journal of Marine Systems*, 32, 107-137.

Huybrechts, P., Gregory, J., Janssens, I., and Wilde, M., 2004. Modelling Antarctic and Greenland volume changes during the 20th and 21st centuries forced by GCM time slice integrations. *Global and Planetary Change*, 42, 83-105.

Iorga, M.C., and Lozier, M.S., 1999. Signatures of the Mediterranean outflow from a North Atlantic climatology 1. Salinity and density fields. *Journal of Geophysical Research*, 104 (C11), 25985-26009, doi:10.1029/1999JC900115.

Kalnay, E., et al., 1996. The NCEP/NCAR 40-Year Re- analysis Project. *Bulletin of the American Meteorology Society*, 77, 437471.

Karnauskas, K.B., Seager, R., Kaplan, A., Kushnir, Y., and Cane, M.A., 2009. Observed Strengthening of the Zonal Sea Surface Temperature Gradient across the Equatorial Pacific Ocean. *Journal of Climate*, 22, 4316-4321, doi:dx.doi.org/10.1175/2009JCLI2936.1.

Kida, S., Price, J.F., and Yang, J., 2008. The Upper-Oceanic Response to

Overflows: A Mechanism for the Azores Current. *Journal of Physical Oceanography*, 38, 880-895, doi:10.1175/2007JPO3750.1.

Kim, S. and Barth, J.A., 2011. Connectivity and larval dispersion along the Oregon coast estimated by numerical simulations. *Journal of Geophysical Research*, 116, C06002.

Lamas, L., Peliz, A., Ambar, I., Barbosa Aguiar, A., Maximenko, N., and Teles-Machado, A., 2010. Evidence of time-mean cyclonic cell southwest of Iberian Peninsula: The Mediterranean Outflow-driven β-plume?. *Geophysical Research Letters*, 37, L12606, doi:10.1029/2010GL043339.

Lambert, S.J., and Boer, G.J., 2001. CMIP1 evaluation and inter-comparison of coupled climate models. *Climate Dynamics*, 17, 83-106.

Large, W.G., McWilliams, J.C., and Doney, S.C., 1994. Oceanic vertical mixing: a review and a model with a nonlocal boundary-layer parameterization. *Reviews in Geophysics*, 32, 4, 363-403, doi:0.1029/94RG01872.

Large, W.G., and Pond, S., 1981. Open Ocean Momentum Flux Measurements in Moderate to Strong Winds. *Journal of Physical Oceanography*, 11, 324-336.

Lavín, A., Diaz del Rio, G., Cabanas, J.M., and Casas, G., 1991. Afloramiento en el Noroeste de la Peninsula Iberica. Indices de afloramiento para el punto 43^{o}N 11^{o}W, Periodo 1966-1989. *Informes Técnicos del Instituto Español de Oceanografía*, 91, 40 pp.

Lavín, A., Diaz del Rio, G., Casas, G., and Cabanas, J.M., 2000, Afloramiento en el Noroeste de la Peninsula Iberica. Indices de afloramiento para el punto 43^{o}N 11^{o}W, Periodo 1966-1989. *Informes Técnicos del Instituto Español de Oceanografía*, 15, 25 pp.

Le Cann, B., and Serpette, A., 2009. Intense warm and saline upper ocean inflow in the southern Bay of Biscay in autumn-winter 2006-2007. *Continental Shelf Research*, 29, 1014-1025, doi:10.1016/j.csr.2008.11.015.

Lemos, R.T., and Pires, H.O., 2004. The Upwelling Regime off the west Portuguese coast, 1941-2000. *International Journal of Climatology*, 24, 511-524.

Levitus, S., Antonov, J., and Boyer, T., 2005. Warming of the world ocean, 19552003. *Geophysical Research Letters*, 32, L02604, doi:10.1029/2004GL021592.

Levitus, S., Antonov, J.I., Boyer, T.P., Baranova, O.K., Garcia, H.E., Locarnini,

R.A., Mishonov, A.V., Reagan, J.R., Seidov, D., Yarosh, E.S., and Zweng M.M., 2012. World ocean heat content and thermosteric sea level change (0-2000 m), 1955-2010. *Geophysical Research Letters*, 39, L10603, doi:10.1029/2012GL051106.

Levitus, S., Antonov, J., Boyer, T.P., and Stephens, C., 2000. Warming of the world ocean. *Science*, 287, 2225-2229.

Levitus, S., Antonov, J.L., Wang, J., Delworth, T.L., Dixon, K.W., and Broccoli, A.J., 2001. Anthropogenic warming of Earth's climate system. *Science*, 292, 267-270.

Locarnini, R.A., Mishonov, A.V., Antonov, J.I., Boyer, T.P., Garcia, H.E., Baranova, O.K., Zweng, M.M. and Johnson, D.R., 2010. World Ocean Atlas 2009, Volume 1: Temperature. S. Levitus, Ed. *NOAA Atlas NESDIS 68*, U.S. Government Printing Office, Washington, D.C., 184 pp.

Lorenzo, M.N., Ramos, A.M., Taboada, J.J., and Gimeno, L., 2011. Changes in Present and Future Circulation Types Frequency in Northwest Iberian Peninsula. *PLoS ONE*, 6(1), e16201, doi:10.1371/journal.pone.0016201.

Macías, D., Franks, P.J.S., Ohman, M.D., and Landry, M.R., 2012. Modeling the effects of coastal wind- and wind-stress curl-driven upwellings on plankton dynamics in the Southern California current system. *Journal of Marine Systems*, 94, 107-119.

Marchesiello P., Debreu, L., and Couvelard, X., 2009. Spurious diapycnal mixing in terrain-following coordinate models: the problem and a solution. *Ocean Modelling*, 26, 3-4, 156-169, doi:10.1016/j.ocemod.2008.09.004.

Marchesiello, P., McWilliams, J.C., and Shchepetkin, A., 2001. Open boundary conditions for long-term integration of regional oceanic models. *Ocean Modelling*, 3, 1-20.

Marchesiello, P., McWilliams, J.C., and Shchepetkin, A., 2003. Equilibrium Structure and Dynamics of the California Current System. *Journal of Physical Oceanography*, 33, 753-783.

Marta-Almeida, M., Dubert, J., Peliz, A., and Queiroga, H., 2006, Influence of vertical migration pattern on retention of crab larvae in a seasonal upwelling system. *Marine Ecology Progress Series*, 307, 1-19.

Mason, E., Colas, F., Molemaker, J., Shchepetkin, A.F., Troupin, C., McWilliams, J.C., and Sangrà, P., 2011. Seasonal variability of the Canary Current: A numerical

study. *Journal of Geophysical Research*, 116, C06001, doi:10.1029/2010JC006665.

Mateus, M., Riflet, G., Chambel, P., Fernandes, L., Fernandes, R., Juliano, M., Campuzano, F., de Pablo, H., and Neves, R., 2012. An operational model for the West Iberian coast: products and services. *Ocean Science*, 8, 713-732.

Mazé, J.P., Arhan, M., and Mercier, H., 1997. Volume budget of the eastern boundary layer off the Iberian Peninsula. *Deep-Sea Research I*, 44, 9-10, 1543-1574. doi:10.1016/S0967-0637(97)00038-1.

McCartney, M.S., and Talley, L.D., 1982. The Subpolar Mode Water of the North Atlantic Ocean. *Journal of Physical Oceanography*, 12, 11691188.

Meehl, G.A., Covey, C., Delworth, T., Latif, M., McAvaney, B., Mitchell, J.F.B., Stouffer, R.J., and Taylor, K.E., 2007. The WCRP CMIP3 Multimodel Dataset: a new era in climate change research. *Bulletin of the American Meteorology Society*, 1383-1394.

Miranda, P.M.A., Alves, J.M.R., and Serra, N., 2012. Climate change and upwelling: response of Iberian upwelling to atmospheric forcing in a regional climate scenario. *Climate Dynamics*, doi: 10.1007/s00382-012-1442-9.

Mote, P.W. and Mantua, N.J., 2002. Coastal upwelling in a warmer future. *Geophysical Research Letters*, 29 (23), 2138, doi:10.1029/2002GL016086.

Nakićenović, N., Alcamo, J., Davis, G., de Vries, B., Fenhann, J., Gaffin, S., Gregory, K., Grubler, A., Jung, T.Y., Kram, T., La Rovere, E.L., Michaelis, L., Mori, S., Morita, T., Pepper, W., Pitcher, H.M., Price, L., Riahi, K., Roehrl, A., Rogner, H.-H., Sankovski, A., Schlesinger, M., Shukla, P., Smith, S.J., Swart, R., van Rooijen, S., Victor, N., and Dadi, Z., 2000. Special Report on Emissions Scenarios: A Special Report of Working Group III of the Intergovernmental Panel on Climate Change. *Cambridge University Press*, Cambridge, U.K., 599 pp.

Narayan, N., Paul, A., Mulitza, S., and Schulz, M., 2010. Trends in coastal upwelling intensity during the late 20th century, *Ocean Science Discussion*, 7, 335-360.

Neshyba, S., 1986. Poleward flows along eastern ocean boundaries (ed.). *Springer-Verlag Publisher*, ISBN 0387971750, 374 pp.

Nolasco, R., Cordeiro Pires, A., Cordeiro, N., Le Cann, B. and Dubert, J., 2013a. A high-resolution modeling study of the Western Iberian Margin mean and seasonal upper ocean circulation. *Ocean Dynamics*, doi:10.1007/s10236-013-0647-8.

Nolasco, R., Dubert, J., Domingues, C.P., Cordeiro Pires, A., and Queiroga, H., 2013b. Model-derived connectivity patterns along the western Iberian Peninsula: asymmetrical larval flow and source-sink cell. *Marine Ecology Progress Series*, doi:10.3354/meps10324.

Nykjaer, L., and Van Camp, L., 1994. Seasonal and interannual variability of coastal upwelling along northwest Africa and Portugal from 1981 to 1991. *Journal of Geophysical Research*, 99 (C7), doi: 10.1029/94JC00814.

Oliveira, P.B., Nolasco, R., Dubert, J., Moita, T., and Peliz, A., 2009. Surface temperature, chlorophyll and advection patterns during a summer upwelling event off central Portugal. *Continental Shelf Research*, 29, 5-6, 759-774.

Otero, P., Ruiz-Villarreal, M., and Peliz, A., 2008. Variability of river plumes off Northwest Iberia in response to wind events. *Journal of Marine Systems*, 72, 1-4, 238-255, doi:10.1016/j.jmarsys.2007.05.016.

Paillet, J., Arhan, M., and McCartney, M.S., 1998. Spreading of Labrador Sea Water in the eastern North Atlantic. *Journal of Geophysical Research*, 103 (C5), 10223-10239, doi:10.1029/98JC00262.

Pardo, P.C., Padín, X.A., Gilcoto, M., Farina-Busto, L., and Pérez, F.F., 2011. Evolution of upwelling systems coupled to the long-term variability in sea surface temperature and Ekman transport. *Climate Research*, 48, 231-246.

Pauly, D. and Christensen, V., 1995. Primary production required to sustain global fisheries. *Nature*, 374, 255-257.

Peliz, A., Dubert, J., Haidvogel, D.B., and Le Cann, B., 2003a. Generation and unstable evolution of a density-driven Eastern Poleward Current: The Iberian Poleward Current. *Journal of Geophysical Research*, 108 (C8), 3268, doi:10.1029/2002JC001443.

Peliz, A., Dubert, J., and Haidvogel, D.B., 2003b. Subinertial Response of a Density Driven Eastern Boundary Poleward Current to Wind Forcing. *Journal of Physical Oceanography*, 33, 1633-1650.

Peliz, A., Dubert, J., Marchesiello, P. and Teles-Machado, A., 2007. Surface circulation in the Gulf of Cadiz: Model and mean flow structure. *Journal of Geophysical Research*, 112, C11015.

Peliz, A., Dubert, J., Santos, A.M.P., Oliveira, P.B., Le Cann, B., 2005. Winter upper ocean circulation in the Western Iberian Basin — Fronts, Eddies and

Poleward Flows: an overview. *Deep-Sea Research I*, 52, 621-646.

Peliz, A., Rosa, T.L., Santos, A.M.P., and Pissarra, J.L., 2002. Fronts, jets, and counter-flows in the Western Iberian upwelling system. *Journal of Marine Systems*, 35, 61-77, doi:10.1016/S0924-7963(02)00076-3.

Peliz, A., Teles-Machado, A., Marchesiello, P., Dubert, J., and Garcia Lafuente, J., 2009. Filament generation off the Strait of Gibraltar in response to Gap winds. *Dynamics of Ocean and Atmosphere*, 46, 36-45, doi:j.dynatmoce.2008.08.002.

Penven, P., Echevin, V., Pasapera, J., Colas, F., and Tam, J., 2005. Average circulation, seasonal cycle, and mesoscale dynamics of the Peru Current System: A modeling approach. *Journal of Geophysical Research*, 110, C10021, doi:10.1029/2005JC002945.

Penven, P., Marchesiello, P., Debreu, L., and Lefevre, J., 2008. Software tools for pre- and post-processing of oceanic regional simulations. *Environmental Modelling Software*, 23, 5, 660-662, doi:10.1016/j.envsoft.2007.07.004.

Pérez, F.F., Padín, X.A., Pazos, Y., Gilcoto, M., Cabanas, M., Pardo, P.C., Doval, M.D. and Farina-Bustos, L., 2010. Plankton response to weakening of the Iberian coastal upwelling. *Global Change Biology*, 16, 1258-1267.

Pierce, D.W., Barnett, T.P., Santer, B.D., and Gleckler, P.J., 2009. Selecting global climate models for regional climate change studies. *Procedures of the National Academy of Science*, 106, 21, 8441-8446.

Pingree, R.D., and Le Cann, B., 1990. Structure, strength and seasonality of the slope currents in the Bay of Biscay region. *Journal of Marine Biology Association of the UK*, 70, 857-885, doi:10.1017/S0025315400059117.

Pond, S., and Pickard, G.L., 1983. Introductory Dynamical Oceanography. *Pergamon Press*, Oxford, 2nd edition, ISBN: 0-08-028728-X.

Pope, V.D., Gallani, M.L., Rowntree, P.R., and Stratton, R.A., 2000. The impact of new physical parametrizations in the Hadley Centre climate model: HadAM3. *Climate Dynamics*, 16, 2-3, 123-146 doi:10.1007/s003820050009.

Preisendorfer, R.W., 1988. Principal component analysis in meteorology and oceanography. *Elsevier*, Ed. Curtis D. Mobley, Vol. 17.

Räisänen, J., and Palmer, T.N., 2001. A Probability and Decision-Model Analysis of a Multimodel Ensemble of Climate Change Simulations. *Journal of Climate*, 14, 3212-3226.

Ramos, A.M., Cordeiro Pires, A., Sousa, P.M., and Trigo, R.M., 2013. The use of circulation weather types to predict upwelling activity along the Western Iberian Peninsula coast. *Continental Shelf Research*, 69, 38-51, http://dx.doi.org/10.1016/j.csr.2013.08.019.

Reboreda, R., Castro, C.G., Álvarez-Salgado, X.A., Nolasco, R., Cordeiro, N., Queiroga, H., and Dubert, J., in review. Oxygen in the Iberian margin: a modelling study. *Progress in Oceanography*.

Reboreda, R., Nolasco, R., Cordeiro, N., Castro, C.G., Álvarez-Salgado, X.A., Queiroga, H., and Dubert, J., submitted. A three dimensional modeling study of the interannual variability (2001-2010) of chlorophyll in the Iberian margin. *Journal of Sea Research*.

Relvas, P., Barton, E.D., Dubert, J., Oliveira, P.B., Peliz, A., da Silva, J.C.B., and Santos, A.M.P., 2007. Physical oceanography of the western Iberia ecosystem: Latest views and challenges. *Progress in Oceanography*, 74, 149-173.

Relvas, P., Luis, J., and Santos, A.M.P., 2009. Importance of the mesoscale in the decadal changes observed in the northern Canary upwelling system. *Geophysical Research Letters*, 36, L22601.

Reynaud, T., Legrand, P., Mercier, H., and Barnier, B., 1998. A new analysis of hydrographic data in the Atlantic and its application to an inverse modeling study. *International WOCE Newsletters*, 32, 29-31.

Richardson, P.L, Bower, A.S., and Zenk, W., 2000. A census of Meddies tracked by floats. *Progress In Oceanography*, 45, 2, 209-250.

Ríos, A.F., Pérez, F.F., and Fraga, F., 1992. Water masses in the upper and middle North Atlantic Ocean east of the Azores. *Deep-Sea Research I*, 39, 3-4, 645-658. doi:10.1016/0198-0149(92)90093-9.

Rivas, D. and Samelson, R.M., 2011. A numerical modeling study of the upwelling source waters along the Oregon coast during 2005. *Journal of Physical Oceanography*, 41, 88-112.

Roeckner, E., Bäuml, G., Bonaventura, L., Brokopf, R., Esch, M., Giorgetta, M., Hagemann, S., Kirchner, I., Kornblueh, L., Manzini, E., Rhodin, A., Schlese, U., Schulzweida, U., and Tompkins, A., 2003. The atmospheric general circulation model ECHAM 5. PART I: Model description. *Max Planck Institute for Meteorology Rep*, 127 pp.

Roy, C., and Reason, C., 2001. ENSO related modulation of coastal upwelling in the eastern Atlantic. *Progress in Oceanography*, 49, 245-255.

Røed, L.P., and Shi, X.B., 1999. A numerical study of the dynamics and energetics of cool filaments, jets and eddies of the Iberian Peninsula. *Journal of Geophysical Research*, 104 (C12), 29817-29841, doi:10.1029/1999JC900175.

Ruiz-Villarreal, M., Álvarez-Salgado, X.A., Cabanas, J.M., Fernández-Pérez, F., González-Castro, C., Herrera-Cortijo, J.L., Piedracoba-Varela, S., and Rosón-Porto, G., 2008. Variabilidade Climática e Tendencias Decadais nos Forzamentos Meteorolóxicos e as Propiedades das Augas Adjacentes a Galiza. Evidencias e Impactos do Cambio Climtico en Galicia, chapter 13, Resultados do proxecto Xunta da Galiza, Spain (http://siam.cmati.xunta.es/resultados-do-proxecto)

Russell, G.L., Miller, J.R., and Rind, D., 1995. A coupled atmosphere-ocean model for transient climate change studies. *Atmosphere-Ocean*, 33, 4, 683-730. doi: 10.1080/07055900.1995.9649550.

Russell, J.L., Stouffer, R.J., and Dixon, K.W., 2005. Intercomparison of the Southern Ocean Circulations in IPCC Coupled Model Control Simulations. *Journal of Climate*, 19, 4560-4575.

Salas-Mélia, D., Chauvin, F., Déqué, M., Douville, H., Guérémy, J.F., Marquet, P., Planton, S., Royer, J.F., and Tyteca, S., 2005. Description and validation of the CNRM-CM3 global coupled model. *CNRM working note*, 103.

Santos, A.M.P., Kasmin, A.S. and Peliz, A., 2005. Decadal changes in the Canary upwelling system as revealed by satellite observations: Their impact on productivity. *Journal of Marine Research*, 63, 359-379.

Saunders, P.M., 1982, Circulation in the eastern North Atlantic. *Journal of Marine Research*, 40, 641-657.

Seidel, D.J., Fu, Q., Randel, W.J., and Reichler, T.J., 2008. Widening of the tropical belt in a changing climate. *Nature Geoscience*, 1, 21-24, doi:10.1038/ngeo.2007.38.

Serra, N., Ambar, I., and Boutov, D., 2010. Surface expression of Mediterranean Water dipoles and their contribution to the shelf/slope — open ocean exchange. *Ocean Science*, 6, 191-209.

Shchepetkin, A.F., and McWilliams, J.C., 2003. A method for computing horizontal pressure-gradient force in an oceanic model with a non-aligned vertical coordinate.

Journal of Geophysical Research, 108 (C3), 3090, doi:10.1029/2001JC001047.

Shchepetkin, A.F., and McWilliams, J.C., 2005. The regional oceanic modeling system (ROMS): a split-explicit, free-surface, topography-following-coordinate oceanic model. *Ocean Modelling*, 9, 4, 347-404.

Sibuet, J.-C., Monti, S., Loubrieu, B., Mazé, J.P., and Srivastava, S., 2004. Carte bathymétrique de l'Atlantique nord-est et du golfe de Gascogne: implications cinématiques. *Bulletin de la Société Géologique de France*, 175, 5, 429-442.

Snyder, M.A., Sloan, L.C., Diffenbaugh, N.S., and Bell, J.L., 2003. Future climate change and upwelling in the California Current. *Geophysical Research Letters*, 30, 15, 1823, doi:10.1029/2003GL017647.

Stevens, I., Hamann, M., Johnson, J.A., and Fiúza, A.F.G., 2000. Comparisons between a fine resolution model and observations in the Iberian shelf-slope region. *Journal of Marine Systems*, 26, 1, 53-74, doi:10.1016/S0924-7963(00)00038-5.

Stouffer, R.J., Yin, J., Gregory, J.M., Dixon, K.W., Spelman, M.J., Hurlin, W., Weaver, A.J., Eby, M., Flato, G.M., Hasumi, H., Hu, A., Jungclaus, J.H., Kamenkovich, I.V., Levermann, A., Montoya, M., Murakami, S., Nawrath, S., Oka, A., Peltier, W.R., Robitaille, D.Y., Sokolov, A., Vettoretti, G., and Weber, S.L., 2006. Investigating the Causes of the Response of the Thermohaline Circulation to Past and Future Climate Changes. *Journal of Climate*, 19, 1365-1387.

Talley, L.D., and McCartney, M.S., 1982. Distribution and Circulation of Labrador Sea Water. *Journal of Physical Oceanography*, 12, 11891205.

Tebaldi, C., and Knutti, R., 2007. The use of the multi-model ensemble in probabilistic climate projections. *Philosophical Transactions of the Royal Society A*, 365, 1857, 2053-2075, doi:10.1098/rsta.2007.2076.

Tomczak, M., and Godfrey J.S., 2003. Regional Oceanography: an Introduction. *Elsevier Science*, 2nd edition, pdf version 1.1, ISBN: 8170353068.

Torres, R., and Barton, E.D., 2006. Onset and development of the Iberian poleward flow along the Galician coast. *Continental Shelf Research*, 26, 10, 1134-1153, doi:10.1016/j.csr.2006.03.009.

Torres, R., and Barton, E.D., 2007. Onset of the Iberian upwelling along the Galician coast. *Continental Shelf Research*, 27, 13, 1759-1778, doi:10.1016/j.csr.2007.02.005.

Torres, R., Barton, E.D., Miller, P., and Fanjul, E., 2003. Spatial patterns of

wind and sea surface temperature in the Galician upwelling region. *Journal of Geophysical Research*, 108 (C4), 3130, doi:10.1029/2002JC001361.

Troupin, C., Machín, F., Ouberdous, M., Sirjacobs, D., Barth, A., and Beckers, J.-M., 2010. High-resolution climatology of the northeast Atlantic using Data-Interpolating Variational Analysis (Diva). *Journal of Geophysical Research*, 115, C08005, doi:10.1029/2009JC005512.

Veitch, J., Penven, P., and Shillington, F., 2010. Modeling Equilibrium Dynamics of the Benguela Current System. *Journal of Physical Oceanography*, 40, 9, 1942-1964.

Wang, M., Overland, J.E., and Bond, N.A., 2010. Climate projections for selected large marine ecosystems. *Journal of Marine Systems*, 79, 258-266.

Wilks, D., 2006. Statistical Methods in the Atmospheric Sciences. *International Geophysical Series*, 2nd ed., Vol. 91, Academic Press, 627 pp.

Woolings, T., 2010. Dynamical influences on European climate: an uncertain future. *Philosophical Transactions of the Royal Society A*, 368, 3733-3756, doi:10.1098/rsta.2010.0040.

Wooster, W.S., Bakun, A., and McLain, D.R., 1976. The seasonal upwelling cycle along the eastern boundary of the North Atlantic. *Journal of Marine Research*, 34, 131-141.

Yukimoto, S., Noda, A., Kitoh, A., Sugi, M., Kitamura, Y., Hosaka, M., Shibata, K., Maeda, S., and Uchiyama, T., 2001. The New Meteorological Research Institute Coupled GCM (MRI-CGCM2) — Model Climate and Variability. *Papers in Meteorology and Geophysics*, 51, 2, 47-88.

Zenk, W., and Armi, L., 1990. The complex spreading pattern of Mediterranean Water off the Portuguese continental slope. *Deep-Sea Research I*, 37, 12, 1805-1823, doi:10.1016/0198-0149(90)90079-B.